

**Alma Mater Studiorum
Università degli Studi di Bologna**

SCUOLA DI SCIENZE
Dipartimento di Fisica ed Astronomia
Corso di Laurea Magistrale in Astrofisica e Cosmologia

**Internal kinematics and stellar populations for the
largest sample to date of galaxies with
counter-rotating stellar disks**

Tesi di Laurea Magistrale

Presentata da:
Davide Bevacqua

Relatrice:
Chiar.ma Prof. Silvia Pellegrini

Correlatore:
Chiar.mo Prof. Michele Cappellari

**Sessione III
Anno Accademico 2019/2020**

“Noli turbare circulos meos.”

— Archimede, ultime parole.

Contents

Abstract	1
Sommario	3
1 Introduction	5
2 Dynamical description and kinematic classification of ETGs	9
2.1 The Jeans Equations	9
2.1.1 The anisotropy parameters	11
2.2 The SAURON and ATLAS ^{3D} surveys	12
2.2.1 Kinematic classification of ETGs	12
2.2.2 The anisotropy diagram revised	14
2.2.3 The $(\lambda_{Re}, \varepsilon)$ diagram	17
2.3 The 2σ -galaxies	19
2.3.1 Origin of the peaks in σ	20
2.3.2 Misclassification of 2σ -galaxies as NRRs	22
2.3.3 A new denomination for counter-rotating galaxies (CRD) and the problem with KDCs	25
2.3.4 Possible formation scenarios for CRDs	28
2.4 The MaNGA survey	31
3 Selection of a sample of CRDs from the MaNGA survey	35
3.1 Primary sample and basic visual selection	35
3.2 Further selection criteria	38
3.3 Final sample	45
4 Kinematics and Stellar Populations fitting	50
4.1 Analysis of the MaNGA data with pPXF	50
4.2 Stellar Kinematics	51
4.2.1 Hierarchical clustering of stellar templates	51
4.2.2 Resolution matching of the spectra and spatial binning	54
4.2.3 Single component fitting procedure	55
4.2.4 Two-component fits and χ^2 maps	58

4.2.5	How to read the χ^2 maps	61
4.3	Stellar populations fitting	67
4.3.1	Looking for evidences of different populations with regularized fits	68
5	Summary and Results	73
5.1	Summary on the kinematic class of CRDs	73
5.2	The largest sample of CRDs to date	73
5.3	Results on Kinematics	74
5.4	Results on Stellar Populations	76
5.5	Conclusions and Future Perspectives	79
A	pPXF	81
B	Kinematic and Stellar Population maps of the CRD sample	83
C	χ^2 maps	138
D	Stellar Population weights maps from regularized fits	149
	Aknowledgements	178

Abstract

The pioneering work of the SAURON and ATLAS^{3D} spectroscopic surveys provided a new classification of Early-Type Galaxies, based on the properties of their two-dimensional stellar kinematic maps. In this work we focus on the kinematic class of galaxies with two counter-rotating stellar disks, so far called “ 2σ -galaxies” because of the two peaks in the velocity dispersion map. These galaxies show a variety of observed properties, and we currently do not have a clear picture of how they form and evolve; this is mostly because not many counter-rotators have been found to date. The first major goal of this work was to use the statistical power of the newest integral-field survey MaNGA, which observed $\sim 10,000$ galaxies, to build a large sample of counter-rotating galaxies. Since in this survey the kinematic maps do not always show both evidences of counter-rotation and two peaks in σ , we carefully checked for the presence of at least one of these features to select galaxies candidate to host counter-rotators, and we introduced the acronym ‘CRD’ to designate them. To identify CRDs, we first selected a set of 603 galaxies from the DR16 of MaNGA, and then, by visually inspecting the kinematic maps provided by the survey Pipeline, and applying specific classification criteria, we produced a final sample of 53 CRDs, the largest to date for such galaxies. The second goal of this work was to produce the stellar velocity and velocity dispersion maps for the sample, and search for the presence of two kinematic components in the observed spectra; we found spectroscopically confirmed counter-rotating disks in about 1/3 of the sample. We then compared the velocity fields of the ionized gas emitting in $H\alpha$ and of the stars, and found that in most cases the gas corotates with one of the two stellar disks, but in many cases the gaseous and stellar disks are misaligned, suggesting recent gas accretion by an external source. Finally, we extracted and inspected the age and metallicity maps of the stellar population, looking for radial trends that can provide useful information on the star formation history, and on the formation of CRDs. From a preliminary analysis, we noted that almost all galaxies have higher metallicity in the central regions than in the outer ones; also, some galaxies show radial variations in age. Evidences of multimodality in age and metallicity have also been found by performing regularized fits in thirteen galaxies, suggesting the presence of different stellar populations. Overall, our results support different formation paths for the class of CRDs.

Sommario

Il lavoro pionieristico delle survey spettroscopiche SAURON e ATLAS^{3D} ha portato ad una nuova classificazione delle galassie di tipo ‘early’ basata sulle proprietà delle loro mappe cinematiche. Questo lavoro di tesi pone il focus sulla classe cinematica delle galassie aventi due dischi stellari controrotanti, finora denominate "2 σ -galaxies" per i due picchi nelle mappe della dispersione di velocità che le contraddistinguono. Tali galassie esibiscono una certa varietà nelle proprietà osservate, e non abbiamo ancora un quadro chiaro di come esse si formano ed evolvono; ciò è dovuto principalmente al fatto che ad oggi sono stati trovati solo pochi casi di galassie contro-rotanti. Uno dei principali obiettivi di questo lavoro è stato quello di servirsi del grande numero di galassie ($\sim 10,000$) osservate dalla nuova integral-field survey MaNGA, per costruire un grande campione di galassie contro-rotanti. Poiché le mappe cinematiche prodotte con i dati MaNGA non mostrano sempre entrambe le evidenze di contro-rotazione e dei due picchi in σ , abbiamo incluso nella nostra selezione tutte le galassie che mostrassero almeno una delle due caratteristiche cinematiche, e per designarle abbiamo introdotto l’acronimo ‘CRD’. Per identificare le CRD abbiamo prima selezionato un set di 603 galassie dalla DR16 di MaNGA, e in seguito, ispezionando visivamente le mappe cinematiche prodotte dalla Pipeline, utilizzando specifici criteri di classificazione, abbiamo ottenuto un campione finale di 53 CRDs, che è il più grande ad oggi. Il secondo obiettivo di questo lavoro è stato quello di produrre le mappe di velocità e dispersione di velocità stellari per l’intero campione, e di cercare evidenze di due componenti cinematiche nello spettro osservato; abbiamo ottenuto la conferma spettroscopica di dischi contro-rotanti in circa 1/3 del campione. In seguito, abbiamo confrontato le mappe di velocità stellare con quelle del gas ionizzato ($H\alpha$), e abbiamo trovato che nella maggior parte dei casi il gas corruota con uno dei due dischi stellari; tuttavia, in alcuni casi il disco gassoso è disallineato rispetto alla rotazione dei due dischi, il che suggerisce accrescimento recente di gas da una sorgente esterna. Infine, abbiamo estratto e ispezionato le mappe di età e metallicità della popolazione stellare, cercando evidenze di trend radiali, che possono fornire utili informazioni riguardo alla storia di formazione stellare, e quindi alla formazione delle CRD. Da una analisi preliminare, abbiamo trovato che quasi tutte le galassie hanno metallicità più elevata nelle regioni centrali che in quelle esterne; inoltre, alcune galassie mostrano variazioni radiali in età. Facendo fit regolarizzati, abbiamo poi trovato evidenze di multimodalità in età e metallicità in tredici galassie, il che suggerisce la presenza di popolazioni stellari differenti. Nel complesso, i nostri risultati supportano differenti meccanismi di formazione per la classe delle CRD.

Chapter 1

Introduction

In this chapter, we introduce the thesis work by giving a brief description of those galaxies classified as 'Early-Type', and of the newest developed technology to study them spectroscopically. Then, an overview of the thesis work is presented.

In 1926 Edwin Hubble proposed a classification scheme for galaxies, based on their morphological appearance. Three main classes were distinguished: galaxies with evidences of spiral arms (S or SB, the latter for spirals with a bar), galaxies with elliptical shape (E)¹ and galaxies with irregular shape (Irr). Conjecturing an evolutionary sequence along with the morphological one, Hubble called the ellipticals "Early-Type galaxies" (ETGs) and the spirals "Late-Type galaxies" (LTGs), since he thought ETGs could somehow develop spiral arms and thus evolve into LTGs. ETGs also included the so called lenticular (S0) galaxies, that were considered the joining link between the two main classes. Regardless of the fact that we now know that ETGs are actually typically older than LTGs, and that, contrary to Hubble's supposition, the latter are often the progenitors of the former, the original nomenclature is still widely used.

For a long time, very little was known about the internal dynamics of ETGs, and the flattening was thought to be caused by the rotation of stars. However, in the '70s measurements of their rotation of ETGs became available: from these observations, it was clear that ETGs exhibit a rich variety in shapes and internal dynamics. In particular, it was evident that more massive ETGs were slowly rotating triaxial systems, oppositely to the previous idea of systems with isotropic rotation. Thanks to this main breakthrough, subsequent studies on the structure and dynamics of ETGs have led to a constantly deeper comprehension of these objects, allowing for a better understanding of the evolution of galaxies in general.

Starting from the Hubble classification of galaxies, our knowledge of the structure of galaxies in general, and of ETGs in particular, has been constantly enriched thanks to the development of new observational techniques and innovative technologies used to study them. One of the major technological advance of the last two decades is the

¹Based on their observed ellipticity $\varepsilon = 1 - b/a$, with b/a being the ratio between the minor and major semi-axes, E-galaxies are subclassified as 'EN', with $N = 10\varepsilon$: ellipticals span in shape from spherical, with $\varepsilon = 0$ (E0), to the the largest observed flattening $\varepsilon = 0.7$ (E7).

Integral-Field Spectroscopy (IFS). The general idea of IFS is to combine imaging and spectroscopy into single observations: the output of an observation is indeed a three dimensional datacube containing the 2D-image of the observed object and, along the third dimension, a spectrum for each pixel of the image. A visual representation of a datacube is shown in Figure 1.1. In particular, this technology brought us to the best understanding of the structure of ETGs we have so far, thanks to the capacity to extract their kinematical properties locally. In fact, since we can obtain a spectrum at every position on a grid of sky coordinates covering a galaxy image, IFS provides us with *local* information about the stellar and gas kinematics as well as stellar population properties.

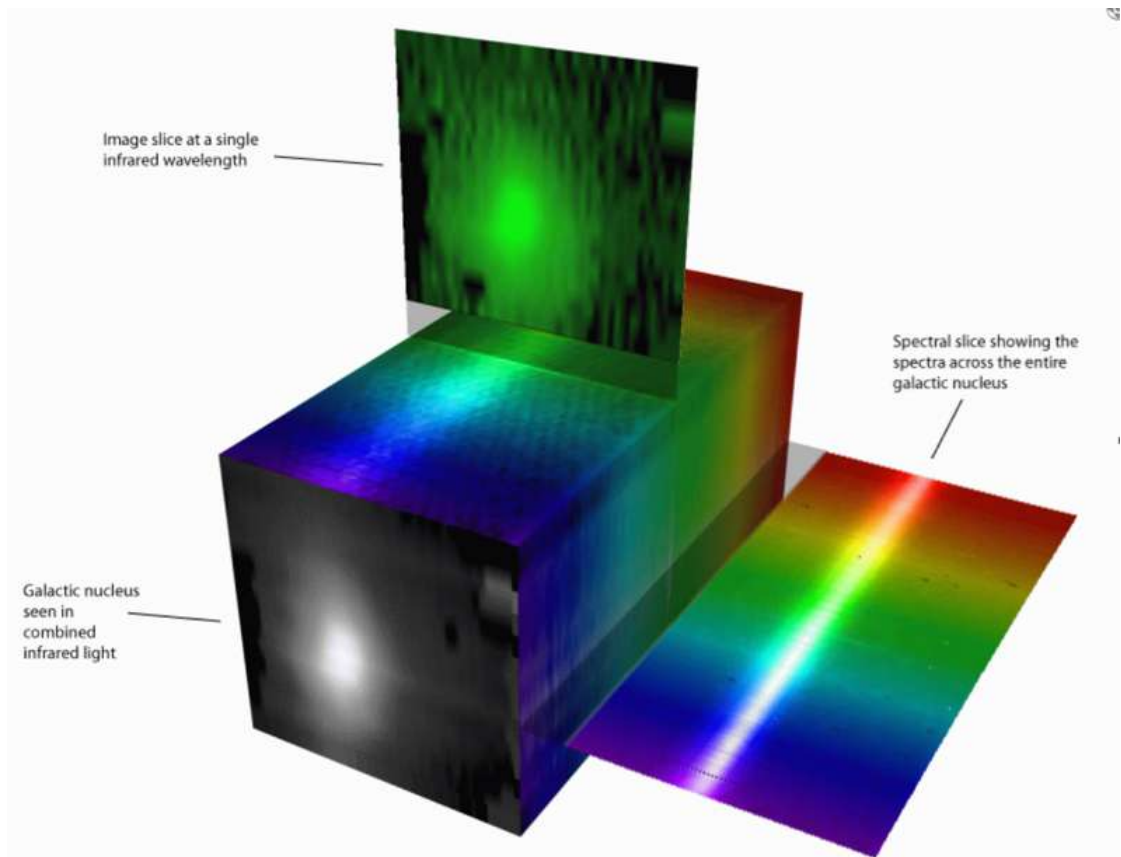


Figure 1.1: Visual representation of a datacube. Image credit: Stephen Todd and Douglas Pierce-Price.

First effective IFS prototypes have been developed in the 90's, but it took a decade of work to improve their performances to an optimal result: that's when the first generation of IFS surveys, which targeted one galaxy at a time, was born. Among the others, the SAURON project first and the ATLAS^{3D} project later opened a new path to the comprehension of the intrinsic shape, structure and population, as well as formation history

and evolution of ETGs. One of the most outstanding results from IFS surveys is that galaxies exhibit a much richer variety of kinematic structures than previously thought. In particular, ETGs have been divided in five different classes, based on their kinematic appearance. The aim of this work is to study the stellar kinematics and populations of those galaxies with two counter-rotating stellar disks.

This work is organised as follows:

- In Chapter 2, we first shortly introduce the Jeans Equations for axisymmetric systems (2.1). Next, in section 2.2, we present the main results provided by the two IFS surveys SAURON and ATLAS^{3D}: the kinematic classification of ETGs, the revised anisotropy diagram and the new $(\lambda_{R_e}, \varepsilon)$ diagram, where λ_{R_e} is the spin parameter, a proxy for the angular momentum. In section 2.3, we focus on galaxies with two counter-rotating stellar disks, originally named 2σ -galaxies. In particular, we present the first counter-rotating galaxy ever discovered (NGC 4550), and we give a description of how the two peculiar peaks arise; then we discuss why these galaxies are regular rotators. Since in the kinematic maps we do not always see both evidences of counter-rotation and the two σ peaks, we introduce the acronym 'CRD' to designate galaxies which show at least one of the two evidences. Afterwards, we discuss the possible formation scenarios for CRDs, and compare them with observations. Finally, in section 2.4 we present one of the newest and the largest IFS survey, MaNGA, which provided the data for the galaxies studied in this work.
- In Chapter 3, we present the sample of MaNGA galaxies from which we selected a subsample of galaxies that exhibits the kinematic features of counter-rotators. First we describe the basic criteria for considering a galaxy as a CRD candidate; then, since the same kinematic features characterizing CRDs can appear in the kinematic maps of galaxies of other classes, we discuss the further accurate checks we made for a proper selection of CRDs. Finally, in section 3.3 we present our sample of best candidates for galaxies with two counter-rotating stellar disks, i.e. CRD candidates.
- In Chapter 4 we introduce pPXF, the Python package to fit the observed spectrum provided by MaNGA, which is described more in detail in Appendix A. Then, we describe the fitting method used for the extraction of the stellar kinematics maps, shown in Appendix B. To find spectroscopical evidences of two counter-rotating disks, we adopted the method of the χ^2 maps; Afterwards, we describe the fitting method used for the extraction of the stellar population properties; finally, we perform regularized fits to look for evidences of multiple populations (4.3.1).
- In Chapter 5 we summarize the thesis work and present the results of our analysis. Finally, we conclude by presenting the forthcoming work and the future perspective for the study of CRD-galaxies.

Chapter 2

Dynamical description and kinematic classification of ETGs

In this Chapter, we describe the structure and dynamics of ETGs, based on Integral-Field Spectroscopy observations from SAURON and ATLAS^{3D}. In particular, we discuss in detail the kinematic class of galaxies with two counter-rotating stellar disks. Finally, we present one of the latest Integral-Field surveys: MaNGA.

2.1 The Jeans Equations

In this section we will see how to describe a stellar system through the distribution of positions and velocities of its stars, and how to link this distribution to observable quantities via the Jeans Equations.

The collisionality of a system of N stars can be evaluated looking at the relaxation time, that represents the time scale needed for stars to change their orbit significantly, due to small encounters between themselves. The relaxation time can be approximated as $t_{relax} \simeq \frac{0.1N}{\ln N} t_{cross}$, where $t_{cross} = R/v$ is the crossing time, namely the time needed for a star with typical velocity v to cross the radius R of the system once. Since galaxies typically have ages shorter than their relaxation time, they are collisionless systems, and their dynamics is governed by the overall gravitational field rather than by local encounters between the stars.

A convenient way to describe a collisionless system of stars of equal mass is by defining a distribution function (DF) f such that $f(\mathbf{x}, \mathbf{v}, t) d^3\mathbf{x} d^3\mathbf{v}$ is the probability to find a star in the phase-space volume $d^3\mathbf{x} d^3\mathbf{v}$ around position \mathbf{x} and velocity \mathbf{v} at a certain time t . If the system is in a *steady state* under the gravitational influence of a potential Φ , the DF satisfies the Collisionless Boltzmann Equation:

$$\sum_{i=1}^3 \left(v_i \frac{\partial f}{\partial x_i} - \frac{\partial \Phi}{\partial x_i} \frac{\partial f}{\partial v_i} \right) = 0. \quad (2.1)$$

Given the probability per unit volume $\nu(\mathbf{x}) \equiv \int f(\mathbf{x}, \mathbf{v}) d^3\mathbf{v}$ of finding a star at \mathbf{x}

regardless of its velocity, we introduce, respectively, the first and second moments of f in v and the velocity-dispersion tensor as follows:

$$\overline{v_i}(\mathbf{x}) = \frac{1}{\nu(\mathbf{x})} \int v_i f(\mathbf{x}, \mathbf{v}) d^3 \mathbf{v} \quad (2.2)$$

$$\overline{v_i v_j}(\mathbf{x}) = \frac{1}{\nu(\mathbf{x})} \int v_i v_j f(\mathbf{x}, \mathbf{v}) d^3 \mathbf{v} \quad (2.3)$$

$$\sigma_{ij}^2 \equiv \frac{1}{\nu(\mathbf{x})} \int (v_i - \overline{v_i})(v_j - \overline{v_j}) f(\mathbf{x}, \mathbf{v}) d^3 \mathbf{v} = \overline{v_i v_j} - \overline{v_i} \overline{v_j} \quad (2.4)$$

where the equivalence in (2.4) follows from (2.2) and (2.3) when explicitly computing the terms inside the integral.

Notice that the velocity-dispersion tensor is symmetric, and therefore it can be diagonalized. The set of diagonalizing orthogonal axes $\hat{\mathbf{e}}_i(\mathbf{x})$, with σ_{11} , σ_{22} and σ_{33} being the semi-axis lengths, defines the so-called velocity ellipsoid. In the particular case of $\sigma_{11} = \sigma_{22} = \sigma_{33}$ the velocity ellipsoid is spherical and the system is said isotropic.

Using cylindrical coordinates (R, z, ϕ) , under the assumption of *axisymmetry* (implying $\partial\Phi/\partial\phi = \partial f/\partial\phi = 0$) we can rewrite equation (2.1) as:

$$v_R \frac{\partial f}{\partial R} + v_z \frac{\partial f}{\partial z} + \left(\frac{v_\phi^2}{R} - \frac{\partial\Phi}{\partial R} \right) \frac{\partial f}{\partial v_R} - \frac{\partial\Phi}{\partial z} \frac{\partial f}{\partial v_z} - \frac{v_R v_\phi}{R} \frac{\partial f}{\partial v_\phi} = 0 \quad (2.5)$$

Multiplying (2.5) by v_R and v_z respectively, and integrating over all velocities, we obtain the two Jeans Equations for an axisymmetric system:

$$JE : \begin{cases} \nu \frac{\overline{v_R^2 - v_\phi^2}}{R} + \frac{\partial(\nu \overline{v_R^2})}{\partial R} + \frac{\partial(\nu \overline{v_R v_z})}{\partial z} = -\nu \frac{\partial\Phi}{\partial R} \\ \nu \frac{\overline{v_R v_z}}{R} + \frac{\partial(\nu \overline{v_z^2})}{\partial z} + \frac{\partial(\nu \overline{v_R v_z})}{\partial R} = -\nu \frac{\partial\Phi}{\partial z}. \end{cases}$$

These equations are still quite general, and, even if one somehow knows Φ , the four quantities $\overline{v_R^2}$, $\overline{v_z^2}$, $\overline{v_\phi^2}$ and $\overline{v_R v_z}$ are unknown and do not uniquely specify a solution.

A unique solution for the JE can be provided by a proper choice of the shape of the velocity ellipsoid. For example, if we assume that the DF depends only on two integrals of motion $f = f(E, L_z)$ with E being the total energy and $L_z = Rv_\phi$ being the angular momentum component along the symmetry axis z , from equation (2.2) we have $\overline{v_R} = \overline{v_z} = 0$, while, from equation (2.3), $\overline{v_i v_j} = 0$ for $i \neq j$ and $\overline{v_R^2} = \overline{v_z^2}$ ($= \sigma_R^2 = \sigma_z^2 \neq \sigma_\phi^2$, using the simplified notation $\sigma_{ii} \equiv \sigma_i$). With these assumptions, the second JE then becomes:

$$\frac{\partial(\nu \overline{v_z^2})}{\partial z} = -\nu \frac{\partial\Phi}{\partial z} \quad (2.6)$$

Integrating this equation over z thus provides $\overline{v_z^2}$ which can be substituted in the first JE to $\overline{v_R^2}$ and, isolating $\overline{v_\phi^2}$, we get:

$$\overline{\nu v_\phi^2} = \overline{\nu v_R^2} + R \frac{\partial(\overline{\nu v_R^2})}{\partial R} + R\nu \frac{\partial\Phi}{\partial R} \quad (2.7)$$

If one knows ν and Φ , it is then possible to calculate all moments.

2.1.1 The anisotropy parameters

When studying the dynamics of a stellar system, it is useful to quantify the deviation of the velocity ellipsoid from isotropy. In the literature some parameters have been introduced to describe the shape of the velocity ellipsoid and thus characterize the anisotropy of a system.

From the virial equations we can define a tensor which quantifies the contribution to the kinetic energy from random motions as:

$$\Pi_{ij} \equiv \int \nu \sigma_{ij}^2 d^3\mathbf{x} . \quad (2.8)$$

Using again the cylindrical coordinates, we can introduce the so called global anisotropy parameter, which quantifies the degree of deviation from isotropy, as:

$$\delta \equiv 1 - \frac{2\Pi_{zz}}{\Pi_{RR} + \Pi_{\phi\phi}} , \quad (2.9)$$

We can also define two additional anisotropy parameters:

$$\beta_z \equiv 1 - \frac{\Pi_{zz}}{\Pi_{RR}} , \quad \gamma \equiv 1 - \frac{\Pi_{\phi\phi}}{\Pi_{RR}} . \quad (2.10)$$

With these definitions, β_z describes the global shape of the velocity dispersion tensor in the (v_R, v_z) plane (namely the z -flattening) and γ in the plane orthogonal to v_z . Note that if the anisotropy is spatially constant $\beta_z = 1 - (\sigma_z/\sigma_R)^2$ and $\gamma = 1 - (\sigma_\phi/\sigma_R)^2$.

In the next sections we will see how observed galaxies can be described by these parameters. The results we present often refer to dynamical models constructed with the method called Jeans Anisotropic Modeling (JAM) (Cappellari (2008)). These models are based on a generalization of the axisymmetric JE and they are supported by observations. In particular, three additional assumptions are made: (i) the total mass-to-light ratio is constant (ii) the velocity ellipsoid is aligned with the cylindrical coordinate system (R, ϕ, z) and (iii) the anisotropy is constant and quantified by $\overline{v_R^2} = b\overline{v_z^2}$, where b is a constant. By substituting (iii) in JE, one finds the new solution for $\overline{v_\phi^2}$, which is still very similar to (2.7), and for $b = 1$ the two solutions coincide. With these assumptions, one needs only three parameters to model the kinematics of the galaxy: the inclination, β_z , calculated as $\beta_z = 1 - 1/b$, and the mass-to-light ratio. These parameters are determined by fitting models with the observed kinematics.

The recovery of the observed mean velocities with JAM requires a photometric analysis; since a detailed description of the dynamical modeling is beyond the scope of this work, we address the reader to the reference paper Cappellari (2008) for details.

Here we observe that, with the solution for the (JE) and the best-fit parameters, one can model the streaming velocity $\overline{v_\phi}$ starting from $\overline{v_\phi^2} = \overline{v_\phi}^2 + \sigma_\phi^2$, then $\overline{v_\phi}^2 = \overline{v_\phi^2} - \sigma_\phi^2$. The simple assumption $\sigma_\phi^2 = \sigma_R^2$ produces a map of the mean velocity remarkably close to the observed one: in section 2.3.2 a comparison between observed mean velocities and JAM models is shown.

2.2 The SAURON and ATLAS^{3D} surveys

In the introduction, we have mentioned how the developing of the IFS technology provided important results allowing for a better comprehension of the kinematic structures of galaxies. In particular, with the SAURON survey it was possible to study the inner regions of 72 nearby galaxies, and one of its main results is the distinction of ETGs into 'slow' and 'fast' rotators (Emsellem et al. (2007)), which gives us a different and more physically meaningful distinction of these galaxies than the simple morphological classification into ellipticals 'E' and lenticulars 'S0'. This distinction reflects important differences in the structures of the two types: in general, slow rotators are massive and luminous systems, they have round morphologies and the kinematics are typically dominated by random motions; on the other hand, fast rotators are generally less massive and fainter, and they are consistent with axisymmetric oblate systems with significant amounts of ordered rotation.

Comparing these results with cosmological simulations can provide important constraints on the formation and evolution of ETGs. The sample of the SAURON survey, however, was too small and the selection criteria of galaxies impose restrictive biases for a quantitative statistical comparison. This is what led to the ATLAS^{3D} survey, where a sample of 260 early-type galaxies within the local 40 Mpc (redshift $z < 0.01$) have been observed. The ETGs were selected to sample a wide range of masses, shapes and morphologies, in order to get statistically substantial results. In the following sections we discuss the results from SAURON and ATLAS^{3D}; we refer to the review of Cappellari (2016a) (C16 for short) for an extensive discussion.

In section 2.2.1 we introduce the different kinematic classes observed by SAURON and ATLAS^{3D}, and discuss more in detail the distinction between slow and fast rotators. In section 2.2.2 we will present the anisotropy diagram, revised thanks to the IFS technology, and discuss the magenta line, which empirically separate the galaxies which exhibit regular rotation and galaxies with a complex velocity field, as introduced in 2.2.1. Finally, in section 2.2.3 we will introduce the (λ_R, ε) diagram.

2.2.1 Kinematic classification of ETGs

One of the major outcome of the SAURON and ATLAS^{3D} surveys is that they provided stellar velocity and velocity dispersion maps of hundreds of galaxies. Based on their kinematic maps, ETGs qualitatively divide into two main classes (Emsellem et al. (2004)): galaxies dominated by ordered rotation have been called regular rotators (RR), and, as a contrast, galaxies with complex kinematic structures have been called non-regular rotators (NRR). By inspecting their kinematic maps, RR constitute a uniform class of

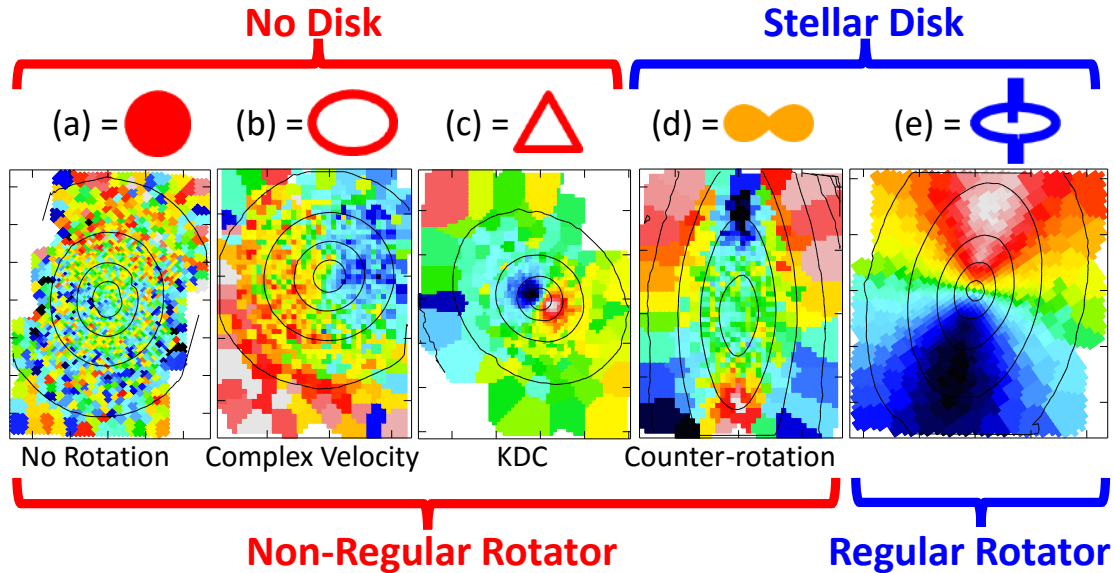


Figure 2.1: Kinematic classification of ETGs. Based on the properties of their kinematic maps, ETGs have been divided into five kinematic classes: (a) No clearly detectable rotation (NGC 4374), (b) clear but nonregular rotation (NGC 4552), (c) kinematically distinct cores (KDCs) (NGC 5813), (d) counter-rotating disks (NGC 4550), and (e) regular, extended, disk-like rotation (NGC 2974). Symbols above the maps correspond to the different morphological classes and will be often used. Figure from C16.

disk-like objects with regular kinematics. Oppositely, NRR exhibit a variety of kinematic structures which have been further divided into four subclasses (Krajnovic et al. (2011)), shown in Figure 2.1: (a) galaxies with no rotation (NR), (b) galaxies with clear but not bi-symmetric or irregular rotation (say complex rotation = CR), (c) galaxies with a kinematically decoupled core (KDC) and (d) galaxies with two counter-rotating stellar disks (2σ -galaxies). On the other hand, all RR exhibit a hourglass-shaped velocity map (e). We point out that the presence of stellar disks in (d) and (e), while generally absent in (a),(b) and (c), already suggests a crucial difference between these two groups of kinematic classes, which reflects different structures and evolutionary paths. In section 2.3.2 we will see how 2σ -galaxies have been misclassified as NRR, while truly being RR.

A second, more quantitative¹ classification, based on the amount of rotation, has been introduced by Emsellem et al. (2007), and ETGs have been divided into two main classes: slow rotators (SR) and fast rotators (FR). From the dynamical modeling of these galaxies (Cappellari et al. (2007)) it turned out that FR are consistent with oblate axisymmetric flattened systems, but also with a significant range in velocity anisotropy. They are less massive than SR, they may present relatively recent star formation and

¹See equation (2.20) in section section 2.2.3

they are α -enhanced. All FR with sufficiently high inclination have photometric evidences for the presence of disks; conversely, at low inclinations disks cannot be distinguished using photometry. However, dynamical models show that all apparently round and non-disky *fast* rotators are in fact inclined disks, and they are intrinsically quite flat. As a result, given their intrinsic nature, they seem to form a parallel sequence to spiral galaxies (Cappellari et al. (2011)). On the other hand, SR are very different. They are intrinsically rounder than FR, they are in general triaxial, they have evidences of kinematic twists and they typically do not have significant net rotation, with the exception for those galaxies with a kinematically decoupled core. SR are older and more massive than FR, they are passive and alpha-enhanced. They essentially reflect our classical idea of ETGs and they form an empirically separated class from FR and spirals (Cappellari et al. (2011)).

The difference between the two classifications, RR and NRR versus FR and SR, is that the former relies on the appearances of kinematic maps, that can be regular or non regular, while the latter is a quantitative distinction between galaxies that have high or low rotation. Though, broadly speaking, with the exception of 2σ -galaxies, NRR are also SR and RR are also FR.

2.2.2 The anisotropy diagram revised

The main observables used to study the kinematics of ETGs are the mean velocity V and the velocity dispersion σ . To characterize the degree of rotational support and quantify the deviation from isotropy, the so called anisotropy diagram has been introduced (Binney and Tremaine (1987)). In this diagram, the observed ratios between V and σ of galaxies are plotted versus the apparent flattening ε . Before the IFS, the kinematics were measured along the major axis using long-slit spectroscopy, and the diagram was constructed based on these observables. Afterwards, with the advent of IFS, it was possible to introduce an extended and improved formulation of the diagram (Binney (2005)), using integral-field data. It has been defined (Cappellari et al. (2007)):

$$\left(\frac{V}{\sigma}\right)_e^2 \equiv \frac{\sum_{n=1}^N F_n V_n^2}{\sum_{n=1}^N F_n \sigma_n^2} \quad (2.11)$$

where the ' e ' written in subscript indicates that measurements are extended to the effective radius R_e . Here, F_n is the flux of the n -th spatial bin and V_n and σ_n are the corresponding measured mean velocity and dispersion. Then, introducing the notation $\langle \cdot \rangle$ for a luminosity weighted average of a certain quantity over the sky, the ellipticity is defined as:

$$(1 - \varepsilon)^2 = \frac{\langle y^2 \rangle}{\langle x^2 \rangle} = \frac{\sum_{n=1}^N F_n y_n^2}{\sum_{n=1}^N F_n x_n^2} \quad (2.12)$$

where the (x, y) coordinates are centered on the galaxy nucleus and give the position in the plane of the sky.

These observed properties have been compared with theoretical predictions; in particular, motivated by observations (see below), the comparison has been made with axisymmetric models with oblate velocity ellipsoid ($\beta_z = \delta$ and $\gamma = 0$, see equations (2.9)

and (2.10)). As shown by Binney (2005) for such models with *intrinsic* ellipticity ε_{intr} and viewed *edge-on*, we have:

$$\frac{\langle V^2 \rangle}{\langle \sigma^2 \rangle} = \frac{(1 - \delta)\Omega(e) - 1}{\alpha(1 - \delta)\Omega(e) + 1} \quad (2.13)$$

with:

$$\Omega(e) = \frac{0.5[(\arcsin e)/\sqrt{1 - e^2} - e]}{e - (\arcsin e)\sqrt{1 - e^2}} \quad , \quad e = \sqrt{1 - (1 - \varepsilon_{intr})^2} \quad (2.14)$$

where α is a dimensionless number that depends on how the streaming velocity v_ϕ and the stellar density are distributed in the meridional plane. A value of $\alpha \approx 0.15$ has been found to be a good representation of real galaxies.

To compare the theoretical ratio, $\langle V^2 \rangle / \langle \sigma^2 \rangle$, with the observed one, $(V/\sigma)_e^2$, the summation over N should extend to infinite radii and ε should be constant with radius. In practice, the summation is limited to the largest observed radius, which for ATLAS^{3D} is typically $1-2R_e$. More precisely, the luminosity weighting is performed within an ellipse which encloses half of the projected total galaxy light, that has area $A = \pi R_e^2$ and semi-major axis $a = R_e/\sqrt{1 - \varepsilon}$. The observed values of $(V/\sigma)_e$ extended to $1R_e$ are expected to deviate no more than 10% from the values they should assume if extended to infinite radii (Cappellari et al. (2007), Emsellem et al. (2011)). This means that we can consider measurements extending to R_e appropriate for a comparison with the predictions provided by models. Observed values of $(V/\sigma)_e$ and ε are plotted in the anisotropy diagram shown in Figure 2.2.

RR, on average, have significant anisotropy δ , and their velocity ellipsoid is typically oblate (Cappellari et al. (2007)): in terms of the parameters introduced in section 2.1.1, this means $\delta \sim \beta_z$ and $\gamma \sim 0$, typically $\beta_z \gtrsim 0$. Another important finding is that β_z correlates with the intrinsic ellipticity: the β_z inferred from models for RR appear to be always lower than the empirical¹ linear relation:

$$\delta \approx \beta_z = 0.7 \times \varepsilon_{intr} \quad (2.15)$$

Combining (2.13) with (2.15), we obtain the relation plotted on the anisotropy diagram of Figure 2.2 with a magenta line.

The values $(V/\sigma)_e$ and ε plotted in Figure 2.2 are *projected* values, for galaxies are observed at inclination i (with $i = 90^\circ$ being *edge-on*); these observed quantities are related to the *edge-on* values $(V/\sigma)^{edge-on}$ and ε_{intr} by the following equations:

$$\left(\frac{V}{\sigma}\right)_e = \left(\frac{V}{\sigma}\right)_e^{edge-on} \frac{\sin i}{\sqrt{1 - \delta \cos^2 i}} \quad (2.16)$$

$$\varepsilon = 1 - \sqrt{1 + \varepsilon_{intr}(\varepsilon_{intr} - 2) \sin^2 i} \quad (2.17)$$

¹Wang et al. (2020) have recently found a physical explanation for this relation.

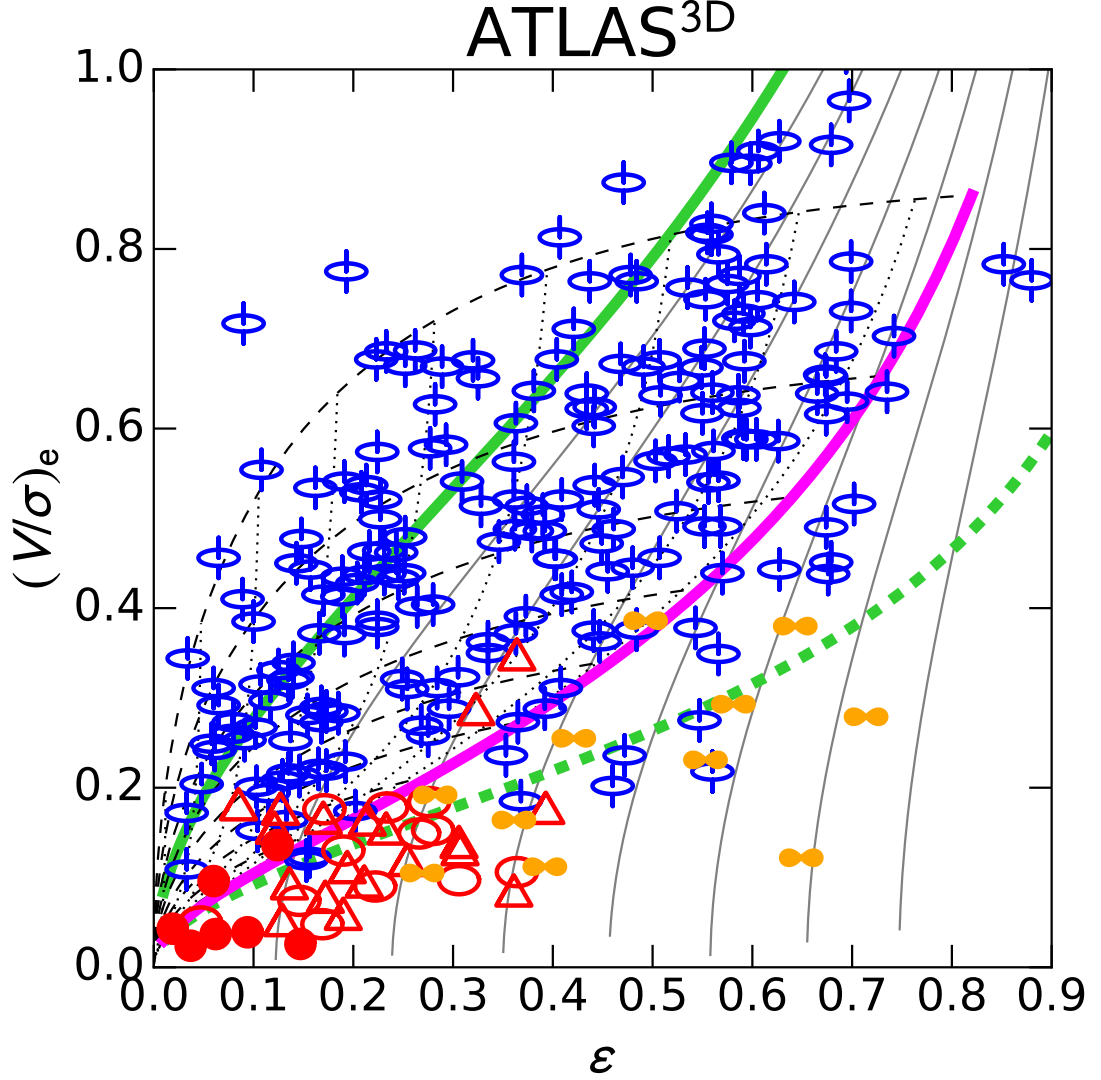


Figure 2.2: The anisotropy diagram. The plotted data are the observed values of $(V/\sigma)_e$ and ε of galaxies from ATLAS^{3D}. Symbols are the same used in Figure 2.1 for the different kinematical classes. The magenta line represents the relation $\delta = 0.7 \times \varepsilon_{intr}$; the black dotted and dashed lines are its projections with fixed intrinsic ellipticity but varying inclination and fixed inclination but varying intrinsic ellipticity, respectively. The solid green line is the equation (2.16) for an edge-on isotropic rotator ($\delta = 0$), and the thin grey lines show increasing global anisotropies, separated by $\Delta\delta = 0.1$. The dashed green line is an approximate separation between slow and fast rotators. Figure from C16.

We can make use of these equations to project the magenta line at different inclinations and intrinsic ellipticities. In particular, in Figure 2.2, by fixing i while varying ε_{intr} , the projections of the magenta line at different fixed inclinations are plotted with dotted black lines; then, by fixing ε_{intr} while varying i , the magenta line is plotted at different fixed intrinsic ellipticities with black dashed lines.

We can see from Figure 2.2 that RR are found to span a vast range of observed $(V/\sigma)_e$ and ε , but they are constrained by the 'leaf-like' region defined by the plotted magenta line and its projections. The fact that the distribution of RR can be well described by the magenta line and its projections, their lack of kinematic misalignment (see section 2.3.2), combined with results from dynamical models, indicates that these galaxies form a uniform family of disk-like galaxies. NRR, conversely, tend to lie below the magenta line and, excluding the 2σ -galaxies, they are confined to a smaller area of low $(V/\sigma)_e$ and ε on the diagram, which reflects their round-shape slowly rotating nature (section 2.2.1). The case of 2σ -galaxies needs a deeper analysis. First, their disk-like nature reflects the fact that they have a much wider distribution of observed ellipticity. They also appear to be frequently flat, at variance with the other NRR. Secondly, the reason why they lie below the magenta line is that the presence of two counter-rotating stellar disks strongly increases the random motion in the tangential direction ($\sigma_\phi > \sigma_R$, $\gamma < 0$) and lowers the mean velocity (being the sum of two disks with opposite directions of rotation); as a result, they have lower $(V/\sigma)_e$ than RR, although they are structurally similar, as it will be discussed. Notice that there are also some galaxies that are classified as RR which lie below the magenta line. These are likely transition objects containing enough counter-rotating stars to produce a detectable decrease of their global rotation, but not enough to produce clear evidence for counter-rotation in the σ field. There is, in fact, no reason to expect a sharp transition between the RR and the counter-rotating disk.

2.2.3 The $(\lambda_{R_e}, \varepsilon)$ diagram

Even though $(V/\sigma)_e$ is a useful tool to examine the dynamical status of a galaxy, it suffers from the major limitation of not considering the spatial distribution of the mean velocity V in the kinematic maps. As pointed out in Emsellem et al. 2007, this can cause an overlapping in the anisotropy diagram of galaxies with very different kinematic structure: for example, a KDC with a velocity peak in its inner (and most luminous) region and zero velocity outside the core, will have its global $(V/\sigma)_e$ amplified by the presence of the KDC, due to the luminosity weighting. For this reason, such a galaxy will occupy the same region on the diagram of a RR with similar $(V/\sigma)_e$ and ε , being the ratio unable to discriminate between large-scale rotation and little or no rotation with a central peak, despite their dramatically different kinematic appearance.

To take advantage of the spatial information, the so called spin parameter has been introduced:

$$\lambda_R(R) \equiv \frac{\langle R|V| \rangle}{\langle R\sqrt{V^2 + \sigma^2} \rangle} = \frac{\sum_{n=1}^N F_n R_n |V_n|}{\sum_{n=1}^N F_n R_n \sqrt{V_n^2 + \sigma_n^2}}, \quad (2.18)$$

where F_n is the flux inside the n -th bin, R_n its distance to the centre, and V_n and σ_n the corresponding mean stellar velocity and velocity dispersion. Notice that, due to the normalization to $\sqrt{V^2 + \sigma^2} \equiv V_{rms}$, the spin parameter is adimensional.

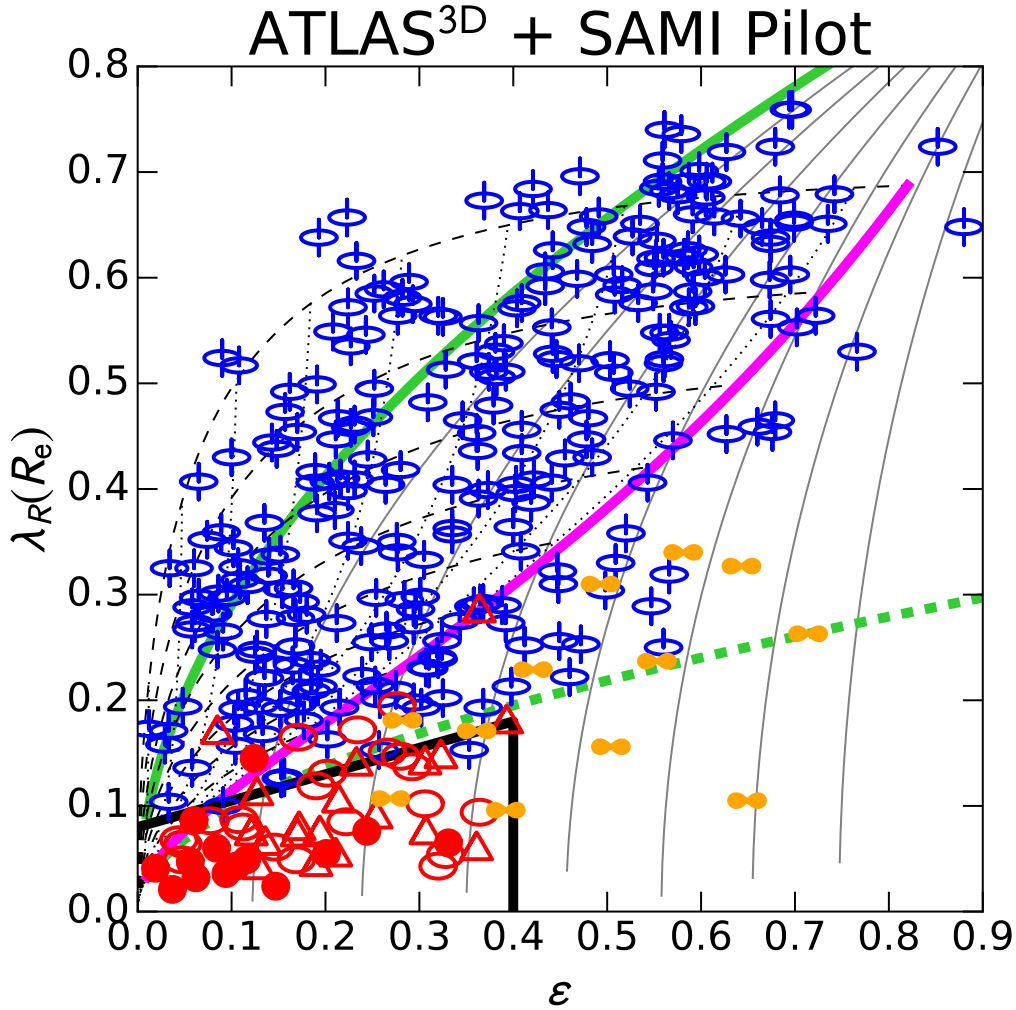


Figure 2.3: The $(\lambda_{R_e}, \epsilon)$ diagram. The plotted values are from the ATLAS^{3D} and SAMI Pilot surveys. Symbols and lines are the same of Figure 2.2. Additionally, the relation 2.20 which separates slow and fast rotators is plotted with a black solid line. Figure from C16.

As mentioned above, the spin parameter is a better discriminant when considering the separation between RR and NRR, and this is because the weighting of the stellar rotation depends both on the observed flux and on the size of the structure. While the difference may not be dramatic and would not impact ETGs with regular stellar velocity fields, it becomes relevant when considering classes of galaxies for which we observe non-regular kinematic features, as for the case of KDCs. This has motivated the use of λ_R instead of $(V/\sigma)_e$. In Figure 2.3 the same galaxies of Figure 2.2 and in addition galaxies from the SAMI-Pilot survey (Croom et al. (2012)) are plotted in the $(\lambda_{R_e}, \varepsilon)$ diagram, where we define $\lambda_{R_e} \equiv \lambda_R(R_e)$.

For simple oblate models, there's a tight correlation between λ_{R_e} and $(V/\sigma)_e$ and it can be approximated as:

$$\lambda_{R_e} \approx \frac{1.1(V/\sigma)_e}{\sqrt{1 + 1.21(V/\sigma)_e^2}} \quad (2.19)$$

We use this relation to plot the magenta line on the $(\lambda_{R_e}, \varepsilon)$ diagram.

It can be noticed that, in general, NRR still lie below the magenta line, with a clearer separation than in the anisotropy diagram; in addition, with the exception of the 2σ -galaxies, all NRR are grouped at low λ_{R_e} and ε , meaning that such galaxies are typically slowly rotating round systems. On the other hand, RR are still well described by the magenta line and its projections, and they span a wide range of λ_{R_e} and ε , meaning that they are in general fast rotating flat systems. To determine these differences quantitatively, Emsellem et al. (2011) *defined* a relation to quantitatively separate FR and SR: with ε_e as the apparent flattening at $1R_e$, in most cases SR are confined within the relation:

$$\lambda_{R_e} < 0.08 + \varepsilon_e/4 \quad \text{with} \quad \varepsilon_e < 0.4 \quad , \quad (2.20)$$

plotted using a solid black line on the diagram of Figure 2.3.

Notice that, in these terms, the dissociation of the 2σ -galaxies from the other NRR appears clearer, spanning a wider range both in λ_{R_e} and in ε , which remarks the different intrinsic nature of these objects.

2.3 The 2σ -galaxies

This section gives a deeper insight into those galaxies which present two counter-rotating stellar disks, so far classified as 2σ -galaxies, that are the subject of this thesis. We first present results of the first galaxy ever found with evidences of two counter-rotating disks, that is the well studied NGC 4550 (which is also the prototype galaxy for the class of 2σ -galaxies shown in Figure 2.1), and we successively explain the origin of the peculiar two peaks in the velocity dispersion profile. Afterwards, we stress out the distinction between 2σ -galaxies and other NRR, concluding that these galaxies are truly misclassified RR. In section 2.3.3 we introduce the term 'CRD' to designate galaxies with either evidence of counter-rotation or of the two σ peaks: " 2σ -galaxies" are then a subset of CRDs. However, evidences of counter-rotation are present in galaxies which host a KDC as well, and

they can give such galaxies similar kinematic appearances to 2σ -galaxies, even though the kinematic structure and intrinsic nature of the two kinematic classes are quite different. For this reason, in section 2.3.3 we discuss the main differences between the kinematic classes of KDC and those with two counter-rotating stellar disks and how to distinguish them. Finally, in section 2.3.4, we examine possible formation scenarios for these galaxies by investigating the predictions of the models and comparing them with observations.

2.3.1 Origin of the peaks in σ

Even though the presence of a counter-rotating *gaseous* disk is not rare, a secondary *stellar* disk is quite unusual, perhaps due to the difficulty of building up such a system: as our knowledge of galaxy formation indeed suggests, the obvious solution of merging two disks with opposite angular momentum does not generally work (see section 2.3.4). In 1992, Rubin et al. first discovered the presence of two cospatial counter-rotating stellar disks in the edge-on S0 galaxy NGC 4550, from the neat split of the absorption lines in its spectrum.

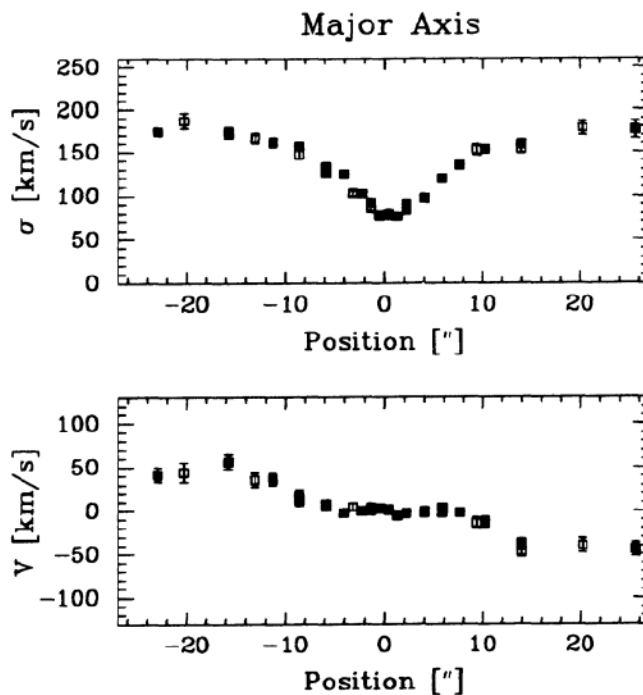


Figure 2.4: Velocity dispersion σ and mean velocity V of NGC4550. Data are measurements along the major axis using long-slit spectroscopy, and V and σ are obtained by fitting a single Gaussian model. Figure from Rix et al. (1992).

The uniqueness of NGC 4550 led Rix et al. (1992) to a more detailed analysis. They first assumed a single gaussian line-of-sight velocity distribution (LOSVD) to determine the best-fitting rotation velocity and velocity dispersion along the major axis. Their results are plotted in Figure 2.4. Focusing on the velocity dispersion plot, the galaxy shows the typical profile of these galaxies: a minimum in the central position and, along the major axis, the two characteristic specular peaks, for which they earned the name of 2σ -galaxies. The mean velocity is instead about 0 in central regions and slightly increases outwards. By fitting a two-Gaussian model, however, they found a striking bimodality in the LOSVD, which confirmed the presence of two counter-rotating disks, with measured mean velocities $v_1 = 150 \text{ km s}^{-1}$ and $v_2 = -110 \text{ km s}^{-1}$ and dispersions $\sigma_1 \approx 45 \text{ km s}^{-1}$ and $\sigma_2 \approx 60 \text{ km s}^{-1}$. Subsequent studies (Sarzi et al. (2006), Cappellari et al. (2007), Johnston et al. (2012)) have shown how the two disks have comparable sizes, masses, kinematics and line-strength, but different ages.

To understand how the two peaks in σ arise, we refer to the study of the lenticular galaxy IC 719 by Katkov et al. (2013). Figure 2.5 shows histograms of measured velocities and LOSVDs at different locations along the major axis. The grey lines correspond to the single Gaussian fit solution, while blue and green lines are the solutions for the two components fit using two Gaussians, with the red line being their sum.

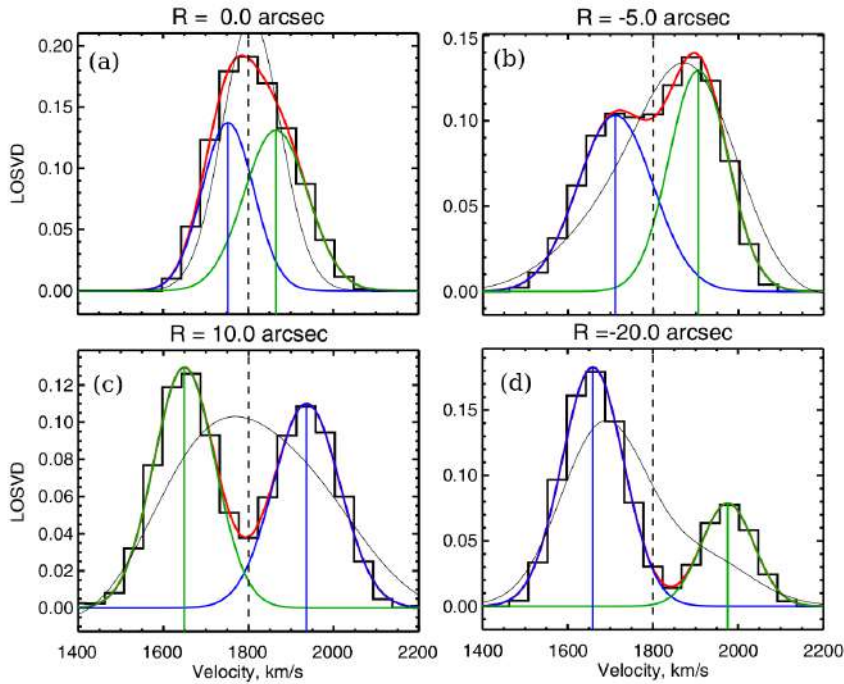


Figure 2.5: Cross-sections of the position-velocity diagram at different radial distances ($R = 0, -5, 10, -20$ arcsec). The dashed black line is the estimated systemic velocity. The solid black histograms are the recovered stellar LOSVDs at given R . The thin grey lines correspond to the stellar LOSVDs fitted with a single Gaussian. The red line is the sum of the two best-fit Gaussians, plotted in green and blue lines, of the two components model. Figure from Katkov et al. (2013)

We can see that in the central region of the galaxy (a), the single component solution well represents the data. This is because in the very inner regions of the galaxy the kinematics is dominated by the presence of the bulge. However, as we move farther out to few arcsec (b) the single component solution does not describe the data as well as in (a); conversely, the two components fit performs better. The distinction between the two components becomes more evident as we move farther out, in parallel with the increase of the dispersion of the single solution, that reaches its largest value at 10 arcsec (d)¹. Here we measure the largest dispersion of the single-component Gaussian, and it is peaked at the recession velocity of the galaxy, i.e. it is zero in the galaxy's reference frame. This is because the two components are well separated and they contribute almost equally to the global kinematics, so the single component Gaussian is wider, and, since the two disks have opposite directions of rotation, the resulting mean velocity is zero. Instead, in inner (b) or outer (d) regions, the single component solution is skewed towards the dominant disk, also resulting in a lower dispersion.

2.3.2 Misclassification of 2σ -galaxies as NRRs

We provide here a more detailed analysis of the many features characterizing counter-rotators. These features persuade us that these galaxies represent a parallel class to that of RR.

Kinematic misalignment. In Figure 2.6 the difference between the photometric major axis PA_{phot} , measured around $R \approx 3R_e$, and the kinematic major axis PA_{kin} , measured around $R \approx R_e$ of 340 galaxies from ATLAS^{3D} and SAMI pilot is plotted versus the apparent ellipticity. From this figure, it is evident that all RR have their kinematic and photometric axes aligned: the few deviant objects appear to be either interacting systems or strongly barred. Such a tight alignment for such a large sample implies axisymmetry for the class of RR. On the other hand, with the exception of some galaxies with very special configurations, most of NRR present misalignment, which is an indicator of tri-axiality. However, *all* the 2σ -galaxies respect this tight correlation, implying that they are axisymmetric systems as the RR.

Stellar rotation dichotomy. The disk nature of RR flattens these systems along the z -axis, and their velocity ellipsoid is (on average) oblate (2.2.2). Therefore, we can construct dynamical models with perfectly oblate velocity ellipsoids ($\sigma_\phi = \sigma_R$, see 2.1), predict the relative mean projected velocity field $V(\sigma_\phi = \sigma_R)$ and compare it with observations. Defining $\kappa = V_{obs}/V(\sigma_\phi = \sigma_R)$, we can check which galaxies deviate from this shape. In Figure 2.7, we can see that while all RR are well reproduced by this modeling, the vast majority of NRR clearly deviate from it, implying a net dichotomy between the two classes. However, the particular case of 2σ -galaxies deserves much

¹Notice that we firstly moved from 0 arcsec to -5 arcsec, and now we move to the opposite direction of the major axis at $R = 10$ arcsec. Nonetheless, because of the symmetry of the two peaks (see for example Figure 2.10), the qualitative analysis holds for $R = -10$ arcsec.

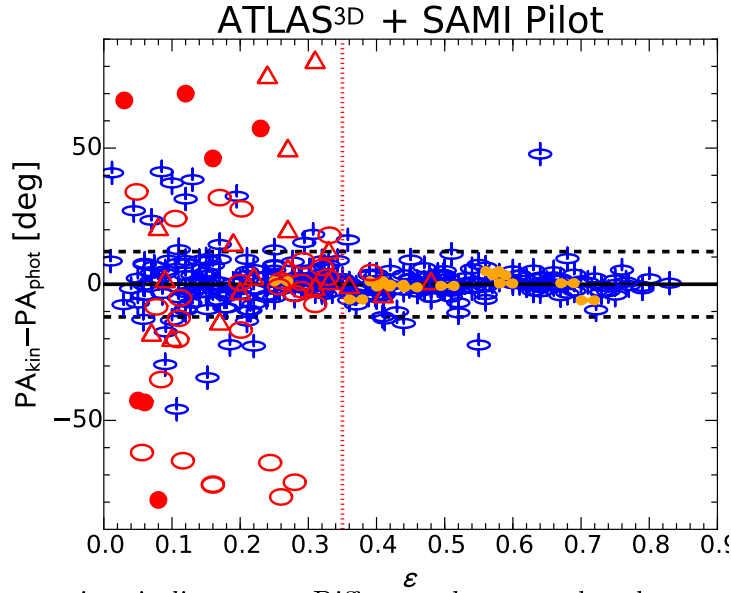


Figure 2.6: Kinematic misalignment. Difference between the photometric major axis PA_{phot} , measured around $R \approx 3R_e$, and the kinematic major axis PA_{kin} , measured around $R \approx R_e$. The plot includes data for 340 ETGs from ATLAS^{3D} and SAMI pilot. Figure from C16.

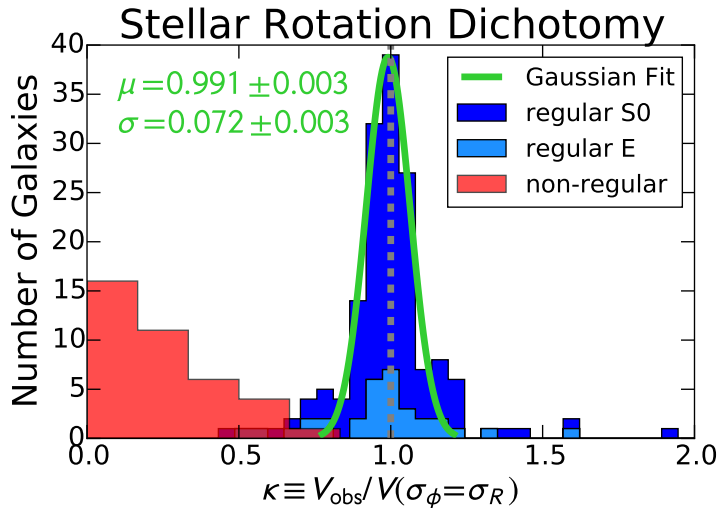


Figure 2.7: Histogram of the ratio κ between the observed velocity V_{obs} and the velocity $V(\sigma_\phi = \sigma_R)$ predicted by a JAM model (2.1). The values are extracted from model A of Cappellari et al. (2013b). The green line is a Gaussian fit to the histogram for the RR only. The distribution peaks with high accuracy at the value $\kappa \approx 1$, which corresponds to an oblate velocity ellipsoid. The NRRs have a completely different distribution, which peaks at $\kappa \approx 0$ and has a broad tail. Figure from C16.

carefulness. In fact, they are not well described by an oblate velocity ellipsoid, since the counter-rotation of the two stellar disks induces tangential anisotropy. However, by looking at the first two panels of Figure 2.8, we can see that the V_{rms} , which is independent of the sign of the velocity field (i.e. it is insensible to the counter-rotation), being a quadratic sum, is well described by models. By taking into account the counter-rotation, e.g. by reversing the sign of κ at a certain radius, we obtain a very good agreement between data and models for the mean velocity as well, as shown in the third and fourth panels in Figure 2.8. Then, the dispersion is obtained as $\sigma = \sqrt{V_{rms}^2 - V^2}$. Furthermore, by modeling the two counter-rotators separately, each of the two counter-rotating components has $\kappa \approx 1$: this is thus a strong evidence that the two disks are in fact two counter-rotating RR. There are eleven 2σ -galaxies in the ATLAS^{3D} sample, and their kinematic maps are all well reproduced by JAM models.

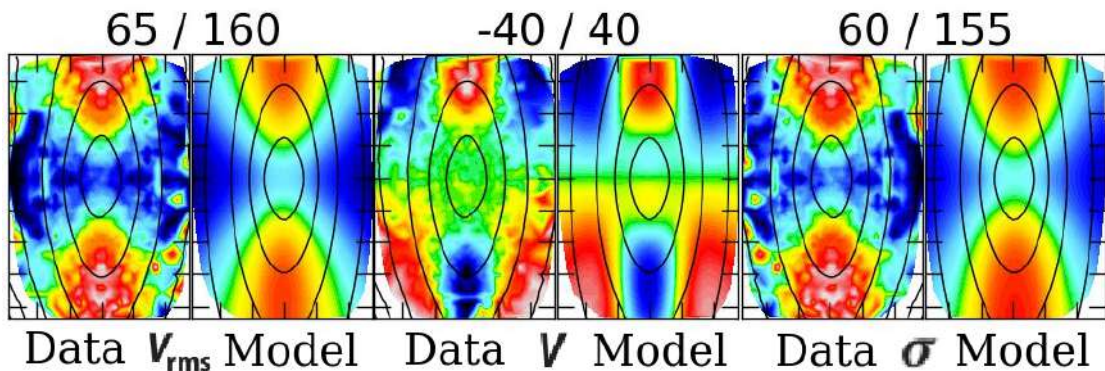


Figure 2.8: Comparison between data and model for NGC4550: V_{rms} (first two panels), mean V (third and fourth panels) and dispersion (fifth and sixth panels). The color scale ranges from low velocities in blue to high velocities in red, while the zero-velocities are in green. In superscript, the velocity ranges in km s^{-1} of each couple (data + model) of maps. The model assumes an oblate velocity ellipsoid, and the velocity is allowed to reverse its sign. The agreement between data and model confirms that the two disks, which globally produce a tangential anisotropy, are in fact oblate when considered separately. Figure from C16.

In conclusion, the tight alignment of the photometric and kinematic major axes, and the fact that the observed kinematics can be well reproduced by models of axisymmetric oblate systems when including two disks, are sufficient evidences to exclude 2σ -galaxies from the NRR classification and consider them as misclassified RR. Moreover, there are additional properties in support to this statement. For example, by looking at their photometry, NRR generally have boxy isophotes, while 2σ -galaxies typically have disk-like isophotes (Krajnović et al. (2013)); additionally, the surface brightness profile of the former usually has a core, while the latter does not (Krajnović et al. (2013)). Another difference is that most of NRR are confined within the equation (2.20), while 2σ -galaxies

are often found to be flatter than $\varepsilon = 0.4$ and tend to have higher λ_{R_e} . We highlight that these additional features are not observed for the whole classes of 2σ and NRR, and then they should not be taken for granted. Table 2.1 summarizes the main differences between 2σ -galaxies and NRR.

	2σ	NRR
Ψ^1	$< 15^\circ$	$> 15^\circ$
Symmetry	Axisymmetric	Triaxial
Rotators	Slow + Fast	Slow
ε	often > 0.4	always < 0.4
Isophotal shapes	Disky	Boxy
Core/Core-less	Core-less	Core

Table 2.1: Main differences between 2σ galaxies and NRR.

2.3.3 A new denomination for counter-rotating galaxies (CRD) and the problem with KDCs

All the galaxies with evidences of counter-rotating disks observed by ATLAS^{3D} exhibit the two σ peaks as well. Instead, the MaNGA survey (section 2.4), which provided the data for this work, does not always allow for the appearance of both features, due to the relatively low spatial resolution; for this reason, we introduce the acronym ‘CRD’, for ‘counter-rotating disks’, to designate all those galaxies which exhibit at least one of the two kinematic features: the inversion of the rotation pattern in the velocity field or the 2σ peaks in the dispersion map. As a consequence, this makes the class of 2σ -galaxies a subclass of CRD-galaxies.

Notice that not all galaxies with the two peaks in σ turn out to have two counter-rotating disks; for example in ATLAS^{3D} there is one case of a galaxy with a KDC exhibiting the 2σ appearance; this is NGC 5813, which has been accurately studied in Krajnovic et al. (2015): in Figure 2.9 the velocity and velocity dispersion maps of the galaxy are shown. From the dispersion map, it is evident the presence along the major axis of two symmetrical peaks (beside the central peak) coincident with the edge of the KDC. This has a striking resemblance to a 2σ -galaxy dispersion map: for a comparison, in Figure 2.10 the kinematic maps of the counter-rotating S0 galaxy NGC 5102 (Mitzkus et al. (2016)) are shown.

¹The kinematic misalignment is formally defined as $\sin(\Psi) = |\sin(PA_{phot}) - \sin(PA_{kin})|$

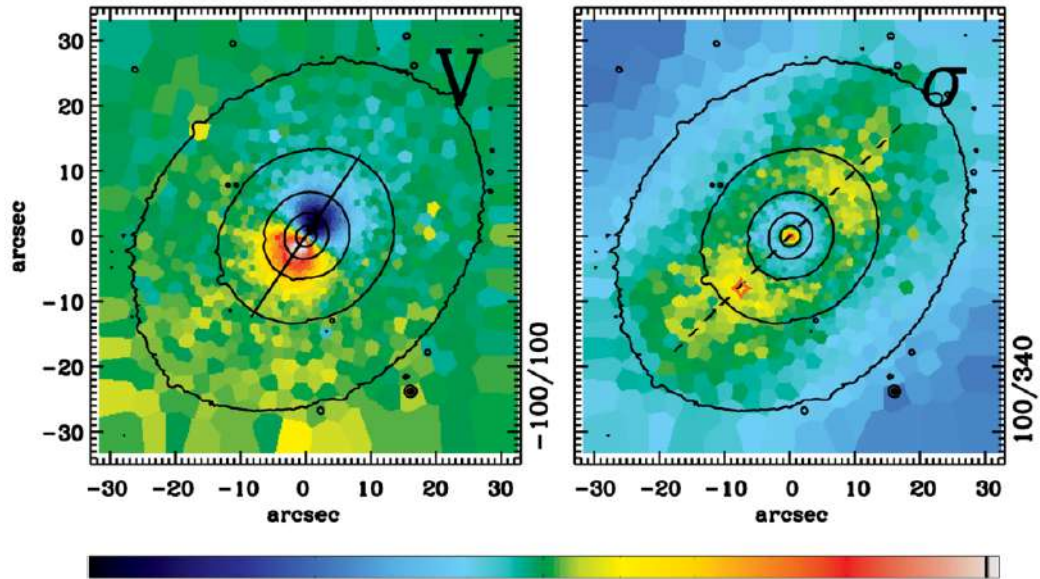


Figure 2.9: Velocity (left) and velocity dispersion (right) maps of NGC5813. The black contours are isophotes. The straight line on the mean velocity map shows the orientation of the KDC and the inner photometric major axis ($PA = 146^\circ$). The dashed line on the velocity dispersion map shows the outer (global) photometric major axis ($PA = 135^\circ$), which coincides with the orientation of the 2σ peaks. Velocities are in km s^{-1} . Figure from Krajnovic et al. (2015)

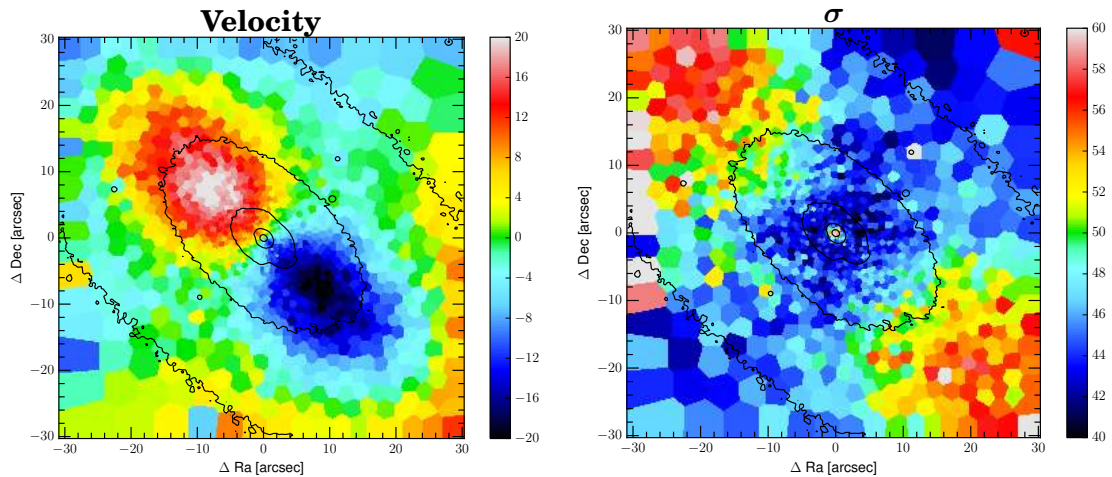


Figure 2.10: Velocity (left) and velocity dispersion (right) maps of NGC 5102. The black contours are the isophotes. Velocities are in km s^{-1} . Notice the peculiar peaks in the dispersion map, similar to those shown in the right panel of Figure 2.9. Figure from Mitzkus et al. (2016).

With a more careful inspection of the kinematic maps of galaxies with a 2σ kinematic appearance, some features can allow for the distinction between the two classes, those with a KDC and those with two counter-rotating stellar disks. First, we notice that NGC 5813 has $\varepsilon = 0.1$ within the region of the KDC and then it becomes flatter in the outer region ($\varepsilon = 0.27$ in the last isophote). This is not the case for NGC 5102 (and disk-like galaxies in general), which is typically flatter and has constant ellipticity. A second difference is the misalignment between the orientation of the KDC in the velocity map and the peaks in the dispersion map, which is related to the variation of the photometric angle and is a hint of triaxiality, while in section 2.3.2 we have seen how galaxies with two counter-rotating disks are well described by axisymmetric models.

Another feature which may help to distinguish CRDs from KDCs is the age. Even though we still do not have enough studies on the populations of the two disks, to date, all galaxies for which the two disks have been spectroscopically decomposed exhibit disks with different ages; we will discuss this subject in section 2.3.4. In KDCs, instead, the two components have the same age. Mass is also a possible discriminant for the two classes: in fact, CRDs typically have stellar masses $< 5 \times 10^{10} M_{\odot}$, while KDCs are mostly observed in slow rotators, which are typically massive galaxies ($M_{*} > 2 \times 10^{12} M_{\odot}$) (Cappellari et al. (2013)). Finally, the extension of a KDC in the velocity maps is always confined within the effective radius, while in CRDs the inversion of the rotation in the velocity map (which corresponds to the peaks in the dispersion map, along the major axis) occurs at $R \gtrsim 1R_e$. In Table 2.2 we summarize the main features that distinguish a galaxy with counter-rotating disks from a KDC galaxy. Since KDCs are mostly found in NRR, we refer to Table 2.1 for other differences. In Chapter 3 we will rely on these features for a proper classification of those galaxies with two counter-rotating stellar disks.

	CRD	KDC
Twists	No	Yes
Stellar Populations	Young + Old	Old
Rotation inversion	$R > R_e$	$R < R_e$
Stellar Mass	$< 5 \times 10^{10} M_{\odot}$	$> 2 \times 10^{12} M_{\odot}$

Table 2.2: Main observed differences between CRDs and KDCs.

Even though NGC 5813 is the only case with the two peaks in σ of the whole ATLAS^{3D} sample, it can not be considered simply as an outlier, for the sample of 2σ -galaxies in ATLAS^{3D} counts only eleven galaxies; then we can expect that a non negligible fraction of galaxies showing the peaks in the dispersion map may truly be KDCs in the MaNGA sample. In Chapter 3 we present our selection method for CRDs, and we remark the criteria to discern a KDC from a CRD; however, one has to consider the possibility of a misclassification whenever the kinematic maps do not allow to discern between the two cases. The galaxies that will be classified as CRDs are said to be ‘best-candidates’ in the light of the discussion made in this section, and in section 3.2.

2.3.4 Possible formation scenarios for CRDs

One of the most puzzling problems regarding CRDs is the process that drives the formation of two counter-rotating stellar disks and match all the observed features characterizing these galaxies; this is mainly due to the relatively small number of studies about counter-rotators and on the controversial results of such studies. Even though ATLAS^{3D} only included ETGs, a counter-rotating stellar disk can be found in spiral galaxies as well, and our study on CRDs is made regardless of the morphological types. Hereafter, we present a summary on the main possible formation scenarios for two counter-rotating stellar disks.

1. Gas accretion in retrograde orbit

- *Minor merger.* Numerical simulations by Thakar et al. (1997) predict that if a massive disk-like galaxy merges with a gas-rich dwarf galaxy in a retrograde orbit, the latter slowly enriches the former with gas that settles in a counter-rotating disk and then form stars. In this scenario, the counter-rotating stellar disk is less massive and less extended, younger and corotating with the gas; the two disks are expected to have different metallicities and α -enhancements. Notice that if a minor merger occurred recently (~ 1 Gyr), the resulting gaseous disk would be misaligned with respect to the stellar rotation (Jin et al. (2016)).
- *Episodic or prolonged accretion.* A counter-rotating stellar disk can be formed by prolonged or episodic accretion of gas, as predicted by simulations (Thakar and Ryden (1996), Thakar and Ryden (1998)). A clear example of a prolonged accretion is reported by Vergani et al. (2007), who found evidences of tidal bridges of neutral hydrogen linking the counter-rotating spiral galaxy NGC 5719 to its close companion galaxy. An episodic accretion has been advocated by Katkov et al. (2013) (see also Pizzella et al. (2018)) to explain the origin of the counter-rotating disk in IC 719 (shown in Figure 2.10); the galaxy is in fact surrounded by a cloud of neutral hydrogen that likely fuelled the gaseous disk and produced episodic events of star formation. From these scenarios we expect the counter-rotating disk to be less massive, younger and less metallic than the primary disk, and corotating with the gas. Again, a recent accretion

episod would result in a misalignment of the gas disk with respect to the stellar disks.

- *Cosmological filaments.* The simulations of Algorry et al. (2014) have shown how distinct filamentary cosmological structures with opposite spins can produce two counter-rotating stellar disks. Initially, the accretion from the two filaments occurs at the same time; the collisional nature of the gas ensures that only one stellar disk forms from gas, which has the same spin of the more massive filament, and whose properties are a mixture of those of the two filaments. After a few Gyr, the accretion along the major filaments stops, but the accretion process continues along the counter-rotating filament, which wipes out the remaining gas and forms the secondary counter-rotating component; the stars in the secondary disk have properties very similar to those of the main component, because the gas is a mixture of that of the second filament and what remained from the first filament. The two counter-rotating disks are then predicted to have different ages but similar metallicities; in particular, the counter-rotating disk is predicted to be younger, less massive, less extended and corotating with the gaseous disk.

2. **Major merger.** Most of major mergers are highly disruptive events, since they enormously heat the progenitor systems and result in a final morphology far from disk-like (Toomre 1977). However, Puerari and Pfenniger (2001) have shown that, with a fine tuning of the initial conditions, a merger between two equally massive disk galaxies with opposite rotations can reproduce the kinematics of the observed counter-rotators; this scenario has been confirmed by Crocker et al. (2009) who reproduced the observed properties of NGC 4550. These major merger simulations predict the two disks to be equally massive and to have the same spatial extension; further, assuming different stellar populations of the progenitors, the two disks are expected to have different ages and metallicities; finally, the corotation of the gas depends on its initial distribution in the two progenitors. This scenario also predicts a different thickness for the two disks, which is a feature observed, in NGC 4550 (Crocker et al. (2009), Johnston et al. (2012)).

3. **Internal instabilities.** Another scenario, suggested by Evans and Collett (1994), contemplates the possibility for a former elliptical galaxy with a triaxial potential or a bar to slowly evolve into an axisymmetric system with two identical counter-rotating stellar disks. The resulting counter-rotating disks are expected to have the same stellar population properties, as well as the same masses and sizes.

Even though few galaxies with two counter-rotating stellar disks have got their stellar populations disentangled (Coccatto et al. (2011), Johnston et al. (2012), Coccatto et al. (2012), Pizzella et al. (2014), Coccatto et al. (2015), Morelli et al. (2017))), they all present a net distinction in ages, thus setting aside the formation of counter-rotation from internal instabilities. To date, however, there is no standard formation scenario which is able to describe all the observed features. In NGC 5719 and IC 719, as discussed above,

evidences of neutral gas streams suggest the formation of the counter-rotating disks by accretion from either the companion galaxy or from the surrounding cloud. However, the other galaxies studied do not seem to have such a large reservoir of neutral hydrogen to form an important counter-rotating stellar disk. For isolated galaxies like NGC 4138 (Thakar et al. (1997), Pizzella et al. (2014)), NGC 3593 (Coccatto et al. (2012)) and NGC 488 (Katkov et al. (2016)), the minor merger scenario seems more suitable. Instead, the formation of counter-rotators by cosmological filaments predicted by models has been found consistent with NGC 4191 (Coccatto et al. (2015)). Finally, observations suggests that NGC 4550 (Crocker et al. (2009)) may instead have been formed from a major merger. In conclusion, it is clear that we do not have a standard model for the formation of counter-rotators, and different formation paths are possible for this kinematic class. Though, these scenarios still do not include all the observed features (see e.g. Morelli et al. (2017)). A wider sample of galaxies is obviously needed for a better understanding of the formation processes, and this is one of the main purposes of this thesis work. In Table 2.3 we summarize the properties predicted by the presented formation scenarios.

	Age	Metallicity	Mass	Size
Minor merger + Episodic or prolonged accretion	Older	Larger	More massive	More extended
	Younger	Lower	Less massive	Less extended
Cosmological filaments	Older	similar	More massive	More extended
	Younger		Less massive	Less extended
Major merger	Depending on the progenitors	Depending on the progenitors	Equal	Equal
Internal instabilities	Equal (Old)	Equal	Equal	Equal

Table 2.3: Summary table on the formation mechanisms for CRDs and the corresponding predicted properties. The text in red and blue represents the primary and secondary (co- and counter-rotating) disks; the text in green indicates that the two disks have the same properties.

2.4 The MaNGA survey

The pioneering work of SAURON and ATLAS^{3D} heralded a new era of integral-field unit (IFU) surveys. Integral field spectrographs are becoming more and more sophisticated since then: in particular, technological advances have brought us to a second generation of surveys which collect data from thousands of objects. The MaNGA (Mapping Nearby Galaxies at APO, where APO stands for Apache Point Observatory) survey Bundy et al. (2014) is the newest survey component of the Sloan Digital Sky Survey (SDSS). The survey's aim is to map $\sim 10,000$ galaxies of all morphological types with stellar mass $M_* > 10^9 M_\odot$ out to $2.5R_e$ in a range of redshift $z = 0.01 - 0.15$.

Over the last decades, the Λ CDM framework has provided a convincing context for galaxy formation. In the "bottom-up" hierarchical clustering scenario, dark matter halos assemble into increasingly massive structures with time, with a growth peak at $z \sim 1 - 3$. Successively, the evolution of galactic structures becomes primarily driven by other mechanisms, like mergers and gas accretion or stripping processes. MaNGA seeks the physical origin of the mechanisms that drive this evolution and, thanks to its statistical power of a large sample of galaxies, it aims to connect them to the environment in which these galaxies live. MaNGA is investigating four key problems: 1) The growth of galaxy disks and the source of gas supply; 2) Roles of stellar accretion, major mergers and secular evolution processes in the growth of bulges and ellipticals; 3) Quenching of star formation due to external or internal processes and its relation with the environment; 4) Distribution of mass and angular momentum among the galactic components and how has their assembly affected these components through time.

The lack of a statistically significant sample of CRDs is one of the main reasons why we still do not have a clear comprehension of the mechanisms that drive the formation and evolution of these objects; further, their observed properties are different and not coherent with a single picture representing the whole class. For these reasons, MaNGA is very useful because of its large statistics, in terms of number of observed galaxies, which allows for the study of a considerable sample of CRDs, as will be presented in section 3.3. The main disadvantages of the survey are the relatively low resolution and S/N of the observed galaxies, which are important for both the appearance of the kinematic features of CRDs and for the spectroscopic distinction of the two disks. As a conclusion, MaNGA is optimal to build a large sample of galaxies that are good candidates to be CRDs, but it is generally not apt for detailed spectroscopic studies on these galaxies.

To follow, we provide technical details of the MaNGA survey. MaNGA instruments count 1423 circular fibers, each one with a $120\mu m$ core diameter which maps to $2''$ on sky. These fibers are grouped into bundles to form a total of 29 hexagonally shaped¹ integral-field units (IFUs). There are six different configurations for IFUs (shown in Figure 2.11): they range from bundles of 19 to 127 fibers (with diameters between 12 and 32 arcsec on the sky), plus bundles of 7 fibers used to observe the sky.

¹The hexagonal-formatted fiber bundles have $0.5''$ gaps between adjacent fiber cores. To avoid losing spatial information and under-sampling the point-spread function (PSF), three dithered exposures are conducted for each observation. All MaNGA survey exposures are 15 minutes long.

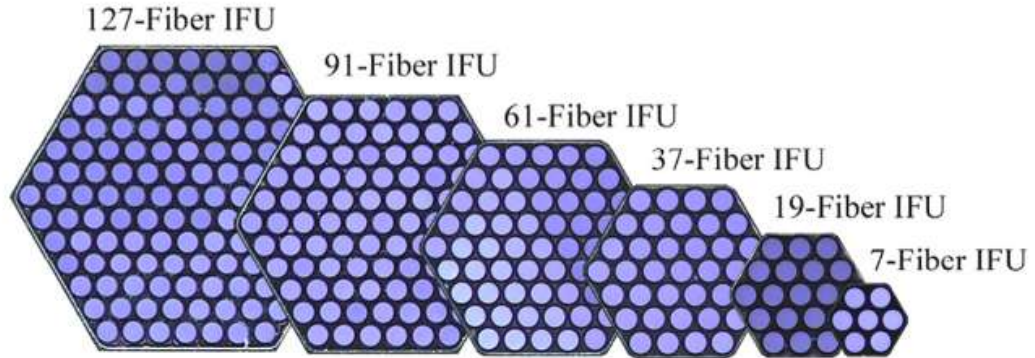


Figure 2.11: The six different configurations of the fiber-bundles of the MaNGA IFUs. Each IFU contains from 7 to 127 fibers (right to left). Figure from Drory et al. 2015.

IFUs are designed to be placed on a different galaxy within the same 3 degree diameter field of view (7 degree^2) of the Sloan 2.5m telescope, thus enabling detailed observations of 17 galaxies simultaneously. The remaining 12 IFUs are "mini-bundles" of 7 fibers. These IFUs are placed on standard stars across the field of view for spectrophotometric calibration.

The fibers feed the two BOSS spectrographs Smee et al. (2013) mounted on the 2.5m Sloan Telescope. Each spectrograph has two cameras, one red and one blue, with a dichroic splitting the light at roughly 600 nm and a full wavelength range from 360 to 1040 nm. With 2 arcsecond diameter fibers used in MaNGA, the spectral resolution R ($\lambda/\delta\lambda$) in the blue channel ranges from 1560-2270, and from 1850-2650 in the red channel. In terms of velocity, the resolution ranges from 50 km s^{-1} to 80 km s^{-1} with a median value of $\approx 72 \text{ km/s}$. The spatial resolution of MaNGA data is in general a function of the observational seeing, and has a median of 2.5 arcsec FWHM. A comparison between MaNGA and ATLAS^{3D} main technical properties is presented in Table 2.4.

	MaNGA	ATLAS ^{3D}
Sample size	$\approx 10,000$	260
Mass selection	$M_* > 10^9 M_\odot$	$M_* > 10^{9.8} M_\odot$
Redshift	0.01 – 0.15	$\lesssim 0.01$
Radial coverage	$1.5 - 2.5 R_e$	$0.6 - 1.5 R_e$
Wavelength range	360 – 1030 nm	480 – 538 nm
Angular FWHM	2.5''	1.5''
Instrumental resolution	50 – 80 km s ⁻¹	98 km s ⁻¹

Table 2.4: Comparison of MaNGA and ATLAS^{3D} surveys.

Chapter 3

Selection of a sample of CRDs from the MaNGA survey

In this section we illustrate the selection criteria that brought us to determine the sample of galaxies that we labeled as CRD.

3.1 Primary sample and basic visual selection

As mentioned in section 2.4, the number of galaxies observed by MaNGA is $\sim 10,000$. However, in this work we refer to the sample provided by Graham et al. (2019), which counts ~ 4500 galaxies from the SDSS Data Release 16 (Ahumada et al. (2020)). From this sample, we excluded galaxies that have been labeled as Irregular or Merger/Close-Pair. In Figure 3.1, we show the $(\lambda_{Re}, \varepsilon)$ diagram of this resulting sample of ~ 4000 galaxies; all the different kinematic classes introduced in section 2.2.1 are present; at variance with ATLAS^{3D}, this sample also includes Spirals.

For this work, we decided to ignore the former kinematical classification and inspect once again galaxies, thoroughly looking for evidences of two counter-rotating disks. Since CRDs are tangentially biased, due to the counter-rotation of the two stellar disks (section 2.2.2), although they can also be found in the leaf-like region among regular ETGs, we consider only galaxies below the magenta line: this sample consists of 603 galaxies (Figure 3.2). Starting from this sample, we made a selection of CRD-galaxies by visually inspecting the kinematic maps provided by the Data Analysis Pipeline (Westfall et al. (2019)) (DAP) together with the Sloan Digital Sky Survey (SDSS) images, paying attention to possible misclassification. In the following, we describe in detail all the selection criteria.

The very basic selection criteria we adopt to classify a galaxy in our subsample of 603 galaxies as CRD are the evidences of counter-rotation in the mean velocity maps and of the presence of the two peaks (or an elongated peak along the major axis) in the velocity dispersion maps; more explicitly, we looked for a resemblance to the V and σ maps of Figure 2.10.

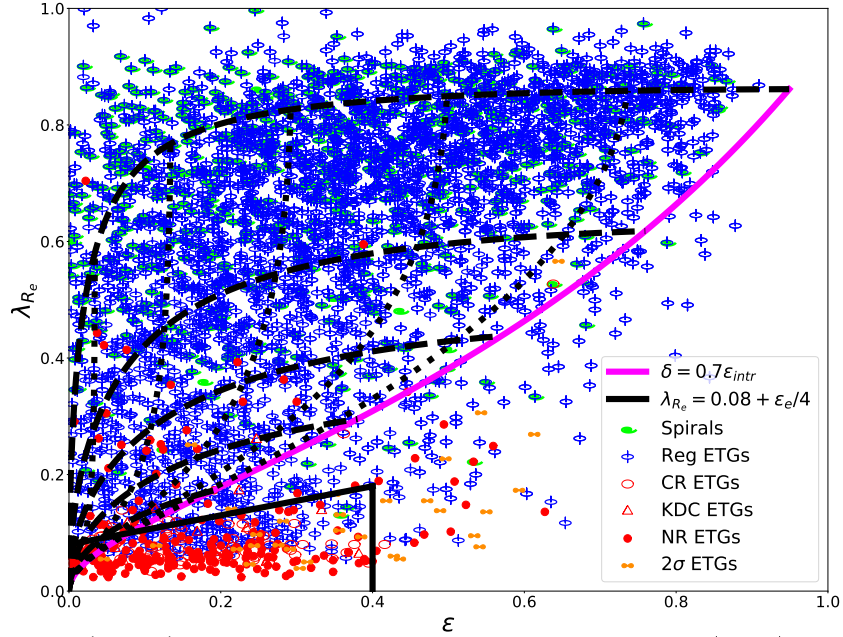


Figure 3.1: The $(\lambda_{R_e}, \epsilon)$ diagram of galaxies from Graham et al. (2019). Irregular and Merger galaxies are not plotted. Lines and symbols are the same of Figure 2.3. In contrast to ATLAS^{3D}, the MaNGA catalogue also include spiral galaxies, here plotted in lime.

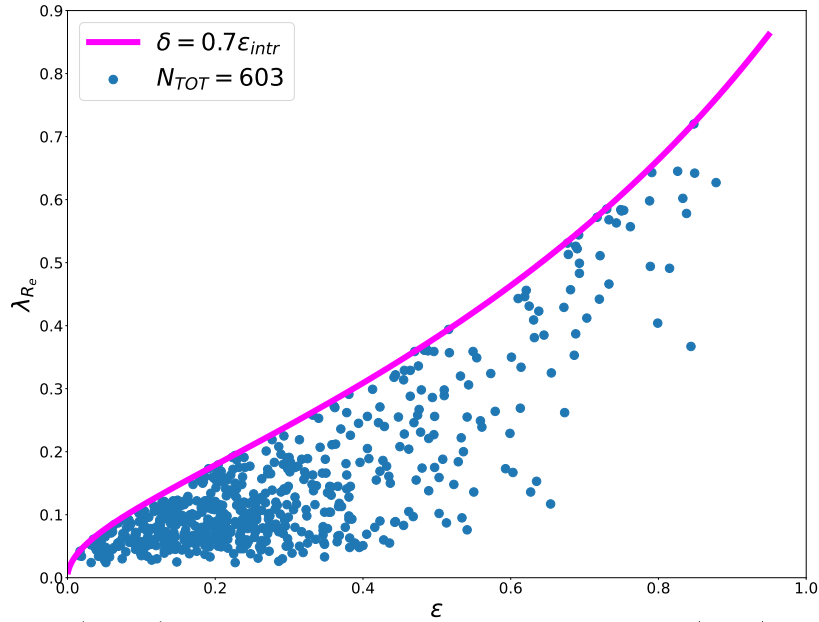


Figure 3.2: The $(\lambda_{R_e}, \epsilon)$ diagram of galaxies from Graham et al. (2019). Only galaxies below the magenta line are plotted. The previous classification (Fig. 3.1) is here ignored, and each galaxy is plotted as a cyan point. This sample counts 603 galaxies; we visually inspected all these galaxies to look for evidences of CRD and then build our sample.

We highlight the fact that the appearance of one of these two features does not imply the other one. In fact, on one hand, if the two components are spectroscopically indistinguishable the counter-rotation pattern does not appear in the velocity field, even though the two peaks in the σ map are present. On the other hand, sometimes we clearly recognize the counter-rotation in the velocity map, but if the two stellar disks counter-rotate with a velocity difference lower than the instrumental resolution, the separation between the two peaks in the dispersion map will not arise clearly, due to low resolution effects. Two examples of galaxy showing one feature but not the other are shown in Figure 3.3. For the same reason, sometimes the dispersion map shows an elongated peak of sigma instead of a net distinction of two peaks, because of the low resolution or low S/N. Therefore, to label a galaxy as CRD, we do not demand for both evidences, i.e. an inversion of rotation in the velocity map and the presence of two peaks (or an elongated one) in the dispersion map; instead, the appearance of one of the two features is sufficient to include a galaxy in our sample of CRD candidates.

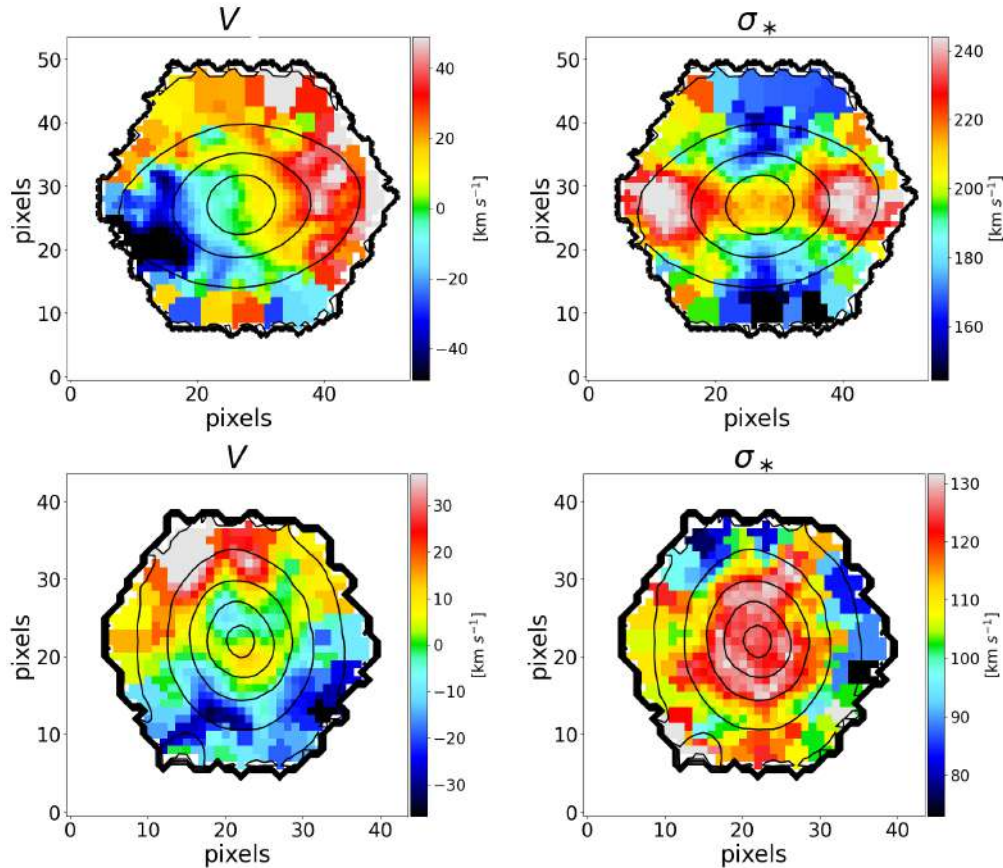


Figure 3.3: Velocity and dispersion maps of two galaxies showing only one of the two CRDs features. *Upper panels:* this galaxy clearly shows the two peaks in σ , but there are no evidences of counter-rotation. *Lower panels:* this galaxy shows evidences of counter-rotation in the velocity map, but the dispersion map does not have the 2σ appearance. Maps are taken from the DAP.

3.2 Further selection criteria

The basics selection criteria described above, namely evidences of counter-rotation or the two peaks in σ , are not sufficient for an accurate selection, because the same kinematic features can actually have different origins, beside the counter-rotation of two stellar disks; this can deceive us into label as CRD galaxies of other kinematic classes, thus leading to a misclassification. Fortunately, there are some peculiarities that can help us discard galaxies that satisfy our inclusion criteria but are not truly CRD, despite their kinematical appearance.

Along with the kinematic maps we always inspect the SDSS image, as it is most useful to check for the presence of external objects or other 'polluters' that may influences the observed kinematics. The further selection checks we made are the following:

- **Presence of external objects:** Figure 3.4 shows the velocity map of a galaxy that appears to exhibit an inversion of the rotation in the northern region. However, the SDSS image reveals the presence of many external objects. We conclude that the observed kinematical maps are influenced by these objects. This is also supported by the highest values we measure in the velocity dispersion map in those same bins where the velocity appears to be inverted. In general, it is common to find external objects near the observed galaxies, but they do not always modify significantly the kinematics. We exclude from our sample galaxies with clear evidence of an external influence in the kinematic maps.
- **Merging Galaxies¹:** If two galaxies are merging, the kinematic maps may show peculiar features, and sometimes the observed map resembles that of a CRD. A representative example is shown in Figure 3.5, where the velocity map shows an inversion of the rotation of the velocity, while the SDSS image indicates that we are looking at a merger. Obviously, we cannot include such objects in our sample.
- **Barred galaxies:** The presence of a bar can influence the kinematics of a galaxy. In particular, the dispersion map appears elongated over the extension of the bar. For example, in Figure 3.6 we can see that the peak of the velocity dispersion is elongated along the major axis. For this reason, such a galaxy could have been classified as CRD. Nonetheless, if we look at the SDSS image we can clearly spot the presence of a bar. Therefore we excluded this and similar galaxies from our sample. Also notice the eye-shaped isophotes, which is another clue for the presence of a bar (Bureau and Athanassoula (2005)). Sometimes, however, the presence of a bar is not evident even in the SDSS image. Yet, a signature of a bar could be present in the velocity map: if we look at Figure 3.7, for example, we can see the sigma peaks in the velocity dispersion map and no evident bars in the SDSS image. If this galaxy is viewed close to face-on, a possible counter-rotation would not be visible. We could then conclude that we are looking at a face-on CRD. However, in

¹Even though we excluded from our sample galaxies classified as Merger/Close-Pair by Graham et al. (2019), some of the 603 galaxies from our sample show evidences of merger.

the velocity map we can see how the zero-velocity bins (in green) form an S-shape pattern: this arises when a bar is present, so we exclude such galaxies from our sample (Cappellari and Copin (2003)).

- **KDC:** As pointed out in section 2.3.3, the fact that we include galaxies with the two peaks in σ regardless of the inversion of the rotation in the velocity maps can lead to a misclassification of KDCs as CRDs. In the ATLAS^{3D} sample, this happens for $\sim 8\%$ of the cases; here we recall the main differences of the two kinematic classes, summarized in Table 2.2. The clearest evidence to identify a KDC is the presence of a kinematic or a photometric twist, which implies that the system is not axisymmetric, and we are not looking at a CRD case. We also exclude galaxies in which the σ peaks look clearly asymmetric or misaligned with respect to the photometric major axis, as another symptom of twists or of the presence of a bar. Furthermore, since KDCs are generally confined within the very inner regions of galaxies, we tend to exclude galaxies where the inversion of rotation occurs at $R < 1R_e$ ¹. Other discriminants can be the ellipticities and stellar masses, for we expect galaxies with a KDC to be rounder than $\varepsilon = 0.4$ and more massive than $2 \times 10^{11} M_\odot$; however, since these two characteristics are not solid constraints for the distinction between the two kinematic classes, we used them just to confirm or contest few uncertain cases. We point out that we included in our sample most of the borderline cases.

In Figure 3.8 we present a summary scheme of the procedure we adopted for the classification of galaxies as CRDs, starting from the visual inspection of the kinematic maps provided by the DAP and the SDSS images.

¹The values of R_e are provided by the MaNGA Pipeline.

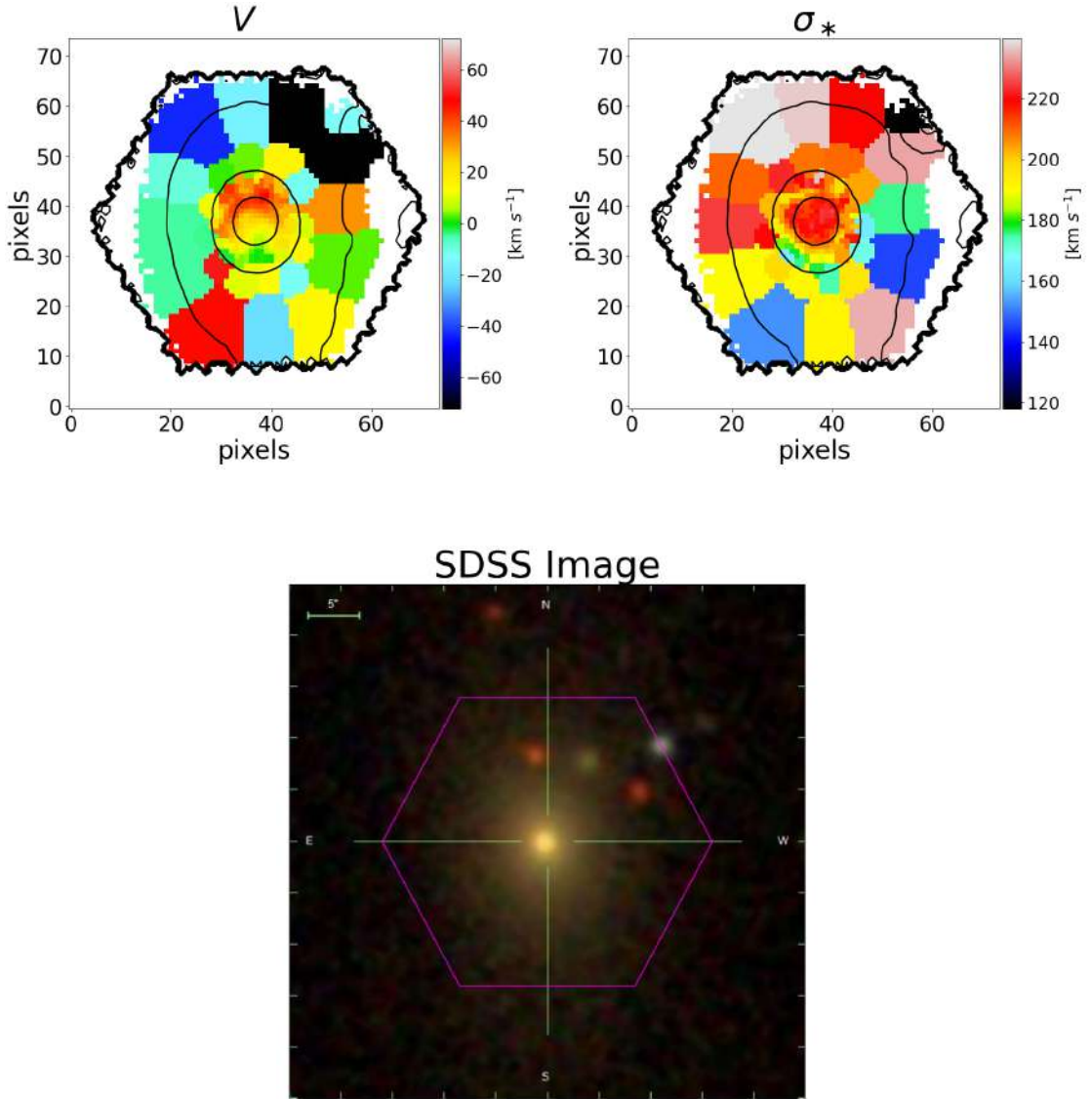


Figure 3.4: Example of how the influence of external objects can give kinematic maps the resemblance of a CRD case. The Figure shows velocity map, velocity dispersion map and SDSS image of the galaxy with MaNGA ID: 1-166739. In the velocity map we see that moving from the center (pixels = (38, 38)) to the north, the galaxy exhibits an inversion of the velocity rotation, from $\approx 50 \text{ km s}^{-1}$ to $\approx -30 \text{ km s}^{-1}$ (pixels = (38, 60)). In the SDSS image, however, we see four objects inside the hexagon that evidently deface the velocity map.

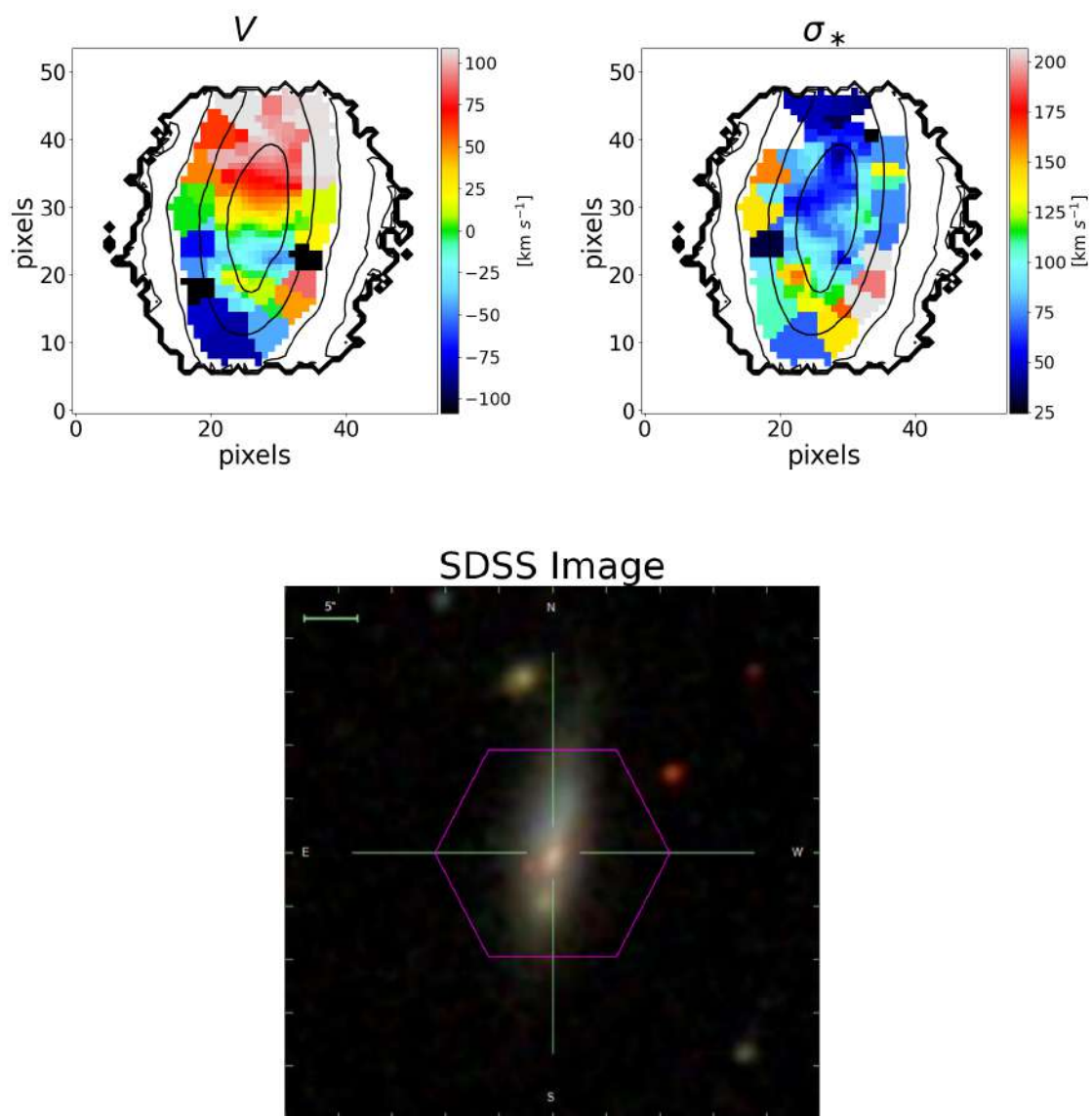


Figure 3.5: Example of how a merger can exhibit kinematic features similar to those of a CRD galaxy. The Figure shows the velocity map, the velocity dispersion map and the SDSS image of the galaxy with MaNGA ID: 1-373878. In the velocity map, starting from the zero-velocity (green) line centered at pixels $\approx (25, 20)$, we can move towards the outer regions, both to the north and to the south, and see an inversion of the sense of rotation. From the SDSS image, however, we see that a merging process is occurring.

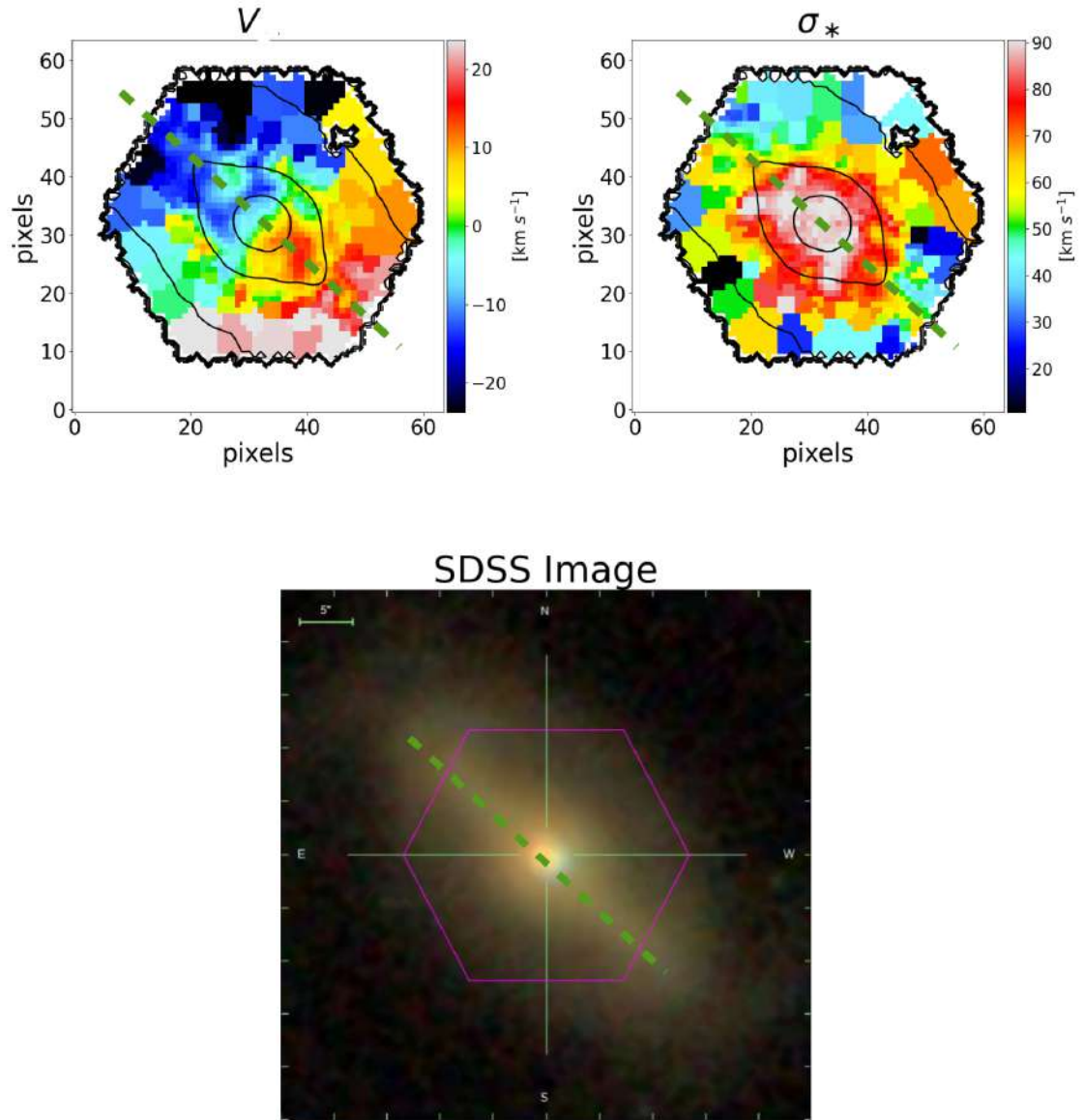


Figure 3.6: Example of a how the presence of a bar gives rise to kinematic features similar to a CRD galaxy. The Figure shows the velocity map, the velocity dispersion map and the SDSS image of the galaxy with MaNGA ID: 1-135524. The velocity dispersion map shows an elongated peak along the major axis (marked with a dark green dashed line). However, from the shape of the galaxy in the SDSS image we can spot the presence of a bar that extends, parallel to the dispersion peak, across the hexagon. Also, the eye-shaped flux contours hints at the presence of a bar.

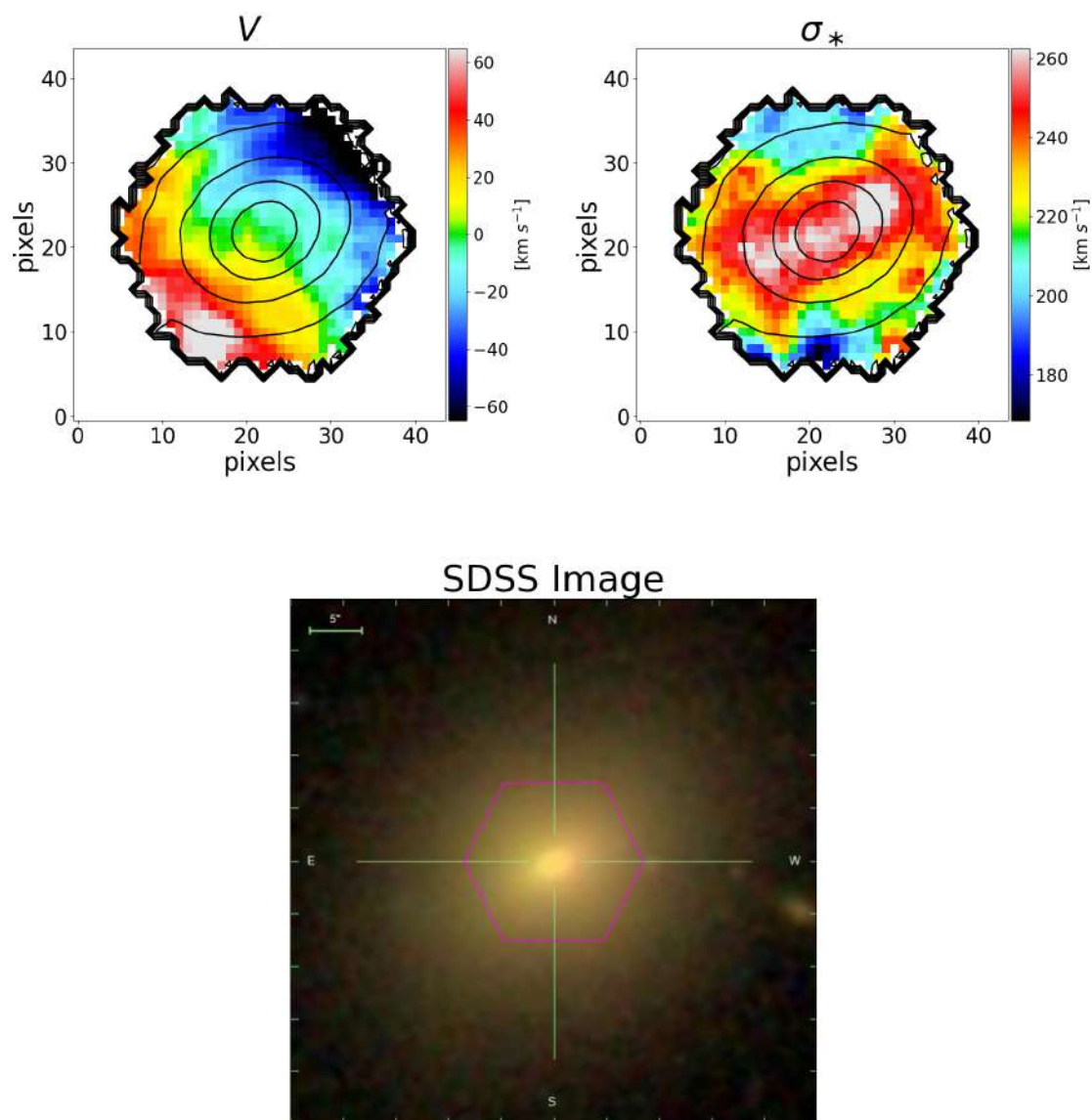


Figure 3.7: Another example of a barred galaxy with kinematic features similar to a CRD galaxy. The Figure shows the velocity map, the velocity dispersion map and the SDSS image of the galaxy with MaNGA ID: 1-593972. In the velocity dispersion map we can clearly see the peaks extended to the third isophote. The velocity map though shows an S-shape zero-velocity pattern, which suggests the presence of a bar, albeit not spottable from the SDSS image.

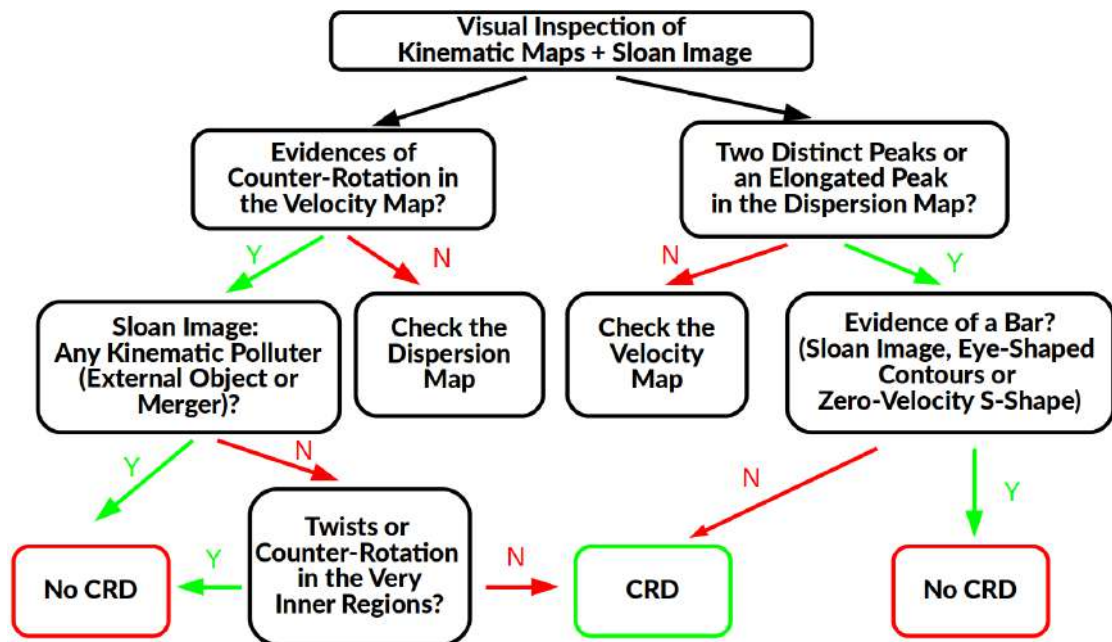


Figure 3.8: Schematic procedure for the inclusion of MaNGA galaxies in our sample of best CRD candidates.

3.3 Final sample

By inspecting with the criteria summarized in Figure 3.8 the kinematic maps and the SDSS images of the subsample of 603 galaxies below the magenta line, we produced a final sample of 53 best candidates for galaxies with two counter-rotating stellar disks: this is the largest sample built to date of such galaxies. The sample includes a spiral galaxy and three galaxies with uncertain morphologies; all the remaining galaxies are ellipticals and lenticulars. In Table 3.1 we list the MaNGA-IDs of the galaxy in our sample, along with their relative Hubble type (H), coordinates (R.A. and DEC.), redshift (z), stellar mass¹ (M_*) and the effective dispersion (σ_e); values are from Graham et al. (2019).

In Figure 3.9 we plot all galaxies in our sample on the $(\lambda_{R_e}, \varepsilon)$ diagram. It is interesting to notice that our sample includes four galaxies (with MaNGA IDs: 1-282035, 1-274545, 1-113698, 1-323764) that, from the SDSS image, appear to be formed just recently; in fact, they all have bluish colors, suggesting ongoing star formation, and in particular the asymmetric morphology of 1-274545 suggest a recent merger. In addition, two galaxies (with MaNGA IDs 1-236144, 1-593328) have an evident dust disk; we show the SDSS images of this galaxies in Figure 3.10. Forming galaxies are plotted in blue and galaxies with a dust disk are plotted in red. The symbol is the same adopted for the classification of 2σ -galaxies (section 2.2.1).

MaNGA-ID	H	R.A.	DEC.	z	$\log(M_*)$	$\log(\sigma_e)$
12-84617	E	231.47876	41.90977	0.0227	9.49	1.92
1-113520	E	317.5022	11.51065	0.0168	10.03	1.96
1-115097	S0	332.20345	13.36474	0.0274	10.54	2.04
1-38347	E	51.25646	-0.19295	0.0366	11.11	2.32
1-339061	E	117.1444	44.68829	0.0204	10.67	2.16
1-44047	E	119.64331	41.57841	0.0414	10.55	2.11
1-44483	S0	119.83486	42.05707	0.0245	10.49	2.11
1-556514	E	117.47538	29.46814	0.0608	11.36	2.3
1-37494	E	44.62547	0.79423	0.0429	10.62	2.09
1-37155	E	44.34947	-0.30941	0.0291	11.32	2.21
1-38543	E	54.03243	-0.59644	0.0234	10.73	2.12
1-47248	E	131.8838	53.90525	0.0465	11.56	2.4
1-137890	S0	137.21934	44.93227	0.0266	10.39	2.07
1-255220	S0	157.84582	42.27718	0.0224	10.23	1.91
1-282035	S0	184.52166	43.08699	0.0379	10.13	1.57
1-251783	E	215.31148	39.65254	0.0256	10.55	2.0
1-419257	S0	201.14052	31.54638	0.0232	10.65	2.07
1-418023	E	205.75334	36.16566	0.0237	10.36	1.91
1-167555	E	153.75261	46.75675	0.0246	9.9	1.88

¹Calculated with equation 2 of Cappellari (2013)

1-274440	S0	155.70868	39.36894	0.0262	10.0	1.83
1-274545	U	157.6859	40.05744	0.0231	10.16	1.91
1-275185	E	157.98762	40.30584	0.0793	11.51	2.39
1-167044	E	149.34688	44.15476	0.0742	11.58	2.38
1-166613	E	144.516	42.97432	0.0468	11.53	2.33
1-246175	S0	219.54619	53.46258	0.0381	10.35	1.96
1-210728	E	247.27996	39.49573	0.0289	10.77	2.08
1-248869	E	244.69082	39.33444	0.0316	11.24	2.32
1-136248	S0	253.79391	36.90631	0.0236	10.84	2.1
1-179561	E	319.75116	-0.96399	0.0195	10.48	1.96
1-635590	E	321.05441	1.11838	0.0494	11.64	2.46
1-113698	S0	319.19405	11.54001	0.0167	9.38	1.78
1-44722	E	120.9189	46.72739	0.0289	9.88	2.04
1-45016	E	122.25628	44.86853	0.0551	11.67	2.32
1-163594	E	115.49432	23.17638	0.0431	11.53	2.36
1-248410	S0	241.20852	42.03581	0.025	9.94	1.83
1-236144	S	226.21185	42.73448	0.0282	10.92	2.06
1-235983	E	223.63646	42.38544	0.0185	10.04	2.02
1-174947	S0	176.35873	49.87904	0.0333	11.0	2.24
1-278079	E	166.08657	46.0561	0.1427	11.96	2.46
1-188530	E	175.81782	55.27771	0.0549	11.0	2.3
1-149172	S0	170.53953	51.13043	0.0207	9.49	1.55
1-94773	E	249.30243	44.08551	0.0327	10.56	1.94
1-94690	S0	251.37791	43.58164	0.0315	10.56	2.1
1-323766	E	246.176	32.06437	0.0216	10.16	1.87
1-323764	S0	246.05405	31.87586	0.0208	9.94	1.74
1-135244	E	246.90712	42.63823	0.031	11.19	2.33
1-549076	U	232.23514	28.28955	0.0728	11.4	2.43
1-314719	E	226.23181	31.12498	0.0685	11.91	2.36
1-299176	E	129.03256	26.81207	0.0878	11.66	2.38
1-298940	E	127.03681	26.09499	0.0239	10.63	2.04
1-593328	E	219.65708	46.66312	0.0369	11.71	2.4
1-322291	S0	229.79559	43.20456	0.0277	10.2	1.9
1-633000	S0	233.23196	42.43826	0.0197	10.27	1.96

Table 3.1: List of MaNGA IDs, Hubble types (H), coordinates (R.A. and DEC.), redshift (z), stellar masses ($M_* [M_\odot]$) and the effective dispersions ($\sigma_e [\text{km s}^{-1}]$); values are from Graham et al. (2019).

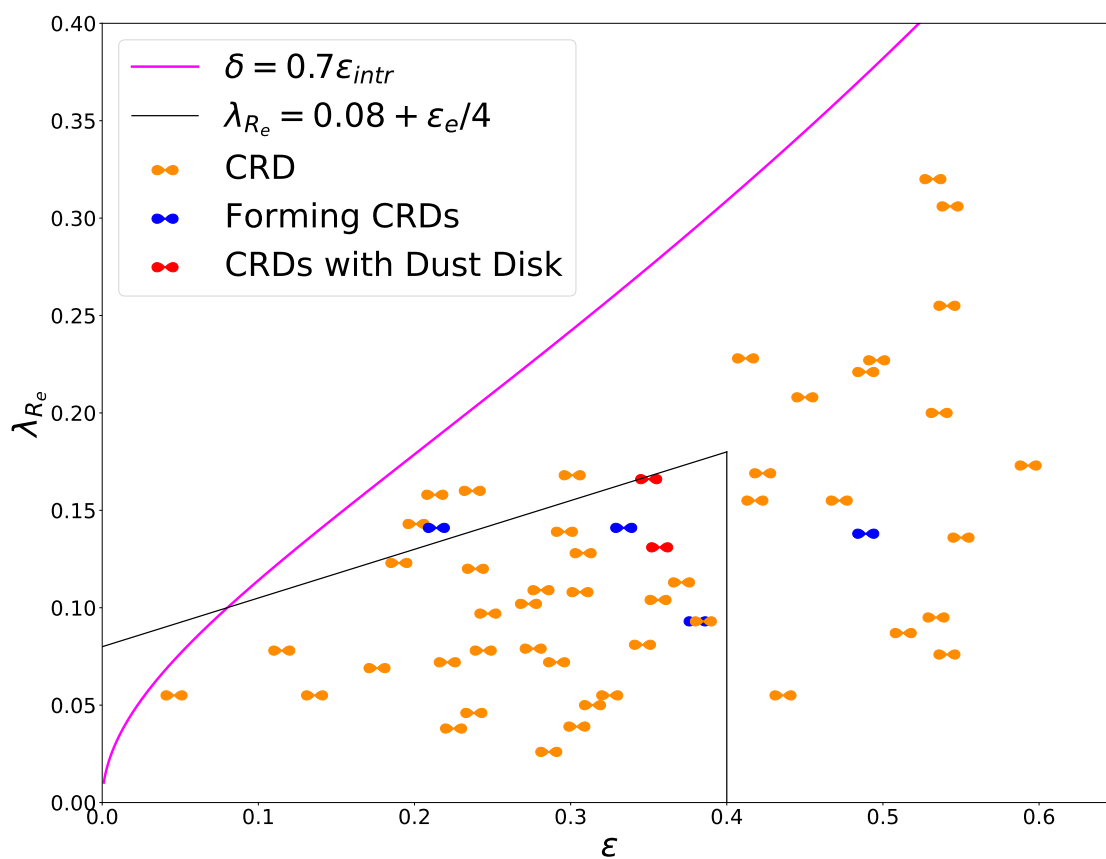


Figure 3.9: Final sample of CRDs. CRDs with evidences of recent formation are plotted in blue. CRDs with an evident Dust Disk are plotted in red.

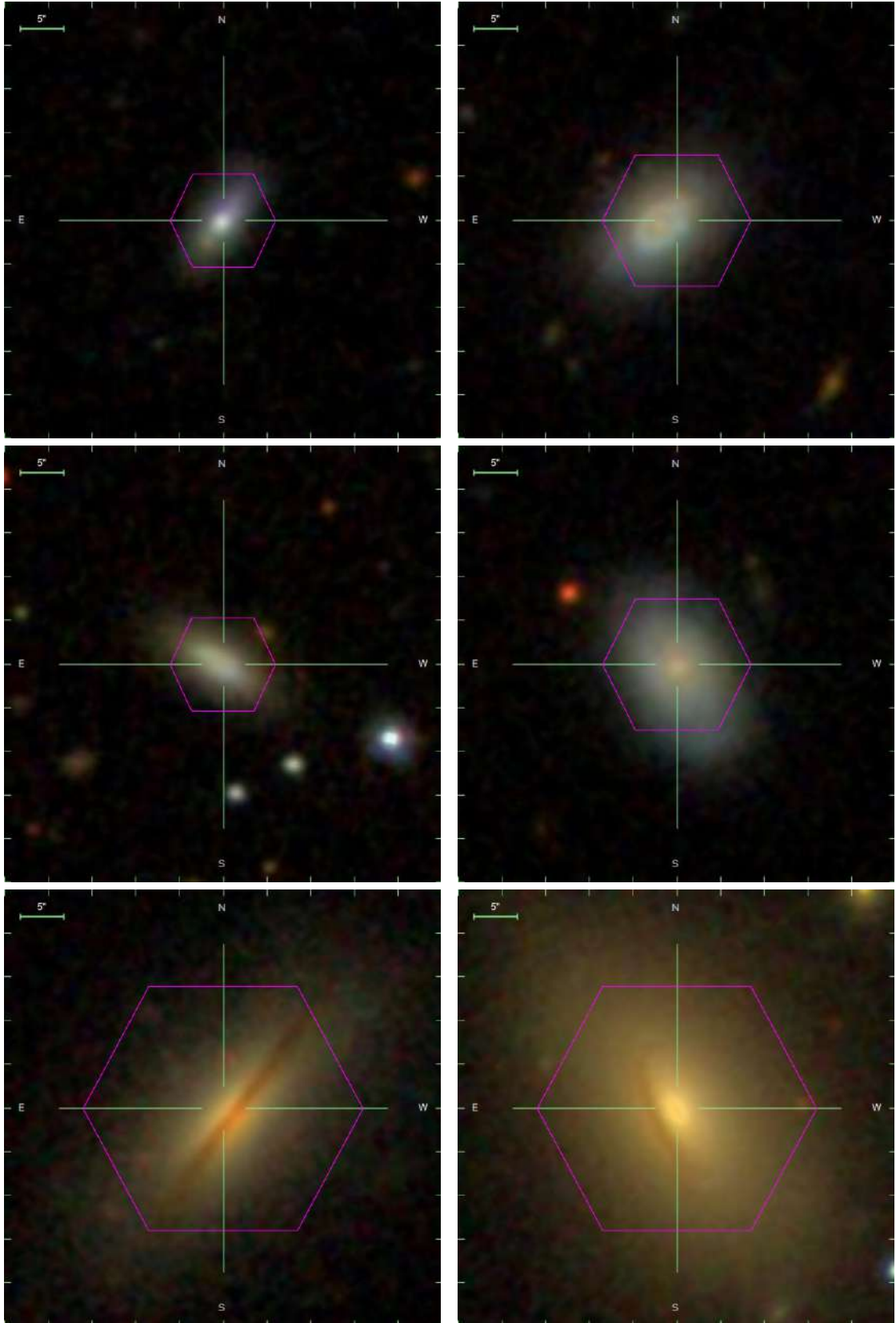


Figure 3.10: SDSS images of CRDs with either appearance of recent formation or of a dust disk. *Upper and middle panels:* galaxies which seem to be formed recently; from left to right, top to bottom, MaNGA IDs: 1-282035, 1-274545, 1-113698, 1-323764. *Lower panels:* galaxies with an evident dust disk; MaNGA IDs: 1-236144, 1-593328.

Chapter 4

Kinematics and Stellar Populations fitting

In this chapter we explain the methods for the extraction of the stellar kinematics, and of the stellar populations properties of our sample of galaxies. Data are provided by the Data Release 16 of SDSS and are available at <https://www.sdss.org/dr16/>.

4.1 Analysis of the MaNGA data with pPXF

The penalized pixel-fitting (pPXF)¹ method (Cappellari (2016b), Cappellari and Em-
sellem (2004)) allows for the extraction of stellar and gas kinematics, as well as for the
determination of the stellar population properties of galaxies via full spectrum fitting.
We address the reader to Appendix A for a description of the fitting procedure. Here we
present the parameters one has to set for the fit:

- **The input spectrum:** this is the spectrum to be fitted. This generally corre-
sponds to the observed spectrum from which one wants to measure the kinematics
or the stellar population properties. It can be, for example, the spectrum of a single
spatial bin or of a sum of different spatial bins, as well as a synthetic spectrum.
- **The templates:** these are the spectra used to fit the input spectrum; one can
use a single spectrum or a library of spectra as templates. In this work, we use a
subset of stellar templates from the MILES library (section 4.2.1) for the kinematic
extraction, and the simple stellar population (SSP) models provided by Vazdekis
et al. (2010) to fit the stellar population properties (section 4.3).
- **The noise:** this is the error associated to the input spectrum for each spectral
pixel. To fit our data we assume a constant noise with wavelength; section 4.2.3
describes how we verified the validity of this assumption.

¹Available at <https://pypi.org/project/ppxf/>

- **The velocity scale:** in pPXF, fits are performed in pixel space; therefore, the wavelength sampling of the spectra $\Delta\lambda$ corresponds to a sampling of the spectral pixels Δx . In particular, in pPXF the information on the sampling is given in terms of a velocity scale; for logarithmically binned¹ spectra one has:

$$V_{scale} \equiv c \Delta x = c \Delta \ln \lambda, \quad c = \text{speed of light} . \quad (4.1)$$

- **The starting guesses for the moments of the LOSVD:** in this work, we only fit the first two moments of the LOSVD, i.e. V and σ . The input starting mean velocity and velocity dispersion are only needed as guesses for the kinematic fit.

Additionally, pPXF allows for many optional tools to handle the fit. In particular, when fitting the kinematics, we always include additive Legendre polynomials. These correct the continuum, and thus they change the strength of spectral lines, reducing the mismatch between the input and the template spectra; moreover, they account for imperfect sky subtraction or scattered light. However, when fitting stellar populations one wants to preserve the strength of the spectral lines; for this reason we do not consider any additive polynomial. Though, we include multiplicative polynomials, which adjust the shape of the continuum, correcting inaccuracies in the spectral calibration and making the fit insensitive to reddening by dust.

4.2 Stellar Kinematics

For the extraction of the stellar kinematics, we used the datacubes (logarithmically binned in wavelength) provided by the MaNGA Data Reduction Pipeline (Law et al. (2016)) (DRP). We checked the quality of the datacubes by looking at the quality flags provided by the DRP: three of our galaxies (with IDs 1-44483, 1-282035, 1-549076) have 'bad Ω^2 ' and one galaxy (with ID 1-94773) presents a foreground star, so the results on these galaxies were considered carefully.

In the following, we first present the template library used to fit the stellar kinematics. In section 4.2.2 we discuss the problem of matching the resolutions of the template and galaxy spectra, as well as the criterion to bin galaxy spectra. In section 4.2.3 we present our method for the single-component fit to produce the kinematic maps, and in section 4.2.4 the method for the two-component fit; there we also introduce the χ^2 maps, a subject further investigated in the following section.

4.2.1 Hierarchical clustering of stellar templates

To extract the stellar kinematics of galaxies, one generally uses a library of stellar templates of different spectral classes to fit the observed spectra. Libraries with a larger number of templates require larger computation time: for example, for pPXF the execution time is typically $\sim O(N_{tpl})$ for N_{tpl} templates. This is the reason why in this work we prefer to use a subsample of spectra which is representative of the whole library.

¹In this work, we always use logarithmically binned spectra.

²The offset between the three dithered observations (see section 2.4) is $> 0.4''$.

To construct our library of stellar templates, we follow the method used in Westfall et al. (2019)(W19, for short) for the DAP: starting from the MILES stellar template library (Sanchez-Blazquez et al. (2006), Falc3n-Barroso et al. (2011)), which counts 985 stellar spectra, we used a hierarchical-clustering algorithm to find a desired subsample of ~ 50 representative spectra. The general idea of our approach is to create a reduced library is to fit each template with every other one in the MILES library and, for each couple of templates, we measure the 'distance' between two spectra, defined in terms of residuals of the fit, and finally cluster together those spectra with distances less than a fixed value d_{max} ¹.

In practice, we fit each given spectrum S_k of the library using S_j as the template, where S_j is every other spectrum of the library, and, for each couple of spectra, one defines the distance:

$$d_{ij} = \frac{2\delta(S_j - S_k)}{\overline{S_j}} \quad (4.2)$$

where $2\delta(S_j - S_k)$ represents the standard deviation of the residual and $\overline{S_j}$ is the mean flux of the corresponding spectrum. We then construct a 'distance matrix' with elements d_{ij} as the input matrix of the hierarchical-clustering algorithm², which cluster together templates spectra with $d_{ij} < d_{max}$. In our fits we calculate distances between spectra by fitting them with `pPXF` and, for each fit, we include an additive eight-order Legendre polynomial; to fit the stellar kinematics we will use the same polynomials, to have galaxy spectra consistent with the stellar templates.

To reduce the library to the desired number of spectra, we impose a maximum distance of $d_{max} = 0.065$: this yields 55 clusters, where the number of spectra in each cluster varies dramatically, from clusters composed by individual spectra to clusters which count hundreds of stars. To construct our stellar library, we normalize each MILES spectrum to a mean of unity, and then average all spectra in each cluster, in order to have a single representative spectrum for every cluster; we will use these averaged spectra as templates for the actual fit of the kinematics. We finally remove from our library three spectra with prominent emission lines, thus resulting in a final set of 52 templates. In Figure 4.1 we show an example of a cluster of stellar spectra and its corresponding average spectrum.

As one would expect, the use of a subsample of spectra instead of the whole library yields worse fits. In W19, the difference in stellar kinematics as measured using the whole MILES library and its subsample of representative spectra is quantified: as a matter of fact, the level of variation leads to marginal biases in the extracted kinematics, while speeding up the computation time by a factor of ~ 25 . This thus support the validity of our choice of using a subsample of templates instead of the whole library. In parallel with W19, from now on we refer to our distilled library as 'MILES-HC'.

¹The Python code used is available at <https://github.com/micappe/speclus>.

²See the `scipy` documentation on the functions `cluster.hierarchy.linkage` and `cluster.hierarchy.fcluster` for details on the algorithm we used for the clustering of the spectra.

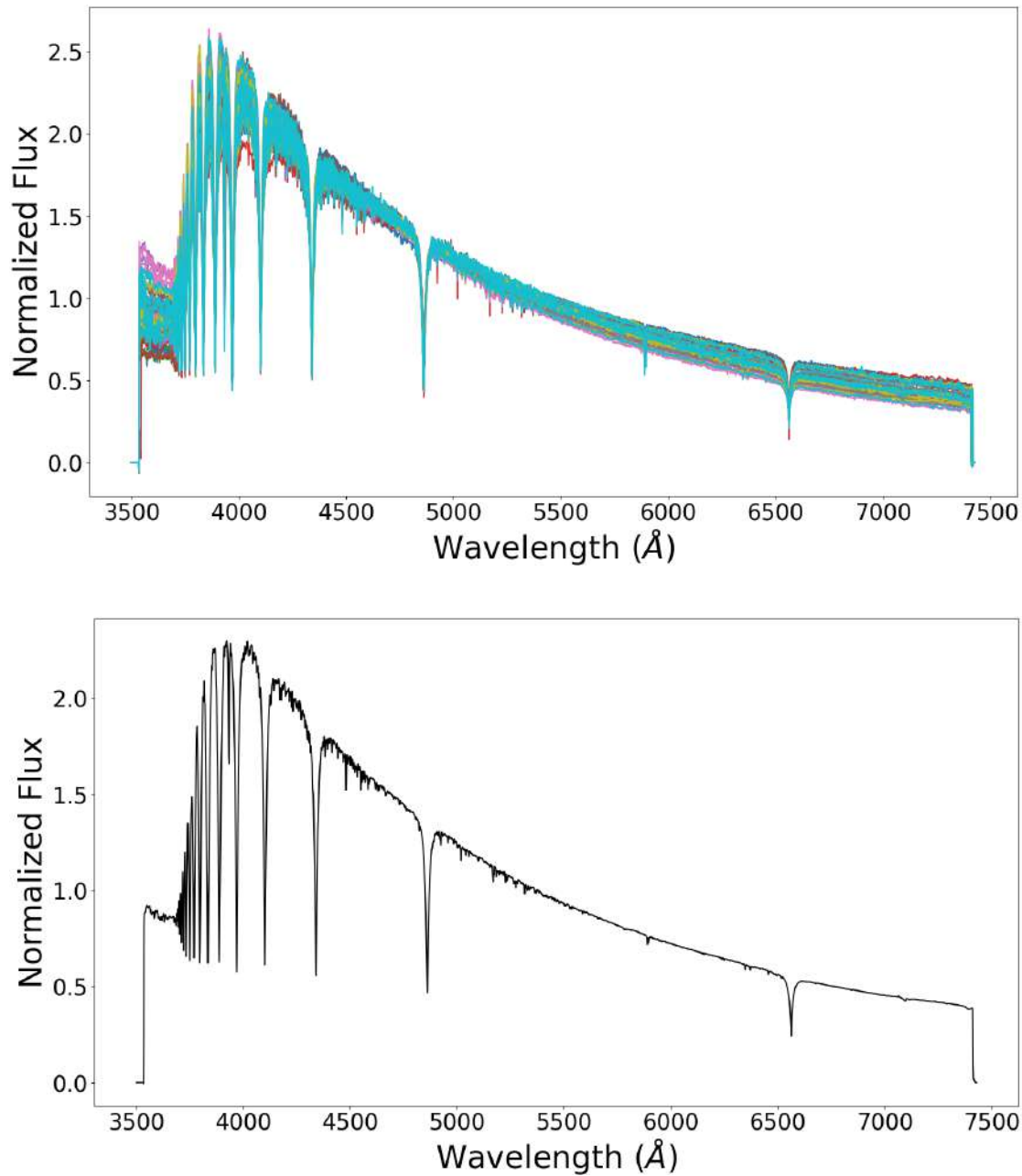


Figure 4.1: Example of a cluster of spectra. The upper panel shows 59 stellar spectra, normalized to their median value, plotted with different colors, of a single cluster. These spectra have been grouped together by the clustering algorithm, using $d_{max} = 0.065$. The lower panel shows the mean spectrum of the 59 spectra shown in the upper panel.

4.2.2 Resolution matching of the spectra and spatial binning

In general, when measuring the stellar kinematics, one wants the templates' spectral resolution to match that of the observed spectra. W19 have discussed in detail the implications of ignoring the requirement of resolution matching when fitting MaNGA spectra with the MILES library. They have found that to use spectra with higher spectral resolution than MaNGA data (the median instrumental resolution σ_{inst} for MaNGA is $\sim 16\%$ larger than that of the MILES library), is actually more convenient, particularly when the intrinsic stellar velocity dispersion is lower than the MaNGA σ_{inst} . For this reason, we perform the fit of V and σ by keeping both template and galaxies spectra at their native resolution. To account for the resolution mismatch, after the fit, the kinematic solution for the stellar velocity dispersion must be corrected for the instrumental resolution, and one then obtains the intrinsic stellar dispersion, σ_* . We refer to Appendix B for the discussion on such correction.

Reliable measurements of the stellar kinematics require spectra with a minimum S/N, especially for the recovery of the velocity dispersion; the galaxies observed by MaNGA though frequently have low S/N. A common approach to reach the target S/N_{min} is to spatially bin neighbouring spaxels¹; this though implies a loss in spatial resolution. W19 showed that for MaNGA data a value of $S/N \geq 10$ per bin is sufficient for reliable measurements of the first two moments of the LOSVD, which is the value they used for the DAP. However, when fitting two kinematic components, as it is the case of this work, it is fundamental to have sufficiently high S/N spectra to make the two components spectroscopically more distinguishable. On the other hand, MaNGA's modest resolution does not allow in general to bin data at very high S/N, for it results in a significant loss of spatial resolution; in particular, since the region of the two peaks and the corresponding inversion of the velocity of counter-rotators is typically $> 1R_e$, galaxies with very low signal can lose their CRDs' kinematical features when binned to high S/N. As an example, in Figure 4.2 we show two kinematic maps² of the same galaxy extracted with two different target S/N: $S/N_{min} = 35$ and $S/N_{min} = 15$, respectively. One can see that when the target S/N is higher (upper panels), even though the dispersion map exhibits a lower σ_* in the center that increases outwards, the overall map is not trustworthy, also because of the presence of high dispersion bins in the 'southern' region of the panel, that deface the 2σ -peaks appearance. On the other hand, when the binning is lower we can distinguish more clearly the two peculiar peaks, and the other high dispersion bins do not seem to influence the 2σ -peaks appearance. Also, the velocity map with a lower S/N binning shows a clearer rotation pattern and, in contrast to the velocity map of the upper panel, it exhibits an inversion of rotation in many bins of the external left-hand region. To compromise between the request of a relatively high S/N, in order to better distinguish the two components, and the need for a relatively low S/N, in order to preserve enough spatial resolution, we choose to bin galaxies either with $S/N_{min} = 25$ or $S/N_{min} = 15$: in practice, we first bin data with $S/N_{min} = 25$ but, if the resulting

¹A spaxel is a 3-dimensional pixel that has a spectrum in the third dimension.

²For the kinematic extraction method of these maps see section 4.2.3.

total number of bins is < 100 , we rebin data at $S/N_{min} = 15$. In this way, all galaxies count > 100 bins, all with $S/N > 15$.

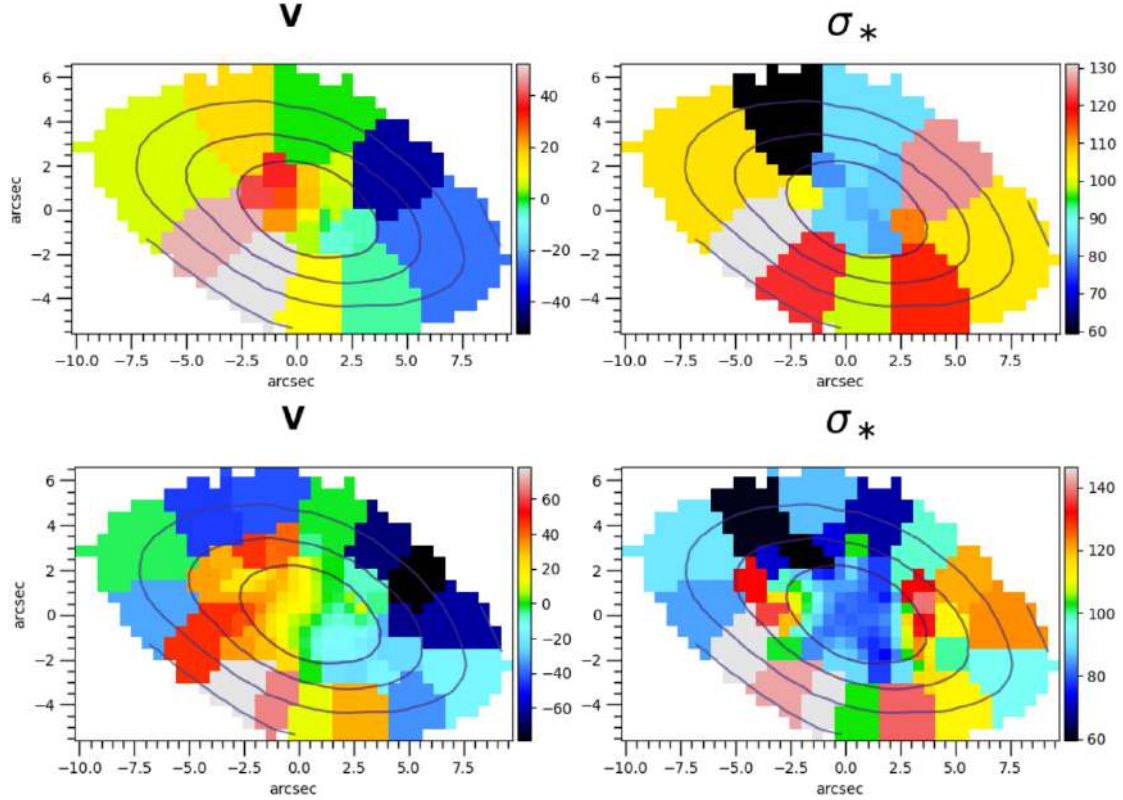


Figure 4.2: Kinematic maps of 1-246175 at two different binnings. *Upper panels:* V and σ_* maps extracted with $S/N_{min} = 35$. *Lower panels:* V and σ_* maps extracted with $S/N_{min} = 15$. This example shows how using a high S/N spatial binning can cause an important loss of spatial resolution; indeed, while the CRD features are present in the maps with lower S/N bins, they disappear when the binning is higher and the kinematic maps appear unclear.

4.2.3 Single component fitting procedure

Here we describe the method for the single component fit used to produce the kinematic maps. Before the actual fit starts, we need to set some parameters. The spectra provided by the DRP are logarithmically rebinned in wavelength; for this reason, we logarithmically rebin the template spectra. The wavelength sampling of the MaNGA spectra is constant: $\Delta \ln \lambda = \ln(\lambda_i/\lambda_{i+1}) \approx 2.3 \cdot 10^{-4}$, where i represents a spectral pixel; for this reason we set a constant velocity scale of $\approx 69 \text{ km s}^{-1}$ (equation (4.1)). Also, since galaxies are observed at redshifts $z > 0.01$, we de-redshift the observed spectra to the

rest-frame. We then flag all spaxels with $S/N < 1$ and restrict the fitting spectral range, which is smaller for MILES than for MaNGA; in particular we fit the spectral range $3940 - 7410 \text{ \AA}$. Finally, we mask regions of gas emission. The fit for the kinematics is then performed in three steps:

1. We first consider as input spectrum the sum of the spectra of all spatial bins, normalized to their median value, and fit it with all the 52 stellar templates of our library. We set the input noise to be constant with wavelength. As initial guesses we use $V = 100 \text{ km s}^{-1}$ and¹ $\sigma = 210 \text{ km s}^{-1}$. We then perform the first fit. In Figure 4.3 we show an example of this fit for a galaxy of our sample.

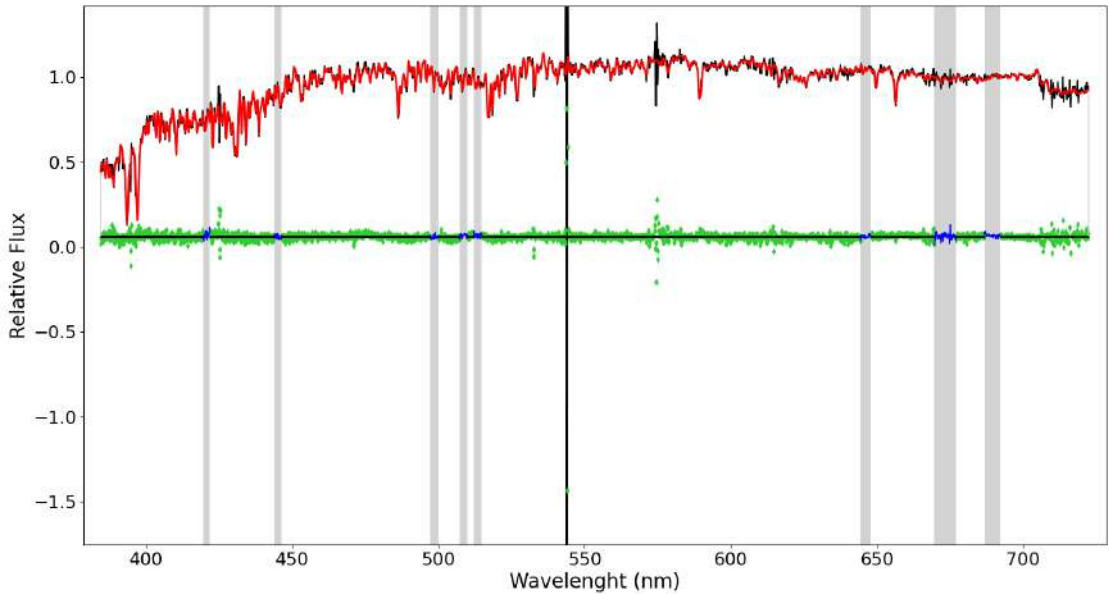


Figure 4.3: Example of the first fit performed on the spectrum resulting from the sum of the spectra of all bins of a galaxy. The black spectrum is the galaxy spectrum. The red spectrum is the best-fit spectrum. The green points are the residuals. The grey columns represent the masked spectral regions. The fit is in general good, although there are some spectral lines which deviate considerably from the best-fit spectrum; these are night emission sky lines.

2. Even though the fit is in general good, Figure 4.3 shows that some spectral lines deviate considerably from the best-fit template; in particular the two most prominent lines are night sky emissions lines. To account for these and other possible outliers, we make a robust estimation of the standard deviation σ_{std} of the residuals and clip all the $> 3\sigma_{std}$ outliers of the spectrum. From the first fit, we also calculate the best-fit spectrum as the weighted sum of the template spectra of the whole library.

¹The choice of $\sigma = 210 \text{ km s}^{-1}$ corresponds to set it to 3 times the velocity scale of the MaNGA spectra, i.e. we choose an input velocity dispersion as large as 3 spectral pixels.

3. We then perform a second fit, this time on every spatial bin of the galaxy. As the template we only use the best-fit spectrum of the previous fit; as the input constant noise we use σ_{std} ; as guesses for the starting V and σ we use the kinematic solutions of the first fit. Finally, we perform the fit and find the kinematic solutions V and σ for each bin. Figure 4.4 shows an example of this second fit, performed on a central bin of a galaxy. We can see that the scatter is very low, without any dramatic residual between the galaxy and the template spectra, thus supporting our assumption of constant noise.

The resulting stellar velocity and velocity dispersion maps obtained for the whole sample are presented in Appendix B. An example is shown in Figure 4.5.

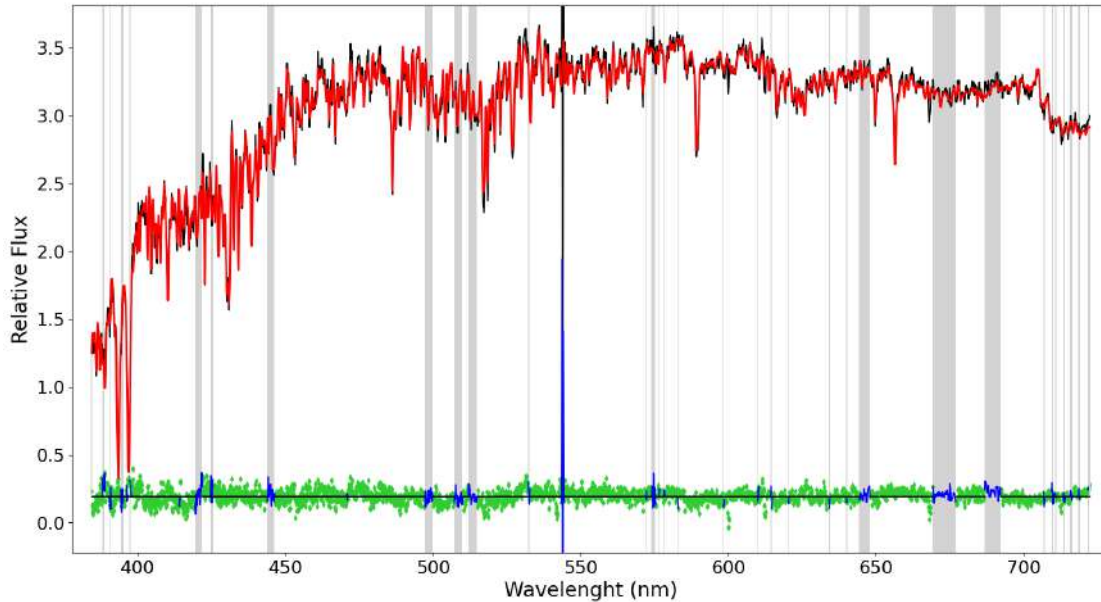


Figure 4.4: Example of the second fit performed on a central bin of the same galaxy of Figure 4.3. Lines and points are the same as in Figure 4.3. Spectral lines deviating $> 3\sigma_{std}$ are masked. The best-fit template spectrum is well representative of the observed spectrum and the errors are very low and regular, without any dramatic residual, thus supporting the assumption of constant input noise.

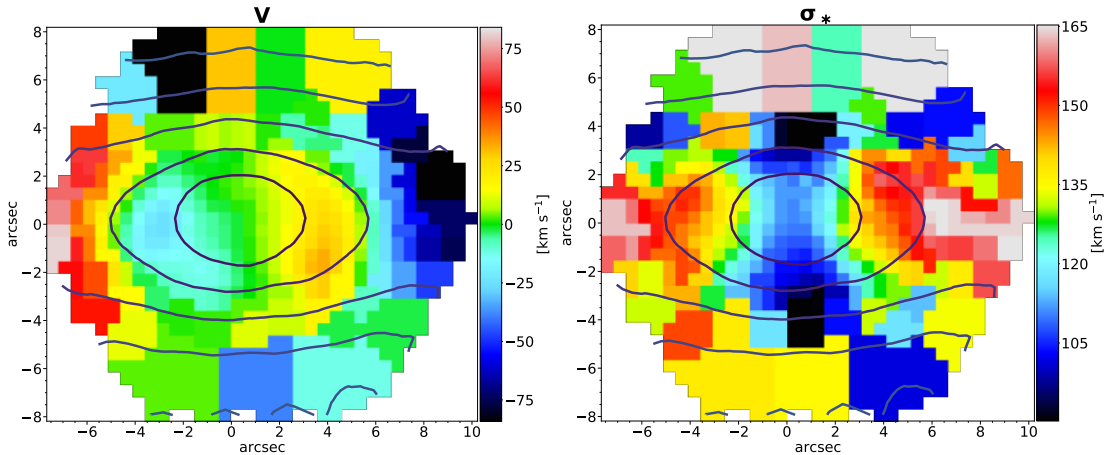


Figure 4.5: Example of V and σ_* maps extracted following the fitting procedure described in section 4.2.3. Formal errors for V and σ_* are 4.3 km s^{-1} and 4.9 km s^{-1} , respectively. These maps refer to the galaxy with MaNGA ID: 1-38543.

4.2.4 Two-component fits and χ^2 maps

In order to find V and σ of the two stellar disks separately, one has to fit two kinematic components. However, even when the presence of two counter-rotating disks is obvious from the kinematic maps, the spectroscopical distinction of the two kinematic components will be particularly challenging if the velocity difference of the two stellar components is $\Delta V < \sigma_{inst}$; moreover, if the velocity dispersions of the two stellar disks are intrinsically large, the LOSVD of the two components will be hardly resolvable; further, the recovery of the two components becomes more difficult if the S/N is low. This is why we do not expect to find many galaxies with spectroscopical evidences of two disks in our sample.

The recovery of the two components present a further complication when performing fits with **pPXF**, for it requires a precise estimate of the input starting velocities of the two components. In fact, the best fit solutions are defined as the ones that minimize the χ^2 ; since **pPXF** uses a *local* minimization algorithm, the *global* minimum will be missed if the input starting velocities are not accurate. More specifically, **pPXF** looks for the two kinematic solutions close to the input starting guesses; if these guesses are somewhat near the single-component solution, **pPXF** will then assign the kinematic values of single component solution to one of the two fitted components, which will be weighted 1, while the other component will be weighted 0, and any kinematic values can thus be assigned to it. **pPXF** will then locally look for better solutions; however, changing the kinematics of the zero-weighted component will not produce any improvement in the fit, and any better solution will not be found; therefore, this will be recognized as a local minimum, and then the single-component velocity and the (random) zero-weighted velocity will be considered as the best fit solutions for the two-component fit.

To overcome this problem, we look for the global minimum by creating a grid of χ^2 values, obtained by fitting each of the two components with a set of input velocities;

for each couple of velocities relative to the two components, we calculate the reduced χ^2 , namely the χ^2/DOF (where DOF are degrees of freedom), and plot it on a map. This method has already been used in Mitzkus et al. (2016) and in Tabor et al. (2016); however, it is the first time this method is applied to such a large sample of galaxies as in this work. Below, we give details on the production of χ^2 maps, and in the following section we explain how to interpret them.

The first step to produce χ^2 maps is to properly choose the input spectrum: instead of fitting each single spatial bin, we construct a spectrum by summing the bins of the region where one of the two peaks arises or, equivalently, where the velocity field is inverted. To do this, we look at the kinematic maps, find the coordinates (x_c, y_c) of one of the two peaks (or of the inversion of rotation), sum all spatial bins within a certain radius r of a circle centered in (x_c, y_c) and normalize the resulting spectrum to the median value of the summed spectra. The choice of considering only areas where the CRDs' features appear is justified by the fact that those are the regions where we expect the separation between the two components to be spectroscopically more evident, as discussed in section 2.3.1; in section 4.2.5 we confirm the trustworthiness of this choice by showing how χ^2 maps change when produced at different regions of the galaxy. If we considered the sum of all spatial bins of the galaxy, the spectrum would be biased towards the major (if any) contributor of the two disks to the total flux and the two components would not be more easily distinguishable, notwithstanding the higher S/N. The more accurate way to approach the problem is by plotting a χ^2 -map for each bin of the galaxy and then find the map where the distinction is more evident, as in Mitzkus et al. (2016); this is though too expensive in terms of computation time, and it would be unnecessary anyway, since we are just looking for a qualitative distinction of the two components. This is why we prefer to consider just the dispersion peaks regions. To define these regions, we considered one of the two peaks and determined the center of the circle and its radius by-eye. In practice, for each galaxy we extracted two χ^2 maps relative to the two peaks and decided to keep the one map where the distinction of the two components were more evident. In Table C.1 we list the coordinates and radii used to extract the spectrum of each galaxy for the fit.

Before fitting two components, we perform a single component fit; from this fit we get: the single component solutions for V and σ ; the σ_{std} used to mask the $> 3\sigma_{std}$ outliers and as the input noise for the two-component fit; the best-fit spectrum, calculated as the weighted sum of all the template spectra. The best-fit spectrum will be used as template to fit both components in the two-component fit; this choice could actually introduce a bias if the two stellar disks had different intrinsic spectra (e.g. because of different ages and metallicities), but the use of all MILES-HC spectra requires a lot of computation time. Another possibility could be to calculate two different best-fit spectra by fitting, for example, two spatial regions of the galaxy where the inner and the outer disk, respectively, prevail. These and other possibilities are currently being tested. For now, we limit our results to the first approach described, i.e. we compute the best-fit spectrum from the single component fit and use it as template to fit both components in the two-component fit.

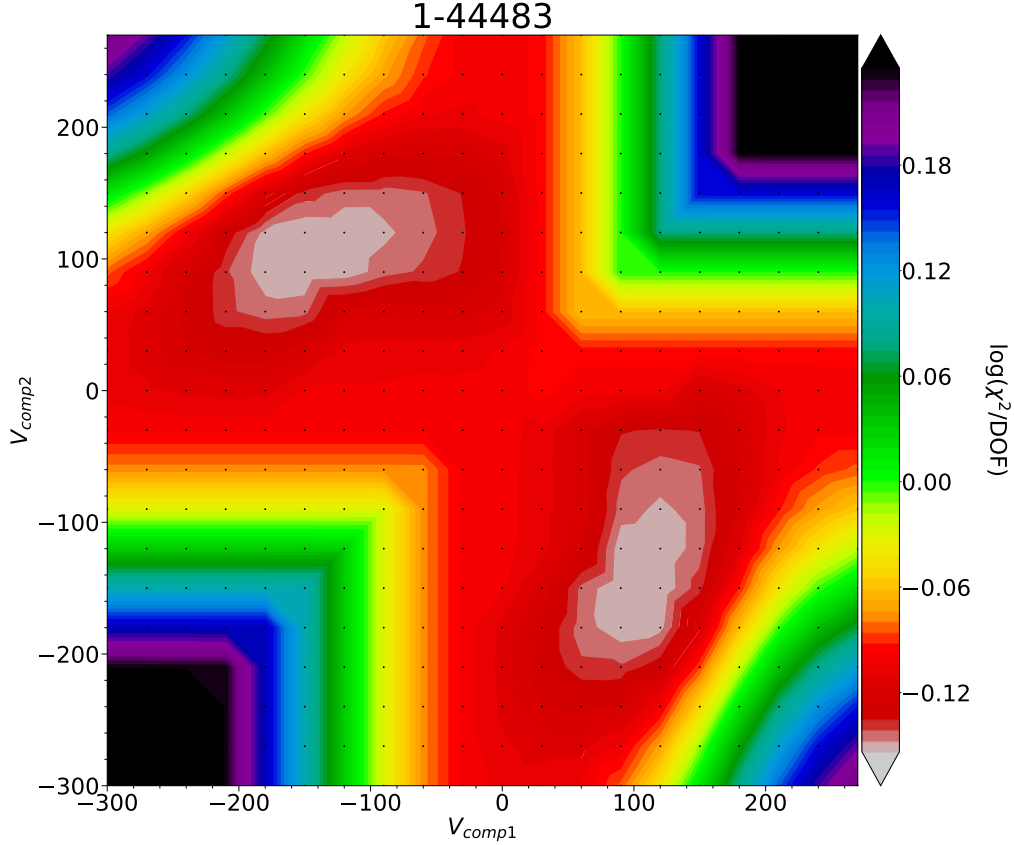


Figure 4.6: Example of a χ^2 map. The black dots on the map represent the V_{comp1} and V_{comp2} values where the reduced χ^2 has been calculated. The MaNGA ID of the galaxy is written in superscript. Notice that *each* χ^2 value plotted in the map is a local minimum for the given V_{comp1} and V_{comp2} ; the global minimum, however, is found in the two white regions.

The χ^2 maps are then produced by fitting two components as follows. For each component, we consider a range of starting velocities, separated by a fixed velocity step V_{step} , and, for each couple of starting velocities, we compute the χ^2/DOF and plot it on the map. In each fit, we impose the velocities to lie within $V_{i,start} - V_{step}/2 \leq V_i \leq V_{i,start} + V_{step}/2$ (where i stands for either comp1 and comp2), to force the best fit solution to lie in the interval around the starting values. In Appendix C we plot the χ^2 maps of our whole sample. In all maps, we fixed the explored velocity range to be $\pm 300 \text{ km s}^{-1}$, and $V_{step} = 30 \text{ km s}^{-1}$. An example is shown in Figure 4.6; we point out that *each* χ^2 value plotted in this map is a local minimum for the given V_{comp1} and V_{comp2} ; instead, the global minimum corresponds to the two specular white regions. This observation is useful to visualize the problem of the recovery of the two components with pPXF described above.

4.2.5 How to read the χ^2 maps

When fitting the spectrum of a galaxy, if the two stellar disks are not spectroscopically distinguishable (or if the galaxy truly has only one disk) the best fit solutions, found in the ranges of velocities used to produce the χ^2 maps, will be those where one component has the velocity of the single-component solution and the other component has any velocity covering the velocity range; this will result in a ‘cross-like structure’ of minimum χ^2 in the χ^2 maps. An example of this cross degeneracy is shown in the left panel of Figure 4.7. To produce this map, we have fitted two components to a synthetic galaxy spectrum composed of a single component, and the resulting χ^2 map has the predicted cross-like shape.

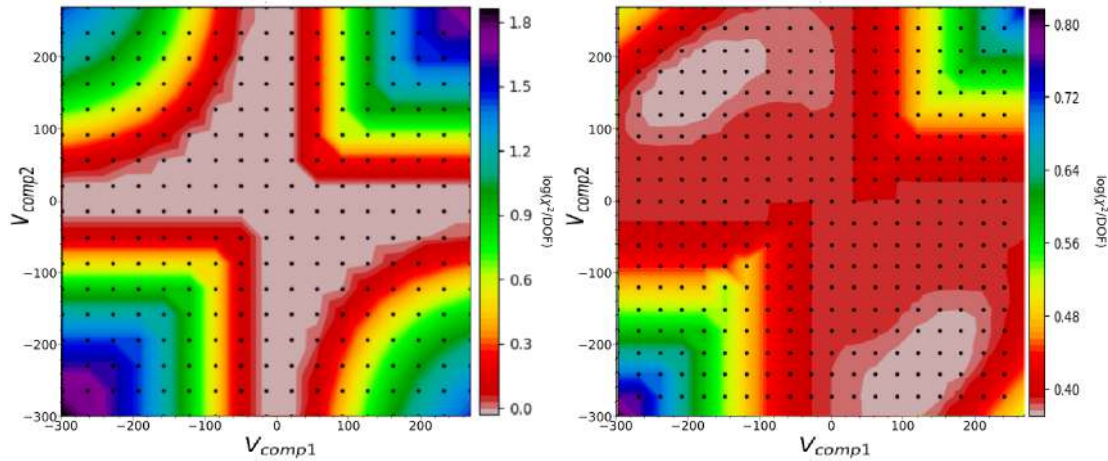


Figure 4.7: χ^2 maps of two synthetic galaxies. *Left panel:* χ^2 -map of a synthetic galaxy with one component. The minimum values of χ^2 are those where one component has the velocity of the single-component solution and the other component has any of the other velocities within the velocity range; here the single component solution is ≈ 0 , for the plotted velocities have been subtracted to the velocity that we used to create the synthetic galaxy spectrum. Notice the cross-like shape of the region of minimum χ^2 . *Right panel:* χ^2 -map of a synthetic galaxy with two counter-rotating components. Here the best-fit solutions are found around the two velocities values used to construct the synthetic galaxy spectrum. Notice the ‘butterfly’ shape and the two well distinct regions of minimum χ^2 .

On the other hand, when two components are present, the global minimum will be found in two specular regions, and the overall map appears with a characteristic ‘butterfly-shape’. Note that ‘comp1’ and ‘comp2’ are just nominal attributions, i.e. they do not specifically designate one of the two counter-rotating disks, and the two fitted components are thus interchangeable for pPXF. The right panel of Figure 4.7 shows the χ^2 -map of a synthetic galaxy with two components that have $V_1 = -200 \text{ km s}^{-1}$,

$\sigma_1 = 120 \text{ km s}^{-1}$, $V_2 = +150 \text{ km s}^{-1}$ and $\sigma_2 = 80 \text{ km s}^{-1}$, respectively. From this picture, we can clearly distinguish two specular regions of minimum χ^2 : in these regions, both components are weighted with a significant fraction of the total weights, i.e. they both contribute importantly to the fit.

We produced the χ^2 maps for the whole sample of CRD galaxies, and we inspected these maps looking for evidences of distinct χ^2 minima. As pointed out in section 4.2.4, given the MaNGA resolution, we expect that the majority of our galaxies are not spectroscopically distinguishable. In fact, out of 53 CRD galaxies, only fifteen show the two χ^2 minima, less than one third of the total sample, and of these only for nine cases the distinction is obvious; we plot the kinematic maps of these nine best cases in Figure 4.8. As mentioned, another reason why our maps may not show two distinct components can be the choice of the templates used for the two-component fits.

Finally, we check the assumption of producing χ^2 maps from a galaxy spectrum derived as the sum of those spatial bins covering one of the dispersion peaks. Figure 4.9 shows four χ^2 maps relative to the galaxy plotted in Figure 4.5, extracted at different locations of the galaxies. By comparing the χ^2 maps with the dispersion map, it is evident that the only χ^2 map showing two distinct components is the one corresponding to the region of the σ peak at $\approx (-6'', 0)$. This confirms the validity of our choice of extracting the χ^2 maps where the σ peaks arise.

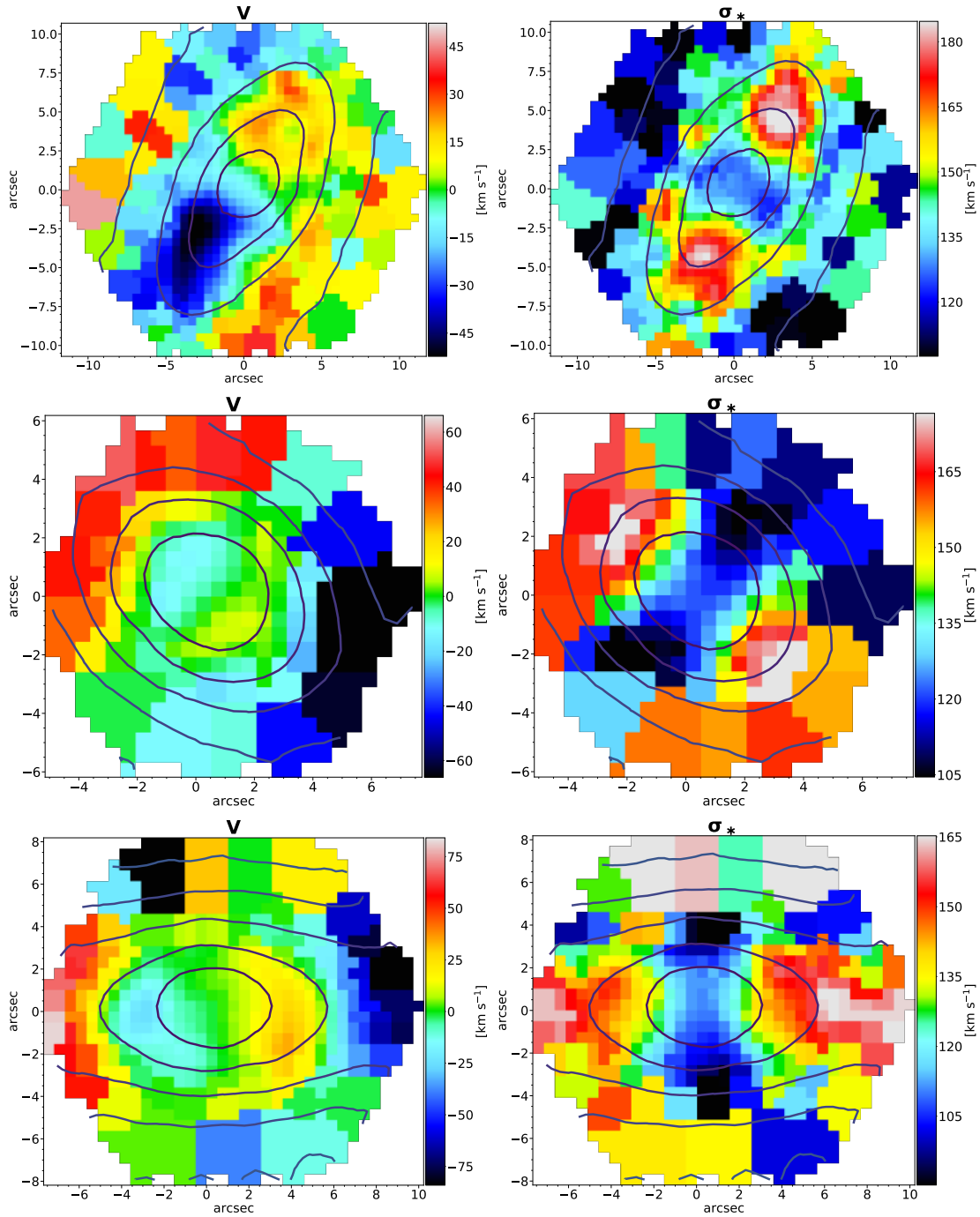


Figure 4.8: V and σ_* maps for galaxies with spectroscopically distinct disks. By analysing χ^2 maps, we found fifteen cases with two distinct minima, i.e. the spectroscopical distinction of the two counter-rotating disks. This figure shows only the nine galaxies where the distinction is obvious. (Top-to-bottom) MaNGA IDs: 1-339061, 1-44047, 1-44483; errors on V : 5.3, 3.9, 4.3 km s⁻¹; errors on σ_* : 5.8, 4.3, 4.9 km s⁻¹.

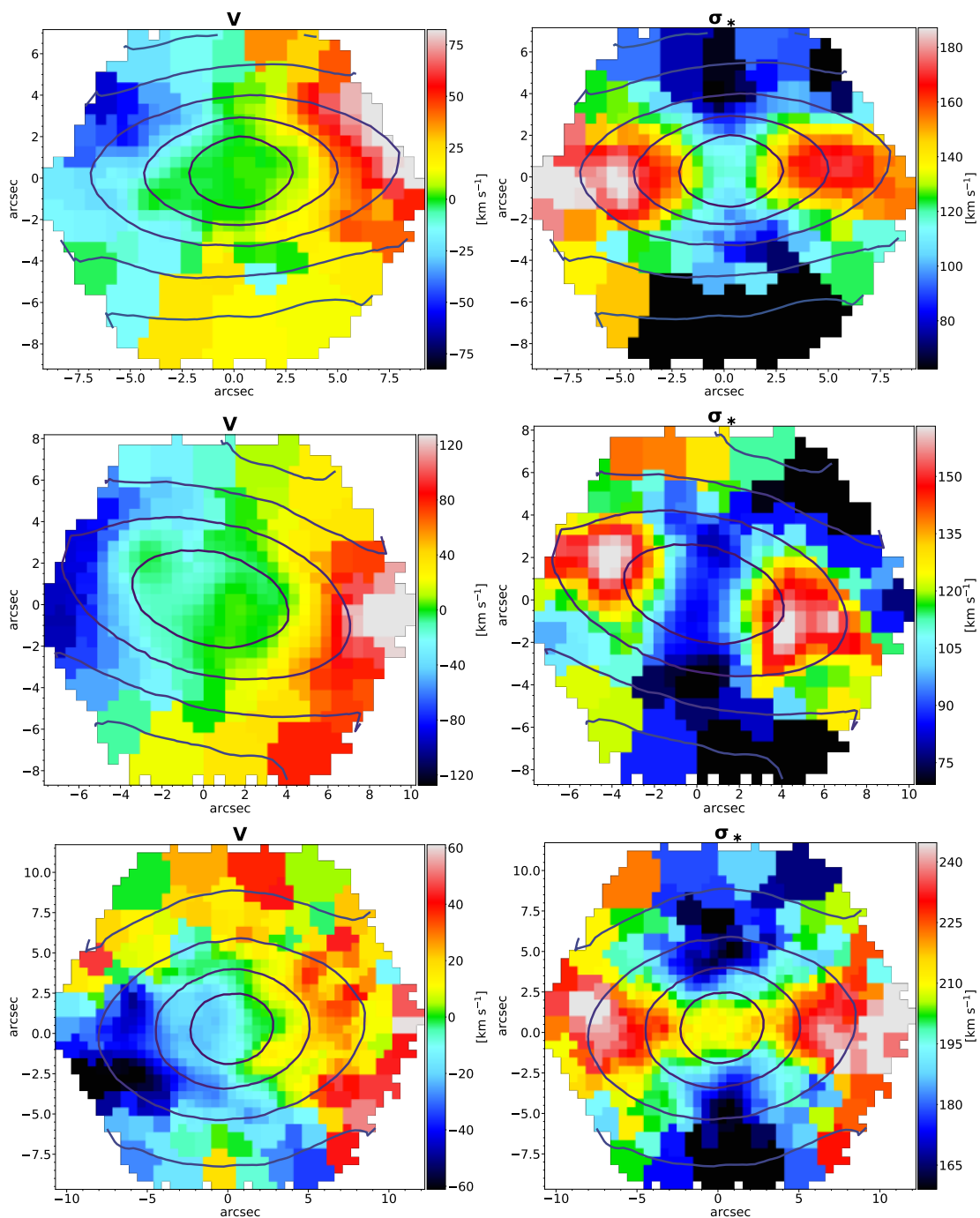


Figure 4.8: (continue) (Top-to-bottom) MaNGA IDs: 1-38543, 1-419257, 1-248869; errors on V : 4.6, 4.6, 5.7 km s^{-1} ; errors on σ_* : 5.2, 5.2, 6.0 km s^{-1} .

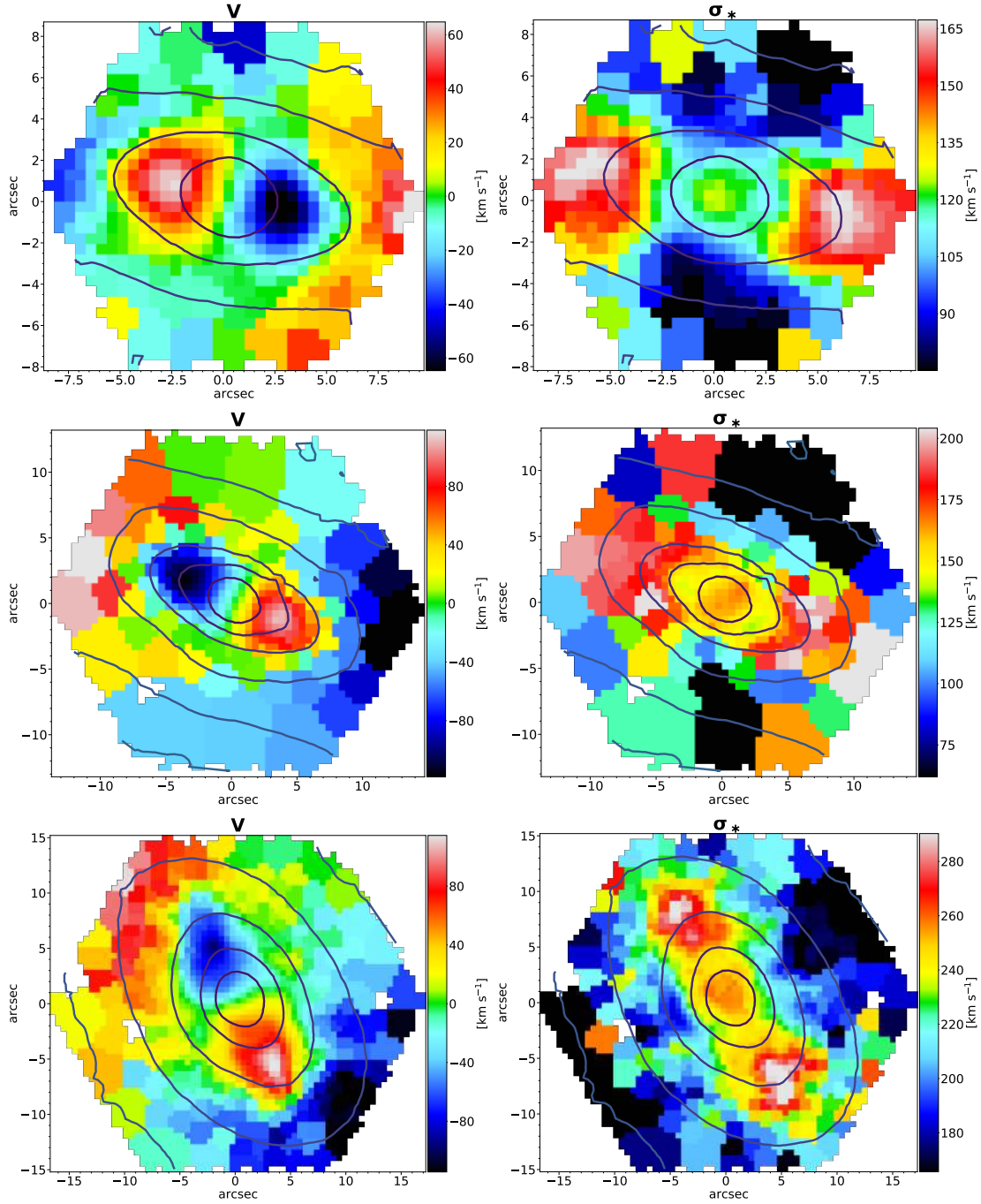


Figure 4.8: (continue) (Top-to-bottom) MaNGA IDs: 1-136248, 1-174947, 1-593328; errors on V : 4.1, 5.2, 8.3 km s^{-1} ; errors on σ_* : 4.8, 5.8, 8.6 km s^{-1} .

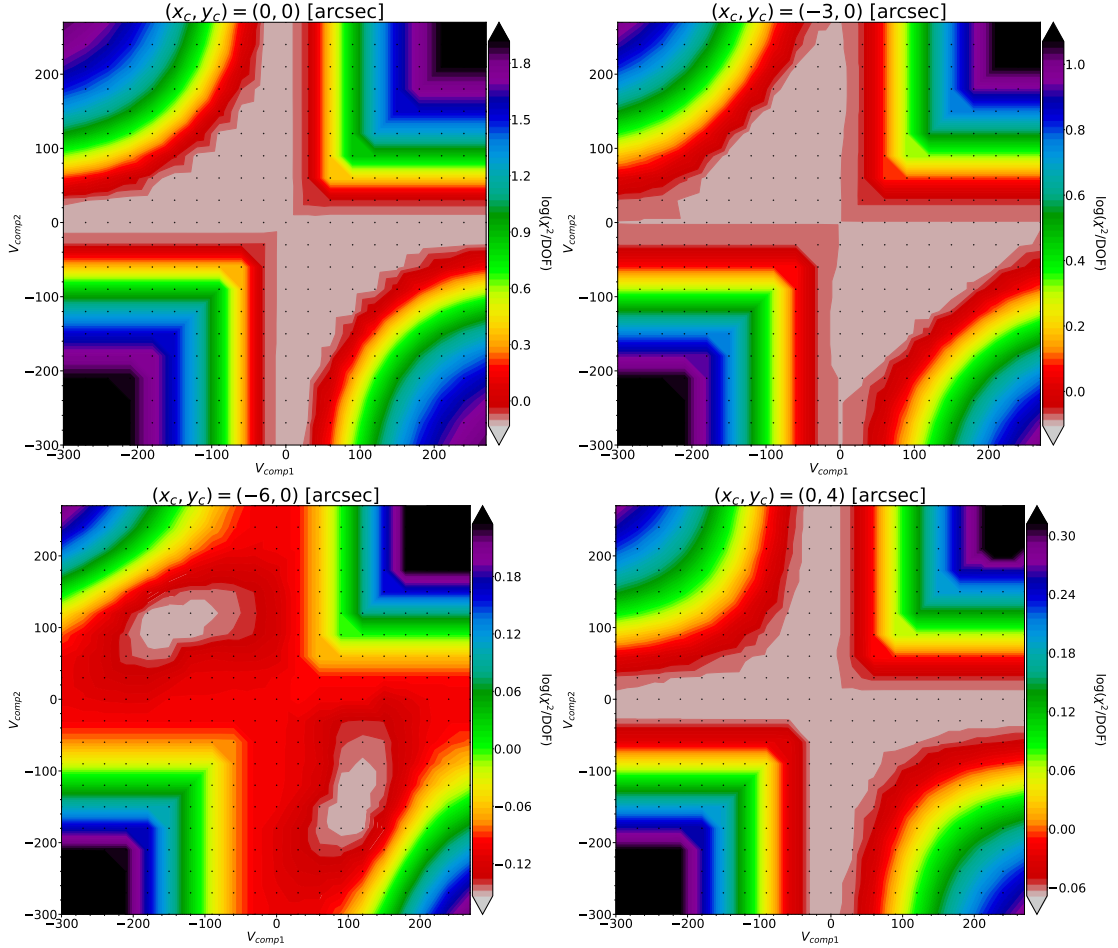


Figure 4.9: χ^2 maps of the same galaxy evaluated at four different spatial locations. *Upper panels:* χ^2 maps extracted at $(x_c, y_c) = (0, 0)$ [arcsec] (left) and $(x_c, y_c) = (-3, 0)$ [arcsec] (right). *Lower panels:* χ^2 maps extracted at $(x_c, y_c) = (-6, 0)$ [arcsec] (left) and $(x_c, y_c) = (0, 4)$ [arcsec] (right). The radius of the circle centered in (x_c, y_c) is fixed at 2 arcsec. The kinematic maps of this galaxy are shown in Figure 4.5; the lower left panel of this Figure corresponds to a σ peak. This example confirms that the best region to extract the χ^2 maps is the region corresponding to the σ peak.

4.3 Stellar populations fitting

In this section we present the method used to produce the stellar population maps (plotted in Appendix B). Since the line strength of the spectral lines is rather sensible to the S/N, we tested if any substantial variation occurs by increasing the target S/N_{min} of the spatial bins. We found that no significant differences in the extracted maps, and for this reason we kept the same spatial binning adopted for the kinematic extraction, described in section 4.2.2.

To extract the stellar populations properties, we simultaneously fit the stellar and the gas kinematics, and we use different templates to fit them. To fit the stellar component, we use the MIUSCAT SSP models (Vazdekis et al. (2010)); in particular, we used the SSP based on the Padova isochrones (Girardi et al. (2000)) with a Salpeter initial mass function (IMF), and we restrict them to the safe range described in Vazdekis et al. (2012); the final library consists of 150 SSP models of twenty-five different ages, ranging between 0.06 Gyr and 15.84 Gyr at logarithmic steps, and six different metallicities $[M/H] = -1.71, -1.31, -0.71, -0.4, 0.0, +0.22$. The templates for the gas emission lines are Gaussians; in particular, we fit the lines of the Balmer series $H\alpha$, $H\beta$, $H\gamma$ and $H\delta$, for which we fixed the flux ratios¹, the [SII] doublet at $\lambda = 6717, 6731 \text{ \AA}$, [OIII] at $\lambda = 5007 \text{ \AA}$ and [NII] at $\lambda = 6583 \text{ \AA}$. Before the fits start, we de-redshift the galaxy spectrum to the rest-frame, normalize the SSP templates to their median value and logarithmically rebin them; further, we apply a mask for the night sky emission lines of the [OI] at $\lambda = 5578, 6301 \text{ \AA}$ and NaI at $\lambda = 5890, 5896 \text{ \AA}$, for these lines can be very strong in MaNGA spectra. When fitting the stellar population, we are interested in the true strength of the spectral lines, and therefore we do not fit any additive polynomial; on the other hand, we use eight-order multiplicative polynomials (see section 4.1).

We extract the stellar population properties performing two fits on each spatial bin. From the first fit, we obtain the two kinematic solutions and the σ_{std} of the residuals. Then, the second fit is performed setting the kinematic solutions of the first fit as the starting guesses for the stellar and gas components, and the σ_{std} as the input noise. From this second fit the average ages and metallicities are calculated as the weighted sums of the individual stellar population values, namely:

$$\text{Log(Age)} = \frac{\sum_i w_i \text{Log(Age}_i)}{\sum_i w_i}, \quad [M/H] = \frac{\sum_i w_i [M/H]_i}{\sum_i w_i} \quad (4.3)$$

where w_i is the weight of the i -th stellar populations and sums are performed over the whole MIUSCAT populations, and the output ages and metallicities are luminosity-weighted; the weights of the gas component are excluded. The errors on age and metallicities are estimated as the rms of the residuals between a smoothed model of the data,

¹The atomic physics predicts that the Balmer lines are tied according to a theoretical decrement (Groves et al. (2011)); we refer to Case B with temperature $T = 10^4 K$ and density $n_e = 10^2 \text{ cm}^{-3}$

computed as a LOESS regression¹, and the actual data.

In Appendix B, we plot the age and metallicity maps for the whole sample. In Figure 4.10 we plot an example of the age and metallicity maps of a galaxy from our sample; this is the same galaxy used as example for the kinematic maps (Figure 4.5) and for the χ^2 maps (Figure 4.6).

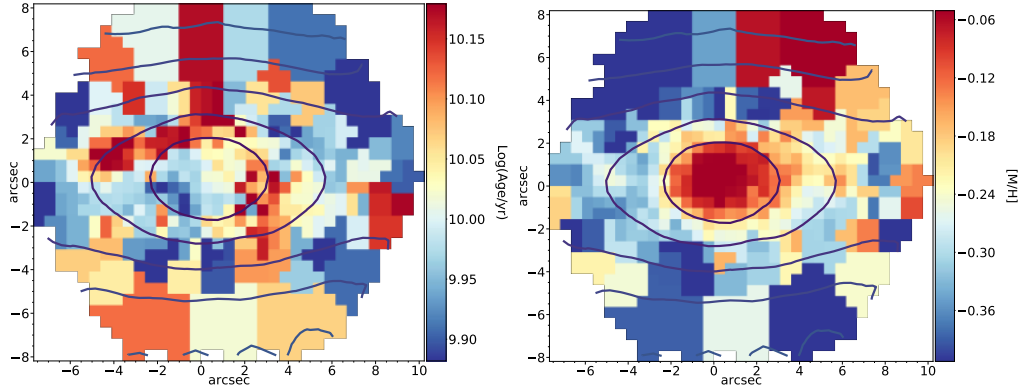


Figure 4.10: Example of stellar population maps. Age (left) and metallicity (right) maps for the galaxy with MaNGA ID: 1-44483. The plotted age and metallicity values on each bin are calculated as the weighted average over the whole library (equation (4.3)), following the fitting procedure described in section 4.3. Error on $\text{Log}(\text{Age})$: 0.080; error on $[\text{M}/\text{H}]$: 0.07

4.3.1 Looking for evidences of different populations with regularized fits

To investigate the presence of different stellar populations in our sample of CRDs, we perform regularized fits. The regularization is a well-known method used to solve ill-posed problems (as the recovery of the stellar population properties (Ocvirk et al. (2006))), and it has many applications in different scientific fields. The understanding of this technique would require a statistical description; here we only give a qualitative description of the effect of regularization on the solution of the stellar population fits. We address the reader to Press et al. (2007) for a mathematical description of the method, and to Cappellari (2016b) for its application with pPXF.

When we perform an unregularized fit of the stellar population properties with pPXF, the best-fit solution may not describe the data best, given that the use of too many parameters for the fit can result in an overfitting of the data. We can visualize this problem in terms of the weights of equation (4.3): in Figure 4.11 we plot the fraction w_i/w_{tot} of the total weights $w_{tot} = \sum_{n=1}^{N_{SSP}} w_n$ of the SSP models used to fit the stellar component of the spectrum of a single spatial bin of a galaxy; each pixel in the map represents

¹Locally Weighted Regression (LOESS) is a method to recover mean trends from noisy data. The package used is available at <https://pypi.org/project/loess/>.

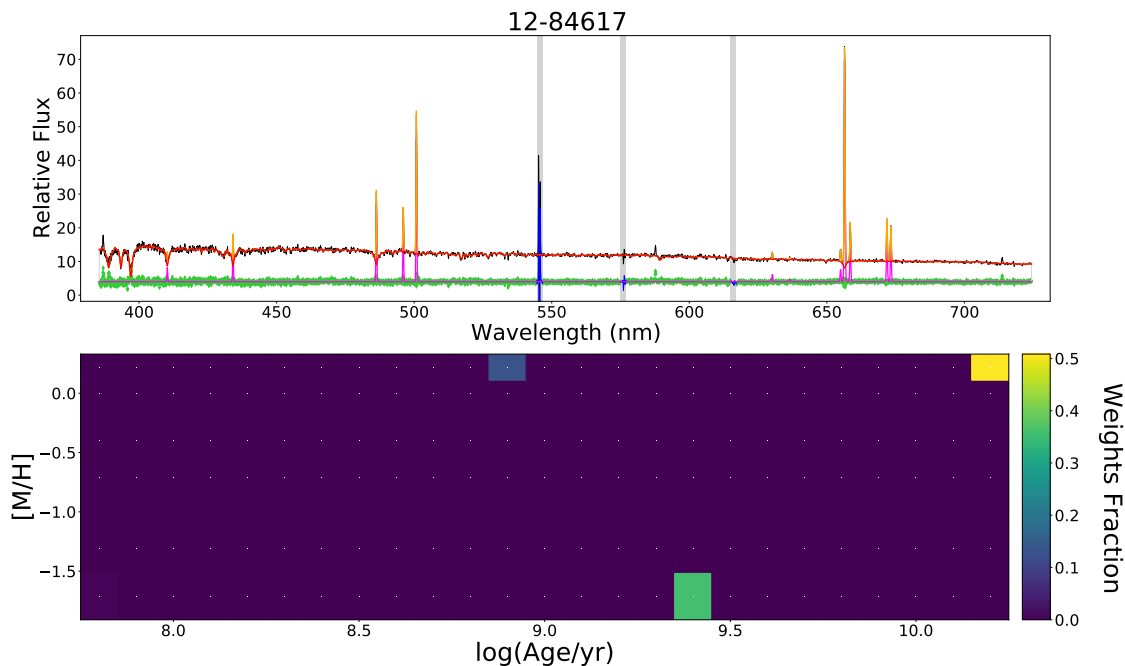


Figure 4.11: Example of an unregularized fit. The lower panel of the figure shows the weights fraction of the SSP models. We should have expected the weights to be more smooth, as SSP with similar ages and metallicities should contribute similarly to the fit.

the $\text{Log}(\text{Age})$ and $[\text{M}/\text{H}]$ of a SSP of the library. As we can see there are only three pixels, corresponding to three different SSPs, which have the highest weights fractions; we should have expected them to be distributed into many close pixels, instead of into few isolated pixels, i.e. we expected SSP with similar ages and metallicities to contribute similarly to the fit.

The regularization can be considered as a method to smooth the weights of the solution during the fit. In practice, `pPXF` first calculates the weight of each SSP model; then, for the i -th SSP, it considers w_{i-1} and w_{i+1} : if these two weights are zero, i.e. if the i -th pixel in the weights fraction map is isolated and surrounded only by zero-weights pixels, the solution for the i -th SSP will be penalized; conversely, the good solutions will be those surrounded by non-zero weights. Qualitatively, a SSP is considered to positively contribute to the fit only if SSPs with similar ages and metallicities also do, and otherwise it is penalized. In Figure 4.12 we show a visual example of the effect of the regularization on the same spectrum of Figure 4.11; we see that the pixel with the highest weight of Figure 4.11 (top right corner) disappeared, while the two other pixels have been smoothed.

By looking at Figure 4.12, a clear bimodality emerges, i.e. there are two distinct ‘blobs’ in the weights fraction map: these suggest the presence of two stellar populations, one younger and more metallic, the other older and less metallic. This bimodality could be due to two different stellar populations relative to the two counter-rotating disks; how-

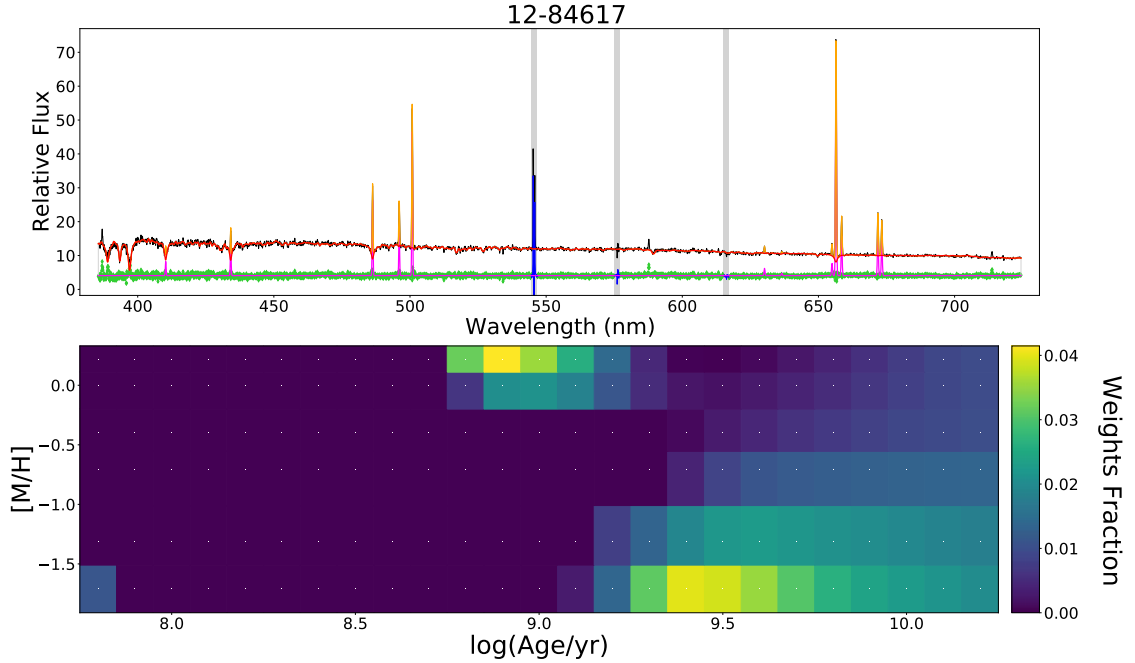


Figure 4.12: Example of a regularized fit of a galaxy with two distinct populations. The Figure shows the weights fraction of the stellar population templates (lower panel), smoothed by the regularization, and the relative fit (upper panel). The two blob in the weights fraction represents the two stellar populations.

ever, to confirm this hypothesis and to figure out which stellar population corresponds to which disk, a spectroscopic decomposition of the two disks is needed.

To find evidences of different populations, we performed regularized for each galaxy in our sample, by fitting $\sim 10 - 20$ spatial bins randomly distributed on the galaxy, and looked for multimodal weights map. As a general result, we found that the CRDs of our sample show both unimodal and multimodal maps. In Figure 4.13 we show an example of unimodality and multimodality (with three blobs). We found multimodality in twelve cases; all the other cases show unimodality or appear too smoothed. Unfortunately, none of the galaxies which exhibit bimodality shows the two minima in the χ^2 maps as well, which would have been ideal targets for a spectroscopical disentangling of the stellar populations of the two disks in a future work.

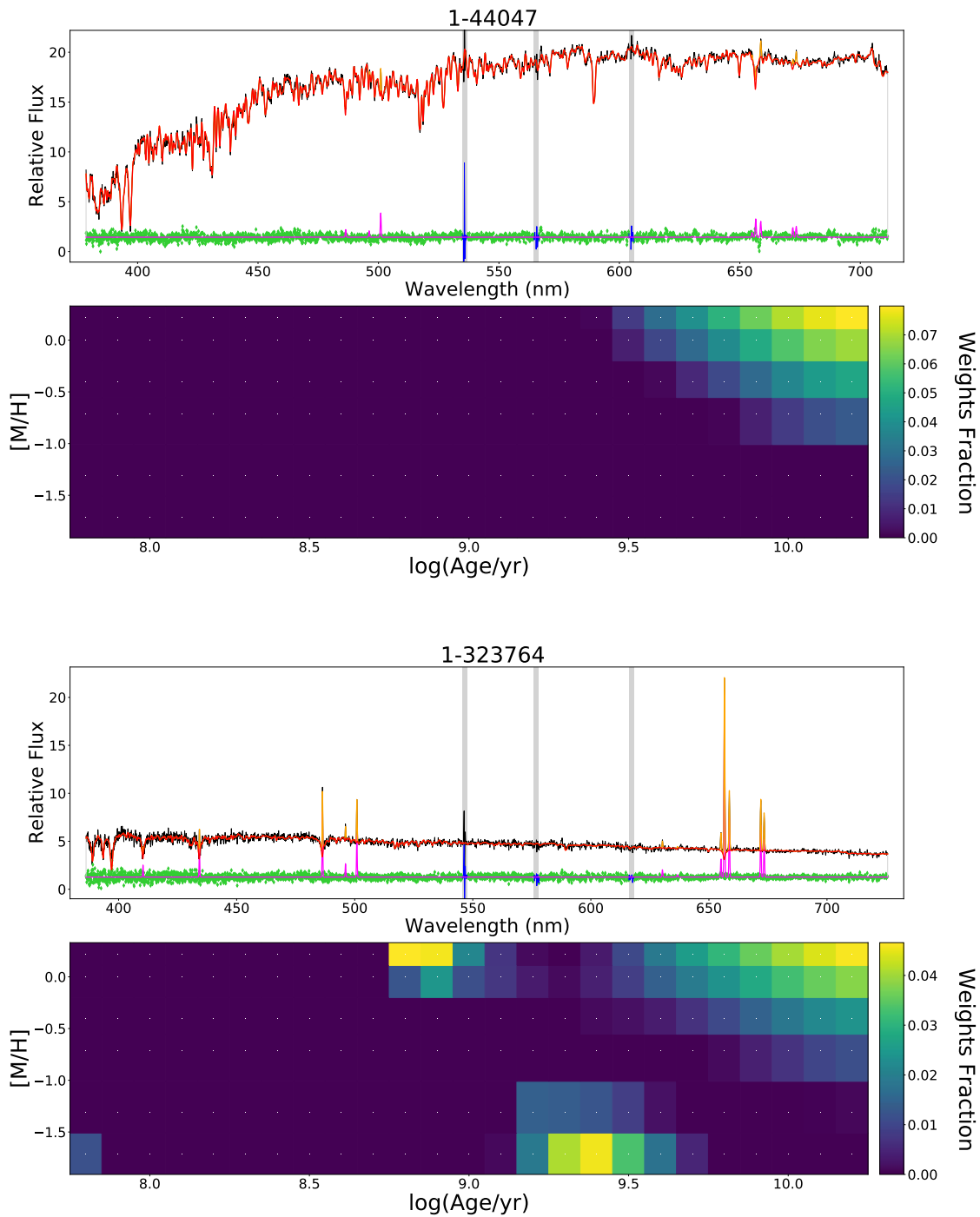


Figure 4.13: Examples of unimodal and multimodal maps. The two upper panels show the stellar population fit and the weights fraction of the SSP templates of a galaxy showing a single blob. The two lower panels show the stellar population fit and the weights fraction of the SSP templates of a galaxy showing three distinct blobs.

Chapter 5

Summary and Results

In this chapter, after a brief summary on the kinematic class of CRDs, the results of this work are presented and discussed.

5.1 Summary on the kinematic class of CRDs

With the two IFS surveys SAURON and ATLAS^{3D} it has been possible to classify ETGs in five different classes, based on their kinematic maps. Here, we focused on the class of galaxies with two counter-rotating stellar disks, so far called ‘ 2σ -galaxies’. In section 2.3 we discussed in detail their internal kinematics and the characteristics that distinguish them from the other classes. Using as an example the first galaxy found with evidences of two counter-rotating stellar disks, we have shown how the two peculiar peaks arise (2.3.1). Next, we discussed how the disk-like nature of counter-rotators clashes with their former classification as NRR, listing in section 2.3.2 all the main differences between 2σ -galaxies and NRR, concluding that galaxies with two counter-rotating stellar disks are in fact misclassified RR. In section 2.3.3 we dismissed the name ‘ 2σ -galaxies’ and introduced the acronym ‘CRD’, for ‘counter-rotating disks’, to designate galaxies with evidences of counter rotation and/or the presence of the two σ peaks; we also cautioned that the kinematic class of galaxies with a KDC can have dispersion maps resembling those of 2σ -galaxies, even though the two kinematic classes are intrinsically different. Afterwards, in section 2.3.4, we presented possible formation scenarios for CRDs: in fact, we currently do not have enough statistics and detailed studies to decide which scenario should be adopted for the formation of counter-rotators.

5.2 The largest sample of CRDs to date

In Chapter 3 we described how our sample of candidates for CRDs was built, starting from a subset of 603 galaxies from the DR16 of MaNGA, and by visually inspecting their kinematic maps. We included in our sample all those galaxies which show either

evidences of counter-rotation or the two peaks in σ , and we used additional criteria for an accurate selection, since the presence of external objects next to the observed galaxy or an ongoing merger, as well as the presence of a bar or of a KDC can give kinematic maps appearances similar to those of CRDs. Our final sample consists of 53 candidate CRD galaxies: this is the largest sample of such galaxies built to date.

This sample is actually smaller than expected, if compared with the ATLAS^{3D} survey; indeed, ATLAS^{3D} found eleven counter-rotating galaxies which constitute 4% of the whole sample of 260 ETGs observed; our sample of CRDs, instead, constitute $\sim 1.7\%$ of all ETGs in the DR16 of MaNGA ($\sim 1.4\%$ if we also consider spirals), notwithstanding the fact that our selection criteria are more inclusive. We expect our statistics on the number of CRDs to be underestimated for two main reasons: (i) galaxies with counter-rotating stellar disks can also be found above the magenta line (see Figure 3.2), while we a priori excluded them from our selection; (ii) because of MaNGA’s modest resolution, the kinematic features of CRDs are not always spottable and, as a consequence, some CRDs could have been excluded from our visual classification. This means that the number of CRDs in MaNGA is likely higher, and the percentage may be thus closer to that of ATLAS^{3D}. One should also consider that the criteria adopted for the selection of galaxies for ATLAS^{3D} and MaNGA surveys are different (see Table 2.4), so a statistical comparison between the two surveys is not straightforward. In conclusion, a more thorough statistical study on the incidence of CRDs is needed.

5.3 Results on Kinematics

In Appendix B we present the velocity and velocity dispersion maps of the whole sample, together with the SDSS images. After we produced the kinematic maps, to have a spectroscopical confirmation of the presence of two counter-rotating disks, we performed two-component fits. In section 4.2.4 we discussed the problem of finding the two kinematic solutions with pPXF and presented the method of χ^2 maps as a possible solution for this problem. As expected, the recovery of two spectroscopically distinct stellar components is difficult for the majority of the galaxies in our sample, mainly because of the relatively low resolution of MaNGA. However, we found nine galaxies where the distinction of the minima is clear, and six galaxies where the distinction is visible, but not obvious; all the remaining cases, instead, present the cross-degeneracy or a flat butterfly-shape (i.e. lacking of the two minima), or the maps appear unclear; we also discussed the limits of this method in the recovery of the two spectroscopic components, and suggested possible improvements. In the literature, this method has been used only twice, and only once for the study of a CRD; here, we provided χ^2 maps of 53 CRD-galaxies, that are shown in Appendix C.

Along with the stellar kinematic maps, we show the velocity fields of the H α , as extracted by the DAP: the rotation of the gaseous disk is indeed related to the history of the galaxy, as mentioned in section 2.3.4. By comparing the gas and stellar velocity maps, we looked for misalignments between the rotation axes of the stellar and the gaseous disks and we found such misalignment in six cases. Figure 5.1 shows the stellar

and gas velocity maps of two galaxies exhibiting alignment and misalignment, respectively, between the rotation of stars and gas. It is interesting to notice that one of the six cases of misalignment, namely 1-282035, is one of the galaxies labelled as ‘forming’, which also shows evidences of multiple population; these observations suggest that we are possibly looking at the early stages of the formation of a CRD-galaxy.

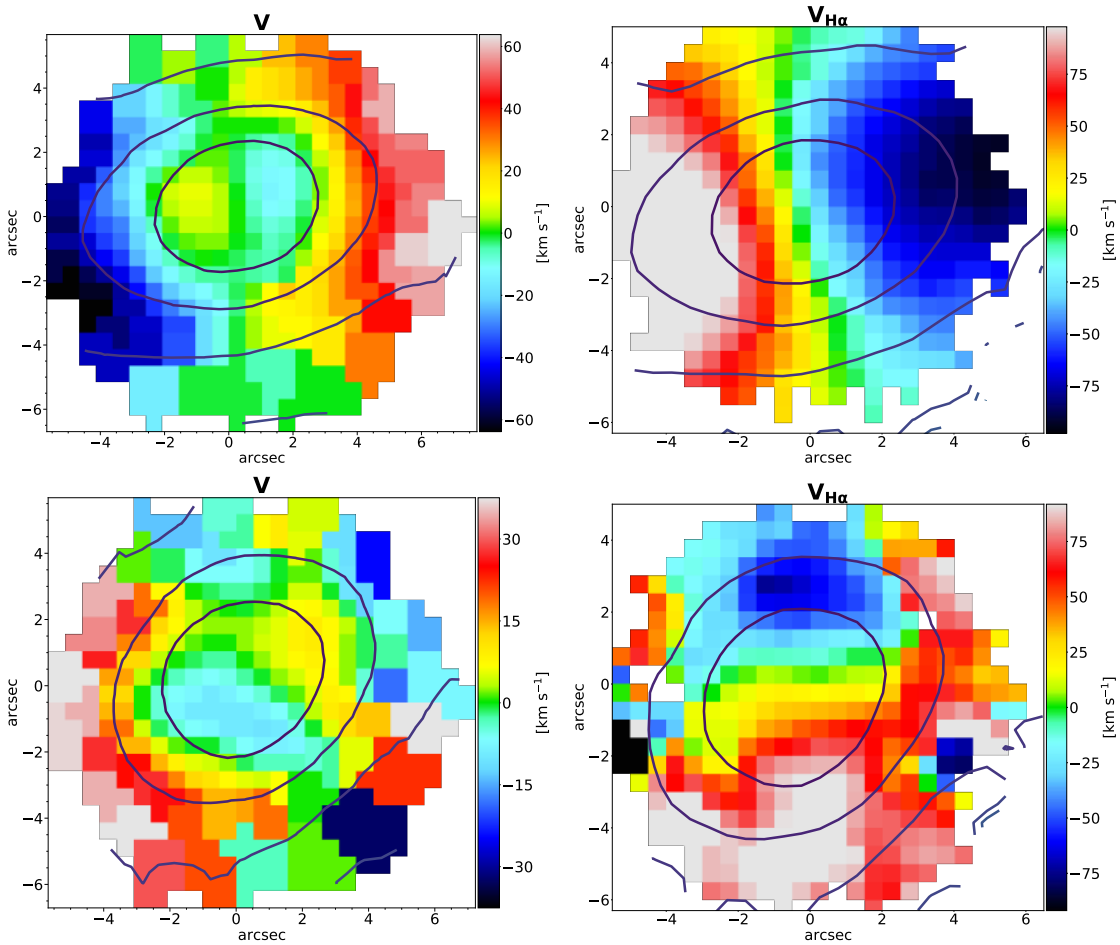


Figure 5.1: Comparison between the stellar and the gas velocity maps of two representative galaxies. *Upper panels*: example of the rotation of the gas aligned with the stellar disks; MaNGA ID: 1-179561; error on V : 3.9 km s^{-1} . In this case, the gas corotates with the inner disk. *Lower panels*: example of gas rotation misaligned with respect to the stellar disks for the galaxy with MaNGA ID: 1-113520; error on V : 4.0 km s^{-1} .

5.4 Results on Stellar Populations

We produced the stellar population maps by using the fitting method described in section 4.3, and we show them in Appendix B. Since different formation scenarios result in different trends in the radial profiles of the stellar population properties (Davies et al.1993; Rawle et al. 2008; Kuntschner et al. 2010 Greene et al. 2013, 2015; Hirschmann et al.2014, Wilkinson et al. 2015; Scott et al. 2013, Li et al. 2018), a study of the age and metallicity gradients would provide very useful information: for example, a negative age gradient suggests an inside-out star formation, while a positive gradient an outside-in star formation. In the following, we make some preliminary considerations based on a visual examination of the stellar population maps, since we have not studied in detail the radial profiles. With the exception of few uncertain cases, all galaxies in our sample show the same metallicity trend, having higher mean metallicity in the central regions than in the outer ones. The age maps, instead, are noisy in most cases; nonetheless, in seven cases the mean population appears younger in the inner regions and older in the outer ones, while the opposite trend is present in five galaxies, which are older in the center and younger outside. An example of a galaxy showing both the age and the metallicity gradients is shown in Figure 5.2.

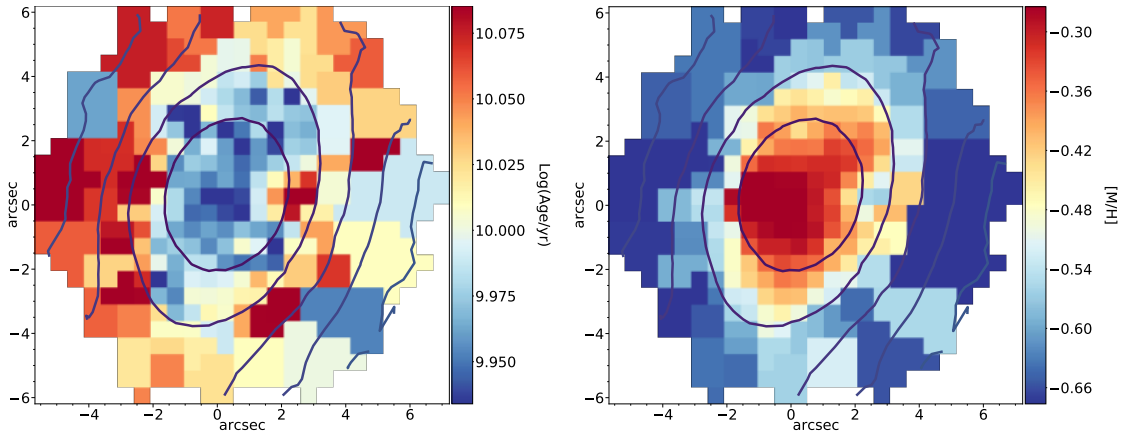


Figure 5.2: Example of a galaxy exhibiting age and metallicity radial trend. These maps refer to the galaxy with MaNGA ID: 1-113520. The two maps show that the central regions are younger and more metallic than the outer ones. Estimated errors for $\text{Log}(\text{Age})$ and $[\text{M}/\text{H}]$ are 0.037 and 0.06, respectively.

Two interesting cases of galaxies showing a positive age trends are 1-163594 and 1-113520; in fact, they both have the gas misaligned with respect to the stellar disks (e.g. 1-113520 is shown in Figure 5.1); the SDSS images do not clearly show evidences of a recent merger, but both galaxies present external objects or blobs in their surroundings. One can speculate that a relatively recent accretion occurred, as the misalignment of the gas indicates, and enhanced the star formation in the central regions, thus producing the observed age trend.

To find evidences of distinct populations, for each galaxy we performed regularized fits (4.3.1). We found that galaxies can exhibit both unimodality and multimodality in the weights fraction map. The multimodality, which supports the presence of different populations, is present in thirteen galaxies; notice that these include all the four galaxies labeled as ‘Forming’ in section 3.3. Twenty-eight galaxies, on the contrary, show unimodal weights maps. The remaining cases are uncertain. In Appendix D we show the weights map for each galaxy. A proper analysis of the stellar population properties requires a spectroscopical decomposition of the two stellar disks; the presented results are meant to point out which galaxies may have evidences of distinct populations or not.

In Table 5.1 we summarize our results on kinematics, on the analysis of the stellar population maps, and on the maps from regularized fits.

MaNGA ID	χ^2	∇Age	# pop	MaNGA ID	χ^2	∇Age	# pop
12-84617	u	\ominus	2	1-113520*	C/FB	\oplus	1
1-115097	D	u	1	1-38347	u	u	1
1-339061	D	u	1	1-44047	D	\oplus	1
1-44483	D	u	1	1-556514	u	u	1
1-37494	C/FB	u	1	1-37155	C/FB	u	u
1-38543	D	u	1	1-47248	D	\ominus	1
1-137890	C/FB	u	3	1-255220	C/FB	\oplus	1
1-282035 [†] *	C/FB	u	3	1-251783	u	u	u
1-419257	D	\oplus	u	1-418023	C/FB	\ominus	u
1-167555*	C/FB	u	u	1-274440	C/FB	null	3
1-274545 [†]	u	u	3	1-275185	u	u	1
1-167044	u	u	1	1-166613	u	u	1
1-246175	u	\ominus	1	1-210728	u	\ominus	1
1-248869	D	u	1	1-136248	D	u	1
1-179561	C/FB	u	3	1-635590	D	u	1
1-113698 [†]	C/FB	u	3	1-44722	u	null	u
1-45016	u	u	1	1-163594*	C/FB	\oplus	1
1-248410	C/FB	u	2	1-235983*	C/FB	u	1
1-236144 [‡]	C/FB	u	u	1-174947	D	u	1
1-278079	u	u	u	1-188530	C/FB	u	1
1-149172	u	u	2	1-94773*	C/FB	u	2
1-94690	D	u	1	1-323766	C/FB	\oplus	2
1-323764 [†]	C/FB	u	3	1-135244	D	u	1
1-549076	D	u	u	1-314719	u	\oplus	1
1-299176	u	u	1	1-298940	u	u	1
1-593328 [‡]	D	u	1	1-322291	C/FB	u	1
1-633000	u	u	2				

Table 5.1: Summary table on the results from the analysis on the kinematics and stellar population properties. The MaNGA IDs are listed; the ‘[†]’ and ‘[‡]’ are the galaxies labelled as ‘Forming’ and ‘Dusty’, respectively; the ‘*’ indicates that the gas and stellar rotations are misaligned. In the ‘ χ^2 ’ column, ‘D’ represents galaxies with distinct minima in the ‘ χ^2 ’ map, while ‘C/FB’ stands for ‘Cross or Flat Butterfly’; the unclear cases are labelled as ‘u’. The ∇Age is the mean age variation from the inner to the outer regions of the maps: ‘ \oplus ’ means that the age increases in the outer regions (i.e. young-to-old variation), while ‘ \ominus ’ means the opposite (i.e. an old-to-young variation); the unclear cases are labelled ‘u’. The ‘# pop’ column summarizes the results on the weights maps of the regularized fits; 1,2 and 3 represent the number of distinct blobs distinguishable in the maps.

5.5 Conclusions and Future Perspectives

After three decades from their discovery, galaxies with counter-rotating stellar disks are still a puzzling subject and represent a challenge from both an observational and a theoretical point of view. In this thesis work we set up the strategy to select CRDs from data provided by the MaNGA survey, and we built a sample of 53 best candidates of CRD-galaxies. To find which of them are truly CRDs, we need kinematic maps from higher resolution data; in fact, a true CRD must show both the counter-rotation and the two σ peaks, while many galaxies in our sample exhibit just one feature. We then suggest to observe such cases with the MUSE instrument of the VLT (which already discovered a CRD in NGC 5102 (Mitzkus et al. (2016))). Further, to study the stellar populations of the two disks, a spectroscopic decomposition of the two components is needed; such spectroscopic analysis has been successfully done e.g. with the VIMOS instrument of the VLT (Coccatto et al. (2011), Coccatto et al. (2012)). Some extension of the presented results can be obtained even using MaNGA data, though, and we are currently pursuing the following lines of investigation:

- We are testing how the χ^2 maps change with the S/N and, in particular, what is the minimum S/N which allows for the spectroscopical distinction of the two components. Further, we are checking if an accurate selection of the template for the fit of the two components may improve significantly the recovery of the two components, thus resulting in a clear appearance of the two minima in the χ^2 maps. Finally, we are investigating new approaches to favour the appearance of the two minima in the χ^2 .
- We are analysing more in detail the results on the stellar population properties. We are properly studying the age and metallicity gradients by looking at their radial profiles, and we will consider the relations of gradients with other physical properties of the galaxies, e.g. their masses, sizes and velocity dispersions. Finally, we will investigate more thoroughly the modality of the stellar populations of the galaxies in the sample.
- To better understand the internal structures of the CRDs, we will model the masses of the two disks, to find how much stellar mass resides in each disk, and how the amount of rotating and counter-rotating mass is related with the observed properties.

Our current knowledge of CRDs presents many unsolved problems: What is the incidence of CRDs among galaxies of all kinematical and morphological types? How do these galaxies form? Are they the result of a single or of different formation mechanisms? Do the observed properties depend on such mechanisms or on a subsequent evolution? Are the ages of the two counter-rotating disks always different or there exist CRDs with the same age? Does the counter-rotation represent only a peculiarity of the general framework of the galaxy evolution or does it constitute an important tile? The recent technological advances and consequent studies laid the foundations to answer these questions; however, much work is still needed for a clear comprehension of galaxies with two counter-rotating stellar disks.

Appendix A

pPXF

This appendix gives a mathematical description of the penalized pixel-fitting (pPXF) method, firstly described in Cappellari and Emsellem (2004) and substantially upgraded in Cappellari (2016b). This method allows for the extraction of the stellar and gas kinematics, as well as for the determination of the stellar population properties of galaxies via full spectrum fitting.

The general idea of this method is that, when fitting moments of the LOSVD ≥ 3 , starting from the residuals between a model spectrum and an observed spectrum, one can implement a penalty function that describes the deviation of the LOSVD from a Gaussian shape and penalizes non-Gaussian solutions (from which the package takes its name). In this work, however, we use pPXF to fit only the first two moments of the LOSVD; for this reason, we limit our discussion on the fitting procedure described in section 3.3 of Cappellari (2016b). For a full description of the method we address the reader to the two reference papers mentioned above.

Fitting procedure

The parametric recovery of the LOSVD in pixel space starts with creating a model spectrum. In pPXF, the model spectrum is an approximation of the observed one: it is assumed to be composed of a weighted mixture of template spectra convolved with the LOSVD and adjusted with additive and multiplicative polynomials, in order to reduce the mismatch with the observed spectrum. More explicitly, after rebinning the wavelength λ as $x = \ln \lambda$, the model spectrum is defined as:

$$G_{mod}(x) = \sum_{n=1}^N w_n \left\{ [T_n(x) * \mathcal{L}(cx)] \sum_{k=1}^K a_k \mathcal{P}_k(x) \right\} + \sum_{l=0}^L b_l \mathcal{P}_l(x) + \sum_{j=1}^J c_j S_j(x) \quad (\text{A.1})$$

where the $\mathcal{L}(cx)$ is the broadening function that can be different for the N templates

T_n , and w_n are the weights; \mathcal{P}_k and \mathcal{P}_l are multiplicative and additive polynomials (of Legendre type or a truncated Fourier series) of degree k and l respectively, with a_k and b_l as constants; finally, S_j are the spectra of the sky, with c_j as constants.

To parametrize the LOSVD $\mathcal{L}_n(v)$, it has become common to use the Gauss-Hermite parametrization introduced by van der Marel and Franx1993, where the first three coefficient are set to $(h_0, h_1, h_2) = (1, 0, 0)$ and only higher coefficients are fitted; in such a way the LOSVD has the form:

$$\mathcal{L}(y) = \frac{e^{-y^2/2}}{\sigma\sqrt{2\pi}} \left[1 + \sum_{m=3}^M h_m H_m(y) \right] \quad (\text{A.2})$$

where $y = (v - V)/\sigma$, with V and σ being the mean radial velocity and the velocity dispersion of the Gaussian, and H_m are the Hermite polynomials.

The best fitting parameters of eq (A.1) are found by minimizing the disagreement between the model spectrum and the observed spectrum. The agreement can be quantified using:

$$\chi^2 = \sum_{n=1}^N r_n^2 \quad (\text{A.3})$$

where r_n are the residuals, defined as:

$$r_n = \frac{G_{mod}(x_n) - G(x_n)}{\Delta G(x_n)} \quad (\text{A.4})$$

with $\Delta G(x_n)$ the measurement error¹ on the observed spectrum $G(x_n)$ at the n -th spectral pixel x_n .

One of the main feature of pPXF is the possibility of fitting different LOSVDs for every individual template (e.g. Johnston et al. (2012), Mitzkus et al. (2016)), which allows for the recovery of the kinematics of multiple components. For example, one can simultaneously fit two different (e.g. counter-rotating) stellar components (as in 4.2.4), as well as the gas emission lines² and the stellar population (as in 4.3) of a galaxy.

¹This corresponds to the input noise we use in fits. See section 4.1.

²For a description of the gas templates see section 3.6 of Cappellari (2016b)

Appendix B

Kinematic and Stellar Population maps of the CRD sample

Here we present our sample of galaxies. Each Figure has the following structure. Upper panels: SDSS image and velocity map of H α ; middle panels: stellar velocity and velocity dispersion maps; lower panels: age and metallicity maps. The MaNGA ID of the corresponding galaxy is written as the title.

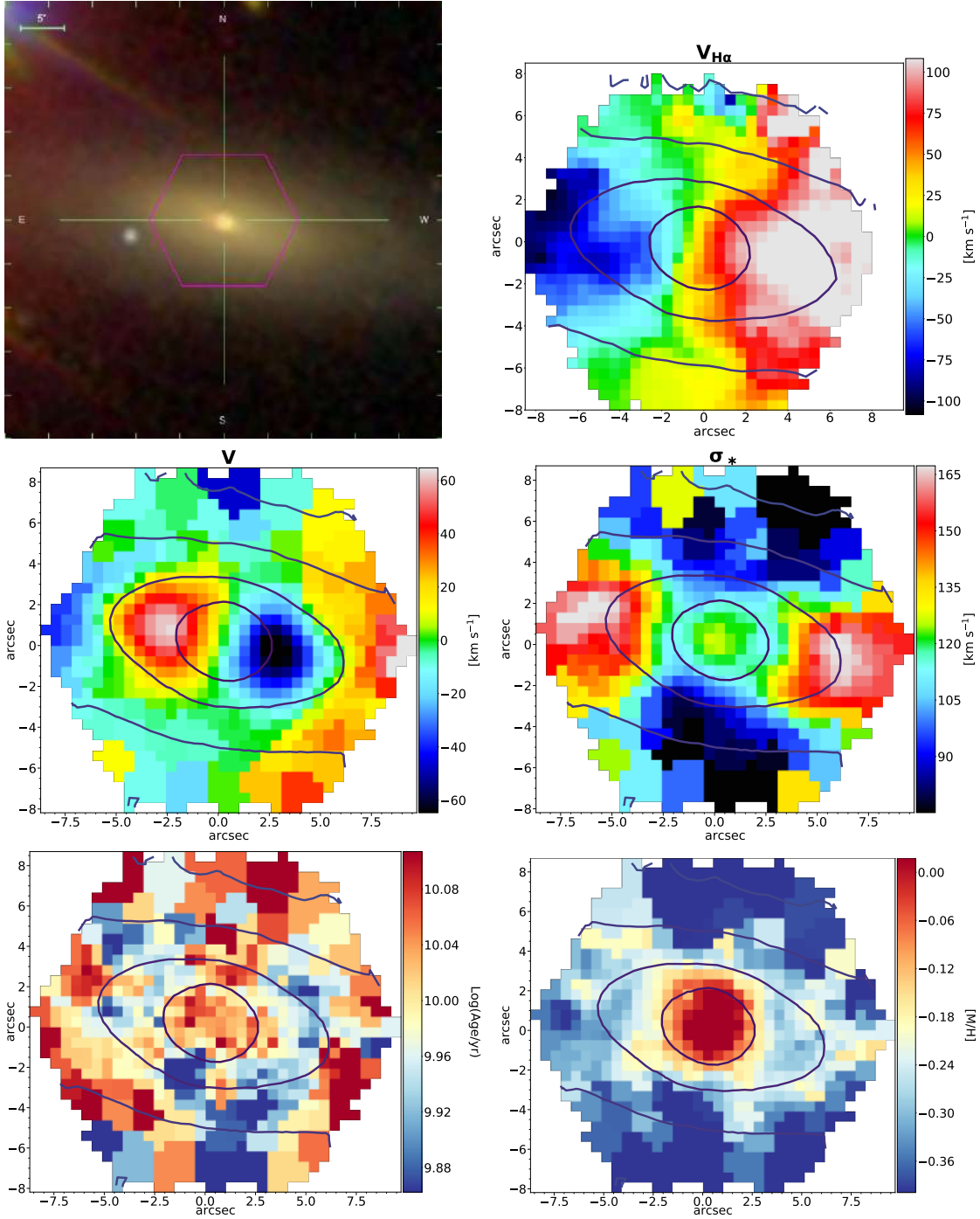
The selection criteria for our sample are described in Chapter 3. SDSS images are available at <https://data.sdss.org/sas/dr16/>. Velocity maps of the gas are provided by the DAP; pixels with S/N < 1 are masked. Stellar kinematic maps have been extracted following the procedure described in section 4.2.3. As discussed in section 4.2.2, we did not match the resolutions of the MaNGA and MILES spectra; to account for the mismatch, we need to correct the extracted velocity dispersion as follows:

$$\sigma_* = \sqrt{\sigma^2 - \sigma_{inst}^2}. \quad (\text{B.1})$$

where σ_* is the intrinsic stellar dispersion, σ is the observed dispersion (i.e. the kinematic solution of the fit) and σ_{inst} is the instrumental correction. The DAP calculated a median value of $\sigma_{inst} \approx 40$ km/s. We then choose this value as the fixed instrumental correction in equation (B.1) for our whole sample. Notice that when $\sigma < \sigma_{inst}$ we get an unphysical numerical value for σ_* ; it has been shown (Cappellari (2016b)) how the recovery of the stellar dispersion with pPXF is reliable even when the measured stellar dispersion is lower than the instrumental resolution. In the presented maps, we decided to set the unphysical values to the minimum value physically meaningful of all fitted spatial bins. Error on the kinematics are the median values of the formal errors of all spatial bins. Stellar population maps have been extracted following the procedure described in section 4.3; error on ages and metallicities are calculated as the rms of the residuals between a LOESS fit of the data and the actual data.

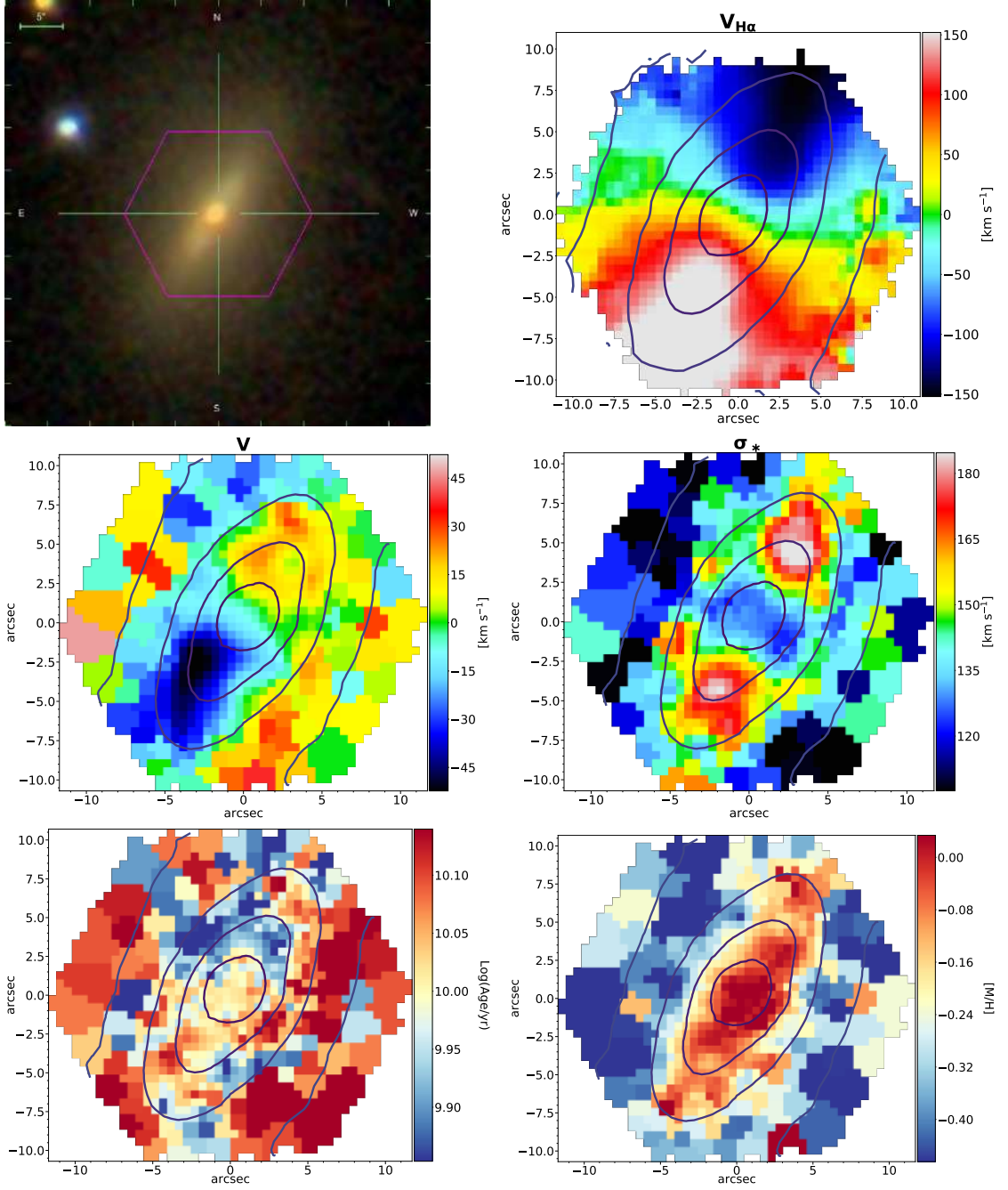
Figure B.1: From top left to bottom right: SDSS image, velocity map of $H\alpha$, stellar velocity map, stellar velocity dispersion, age map and metallicity map. Velocities are in $[\text{km s}^{-1}]$; age is in logarithmic scale, with base 10. Colorbars are shown on the right sides of maps. The MaNGA ID is written as the title; the symbol \otimes is for galaxies with bad quality flags; errors are written at the bottom.

MaNGA ID: 1-136248



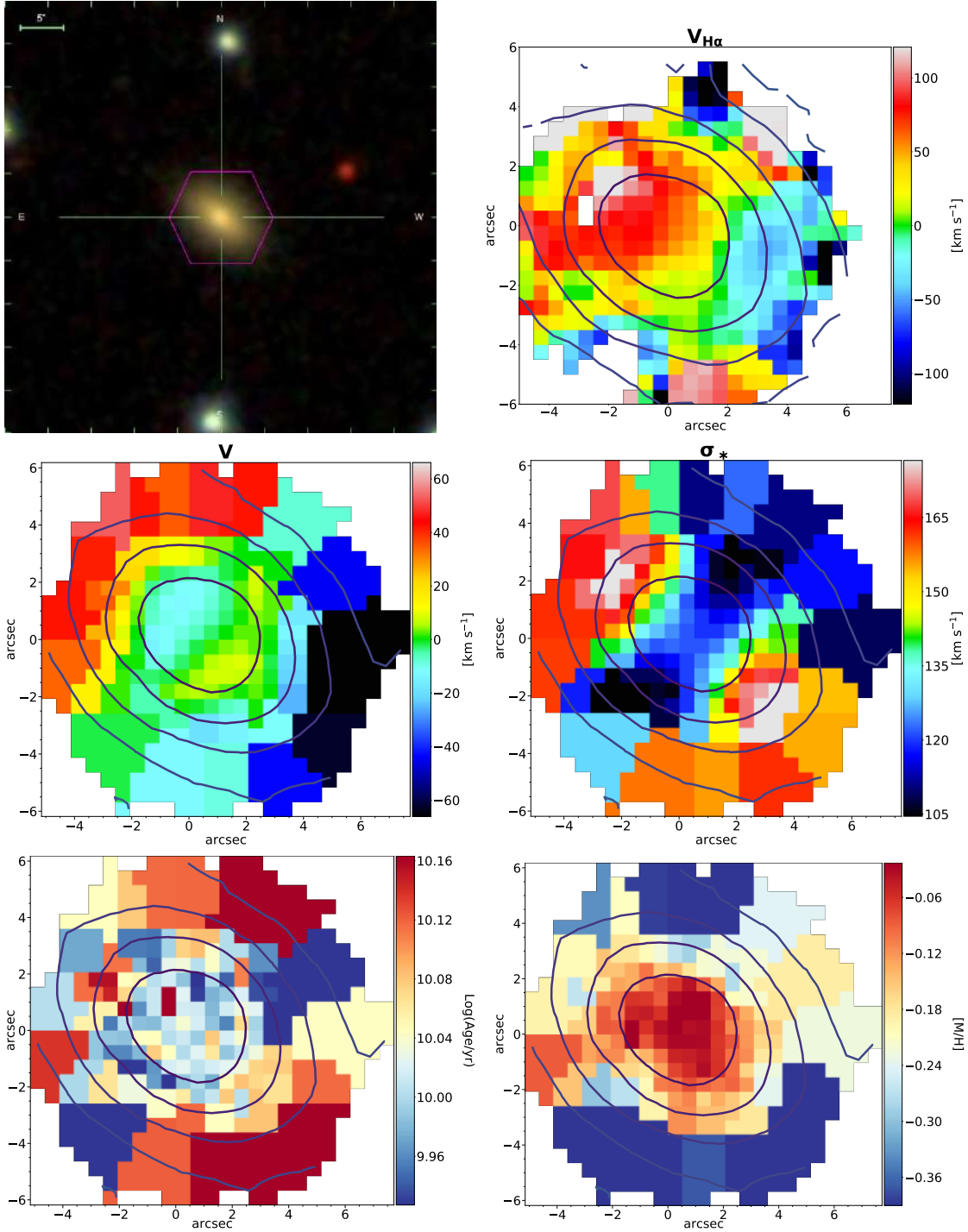
Error on V : 4.1 km s^{-1} ; error on σ_* : 4.8 km s^{-1} ; error on Log(Age) : 0.065; error on $[M/H]$: 0.07.

MaNGA ID: 1-339061



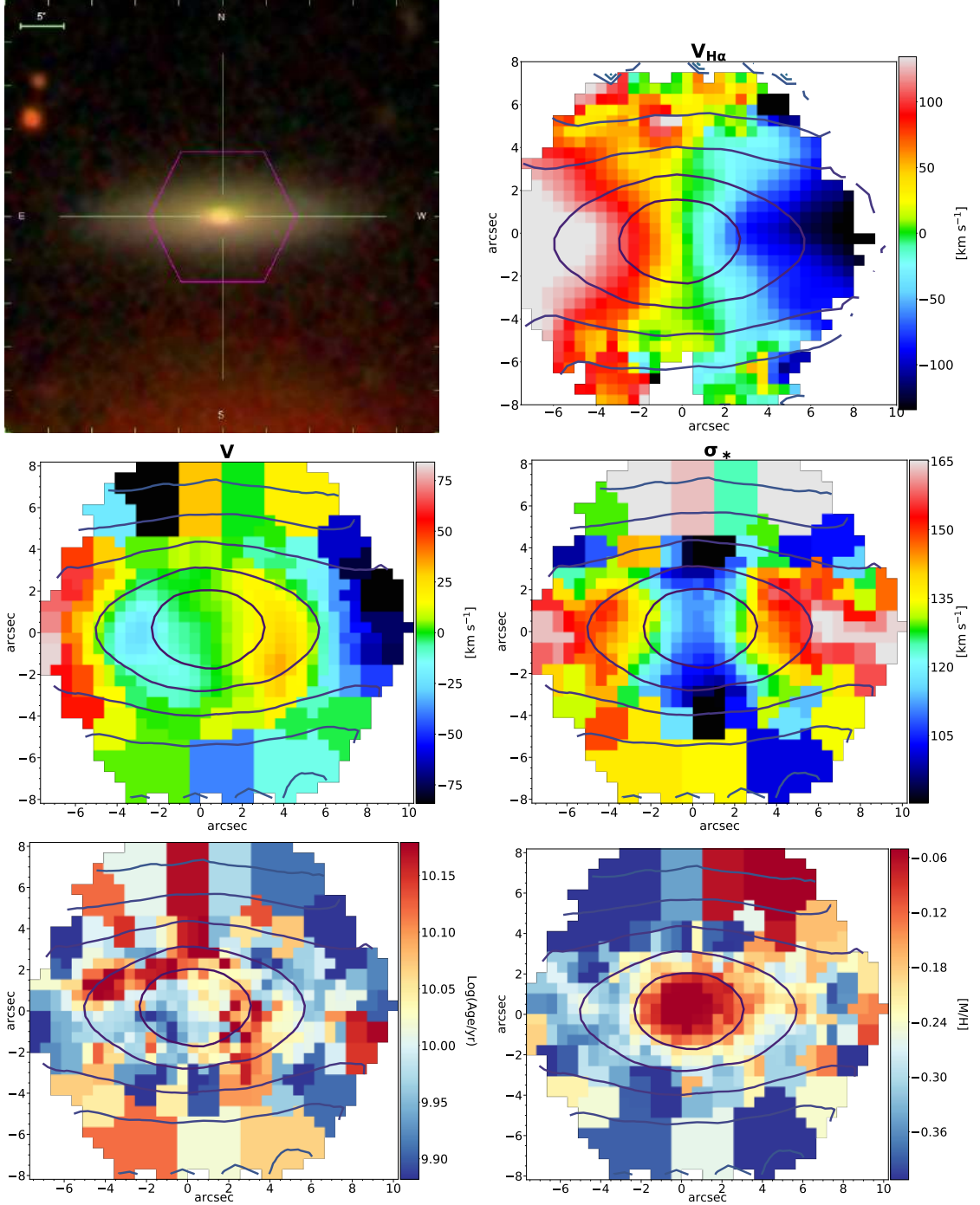
Error on V : 5.3 km s^{-1} ; error on σ_* : 5.8 km s^{-1} ; error on $\text{Log}(\text{Age})$: 0.071 ; error on $[\text{M}/\text{H}]$: 0.10.

MaNGA ID: 1-44047



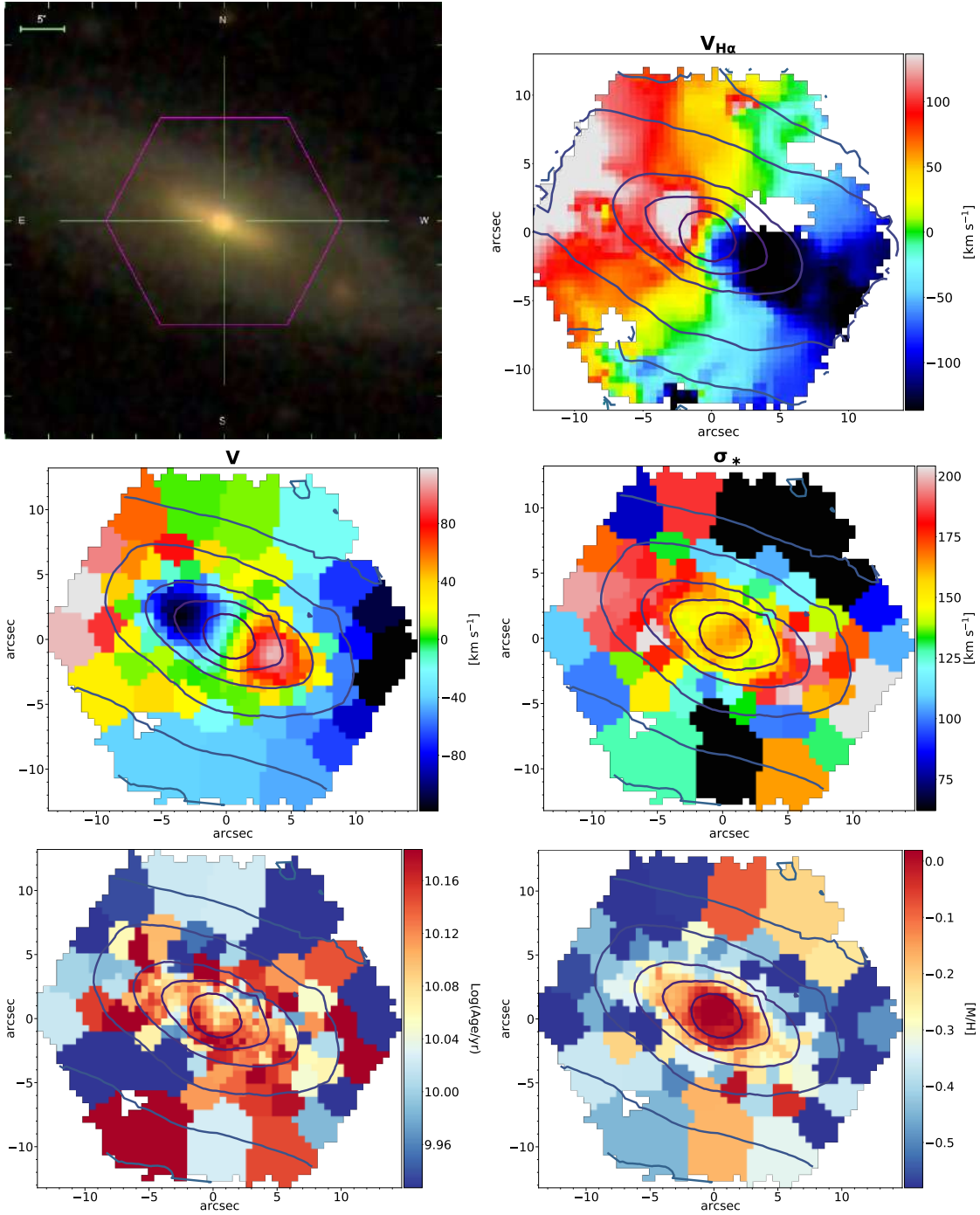
Error on V : 3.9 km s^{-1} ; error on σ_* : 4.3 km s^{-1} ; error on Log(Age) : 0.057; error on $[M/H]$: 0.05.

MaNGA ID: 1-44483 \otimes



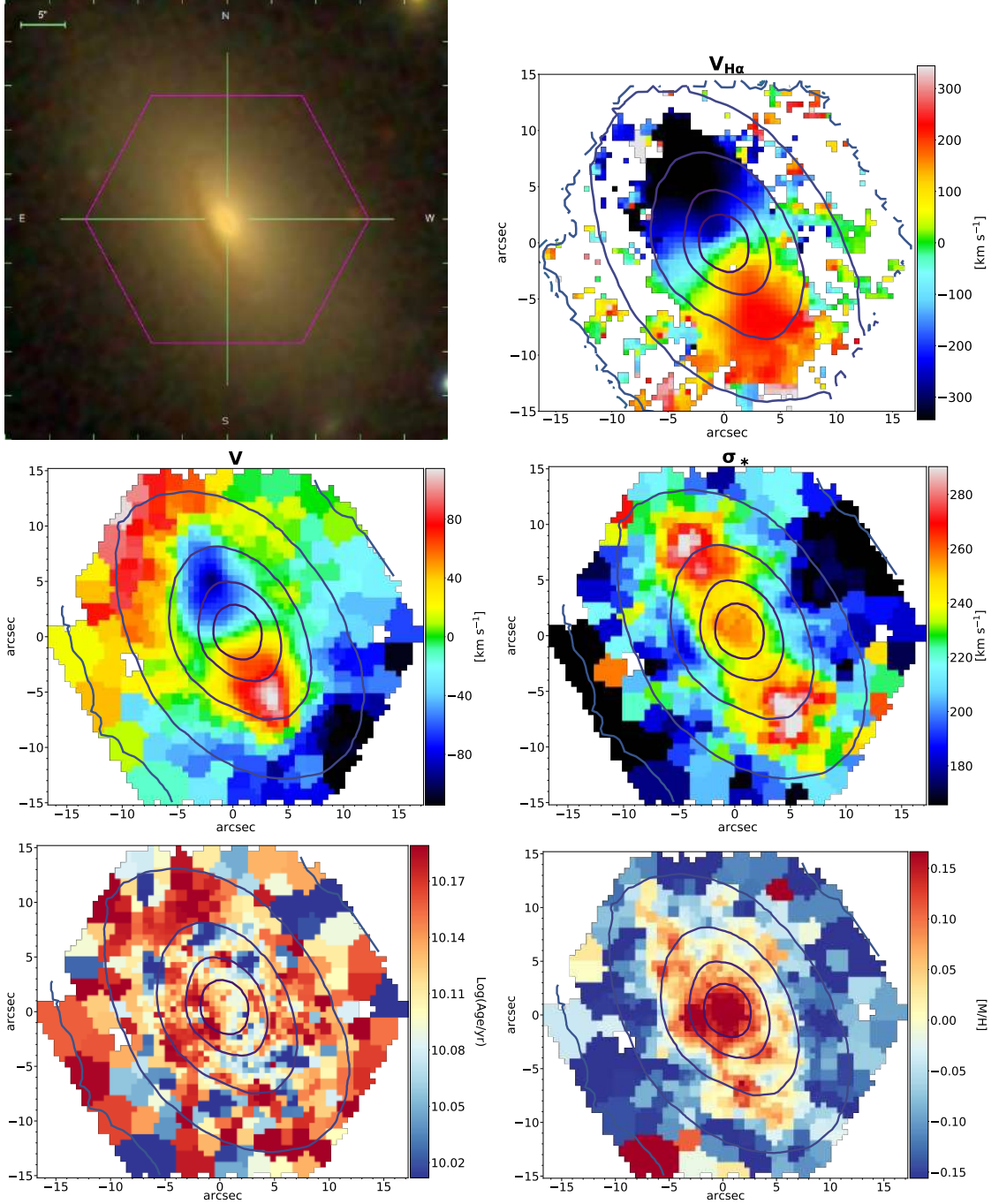
Error on V : 4.3 km s^{-1} ; error on σ_* : 4.9 km s^{-1} ; error on $\text{Log}(\text{Age})$: 0.077; error on $[\text{M}/\text{H}]$: 0.07.

MaNGA ID: 1-174947



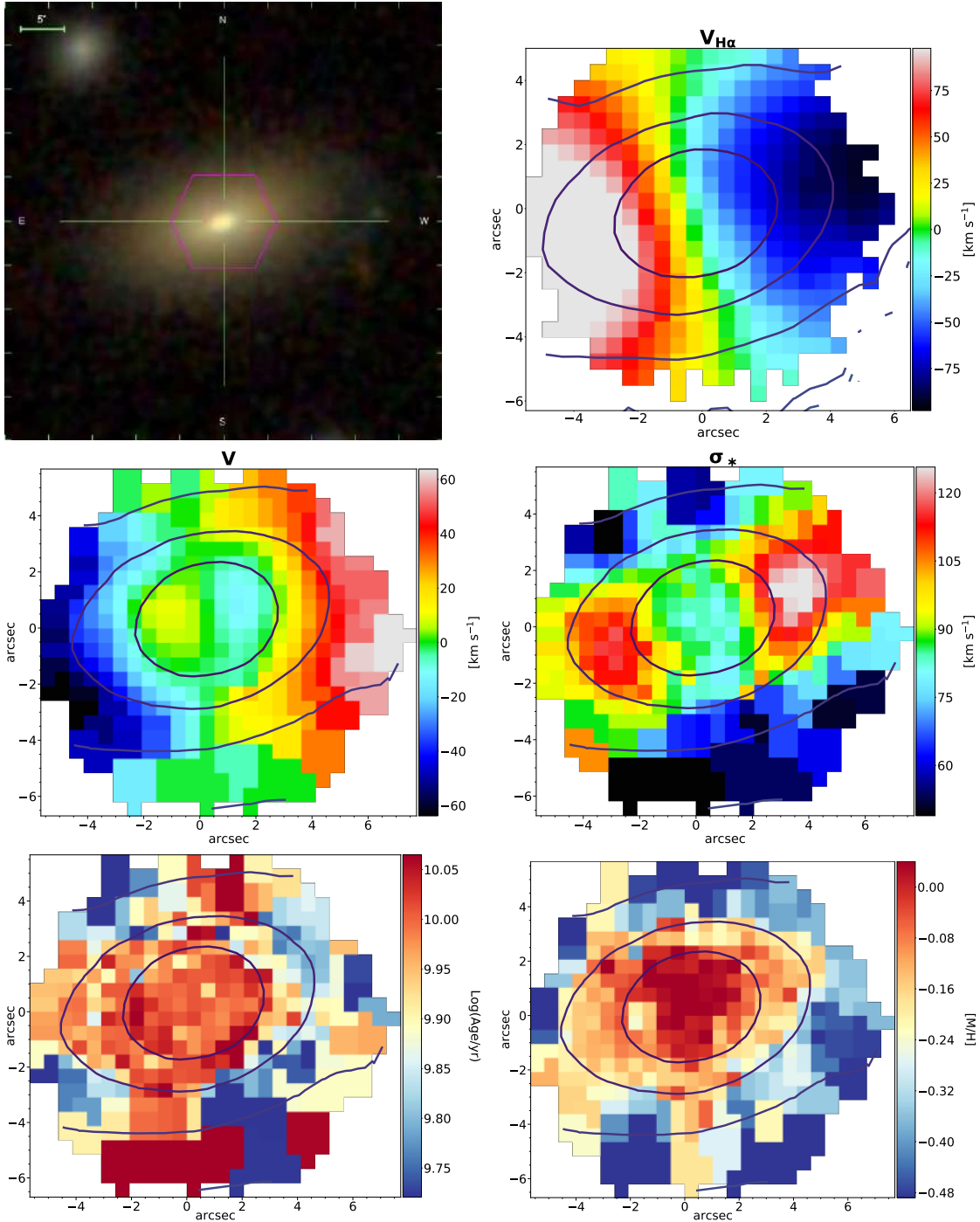
Error on V : 5.2 km s⁻¹; error on σ_* : 5.8 km s⁻¹; error on $\log(\text{Age})$: 0.064; error on $[M/H]$: 0.09.

MaNGA ID: 1-593328



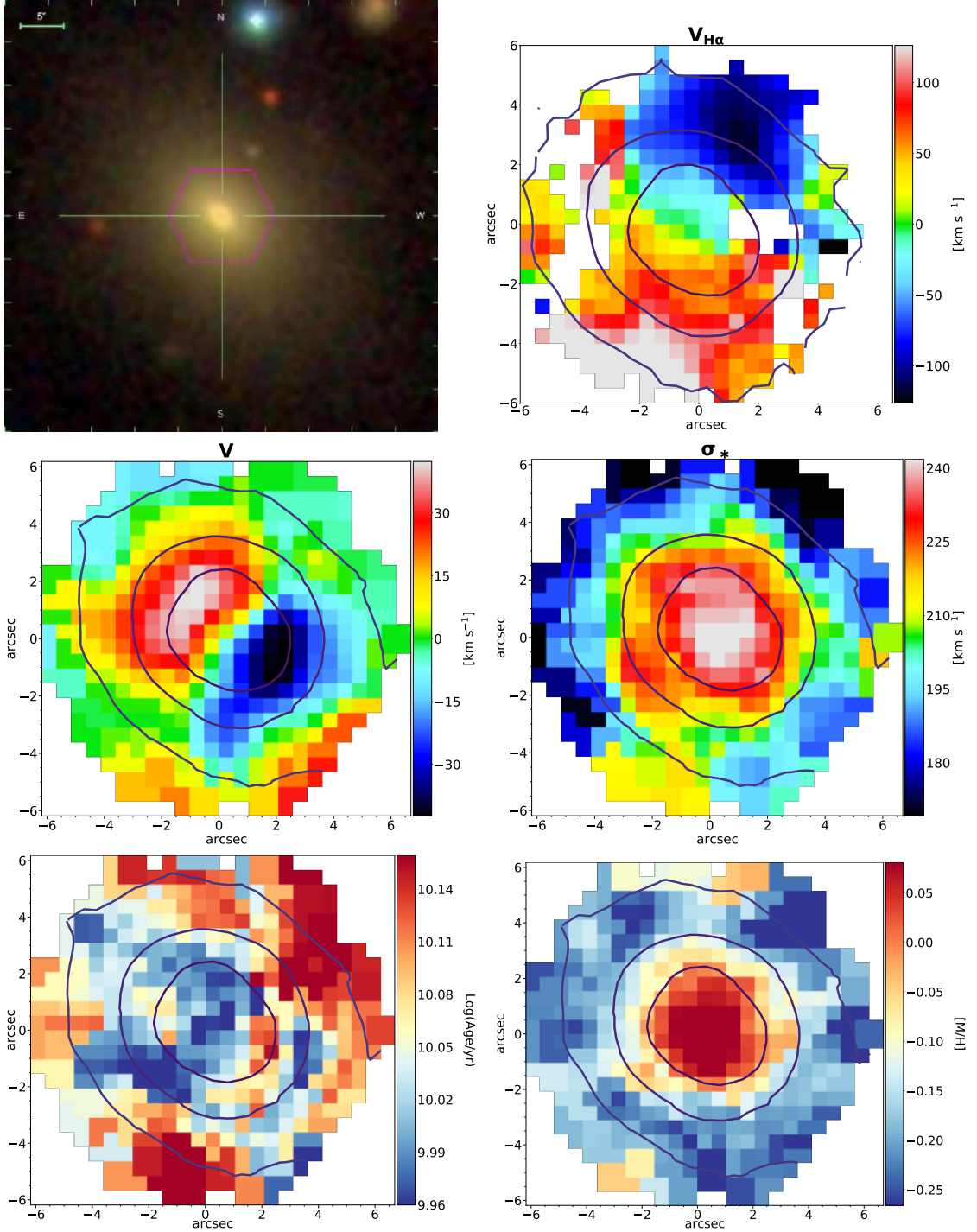
Error on V : 8.3 km s^{-1} ; error on σ_* : 8.6 km s^{-1} ; error on $\text{Log}(\text{Age})$: 0.053 ; error on $[M/H]$: 0.06 .

MaNGA ID: 1-179561



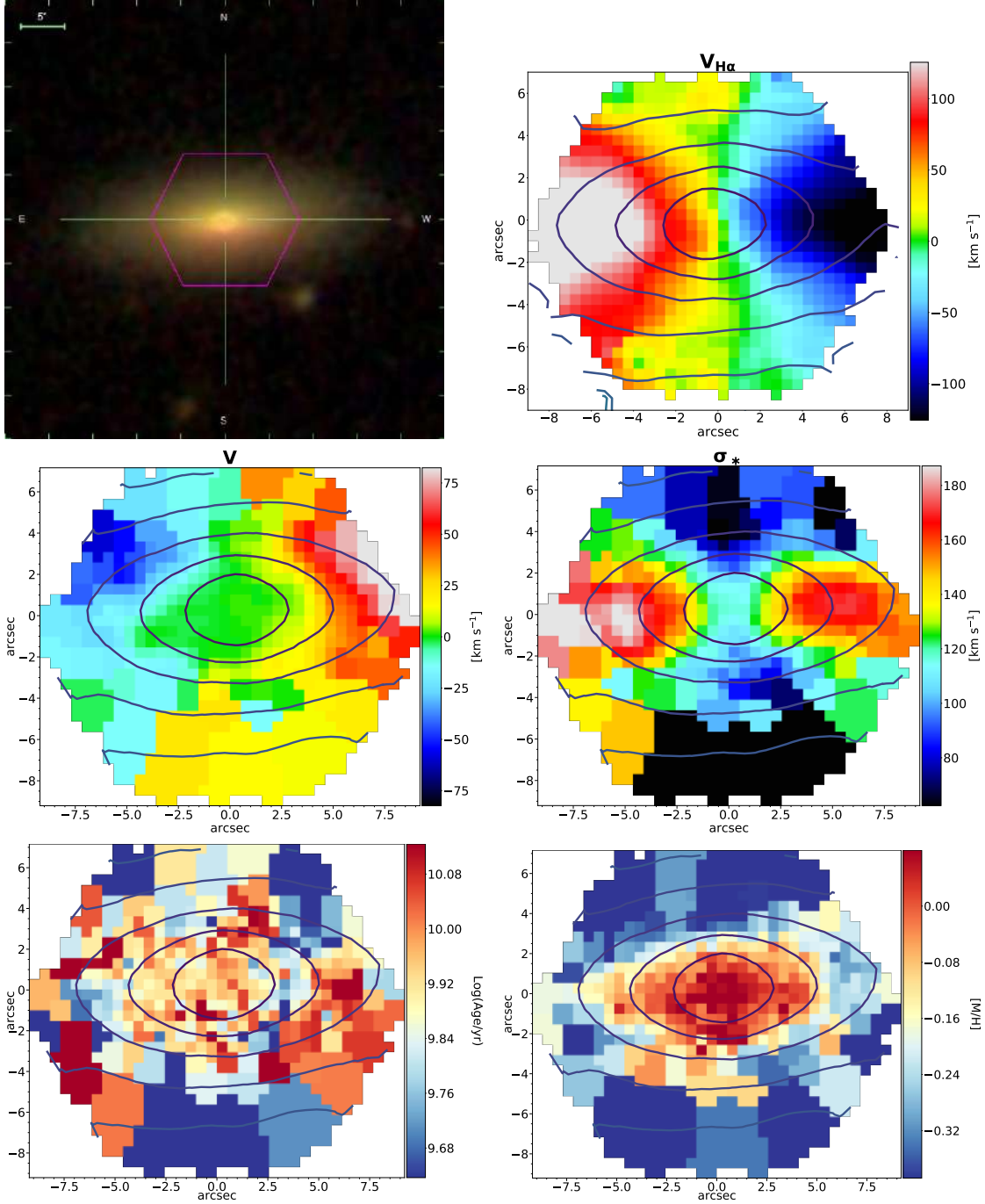
Error on V : 3.9 km s⁻¹; error on σ_* : 4.8 km s⁻¹; error on $\text{Log}(\text{Age})$: 0.091; error on $[M/H]$: 0.11.

MaNGA ID: 1-163594



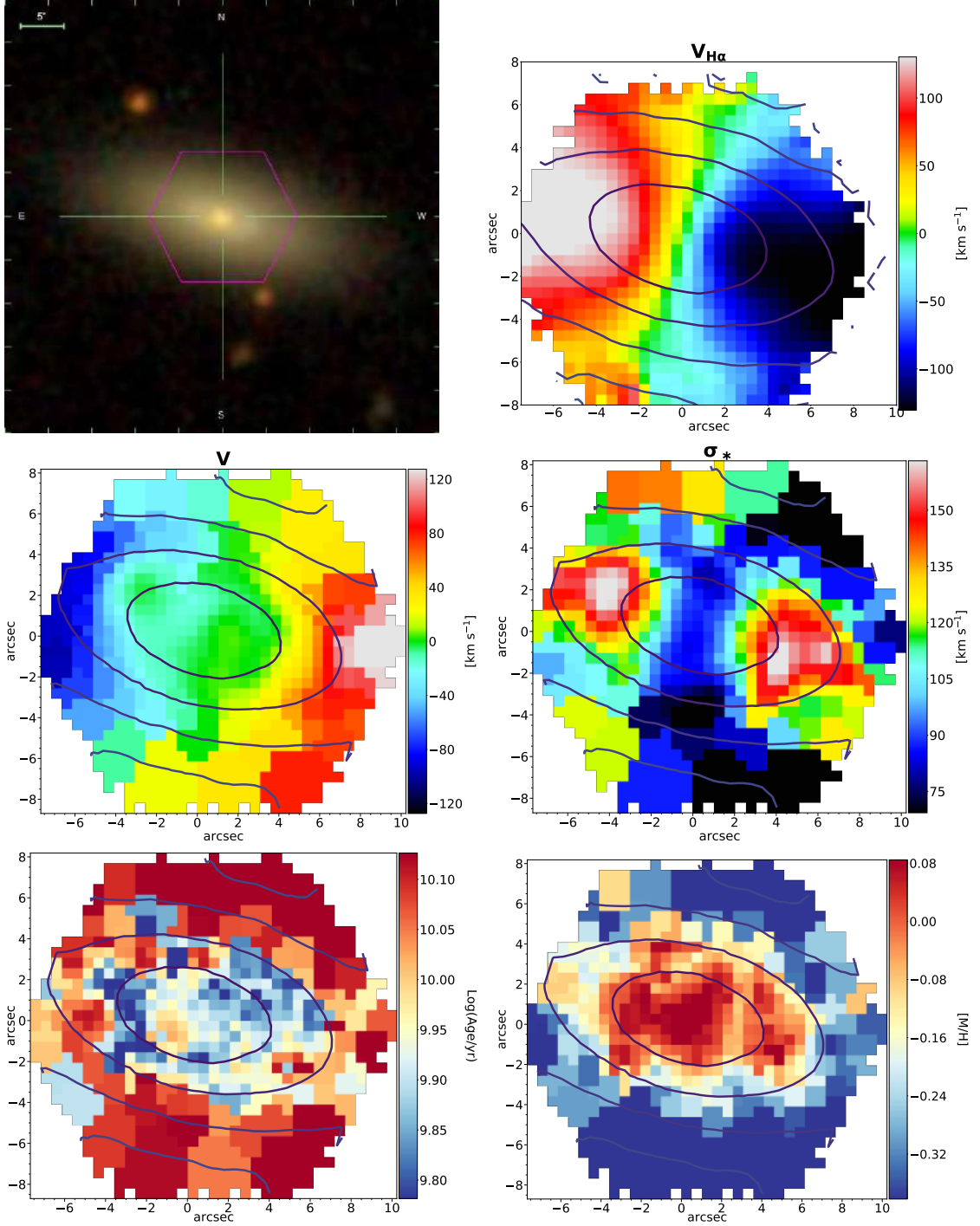
Error on V : 5.1 km s^{-1} ; error on σ_* : 5.3 km s^{-1} ; error on $\text{Log}(\text{Age})$: 0.049; error on $[\text{M}/\text{H}]$: 0.06.

MaNGA ID: 1-38543



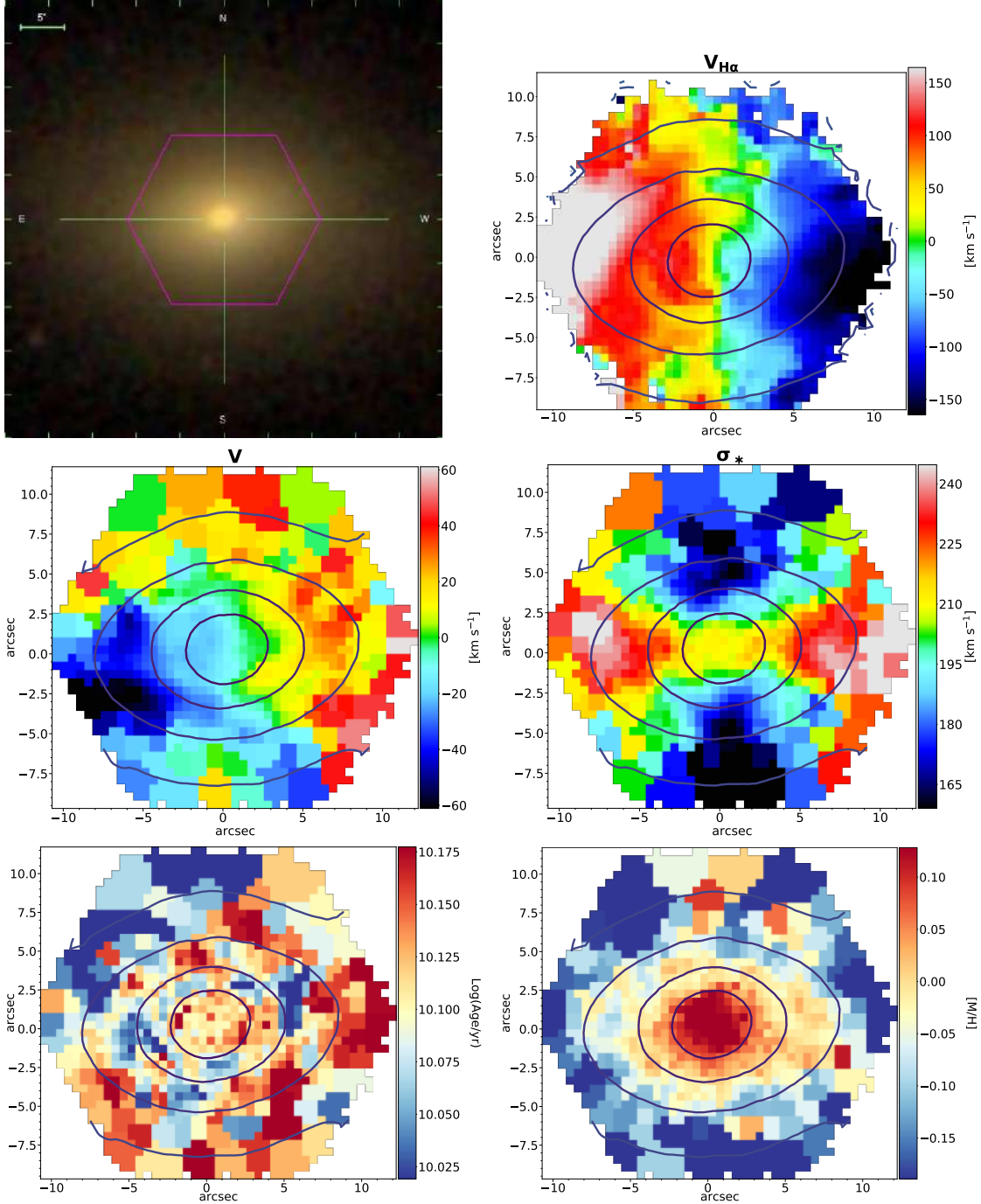
Error on V : 4.6 km s^{-1} ; error on σ_* : 5.2 km s^{-1} ; error on $\text{Log}(\text{Age})$: 0.130; error on $[\text{M}/\text{H}]$: 0.07.

MaNGA ID: 1-419257



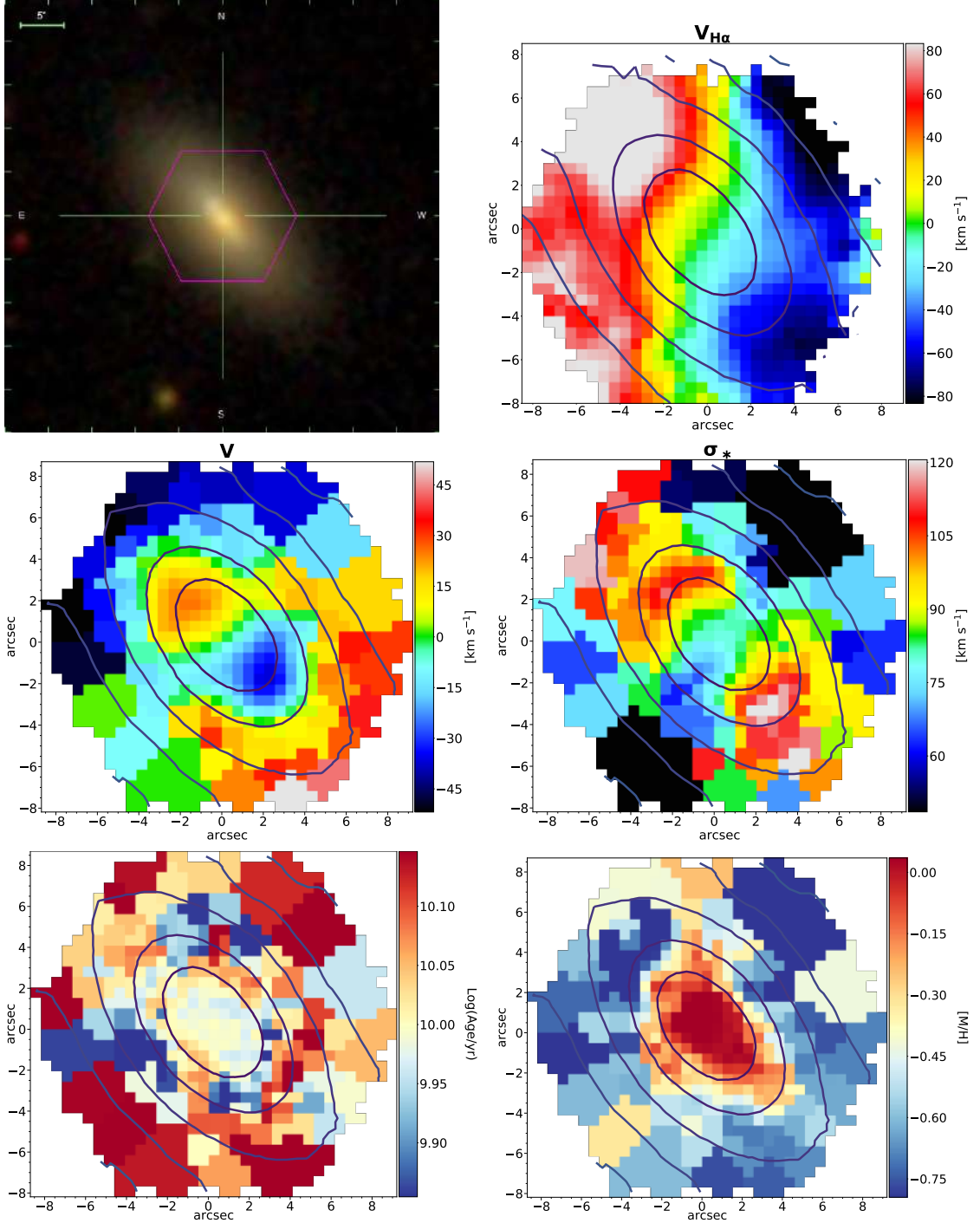
Error on V : 4.6 km s $^{-1}$; error on σ_* : 5.2 km s $^{-1}$; error on $\text{Log}(\text{Age})$: 0.087; error on $[M/H]$: 0.08.

MaNGA ID: 1-248869



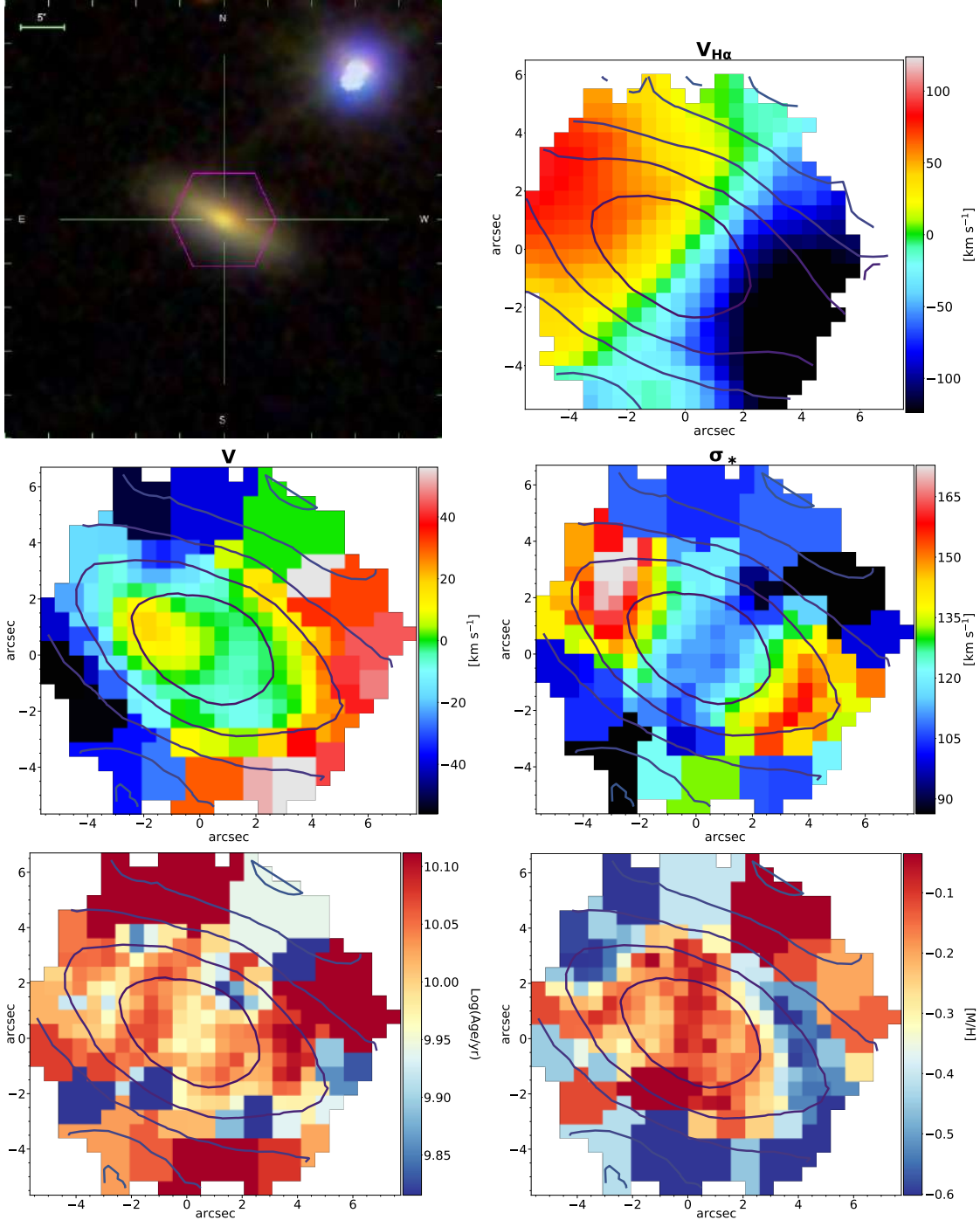
Error on V : 5.7 km s^{-1} ; error on σ_* : 6.0 km s^{-1} ; error on Log(Age) : 0.044; error on $[M/H]$: 0.05.

MaNGA ID: 1-633000



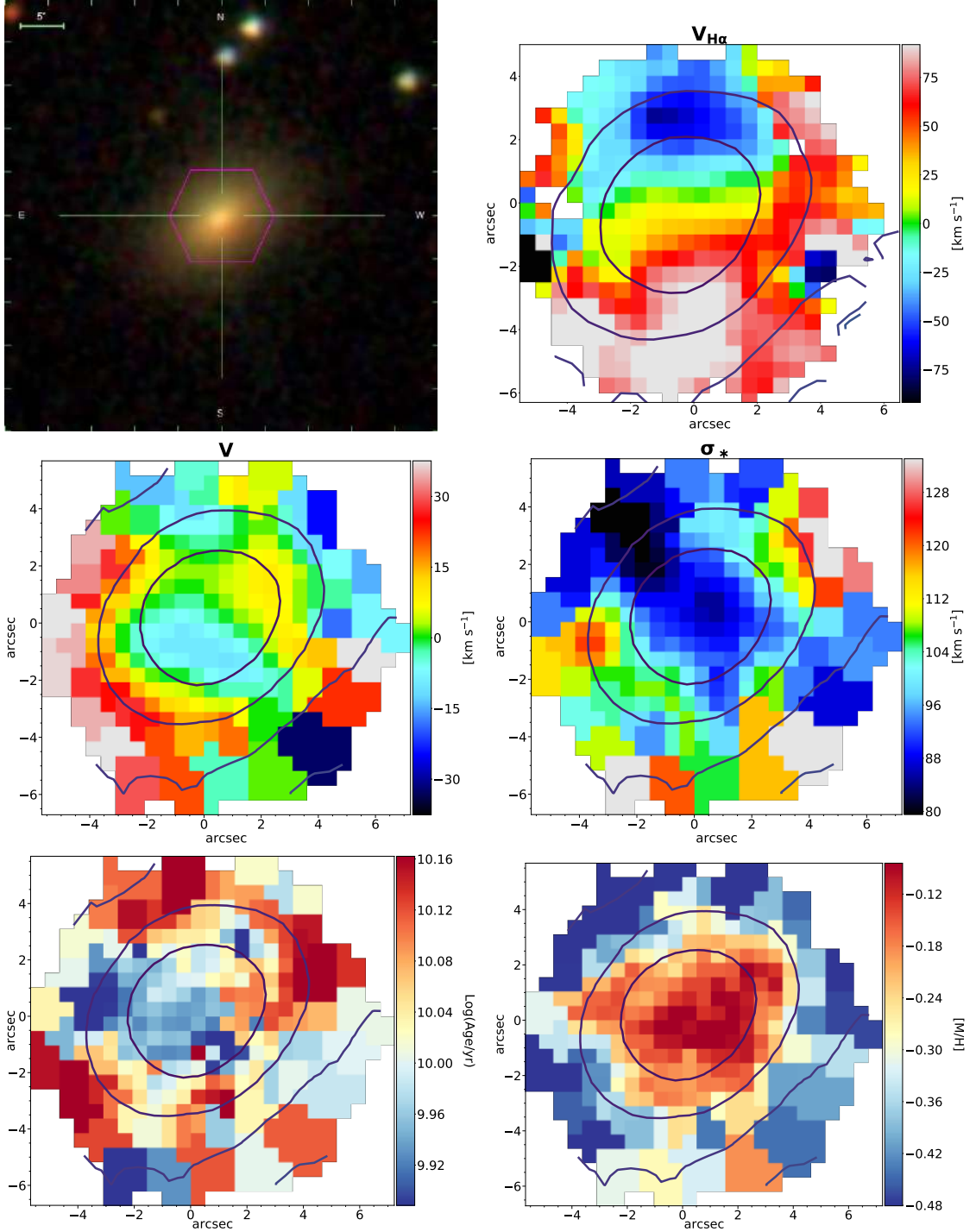
Error on V : 4.0 km s⁻¹; error on σ_* : 4.9 km s⁻¹; error on Log(Age): 0.074; error on [M/H]: 0.15.

MaNGA ID: 1-137890



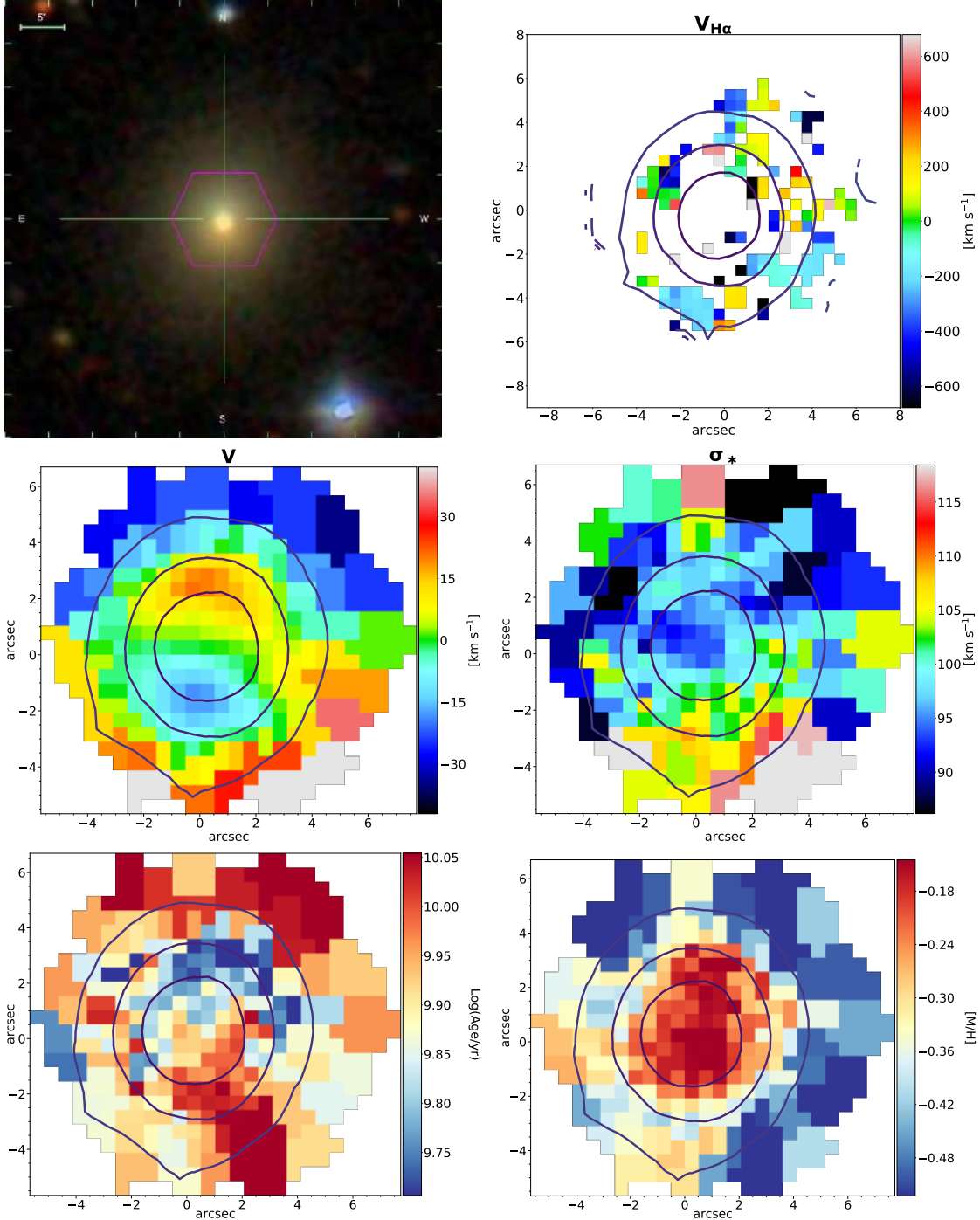
Error on V : 5.7 km s^{-1} ; error on σ_* : 6.4 km s^{-1} ; error on $\text{Log}(\text{Age})$: 0.090; error on $[\text{M}/\text{H}]$: 0.11.

MaNGA ID: 1-113520



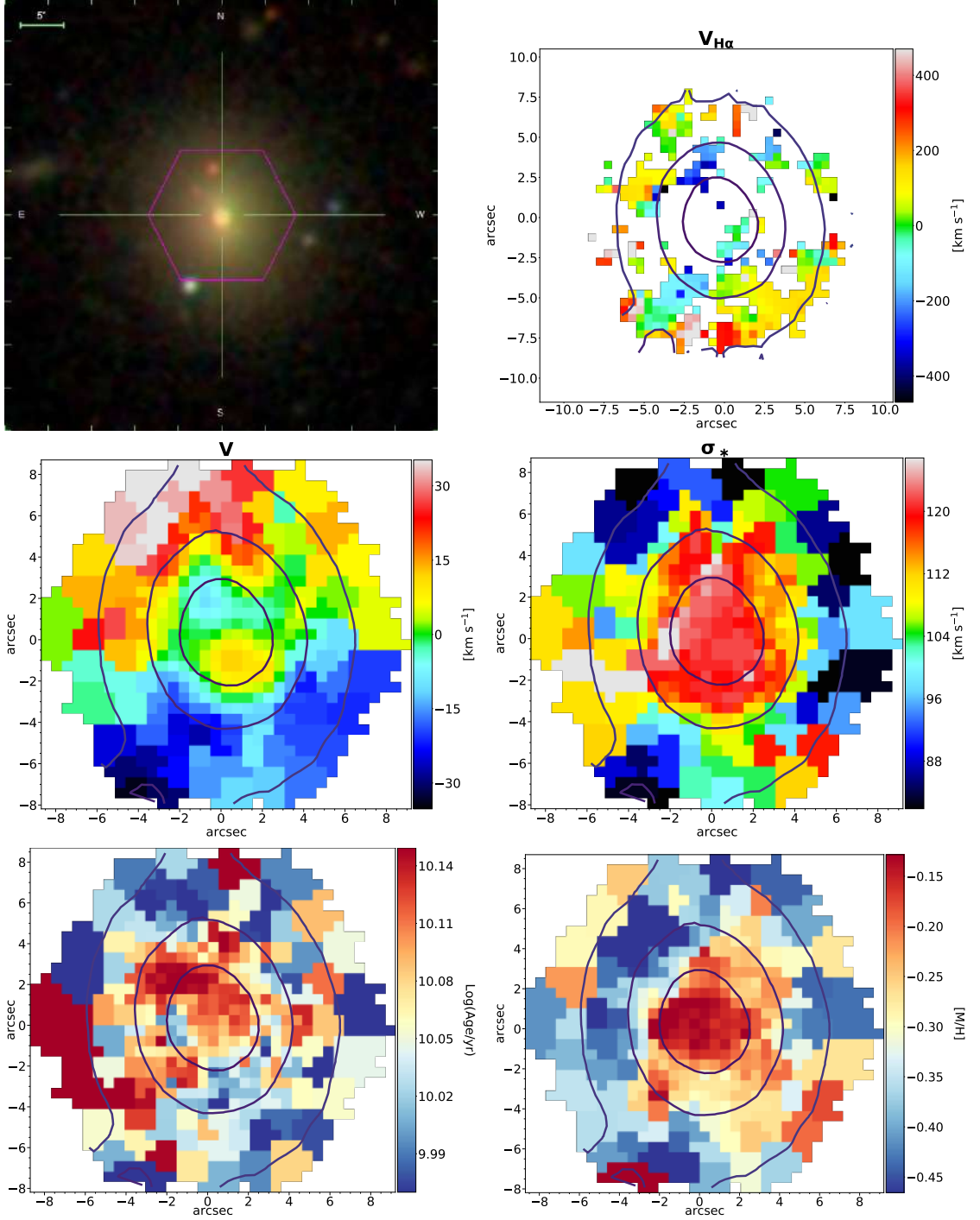
Error on V : 4.0 km s^{-1} ; error on σ_* : 4.8 km s^{-1} ; error on Log(Age) : 0.066; error on $[M/H]$: 0.06.

MaNGA ID: 1-251783



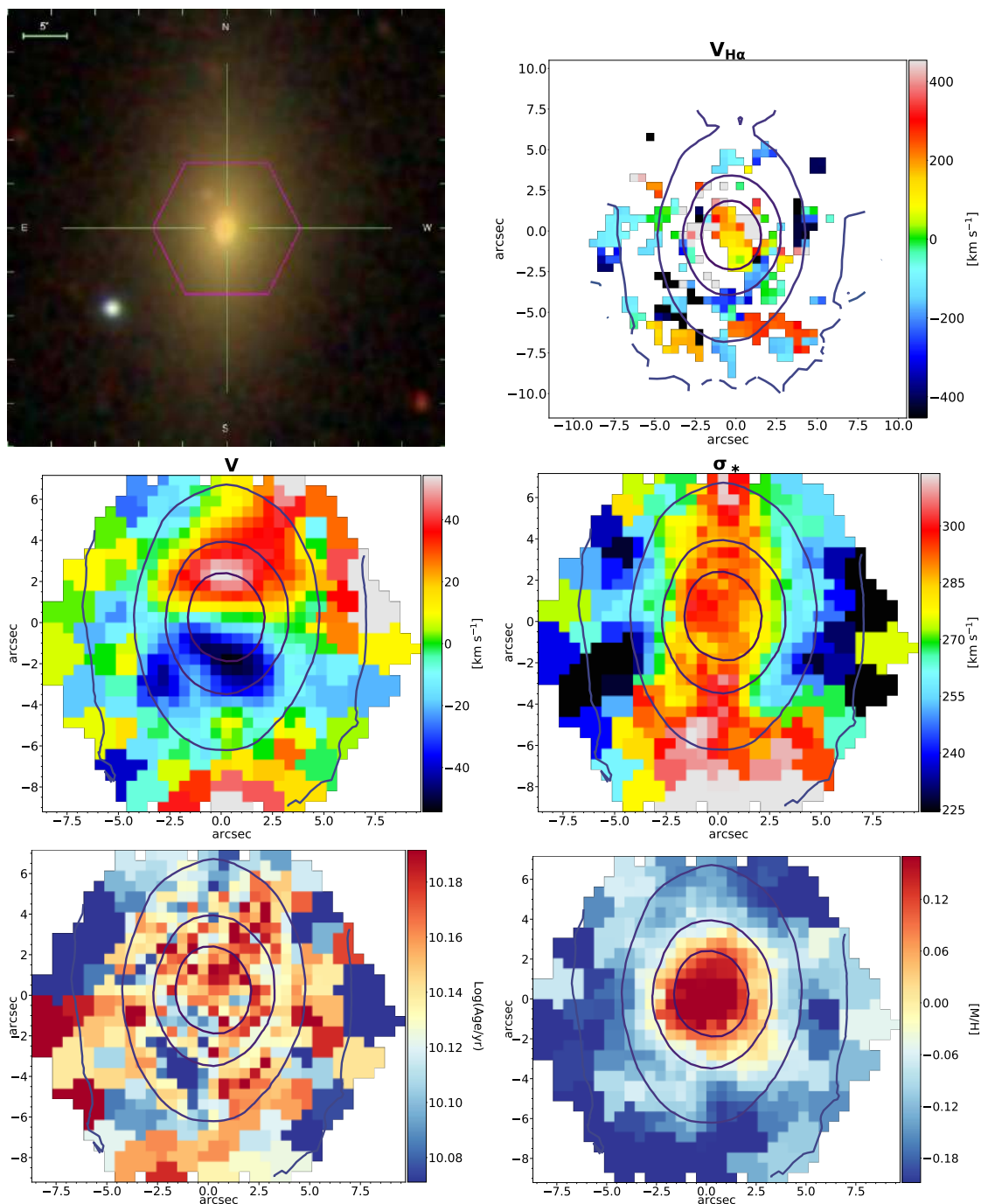
Error on V : 3.1 km s^{-1} ; error on σ_* : 3.7 km s^{-1} ; error on $\text{Log}(\text{Age})$: 0.078; error on $[M/H]$: 0.06.

MaNGA ID: 1-210728



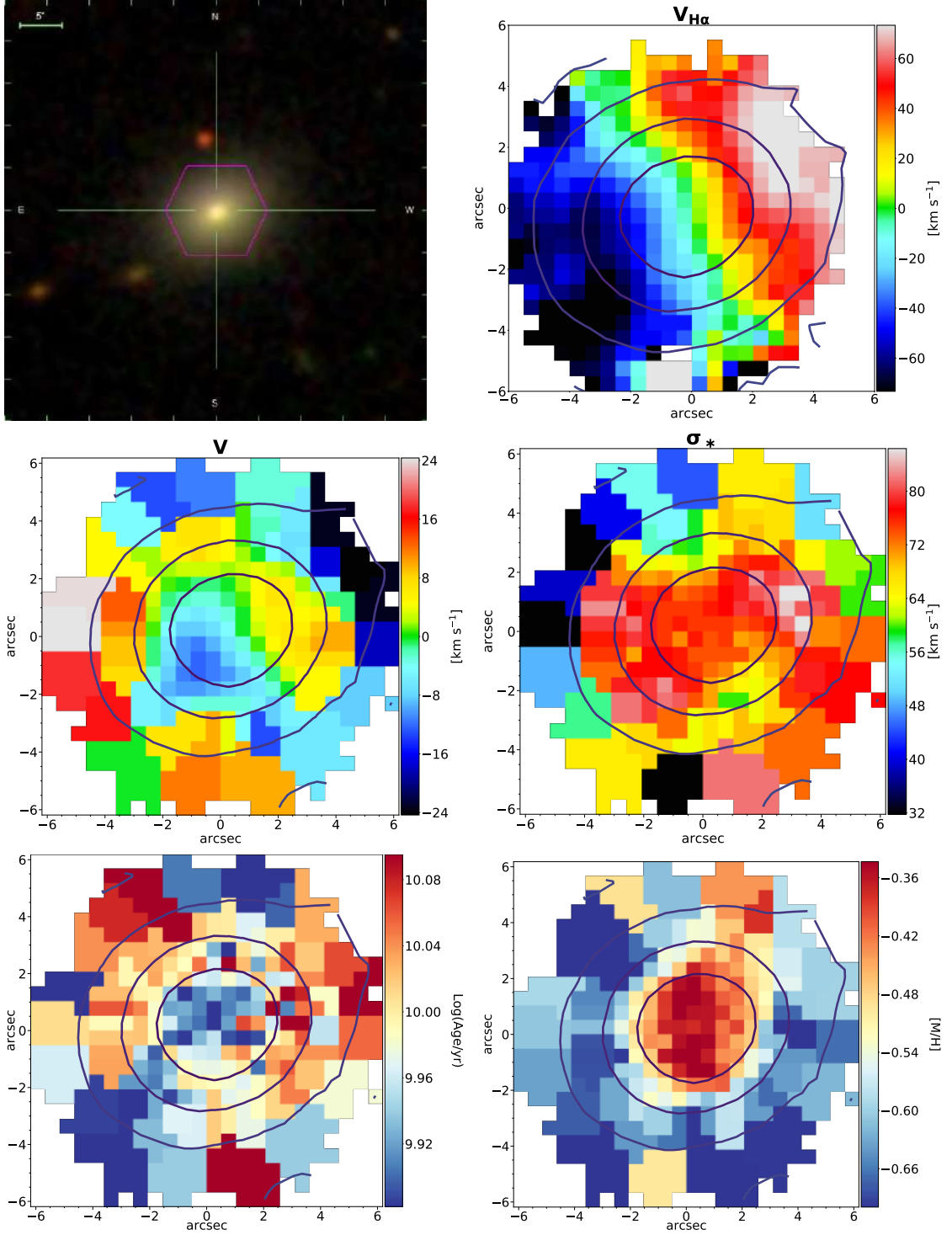
Error on V : 4.3 km s^{-1} ; error on σ_* : 5.1 km s^{-1} ; error on Log(Age) : 0.106; error on $[M/H]$: 0.08.

MaNGA ID: 1-635590



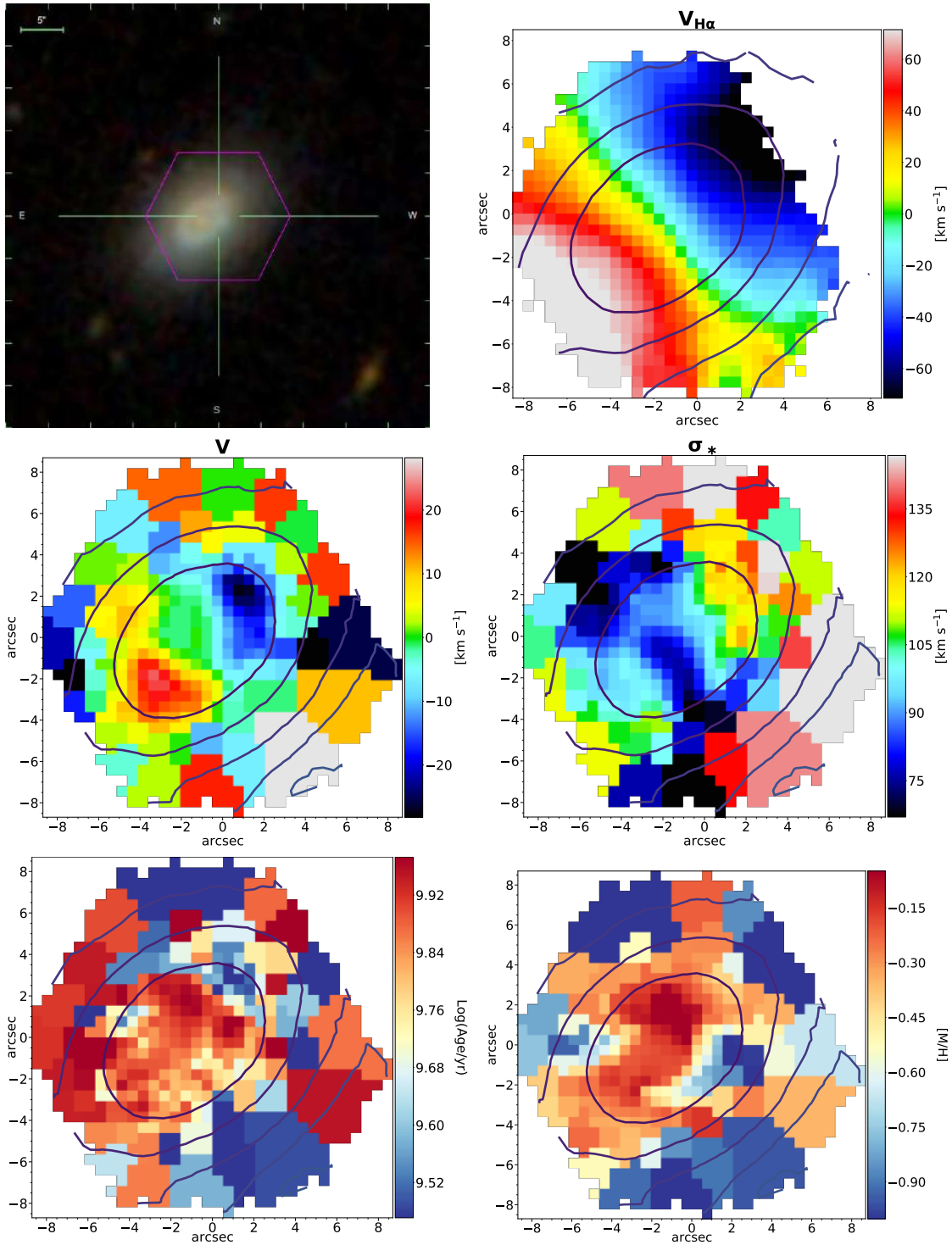
Error on V : 7.5 km s^{-1} ; error on σ_* : 7.7 km s^{-1} ; error on $\text{Log}(\text{Age})$: 0.036; error on $[M/H]$: 0.05.

MaNGA ID: 1-323766



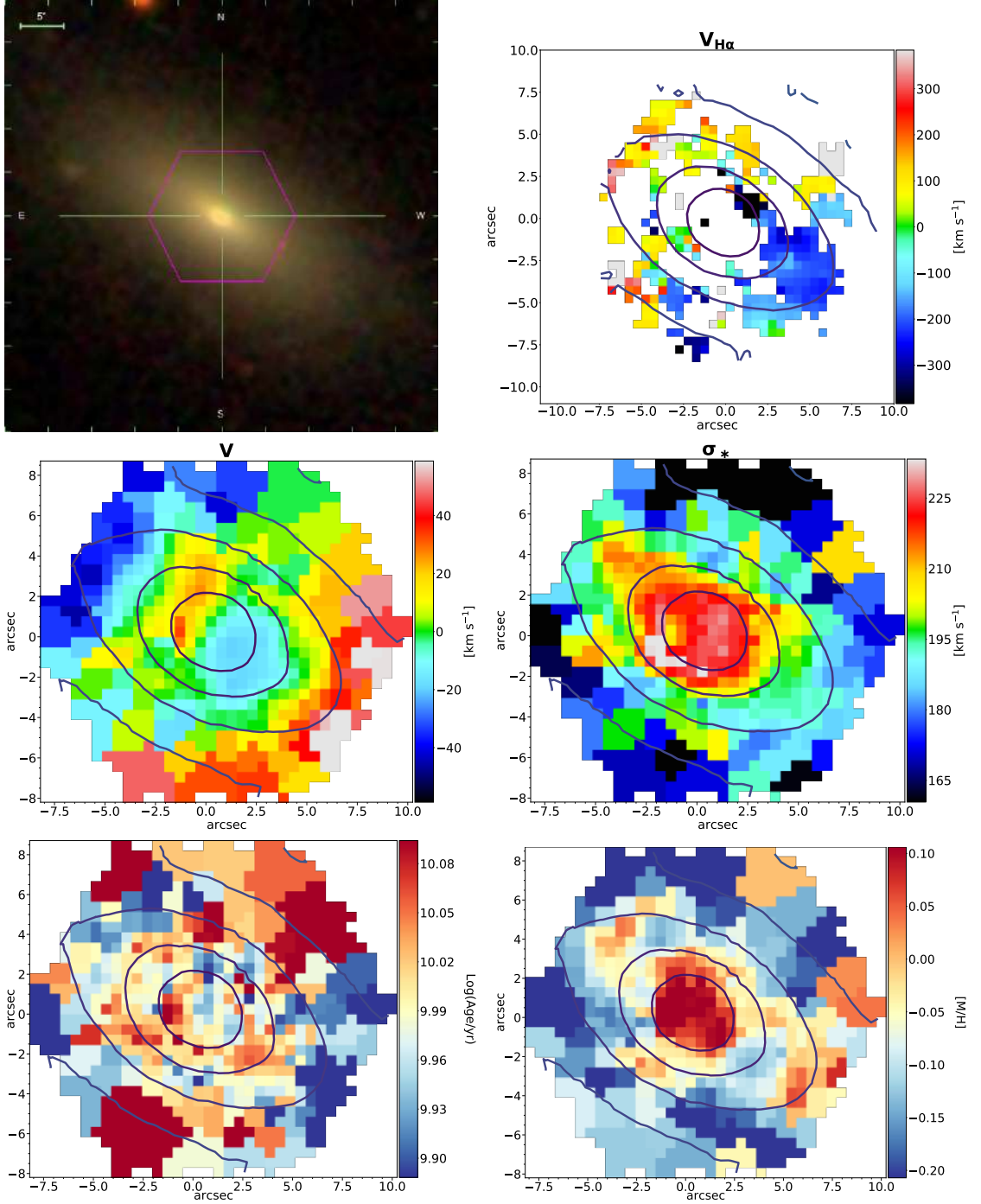
Error on V : 2.9 km s^{-1} ; error on σ_* : 3.7 km s^{-1} ; error on Log(Age) : 0.055; error on $[M/H]$: 0.06.

MaNGA ID: 1-274545



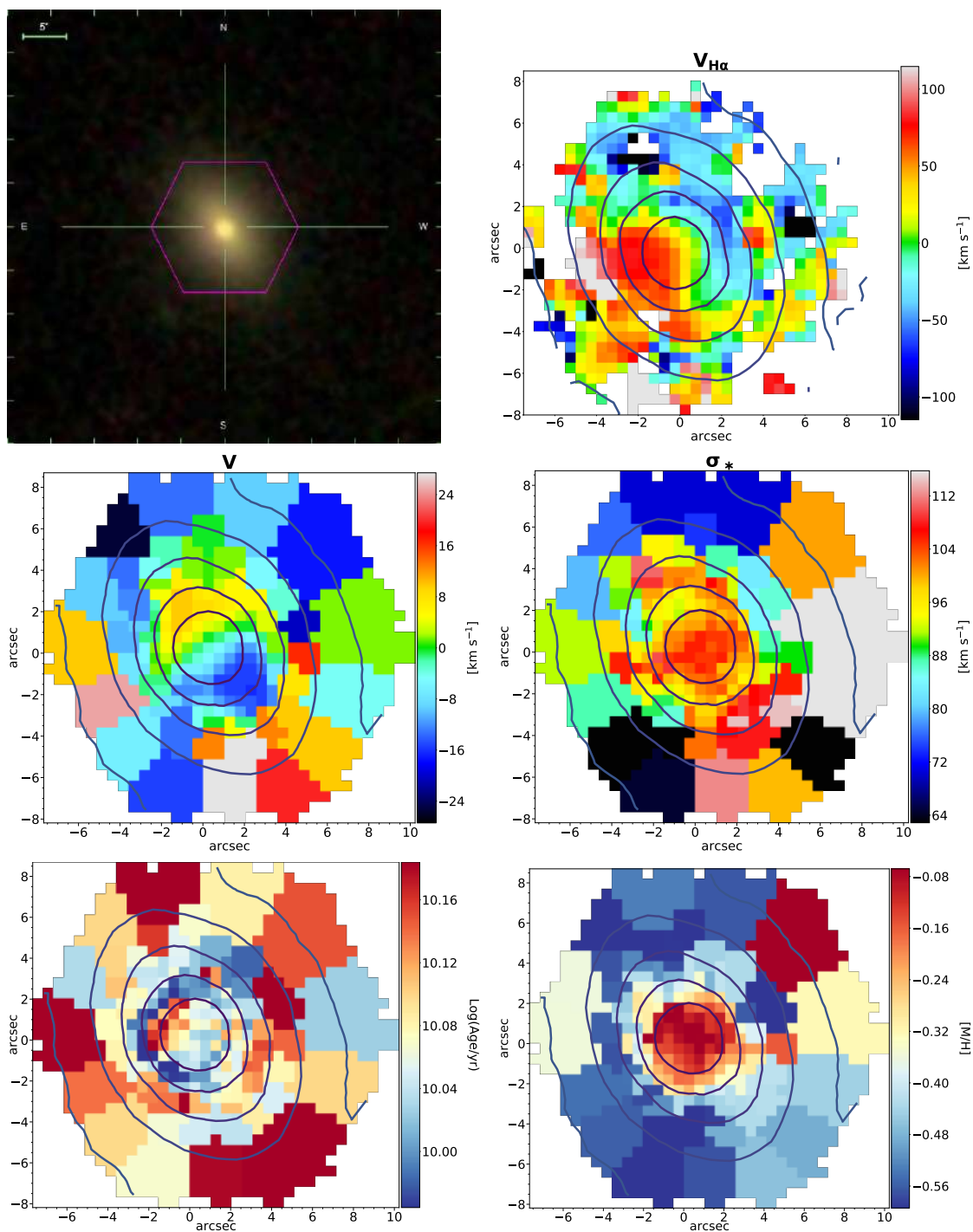
Error on V : 4.8 km s⁻¹; error on σ_* : 5.8 km s⁻¹; error on Log(Age): 0.132; error on [M/H]: 0.18.

MaNGA ID: 1-166613



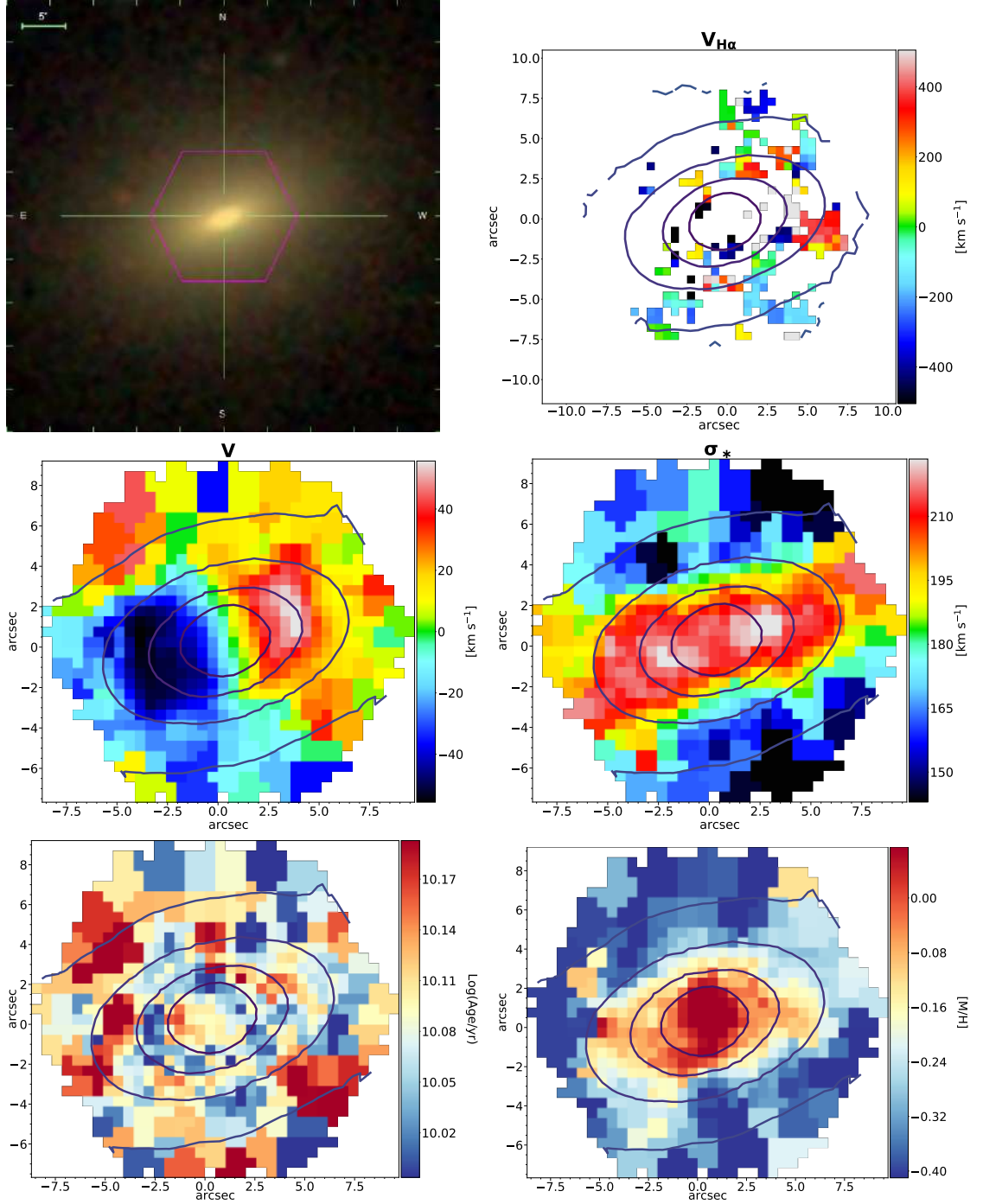
Error on V : 5.4 km s^{-1} ; error on σ_* : 5.7 km s^{-1} ; error on Log(Age) : 0.053; error on $[M/H]$: 0.06.

MaNGA ID: 1-235983



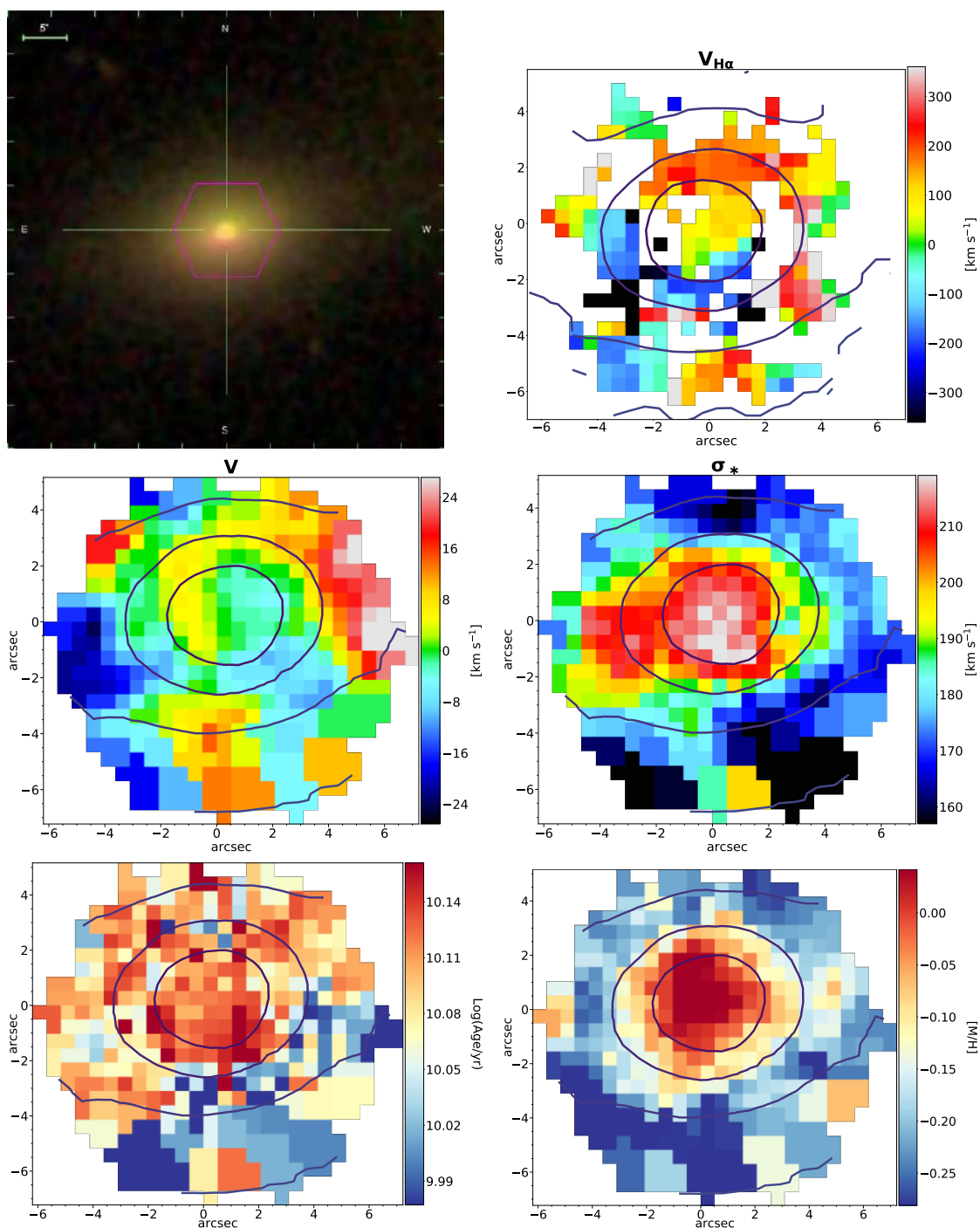
Error on V : 3.5 km s^{-1} ; error on σ_* : 4.2 km s^{-1} ; error on $\text{Log}(\text{Age})$: 0.053; error on $[M/H]$: 0.09.

MaNGA ID: 1-135244



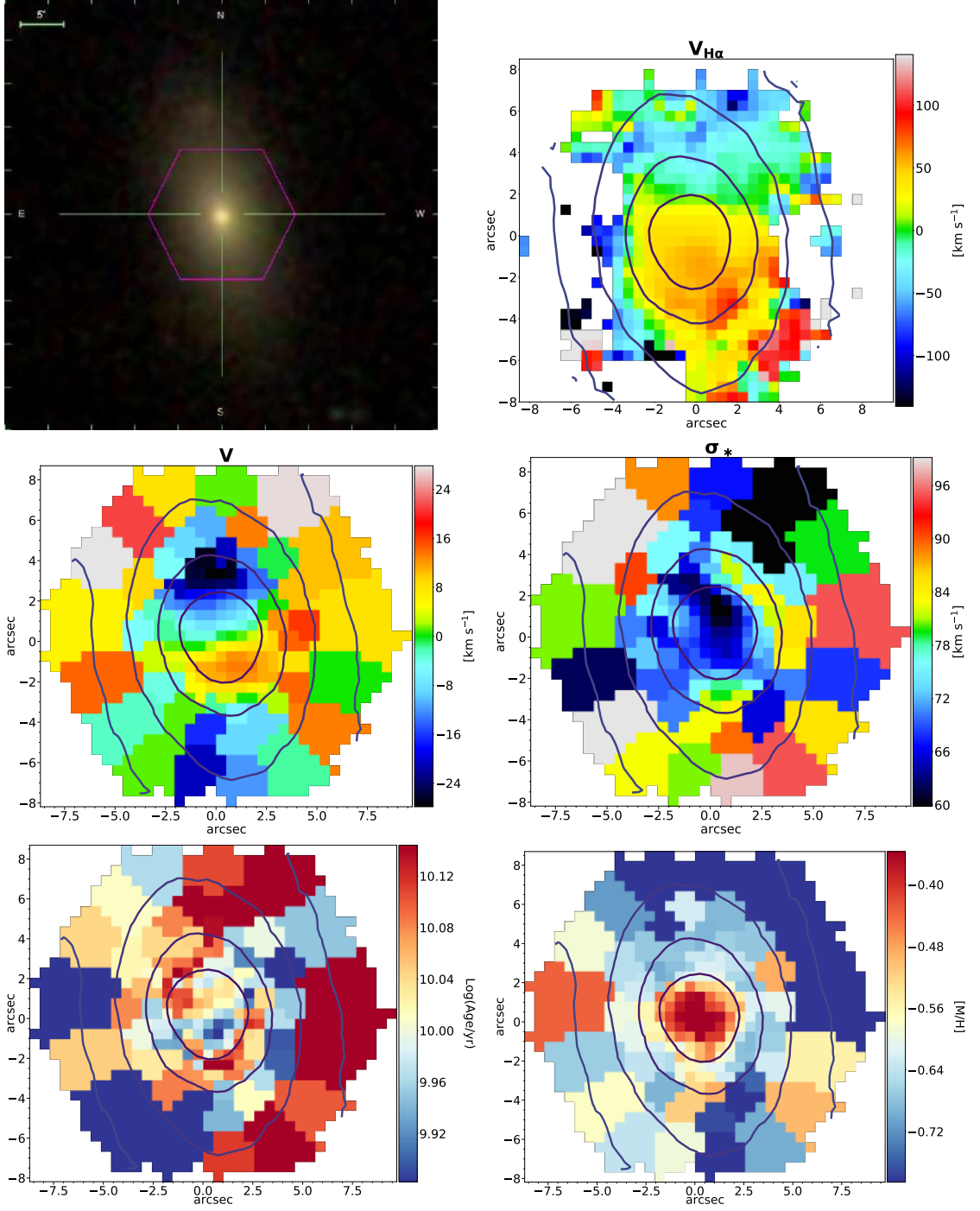
Error on V : 5.7 km s^{-1} ; error on σ_* : 6.1 km s^{-1} ; error on $\text{Log}(\text{Age})$: 0.056; error on $[\text{M}/\text{H}]$: 0.09.

MaNGA ID: 1-38347



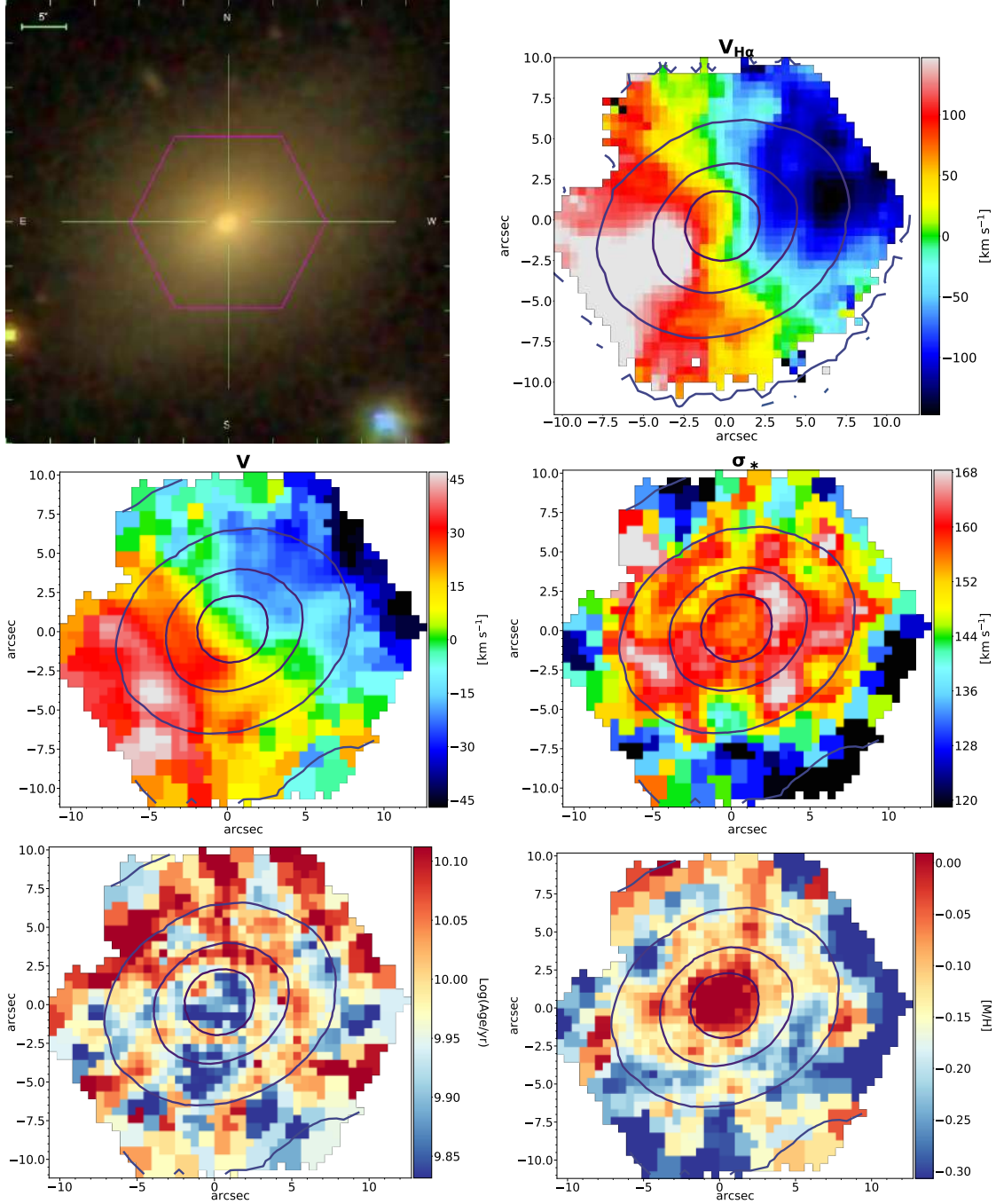
Error on V : 5.2 km s⁻¹; error on σ_* : 5.5 km s⁻¹; error on Log(Age): 0.048; error on [M/H]: 0.06.

MaNGA ID: 1-322291



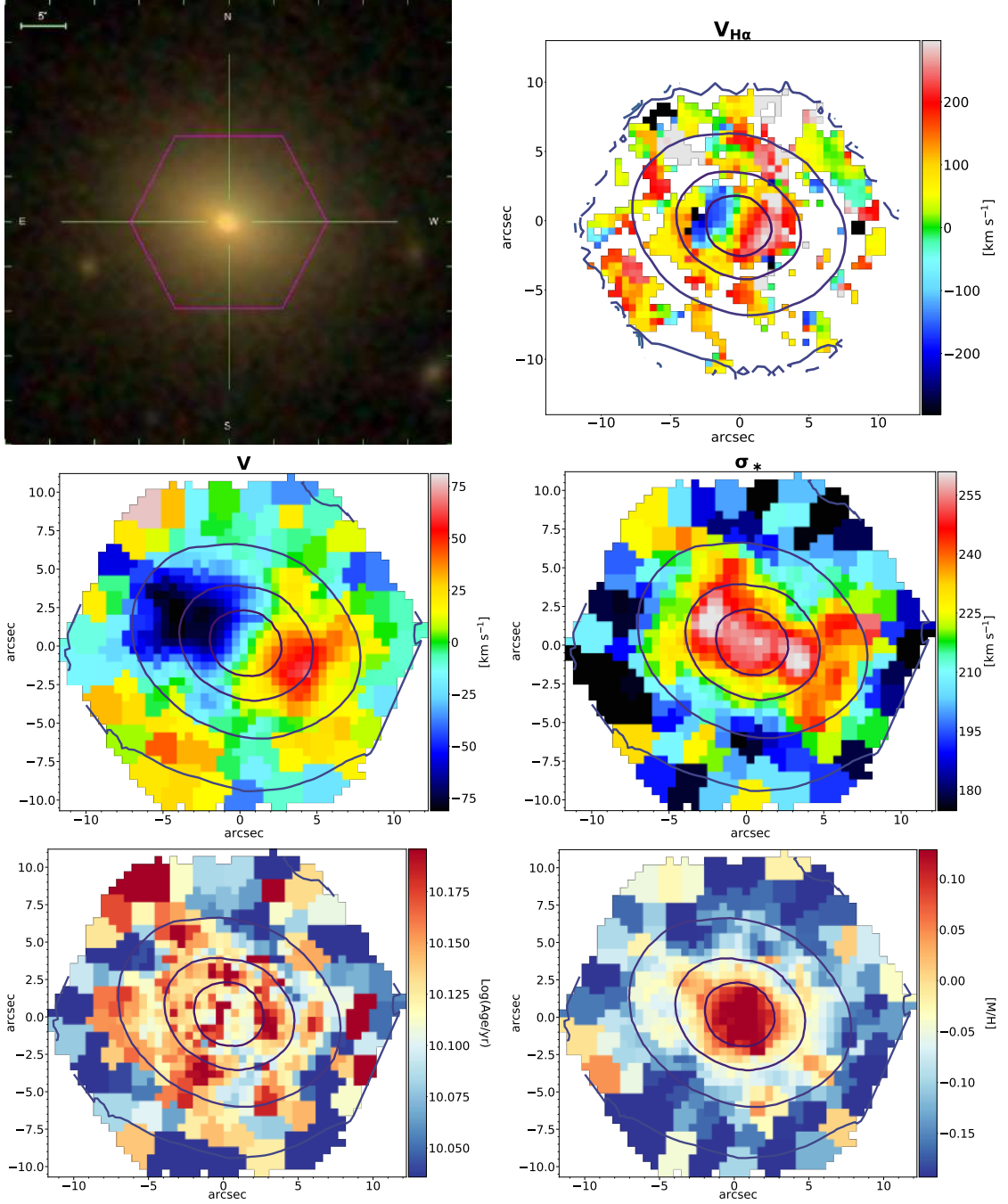
Error on V : 3.5 km s^{-1} ; error on σ_* : 4.5 km s^{-1} ; error on Log(Age) : 0.070; error on $[M/H]$: 0.07.

MaNGA ID: 1-37155



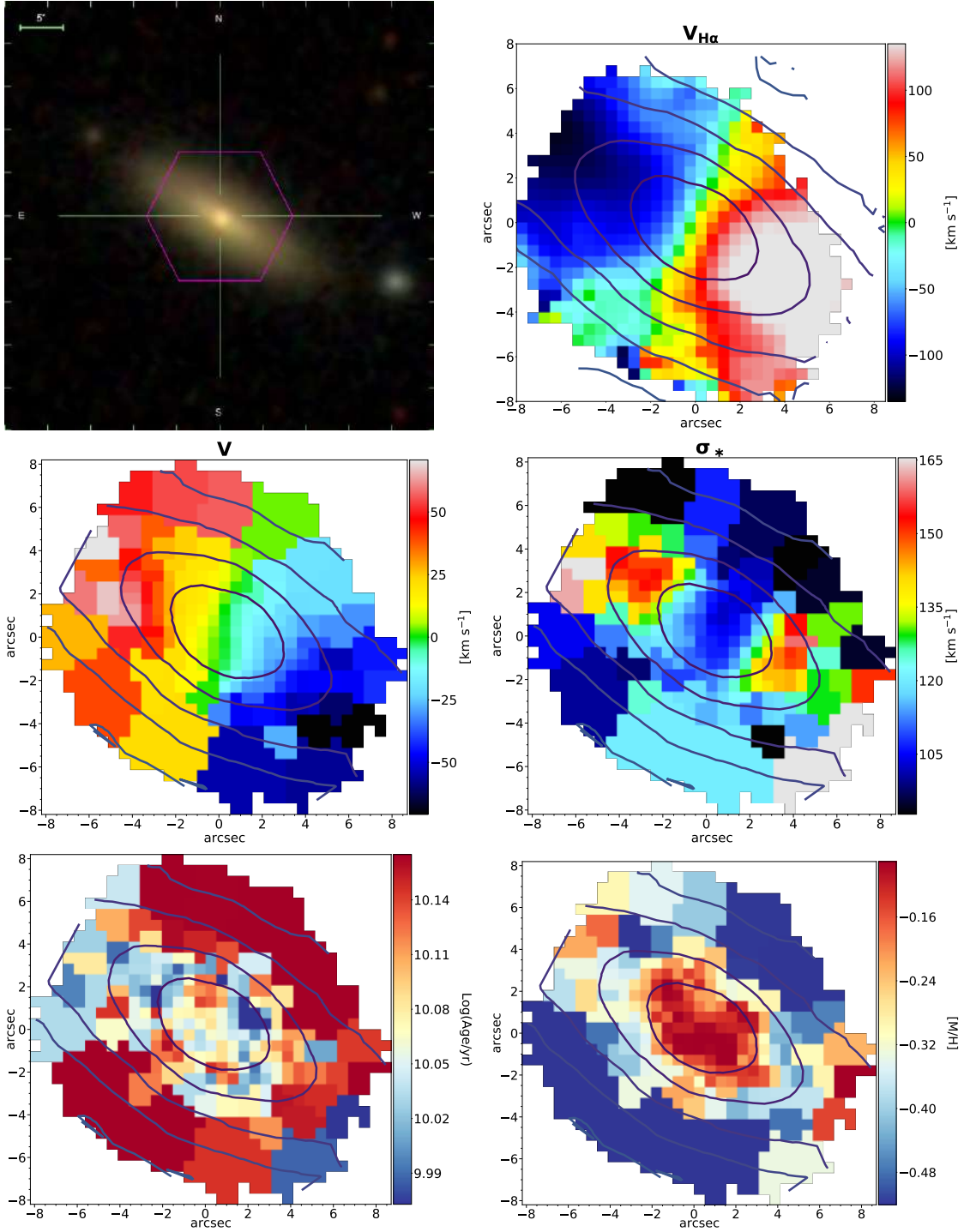
Error on V : 5.0 km s^{-1} ; error on σ_* : 5.4 km s^{-1} ; error on $\text{Log}(\text{Age})$: 0.076; error on $[M/H]$: 0.07.

MaNGA ID: 1-47248



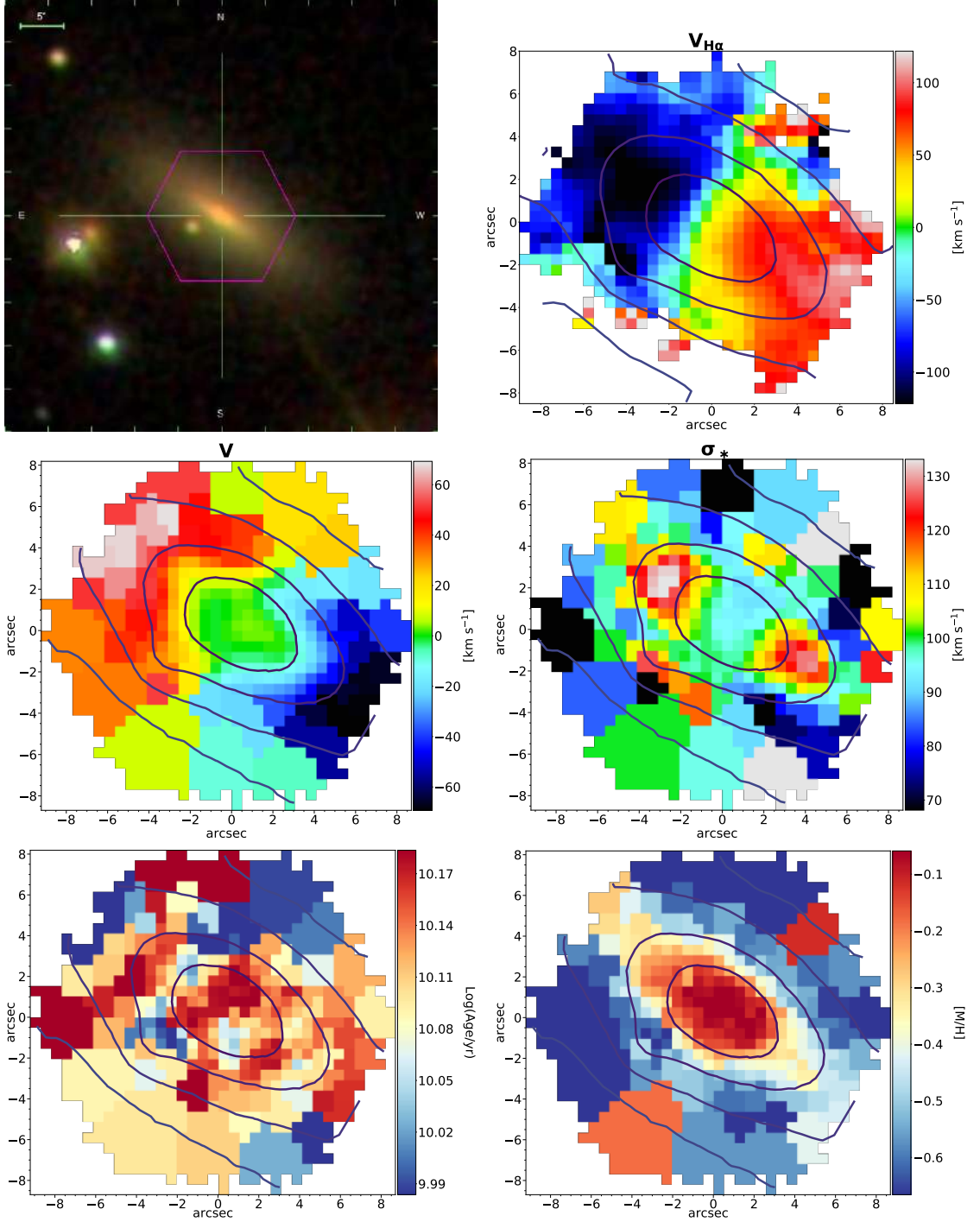
Error on V : 7.5 km s^{-1} ; error on σ_* : 7.8 km s^{-1} ; error on $\text{Log}(\text{Age})$: 0.046; error on $[\text{M}/\text{H}]$: 0.06.

MaNGA ID: 1-94690



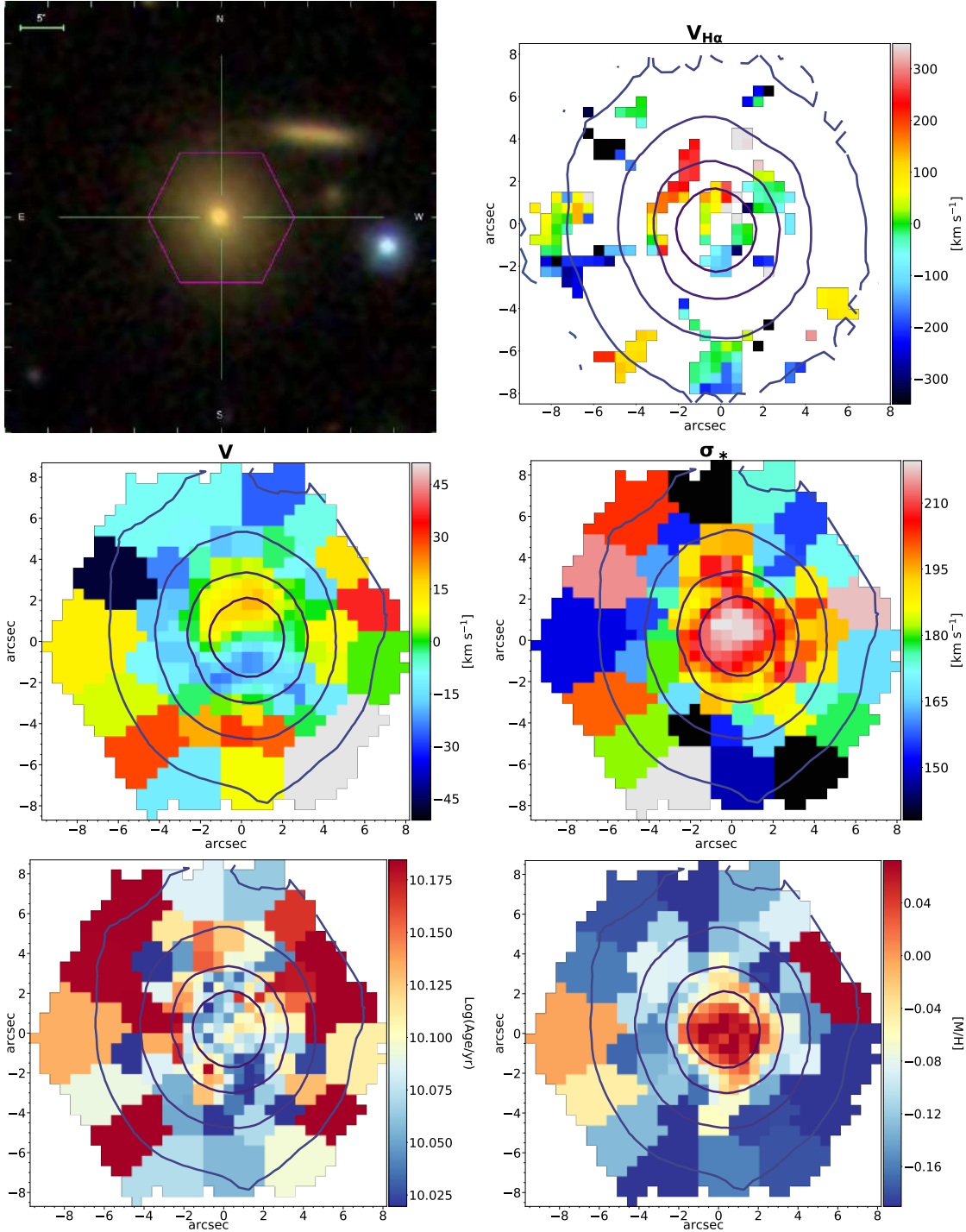
Error on V : 5.1 km s $^{-1}$; error on σ_* : 5.9 km s $^{-1}$; error on Log(Age): 0.049; error on [M/H]: 0.09.

MaNGA ID: 1-115097



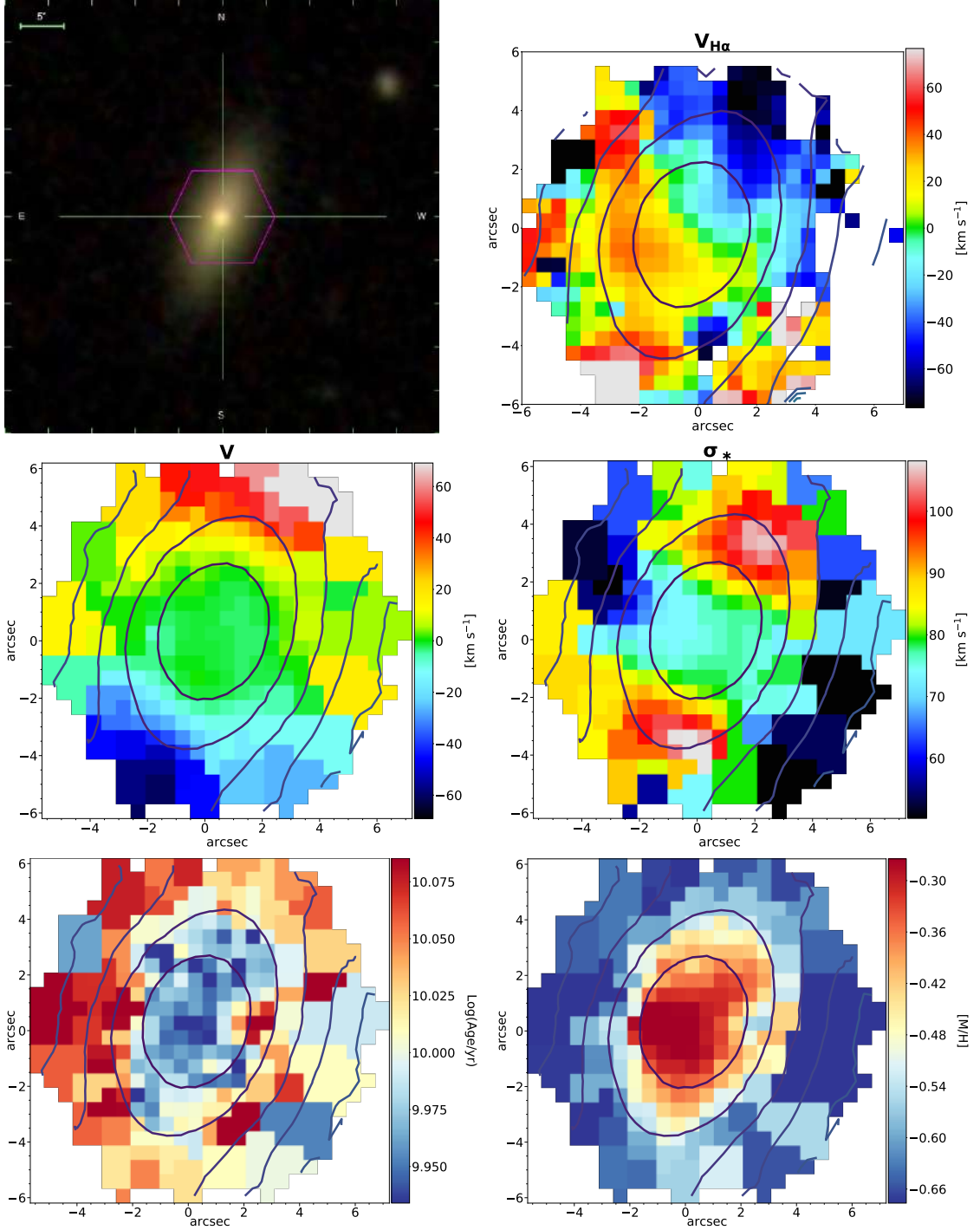
Error on V : 4.9 km s^{-1} ; error on σ_* : 5.9 km s^{-1} ; error on Log(Age) : 0.058; error on $[M/H]$: 0.10.

MaNGA ID: 1-556514



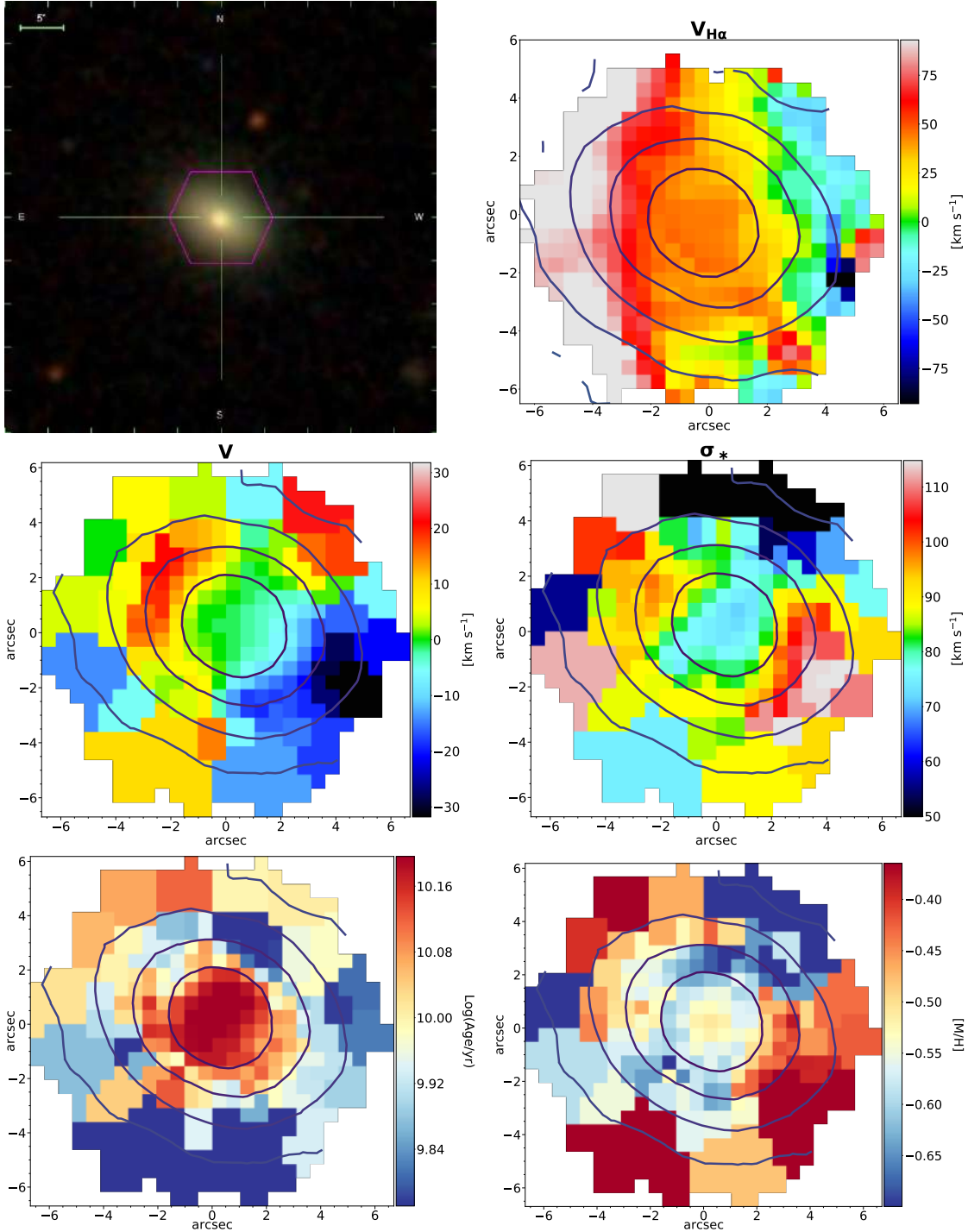
Error on V : 6.1 km s^{-1} ; error on σ_* : 6.5 km s^{-1} ; error on $\text{Log}(\text{Age})$: 0.040; error on $[M/H]$: 0.06.

MaNGA ID: 1-255220



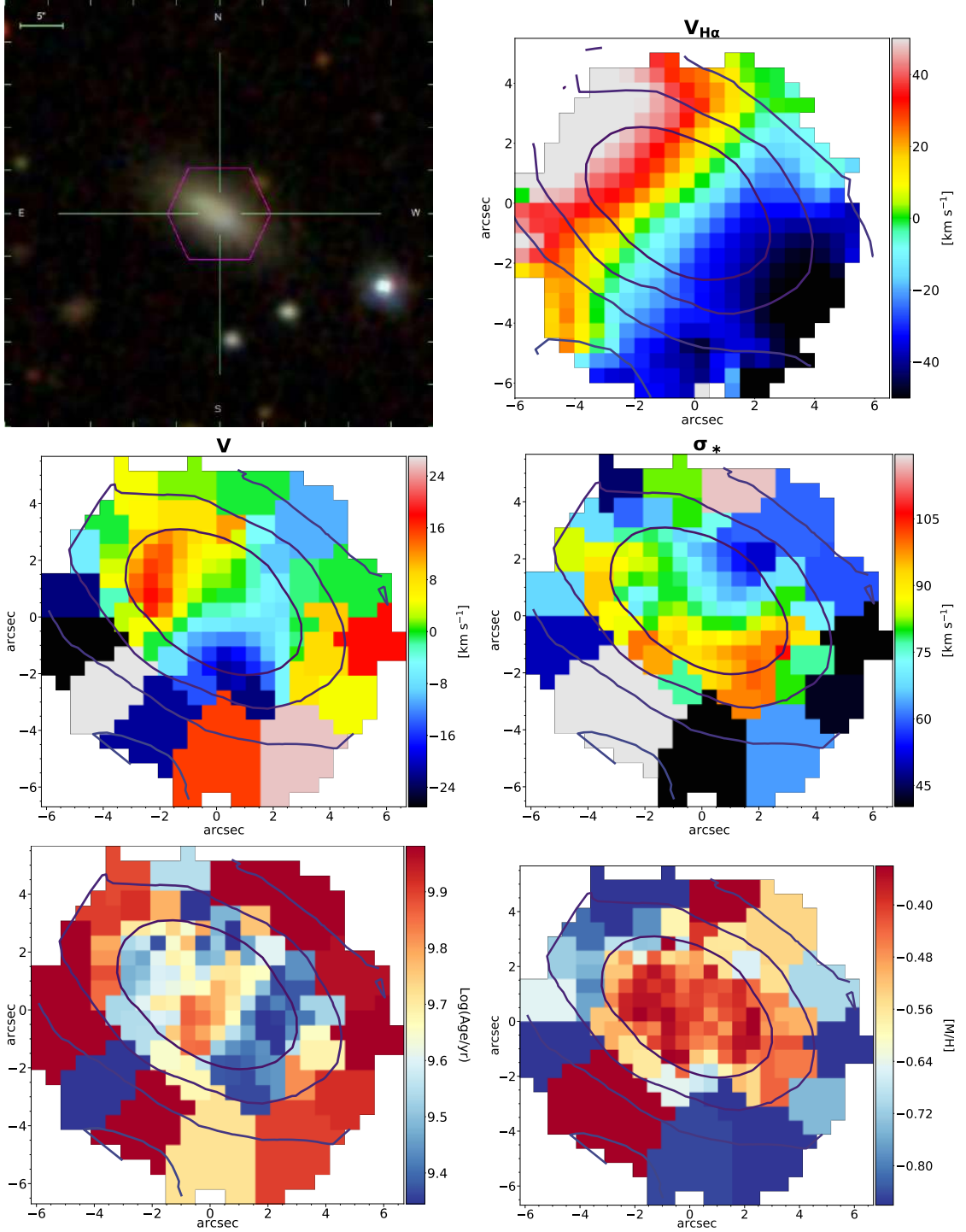
Error on V : 3.0 km s^{-1} ; error on σ_* : 3.7 km s^{-1} ; error on $\text{Log}(\text{Age})$: 0.037; error on $[\text{M}/\text{H}]$: 0.06.

MaNGA ID: 1-418023

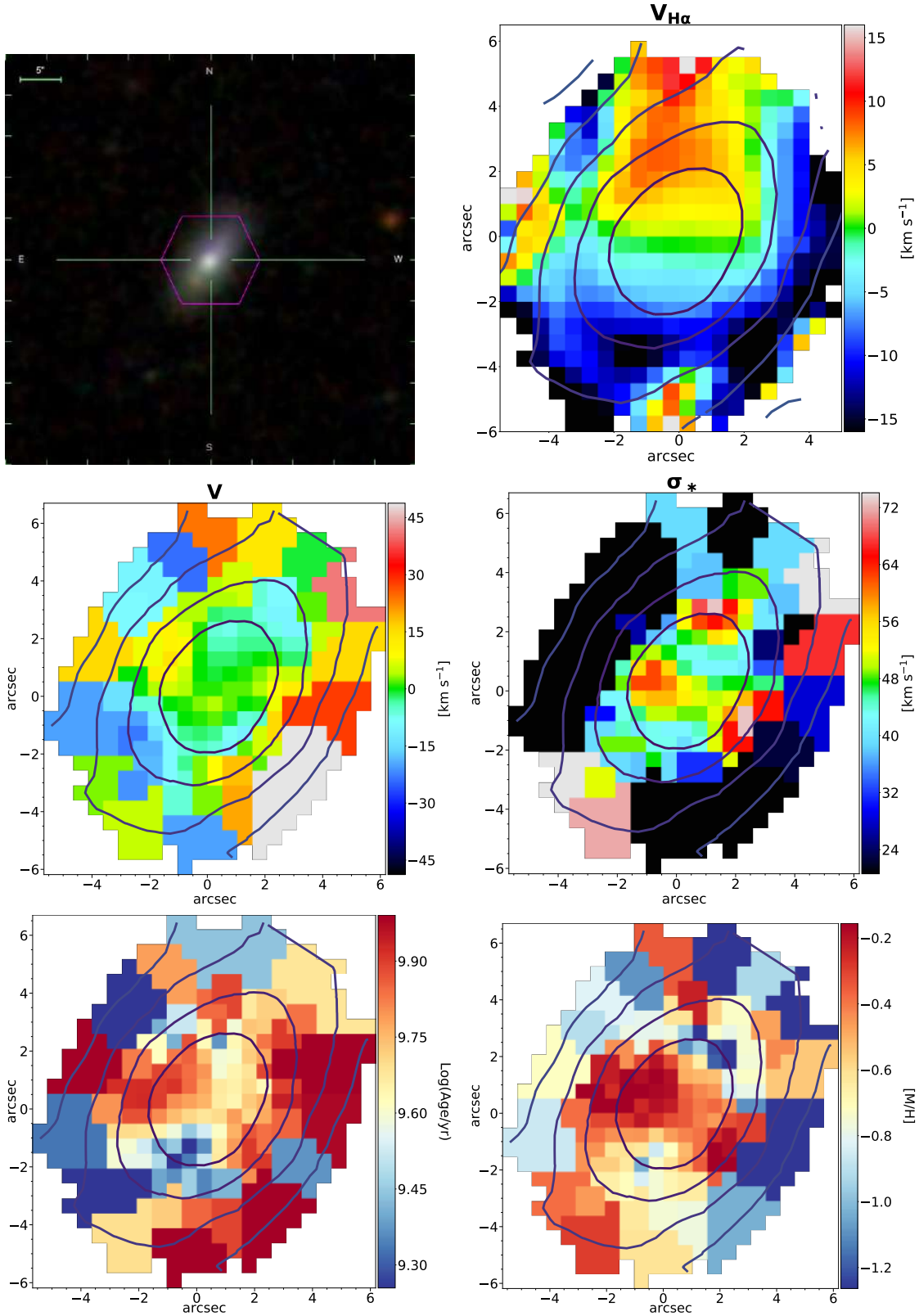


Error on V : 3.5 km s^{-1} ; error on σ_* : 4.4 km s^{-1} ; error on $\text{Log}(\text{Age})$: 0.081; error on $[M/H]$: 0.06.

MaNGA ID: 1-113698

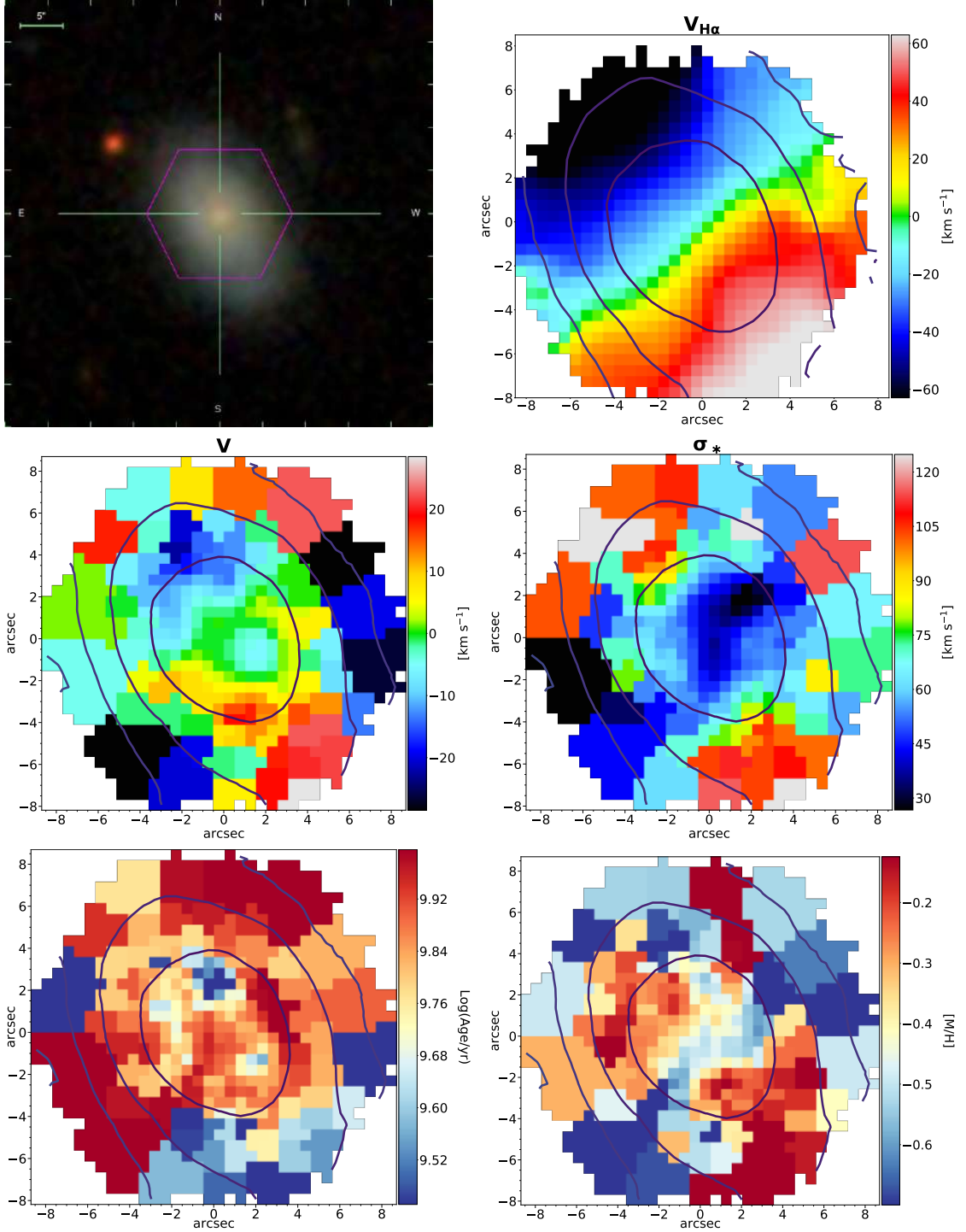


Error on V : 4.6 km s^{-1} ; error on σ_* : 5.9 km s^{-1} ; error on $\text{Log}(\text{Age})$: 0.138; error on $[M/H]$: 0.12.

MaNGA ID: 1-282035 \otimes 

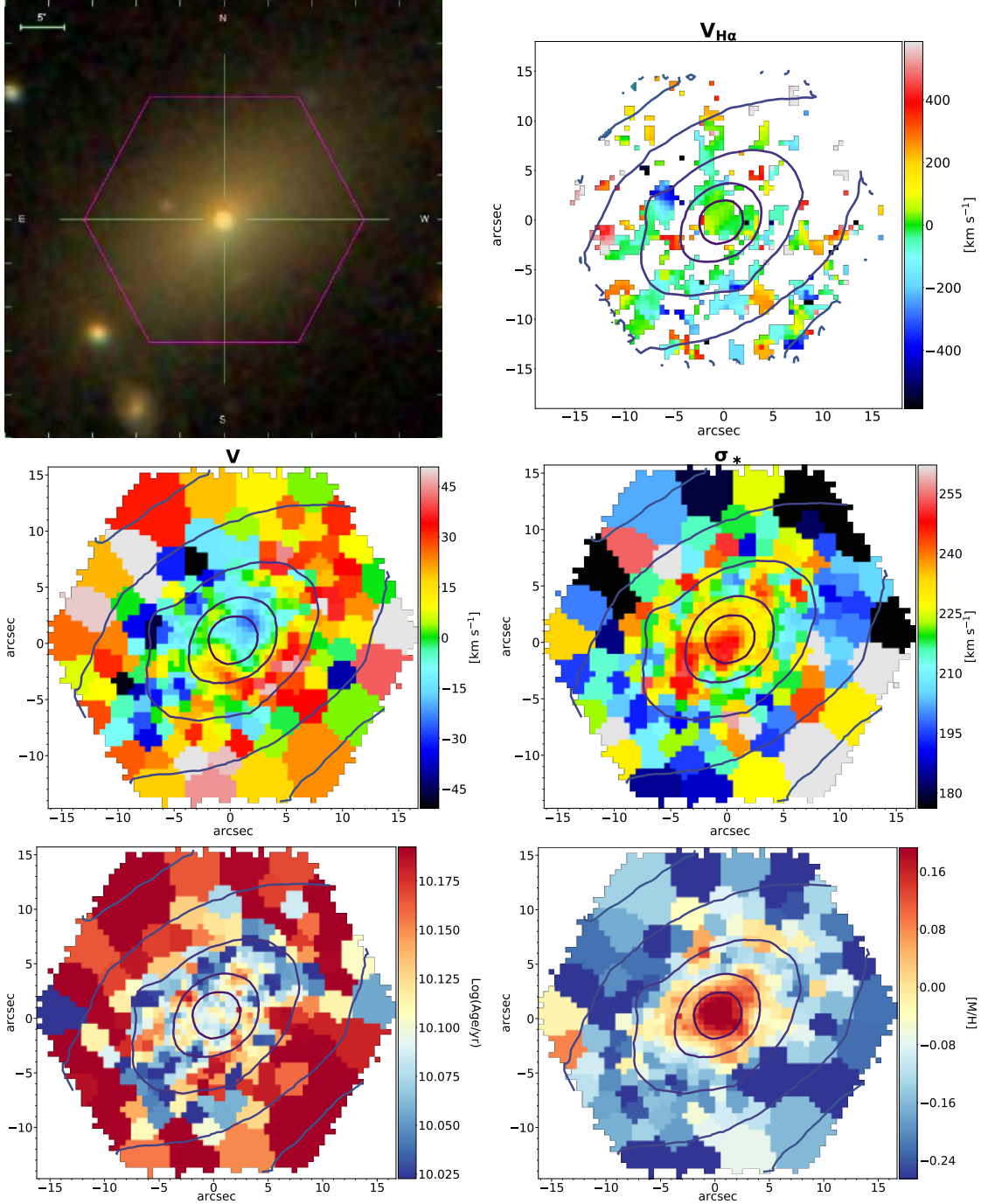
Error on V : 5.8 km s⁻¹; error on σ_* : 9.1 km s⁻¹; error on $\text{Log}(\text{Age})$: 0.148; error on $[M/H]$: 0.22.

MaNGA ID: 1-323764



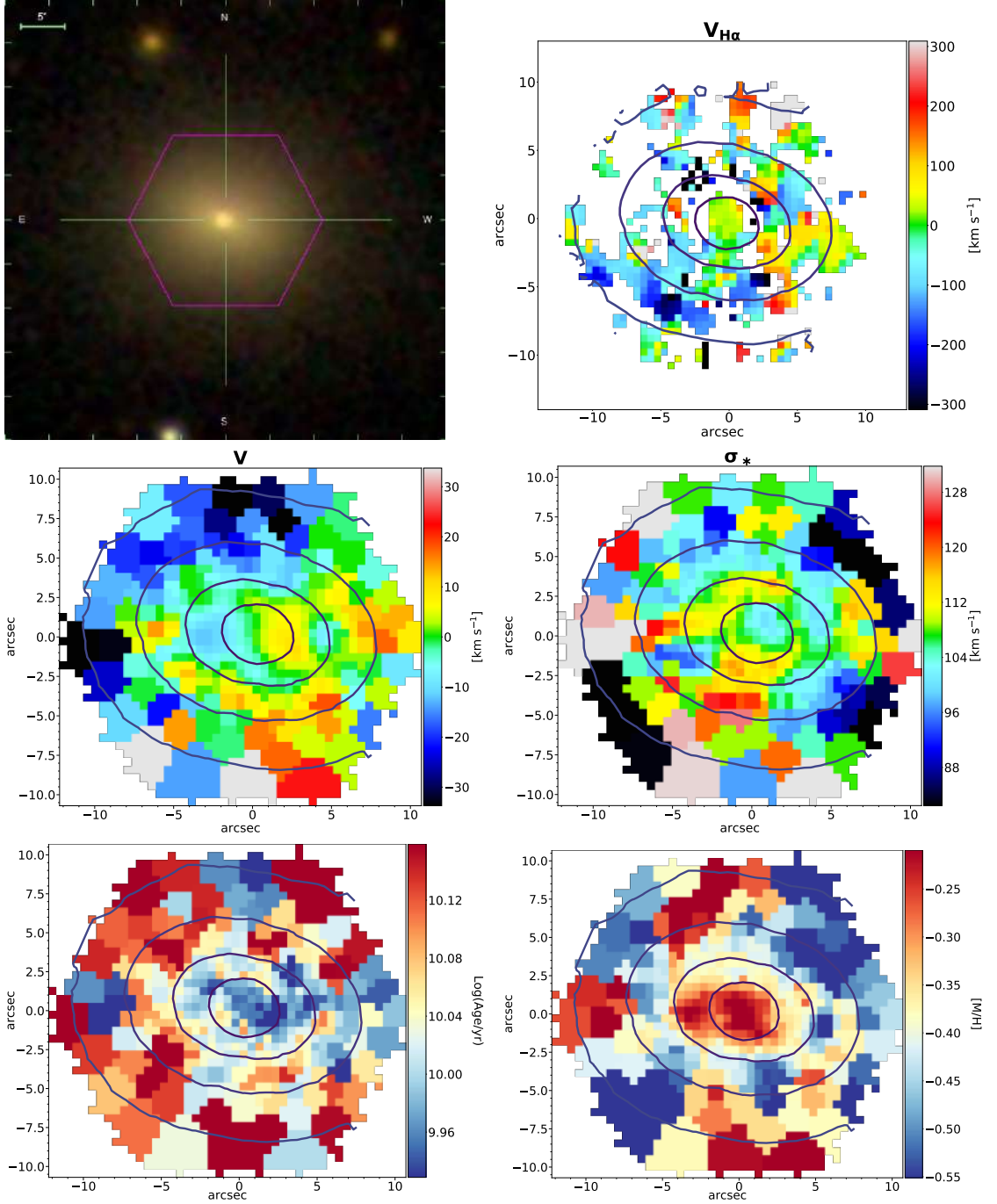
Error on V : 3.8 km s^{-1} ; error on σ_* : 5.5 km s^{-1} ; error on Log(Age) : 0.131; error on $[M/H]$: 0.14.

MaNGA ID: 1-314719



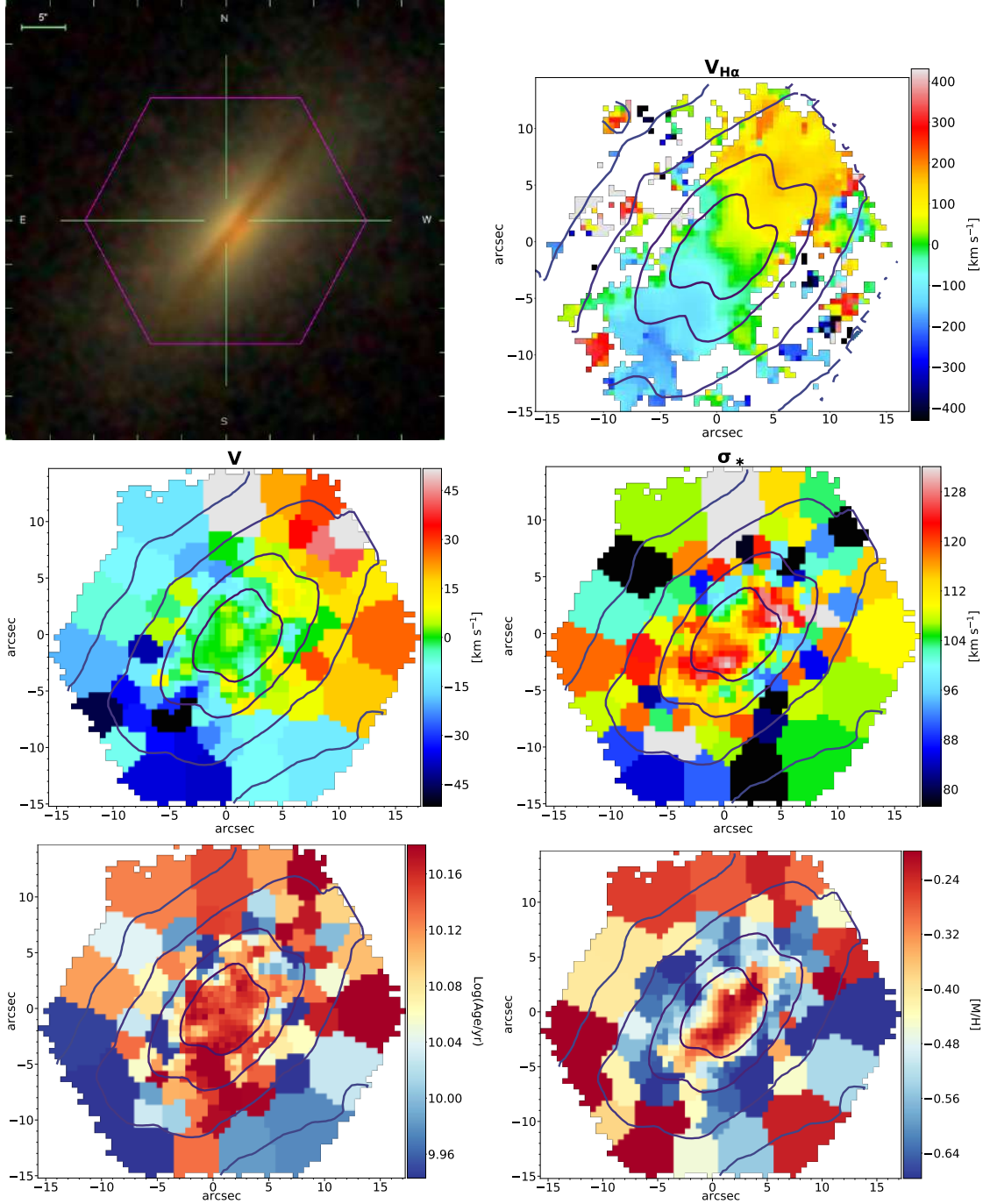
Error on V : 9.2 km s^{-1} ; error on σ_* : 9.3 km s^{-1} ; error on Log(Age) : 0.046; error on $[M/H]$: 0.07.

MaNGA ID: 1-298940



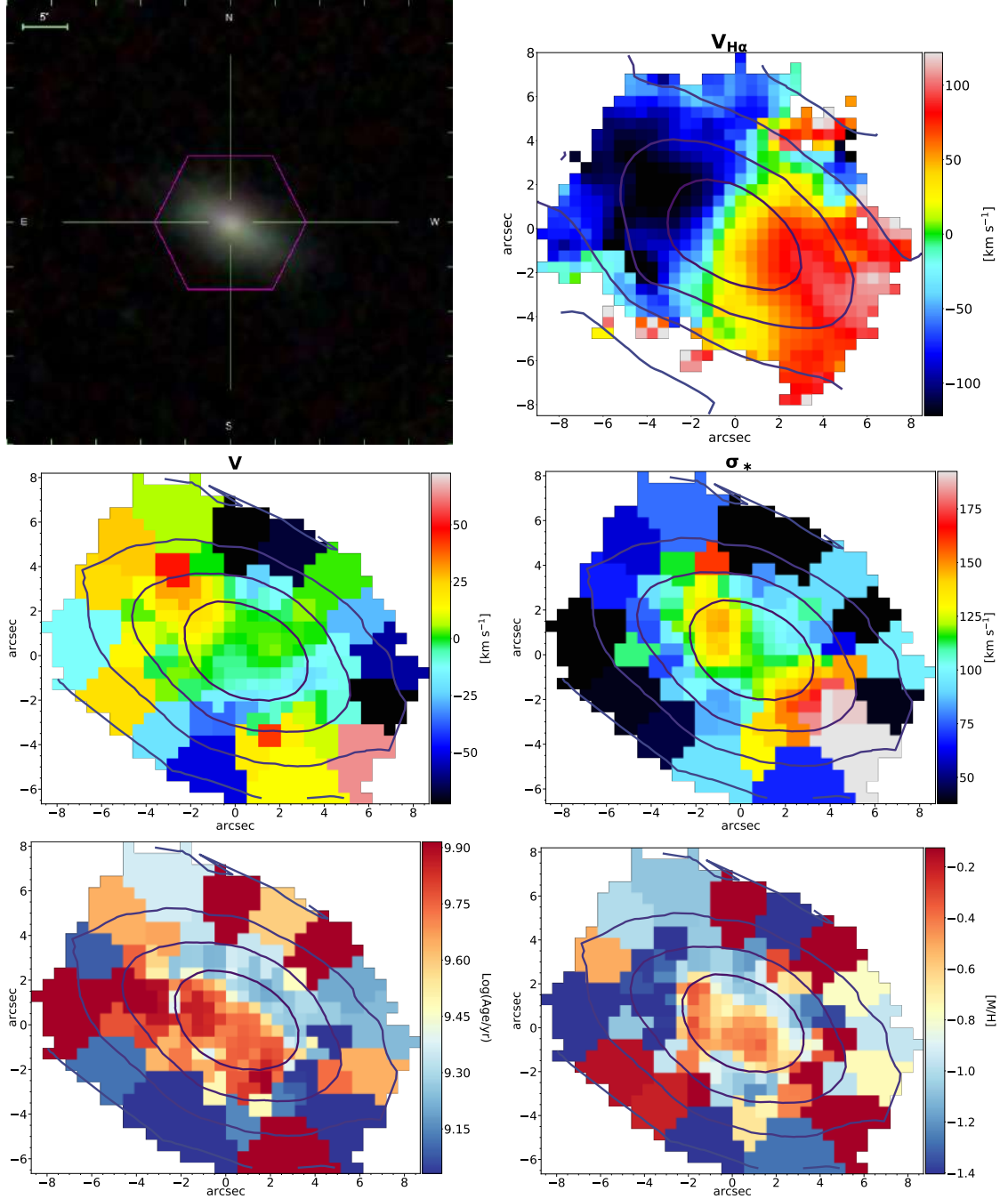
Error on V : 4.3 km s^{-1} ; error on σ_* : 5.1 km s^{-1} ; error on Log(Age) : 0.058; error on $[\text{M}/\text{H}]$: 0.08.

MaNGA ID: 1-236144



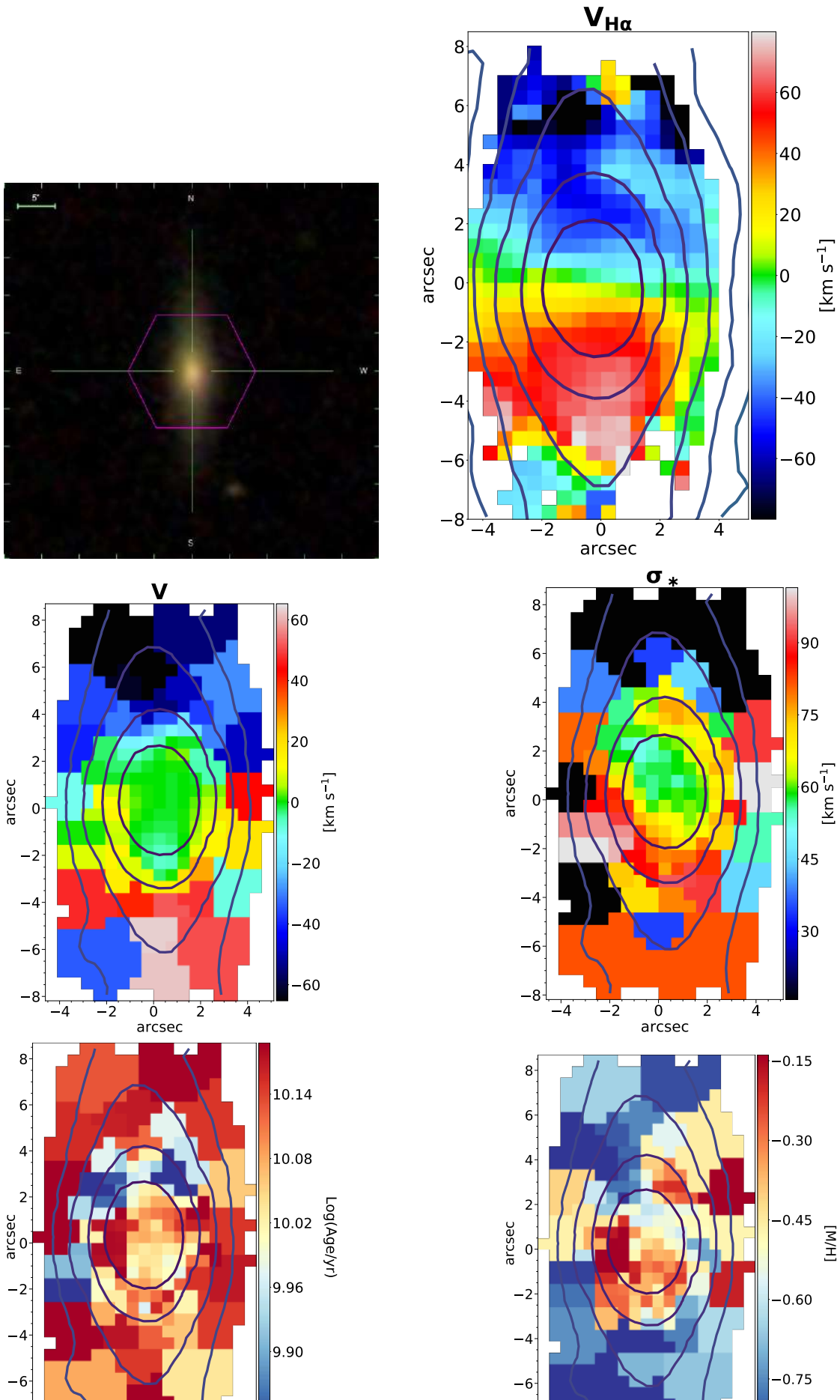
Error on V : 5.9 km s^{-1} ; error on σ_* : 6.8 km s^{-1} ; error on Log(Age) : 0.069; error on $[M/H]$: 0.11.

MaNGA ID: 12-84617

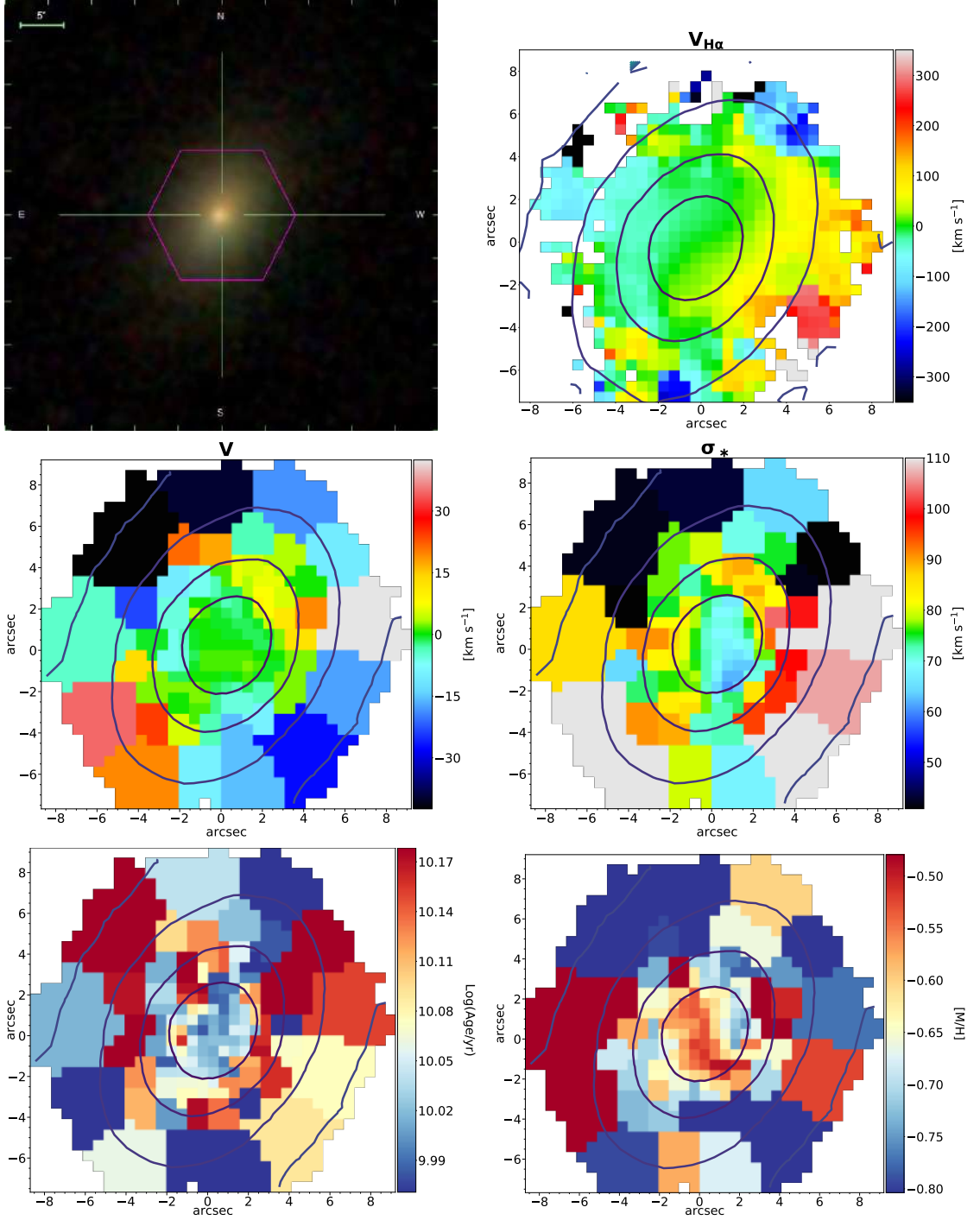


Error on V : 9.5 km s^{-1} ; error on σ_* : 10.7 km s^{-1} ; error on $\text{Log}(\text{Age})$: 0.058; error on $[M/H]$: 0.10.

MaNGA ID: 1-248410

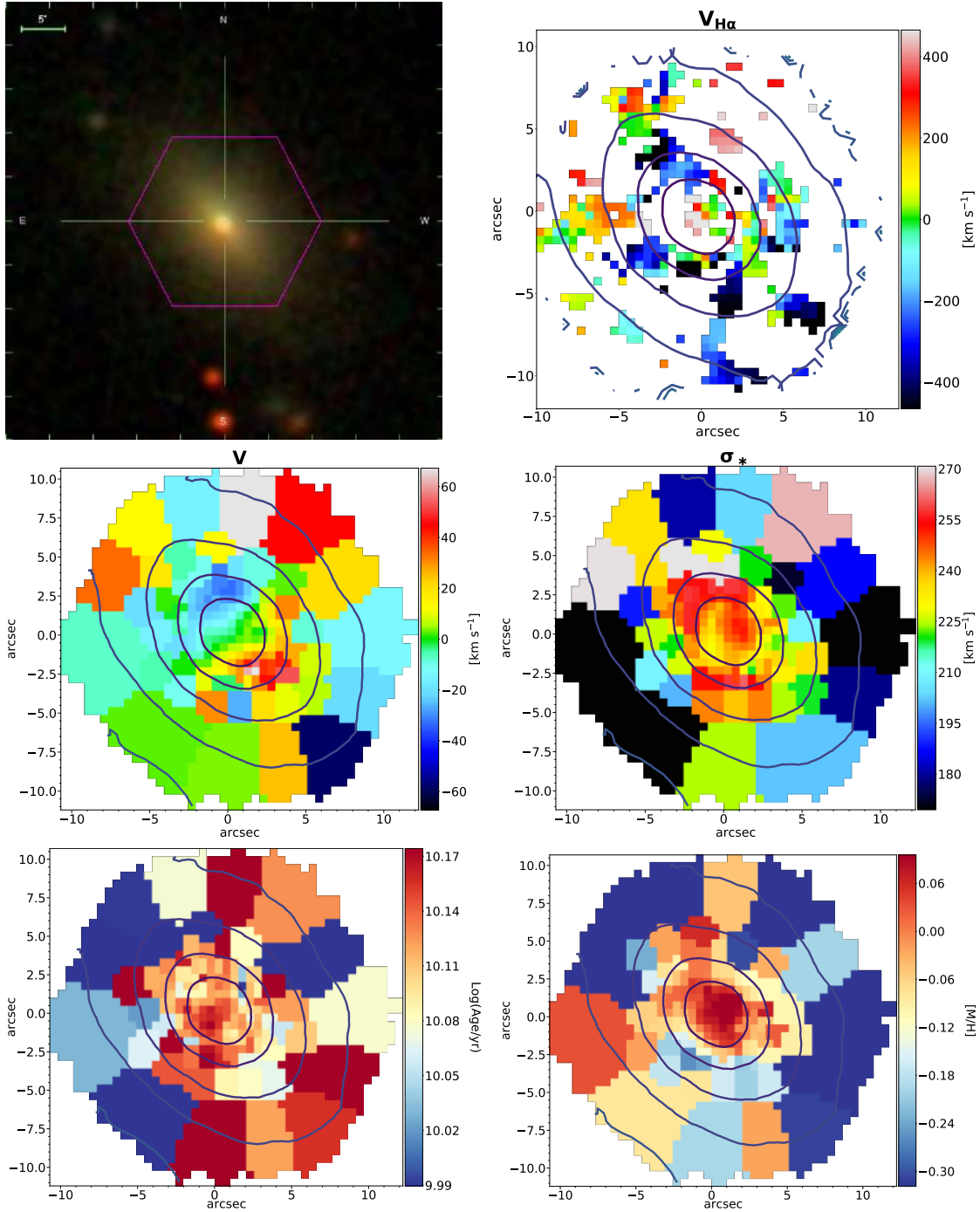


MaNGA ID: 1-167555



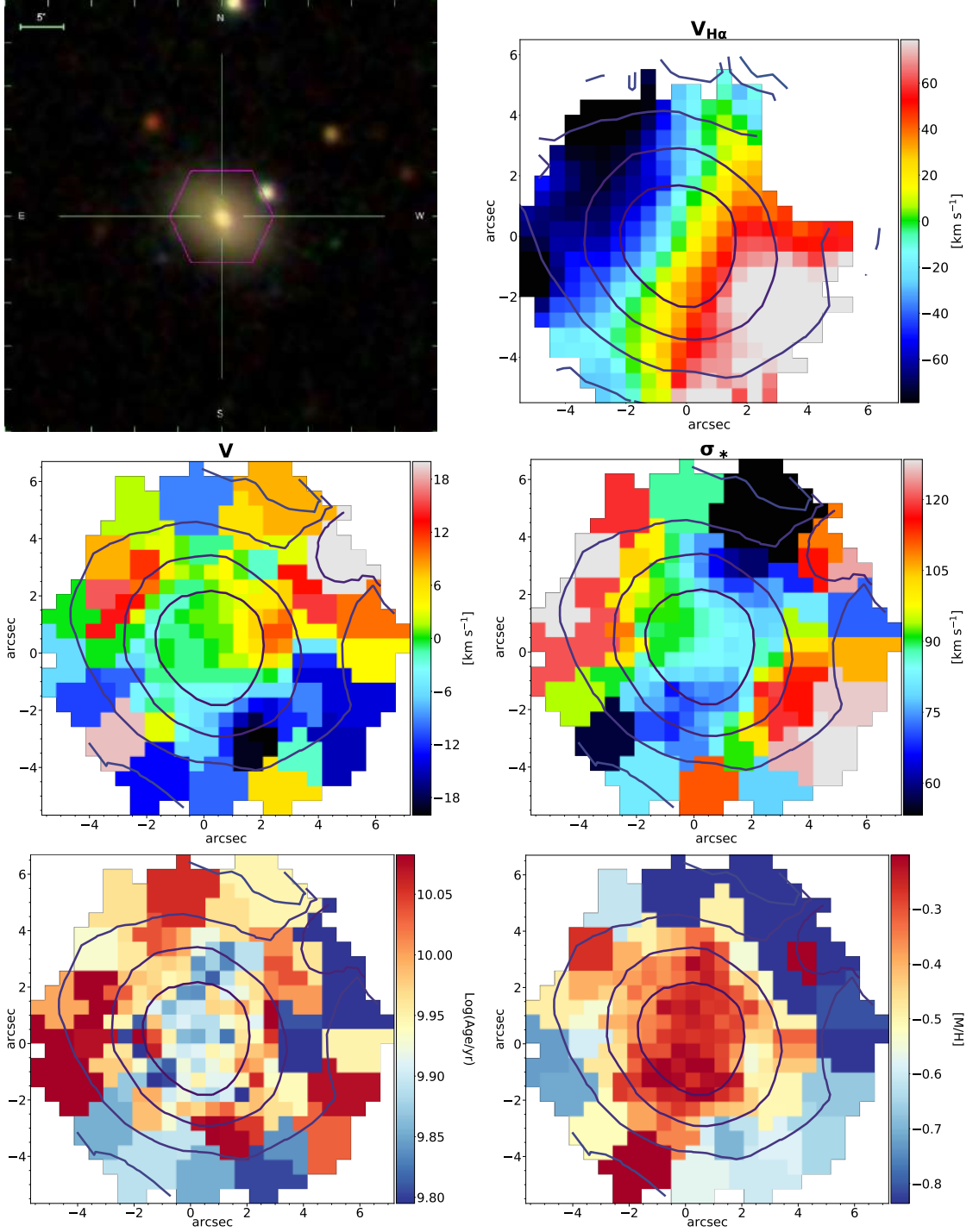
Error on V : 4.1 km s^{-1} ; error on σ_* : 5.3 km s^{-1} ; error on Log(Age) : 0.078; error on $[M/H]$: 0.09.

MaNGA ID: 1-275185



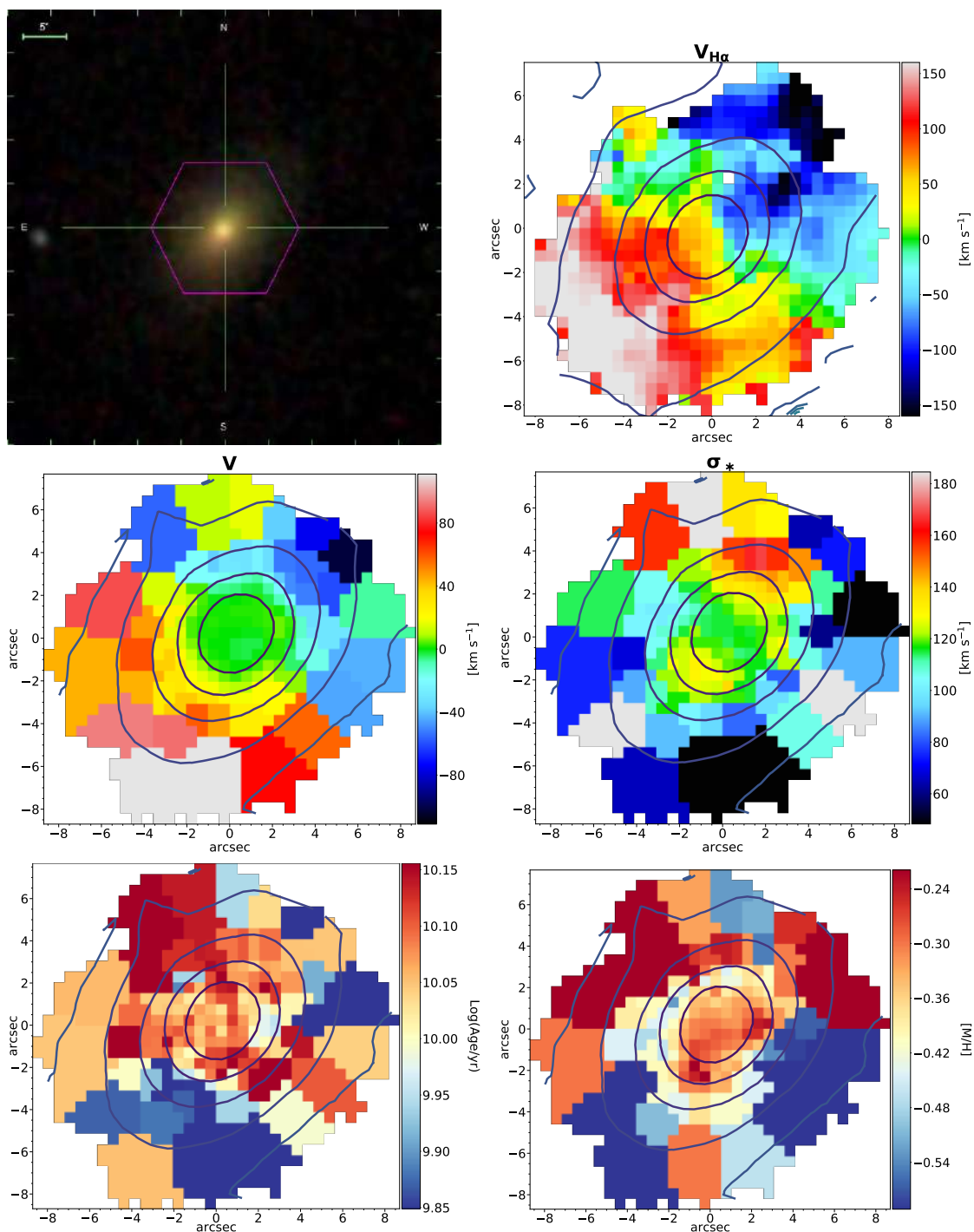
Error on V : 7.7 km s^{-1} ; error on σ_* : 7.9 km s^{-1} ; error on Log(Age) : 0.060; error on $[M/H]$: 0.06.

MaNGA ID: 1-94773 \otimes



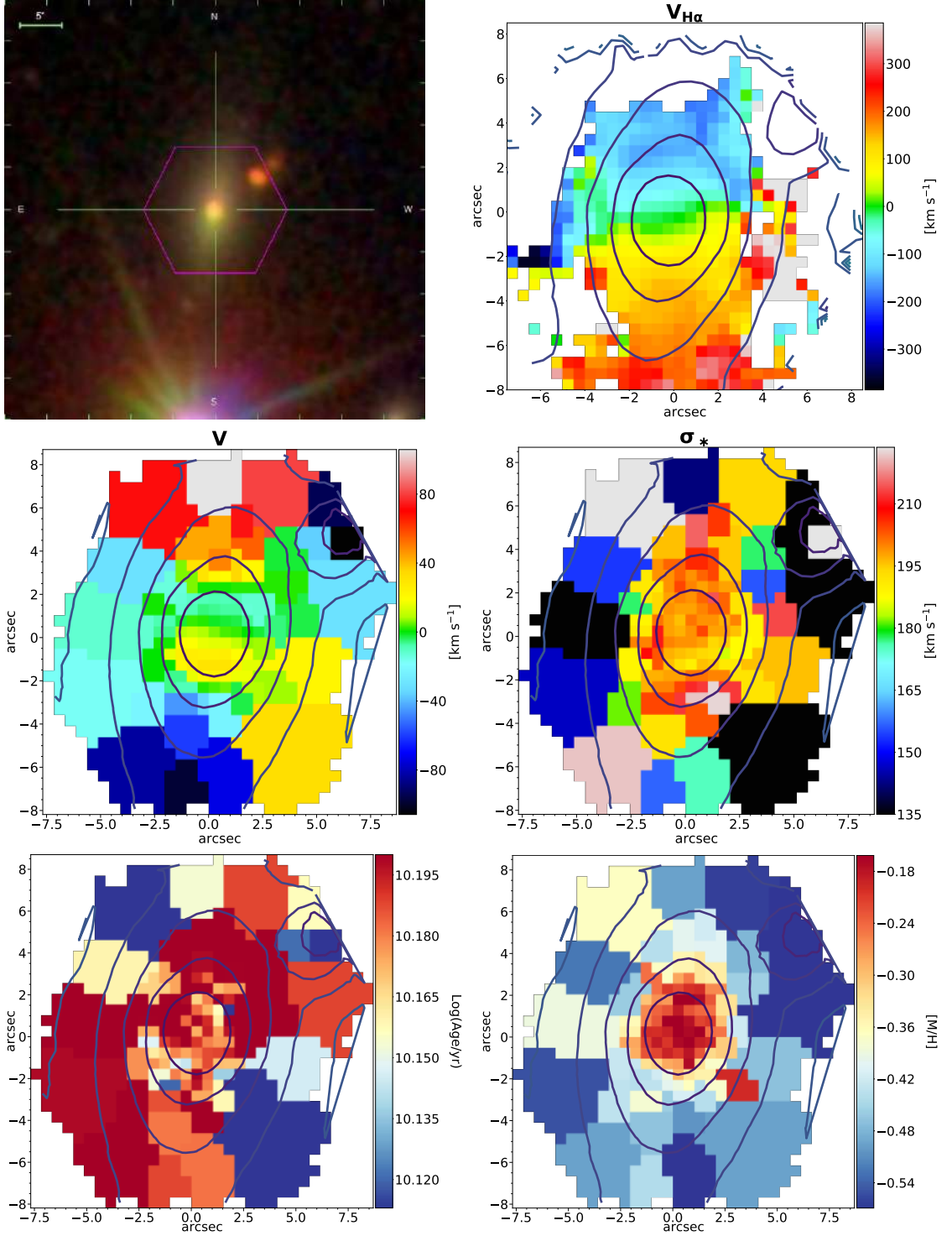
Error on V : 3.6 km s^{-1} ; error on σ_* : 4.5 km s^{-1} ; error on $\text{Log}(\text{Age})$: 0.261; error on $[\text{M}/\text{H}]$: 0.13.

MaNGA ID: 1-37494



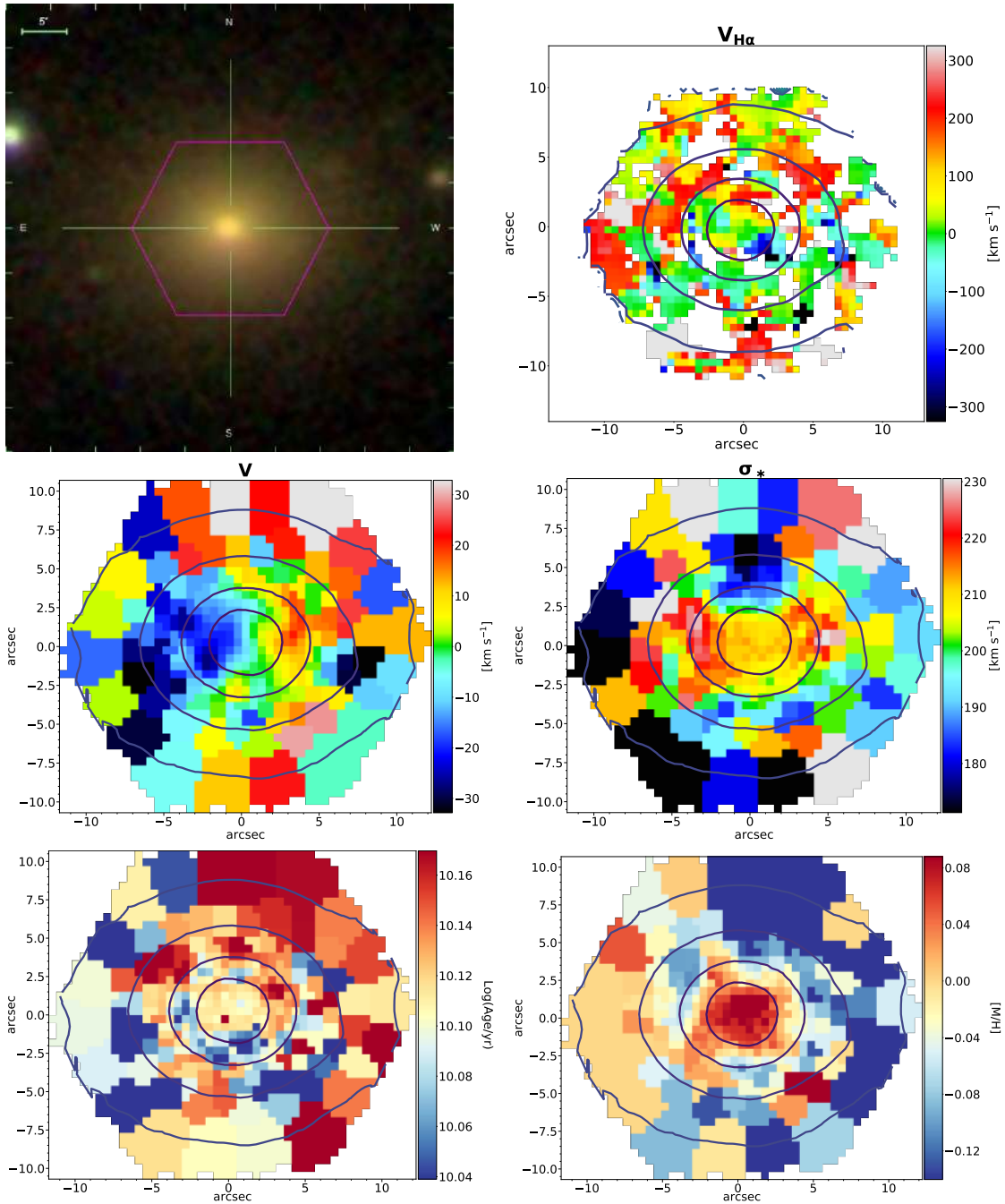
Error on V : 6.3 km s^{-1} ; error on σ_* : 7.3 km s^{-1} ; error on $\text{Log}(\text{Age})$: 0.075; error on $[\text{M}/\text{H}]$: 0.08.

MaNGA ID: 1-188530



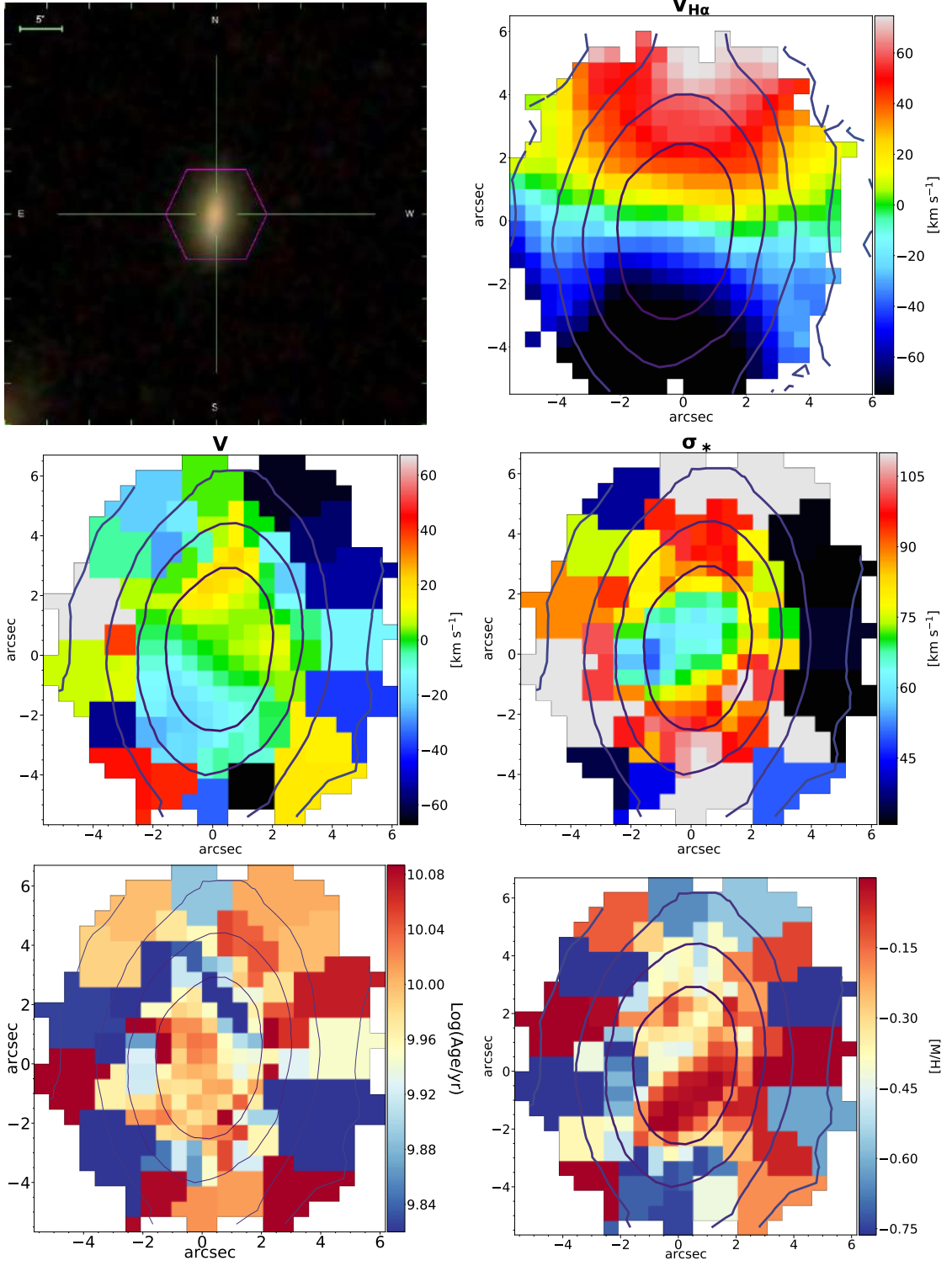
Error on V : 6.9 km s^{-1} ; error on σ_* : 7.4 km s^{-1} ; error on $\text{Log}(\text{Age})$: 0.019; error on $[\text{M}/\text{H}]$: 0.08.

MaNGA ID: 1-45016



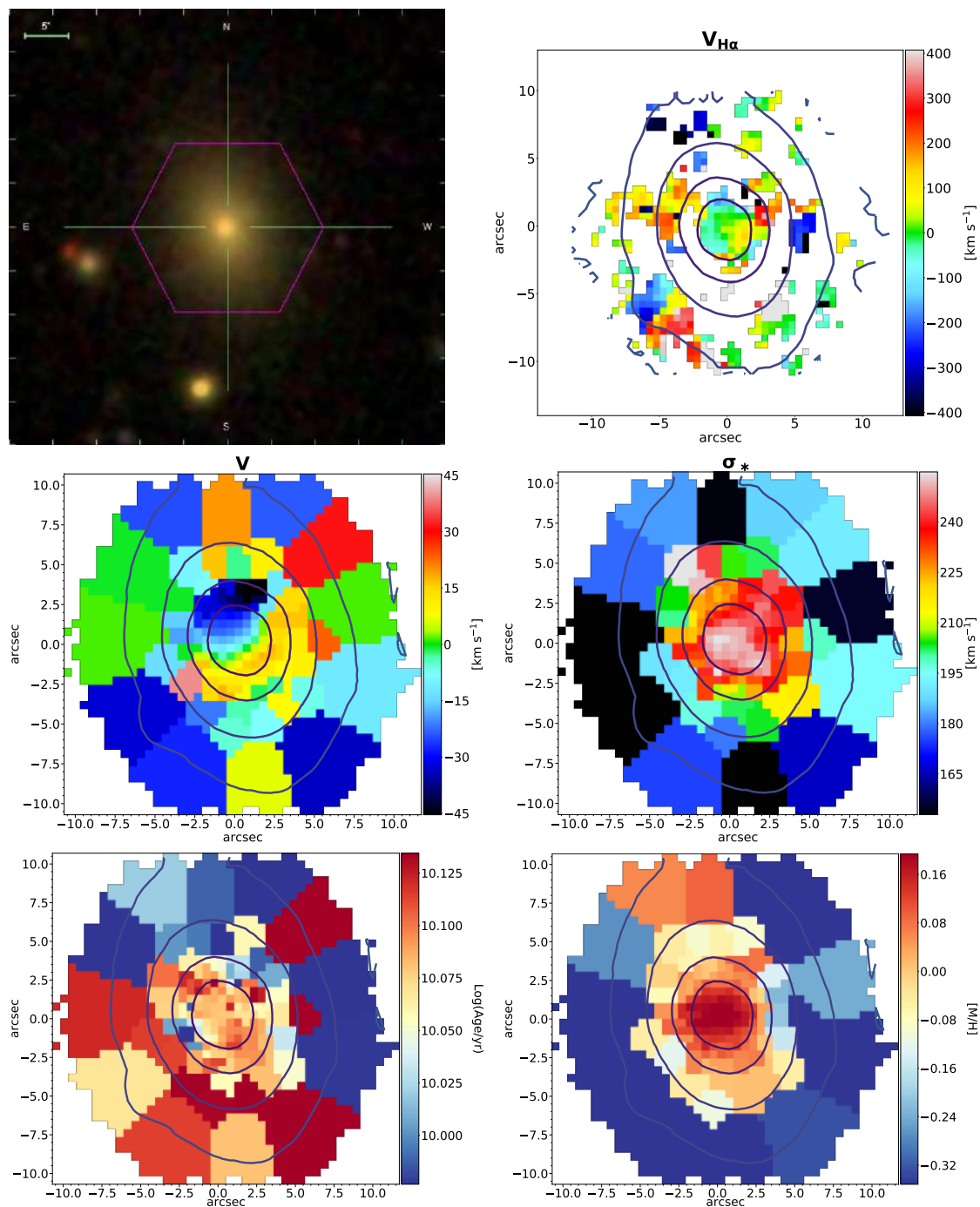
Error on V : 6.2 km s^{-1} ; error on σ_* : 6.5 km s^{-1} ; error on $\text{Log}(\text{Age})$: 0.034 ; error on $[\text{M}/\text{H}]$: 0.04 .

MaNGA ID: 1-274440



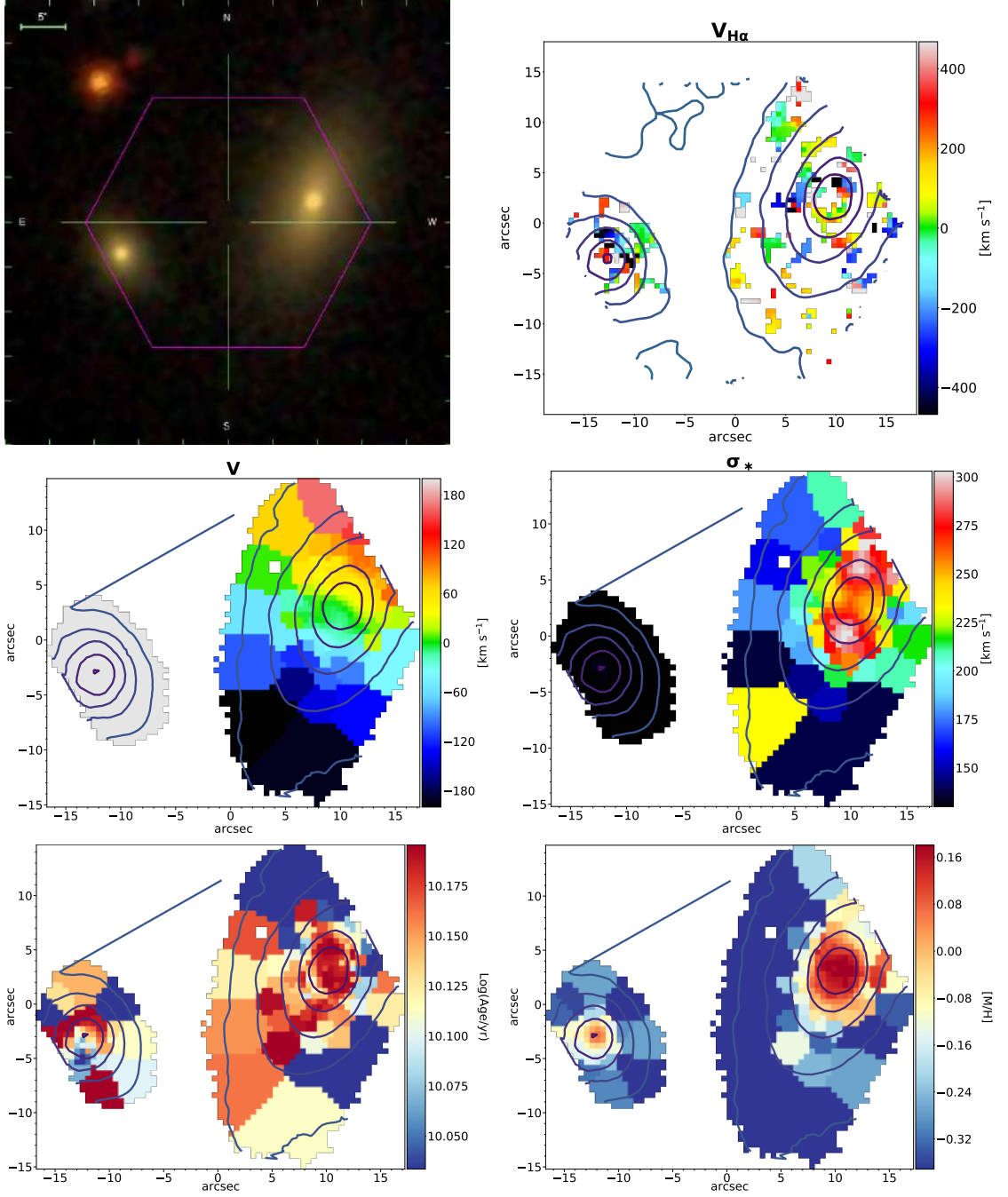
Error on V : 7.3 km s^{-1} ; error on σ_* : 8.8 km s^{-1} ; error on $\text{Log}(\text{Age})$: 0.163; error on $[\text{M}/\text{H}]$: 0.23.

MaNGA ID: 1-299176



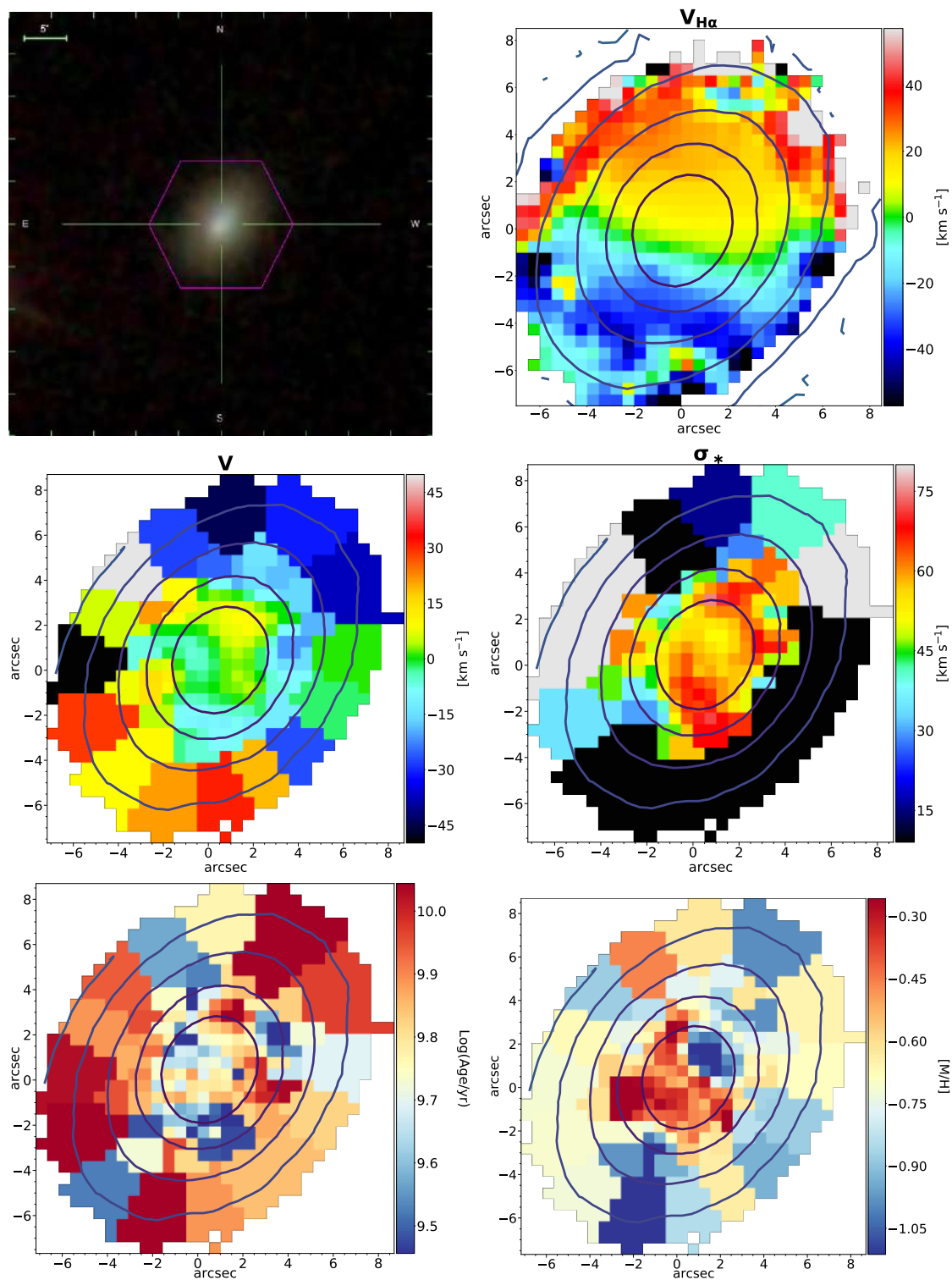
Error on V : 7.7 km s^{-1} ; error on σ_* : 7.9 km s^{-1} ; error on $\text{Log}(\text{Age})$: 0.037; error on $[\text{M}/\text{H}]$: 0.05.

MaNGA ID: 1-549076 \otimes



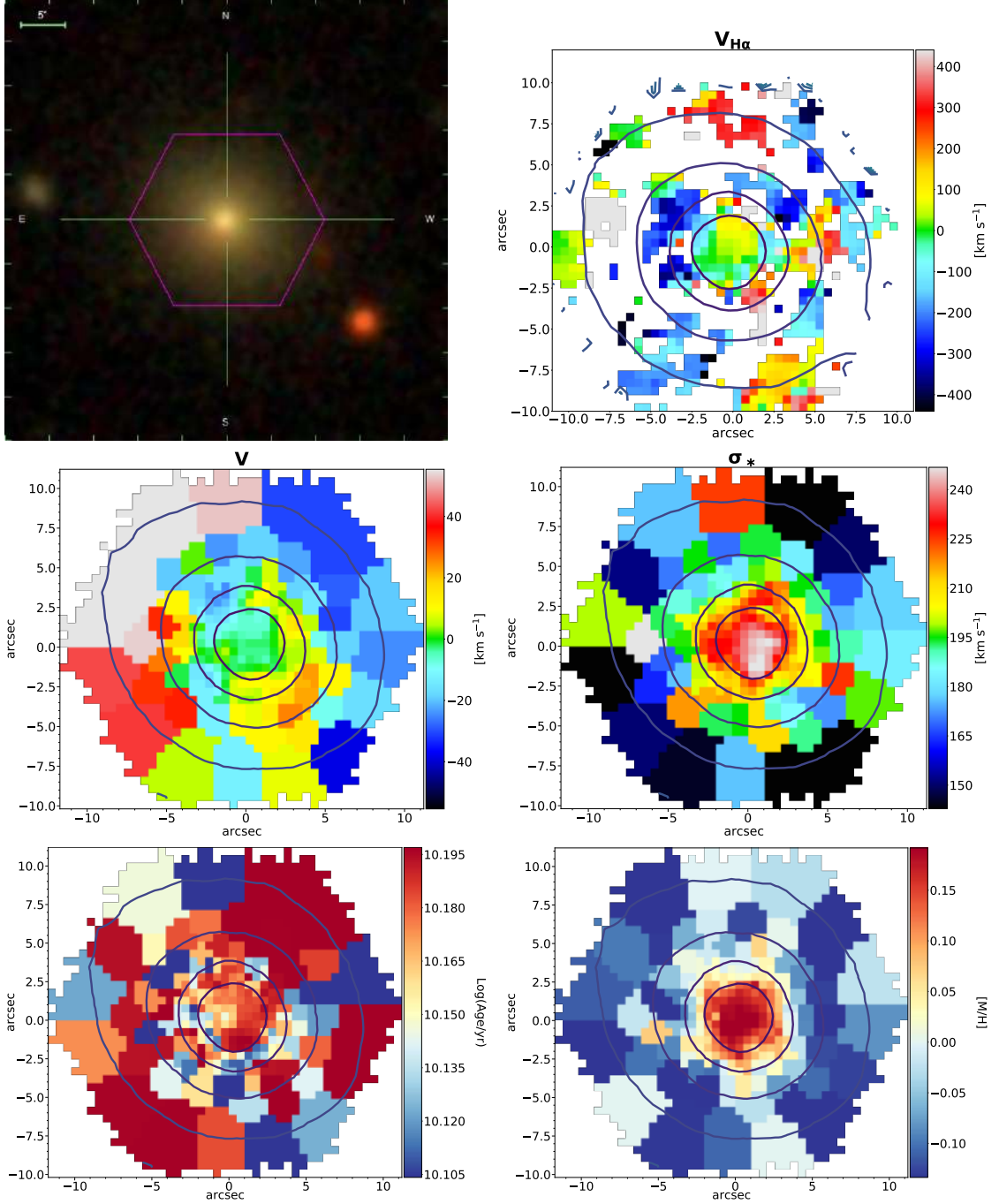
Error on V : 7.2 km s^{-1} ; error on σ_* : 7.4 km s^{-1} ; error on $\text{Log}(\text{Age})$: 0.040; error on $[\text{M}/\text{H}]$: 0.08.

MaNGA ID: 1-149172



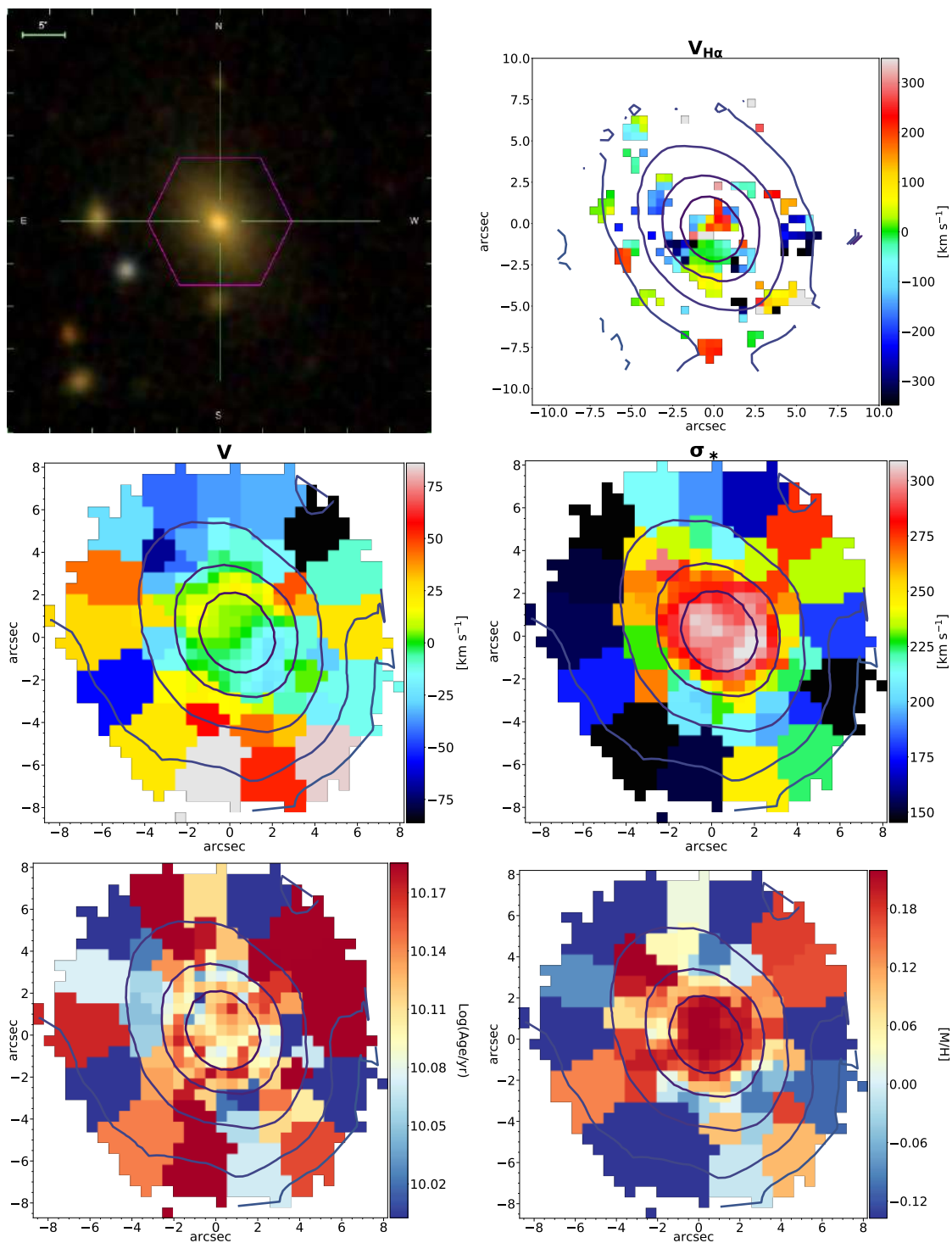
Error on V : 5.1 km s^{-1} ; error on σ_* : 7.0 km s^{-1} ; error on Log(Age) : 0.138; error on $[\text{M}/\text{H}]$: 0.17.

MaNGA ID: 1-167044



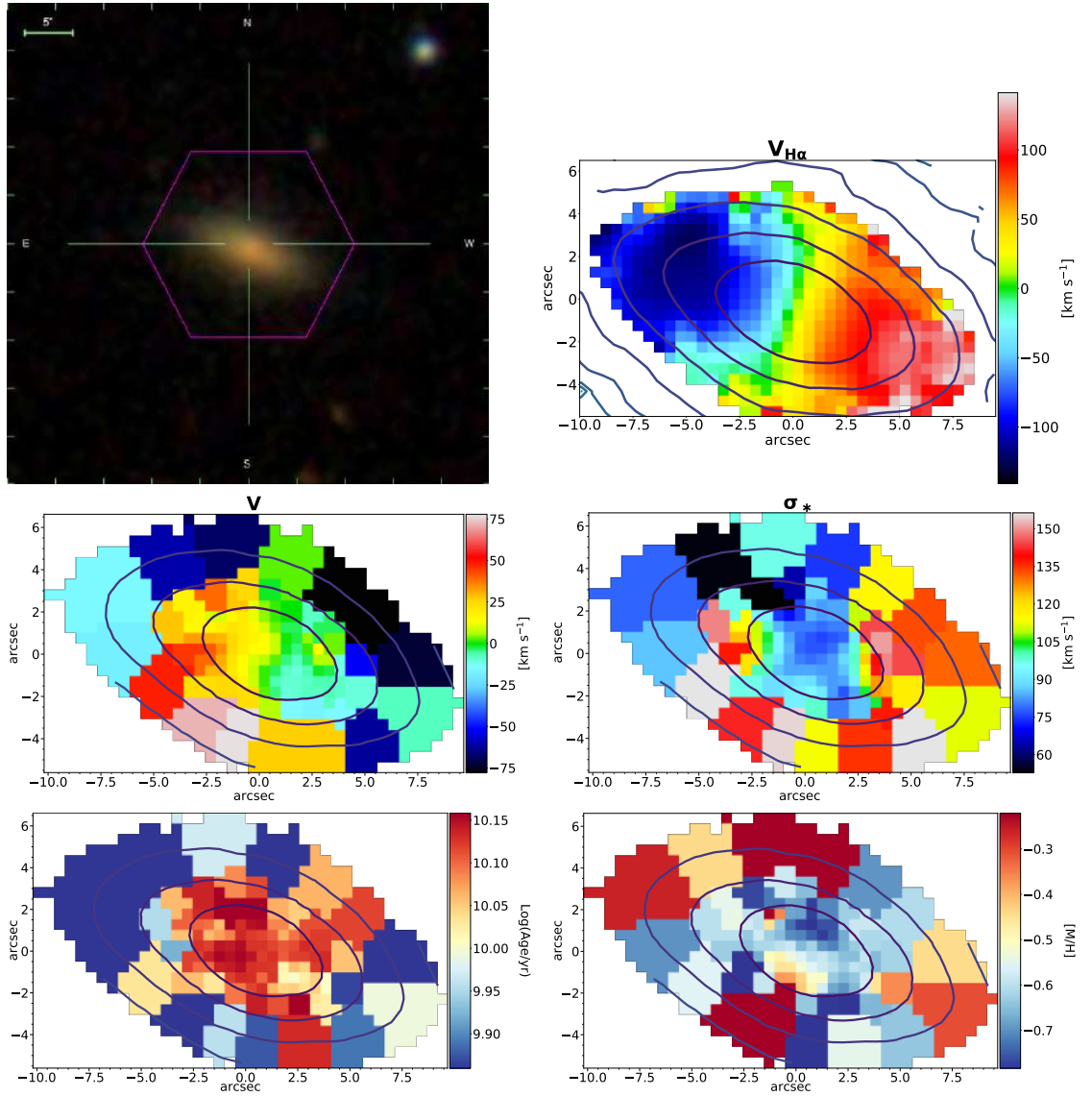
Error on V : 7.2 km s^{-1} ; error on σ_* : 7.4 km s^{-1} ; error on Log(Age) : 0.032; error on $[\text{M}/\text{H}]$: 0.05.

MaNGA ID: 1-278079



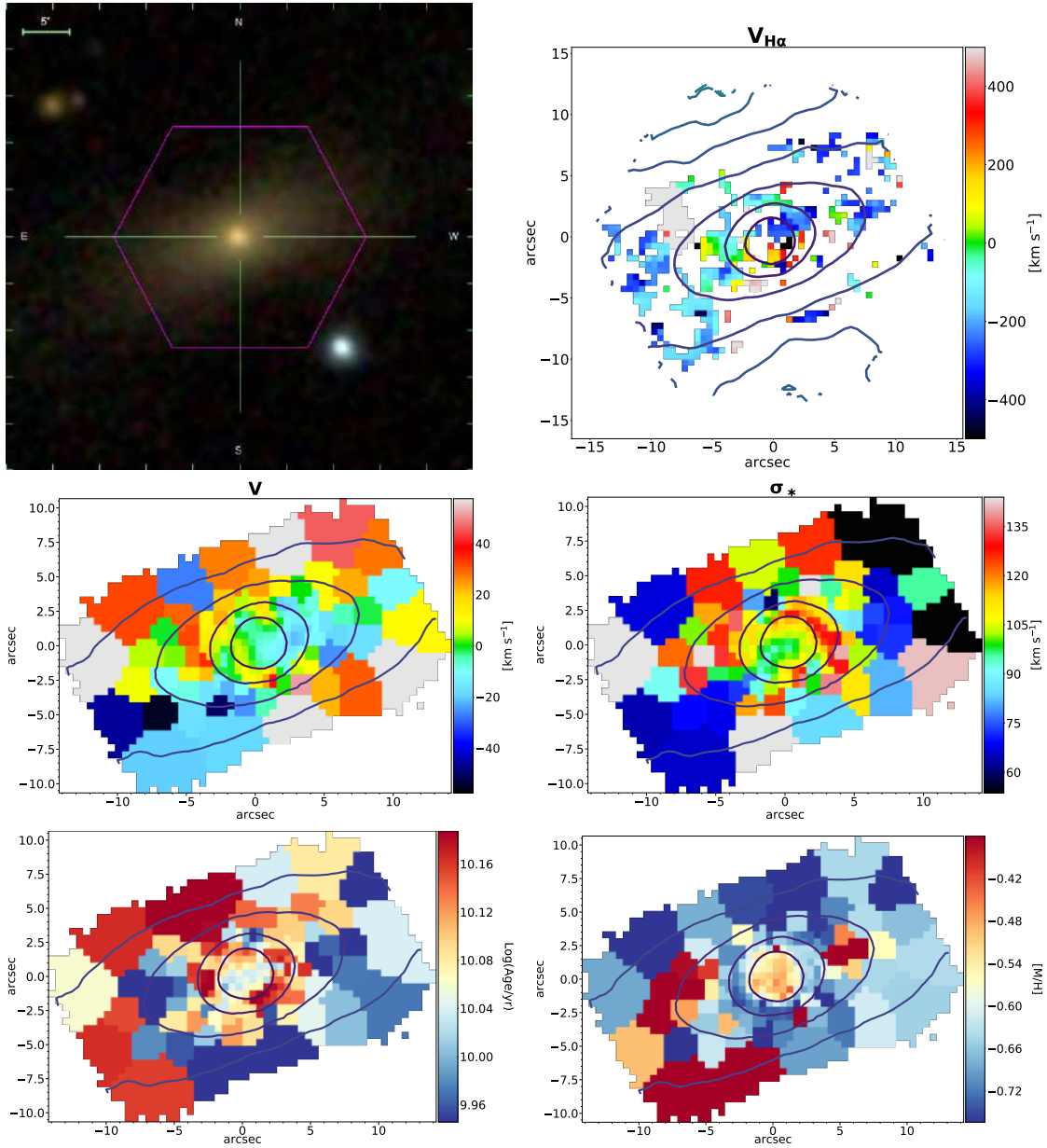
Error on V : 11.5 km s^{-1} ; error on σ_* : 11.7 km s^{-1} ; error on $\text{Log}(\text{Age})$: 0.057; error on $[M/H]$: 0.18.

MaNGA ID: 1-246175



Error on V : 8.6 km s^{-1} ; error on σ_* : 10.7 km s^{-1} ; error on $\text{Log}(\text{Age})$: 0.096; error on $[M/H]$: 0.11.

MaNGA ID: 1-44722



Error on V : 8.6 km s^{-1} ; error on σ_* : 10.2 km s^{-1} ; error on Log(Age) : 0085; error on $[M/H]$: 0.12.

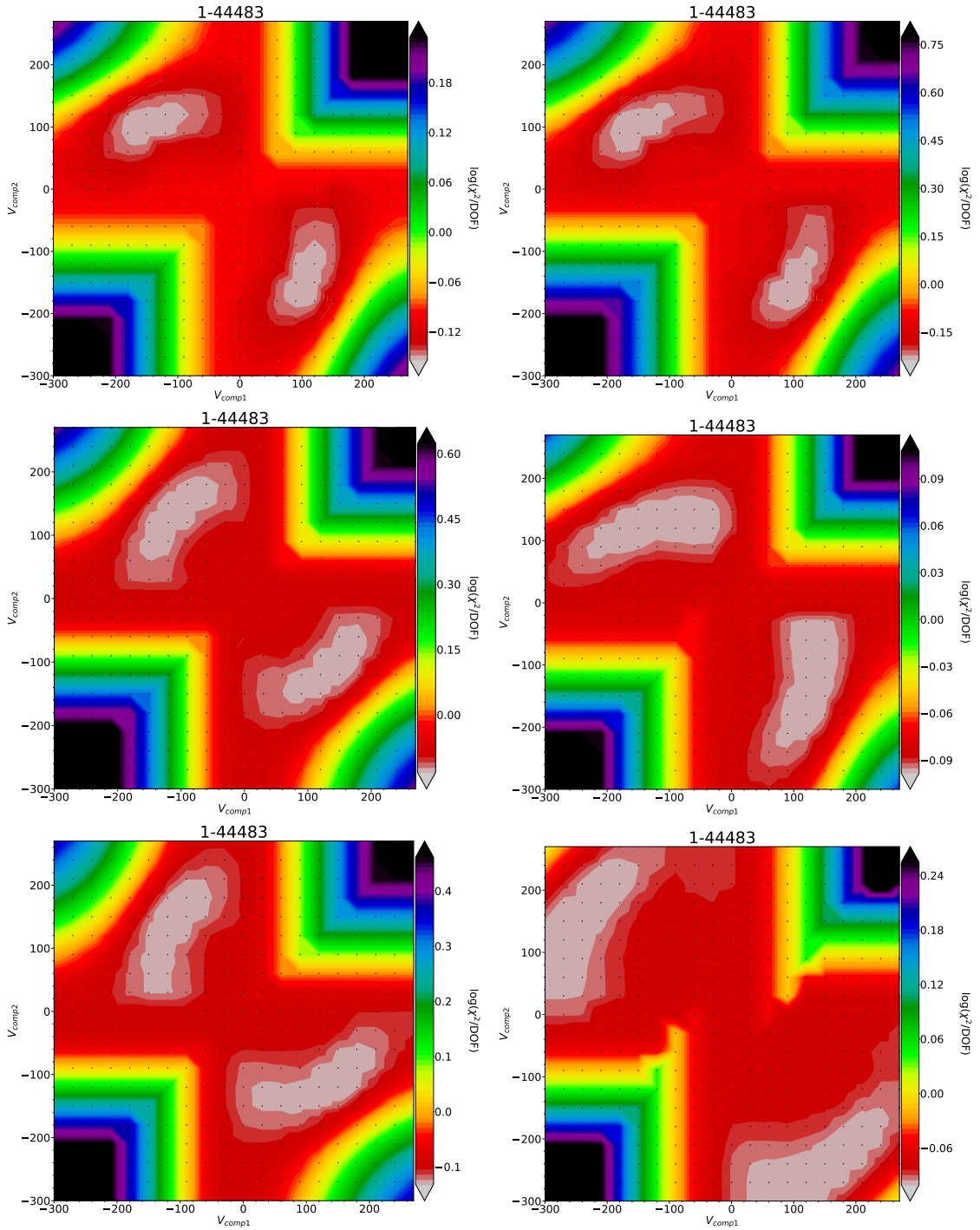
Appendix C

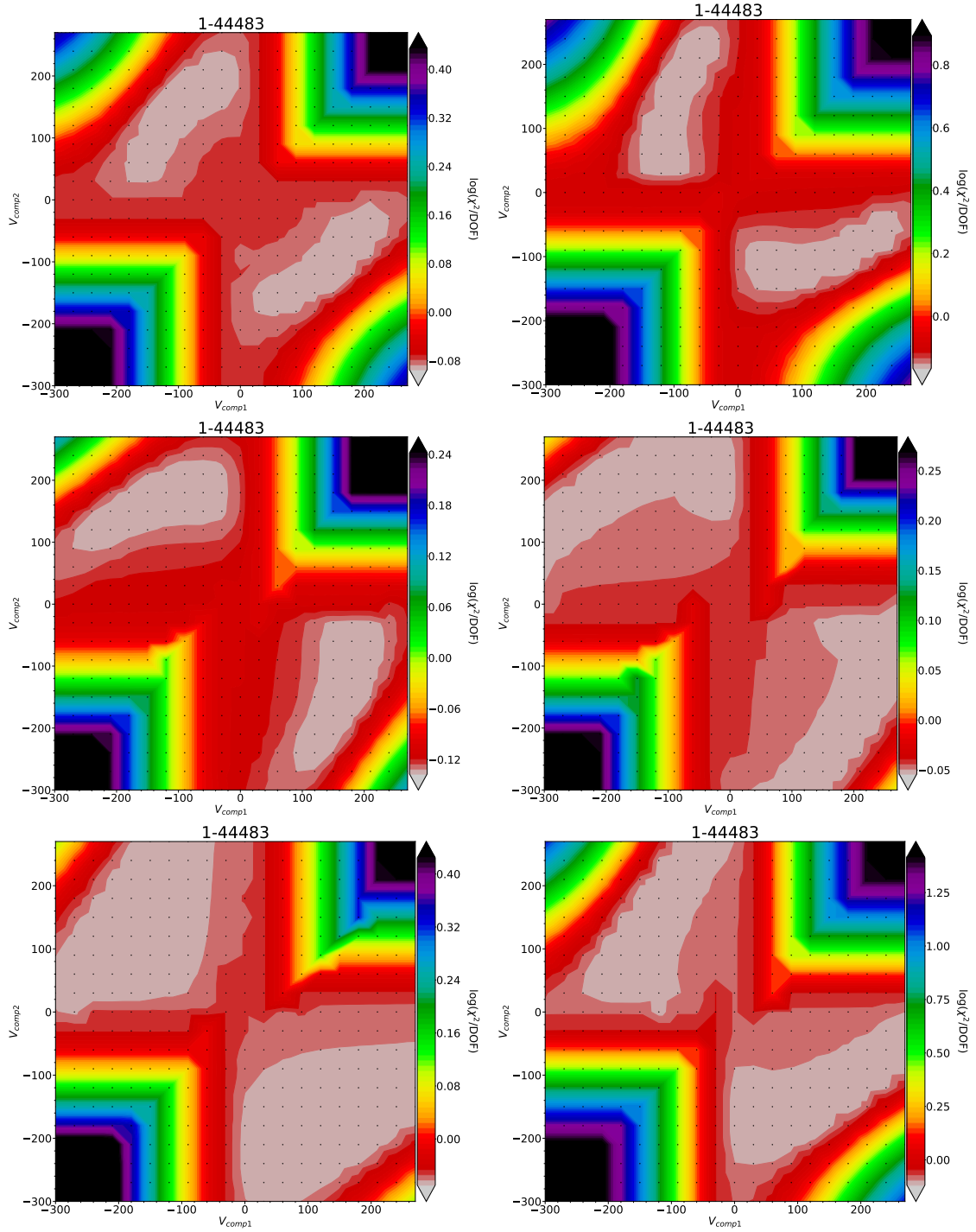
χ^2 maps

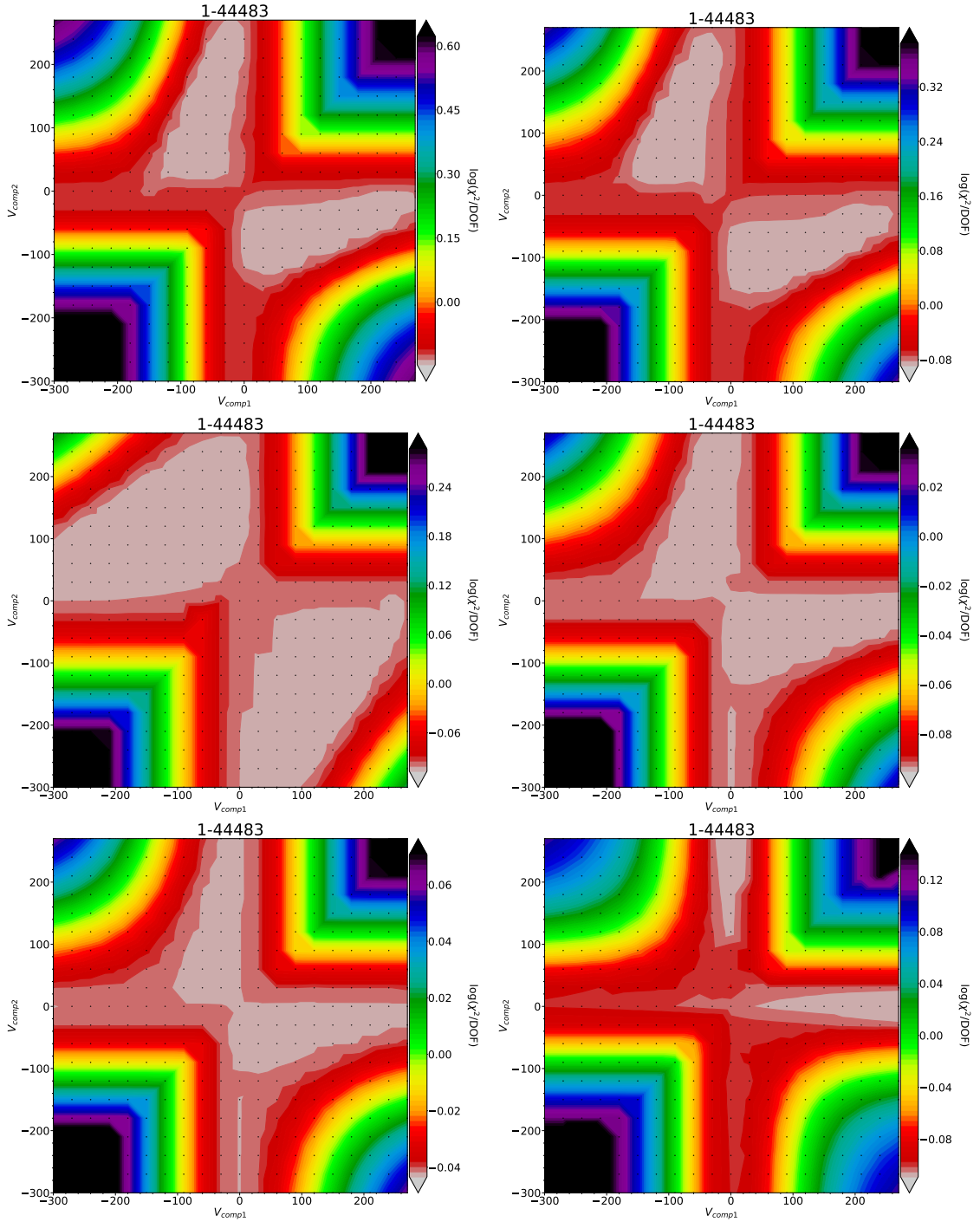
Here we present the χ^2 maps, extracted as described in section 4.2.4, of the whole sample of CRD-galaxies. Each map has the corresponding MaNGA ID as the title. The regions of extraction are listed in Table C.1: these are the regions of the appearance of one of the two σ peaks or, equivalently, of the inversion of rotation in the velocity field. In practice, for each galaxy, we extracted two maps, relatively to the two peaks; here, we only show the one map where the distinction of the two components appears clearer. Each map shows the χ^2 values, in logarithmic scale, calculated for each couple of input V_{comp1} and V_{comp2} .

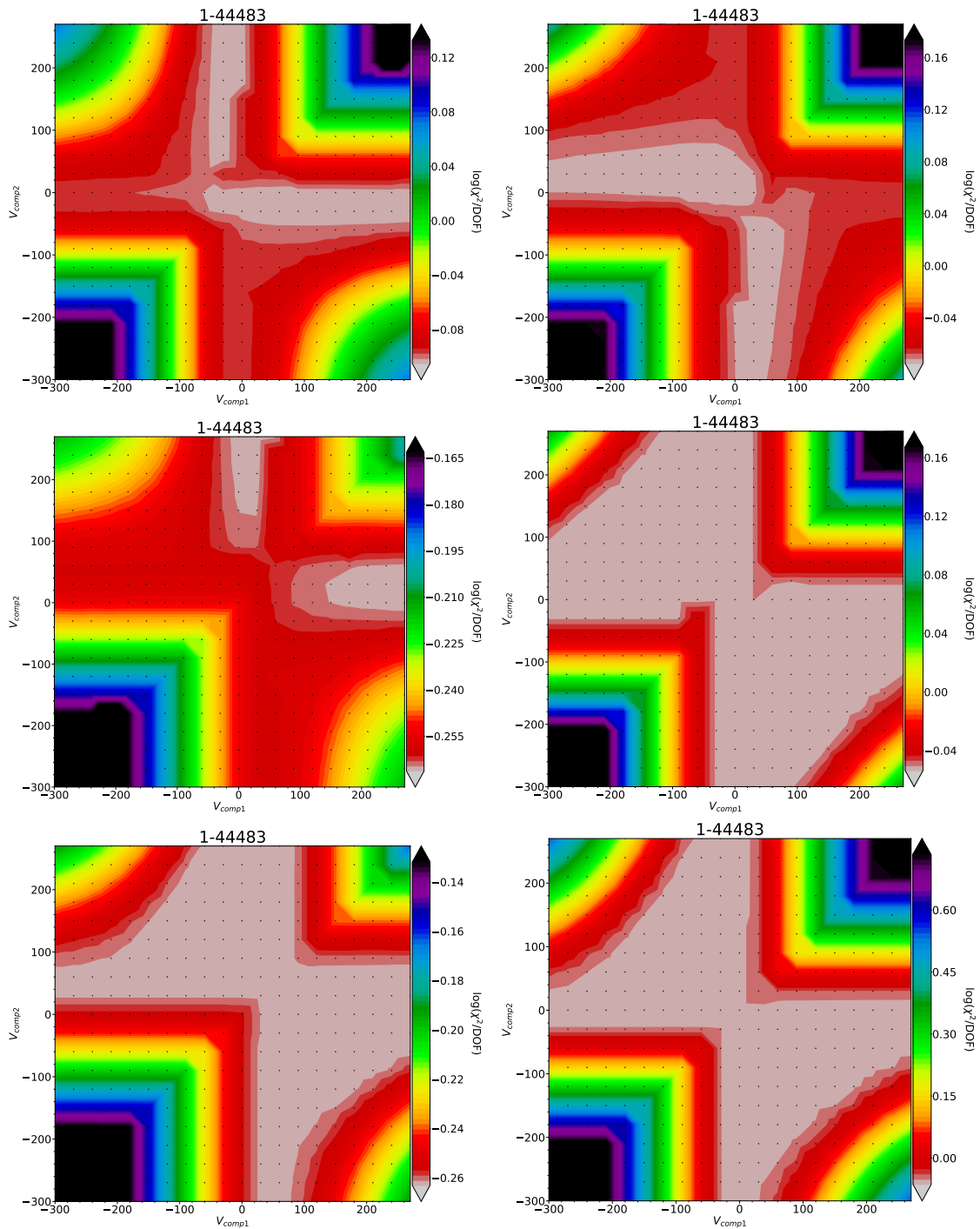
MaNGA-ID	x_c	y_c	r	MaNGA-ID	x_c	y_c	r
12-84617	-1.5	1.4	1.5	1-113520	-2.2	-1.8	1.5
1-115097	-2.7	2.4	2.0	1-38347	2.9	1.3	1.5
1-339061	3.0	4.3	2.5	1-44047	-2.0	2.3	1.7
1-44483	6.0	0.0	1.5	1-556514	0.0	3.8	1.8
1-37494	-1.3	-1.5	1.7	1-37155	-4.6	-2.1	2.0
1-38543	-3.5	0.0	2.5	1-47248	-2.2	1.2	2.0
1-137890	3.7	-1.5	1.5	1-255220	1.9	3.5	1.5
1-282035	-1.0	-0.3	1.5	1-251783	1.0	3.5	1.3
1-419257	4.5	-0.9	2.0	1-418023	-2.3	1.5	1.7
1-167555	4.0	3.5	1.5	1-274440	0.7	3.5	1.5
1-274545	-6	-3.6	2	1-275185	-2.0	5.0	2.3
1-167044	-4	5.6	3	1-166613	-2.2	2.9	2.0
1-246175	-2.7	0.8	1.3.0	1-210728	1.0	-2.5	2.5
1-248869	-7.2	0.5	2.0	1-136248	6.6	-0.9	1.5
1-179561	-2.7	-0.6	2.0	1-635590	0.35	5.8	1.2
1-113698	2.5	-1.4	2.0	1-44722	7.0	2.9	2.5
1-45016	5.1	0.7	2.0	1-163594	-3.1	3.3	1.7
1-248410	0.4	-3.4	1.2	1-235983	3.0	-3.0	1.7
1-236144	0.0	-2.7	1.2	1-174947	-5.8	3.9	3.5
1-278079	2.9	-2.6	2.5	1-188530	0.0	-2.1	1.0
1-149172	-1.5	0.1	2.2	1-94773	-3.0	2.0	1.8
1-94690	-3.0	2.6	1.5	1-323766	3.0	1.8	1.5
1-323764	-3.7	5.0	2.0	1-135244	5.4	2.6	2.0
1-549076	9.7	-0.18	1.2	1-314719	-3.1	-2.8	1.5
1-299176	-1.1	4.6	3	1-298940	4.0	-0.7	1.7
1-593328	-3.8	8.5	1.2	1-322291	1.0	-3.2	1.6
1-633000	2.9	-3.0	1.2				

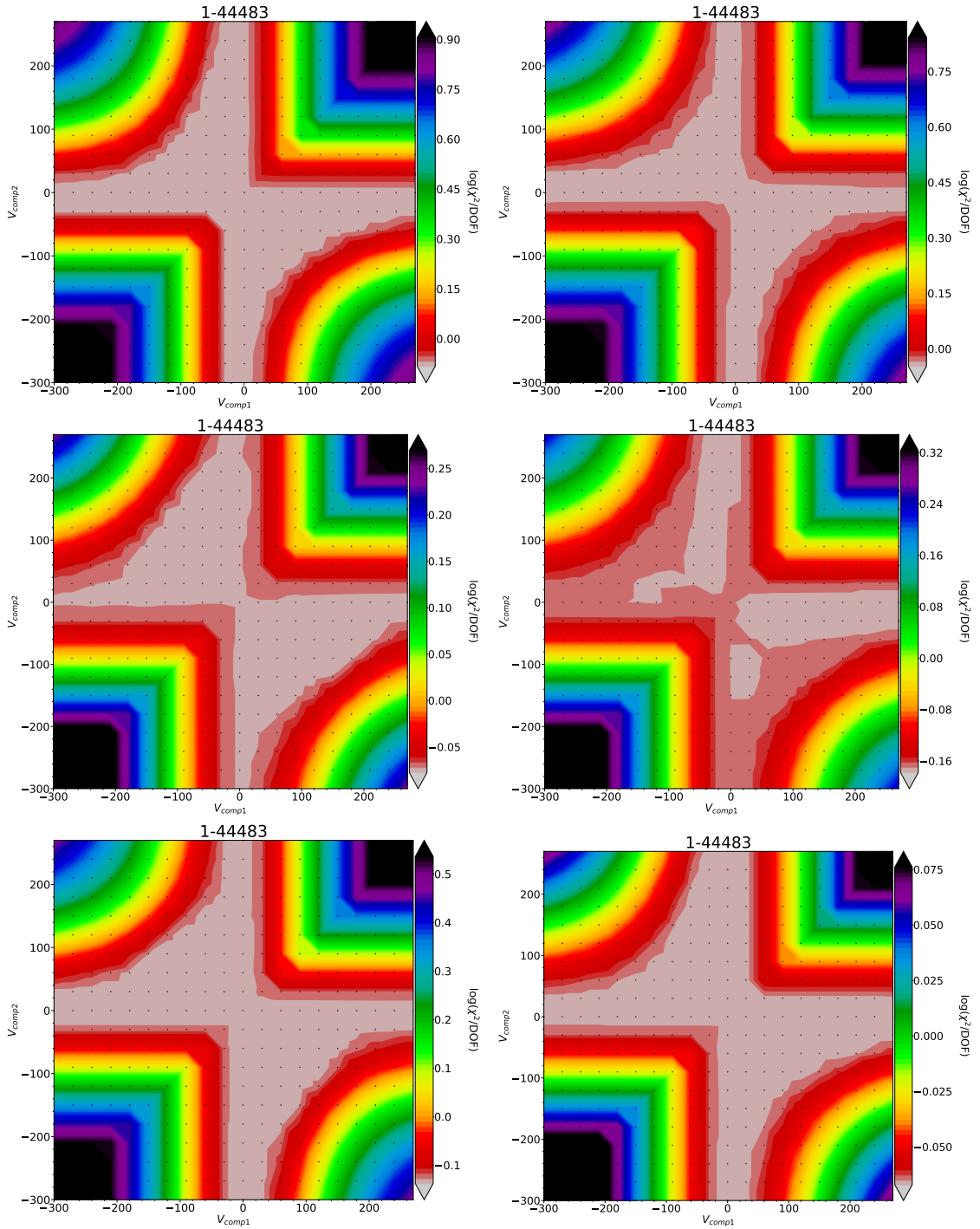
Table C.1: MaNGA IDs, central coordinates (x_c, y_c) ([arcsec]) and radii r ([arcsec]) of circles corresponding to the extraction regions the χ^2 maps.

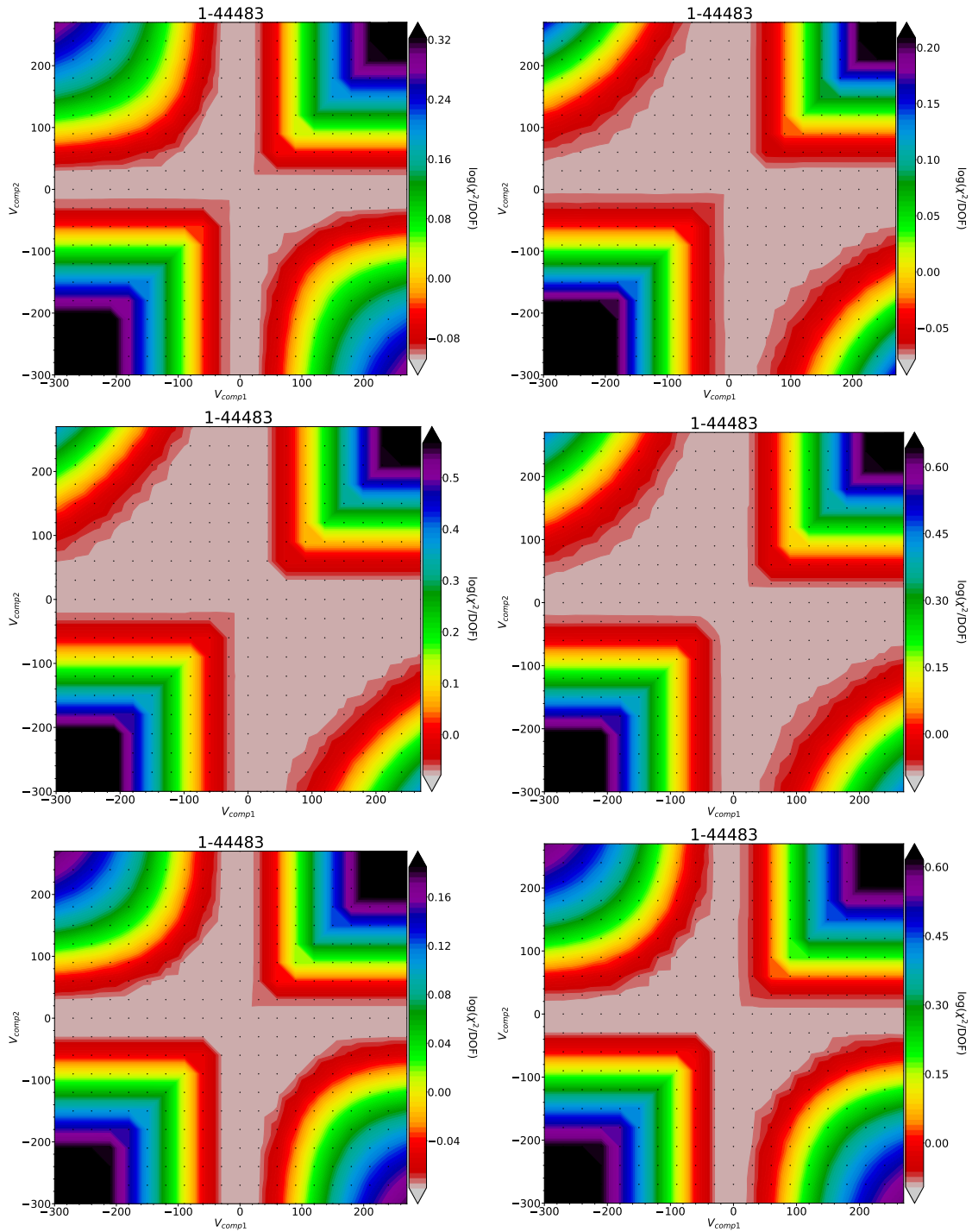


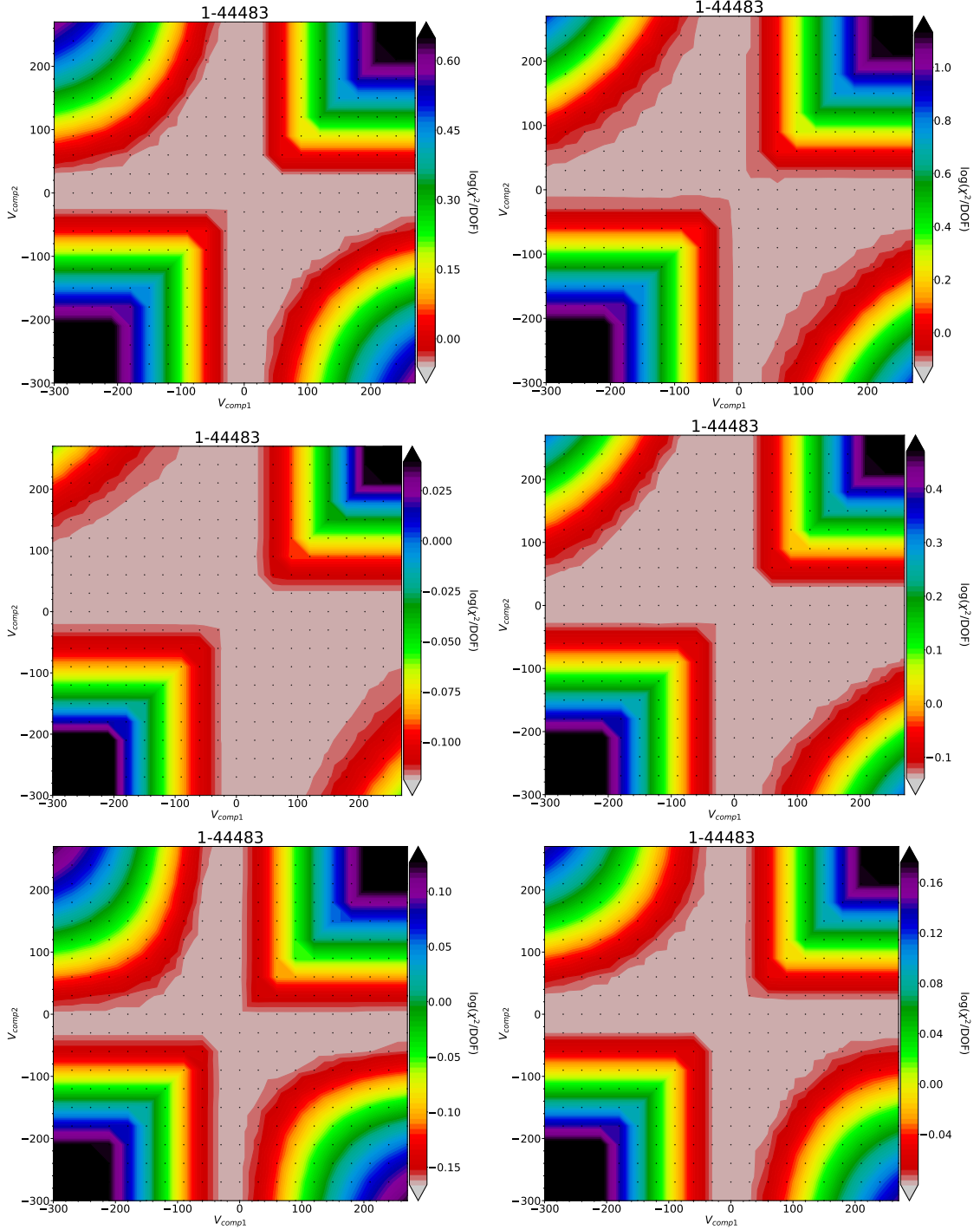


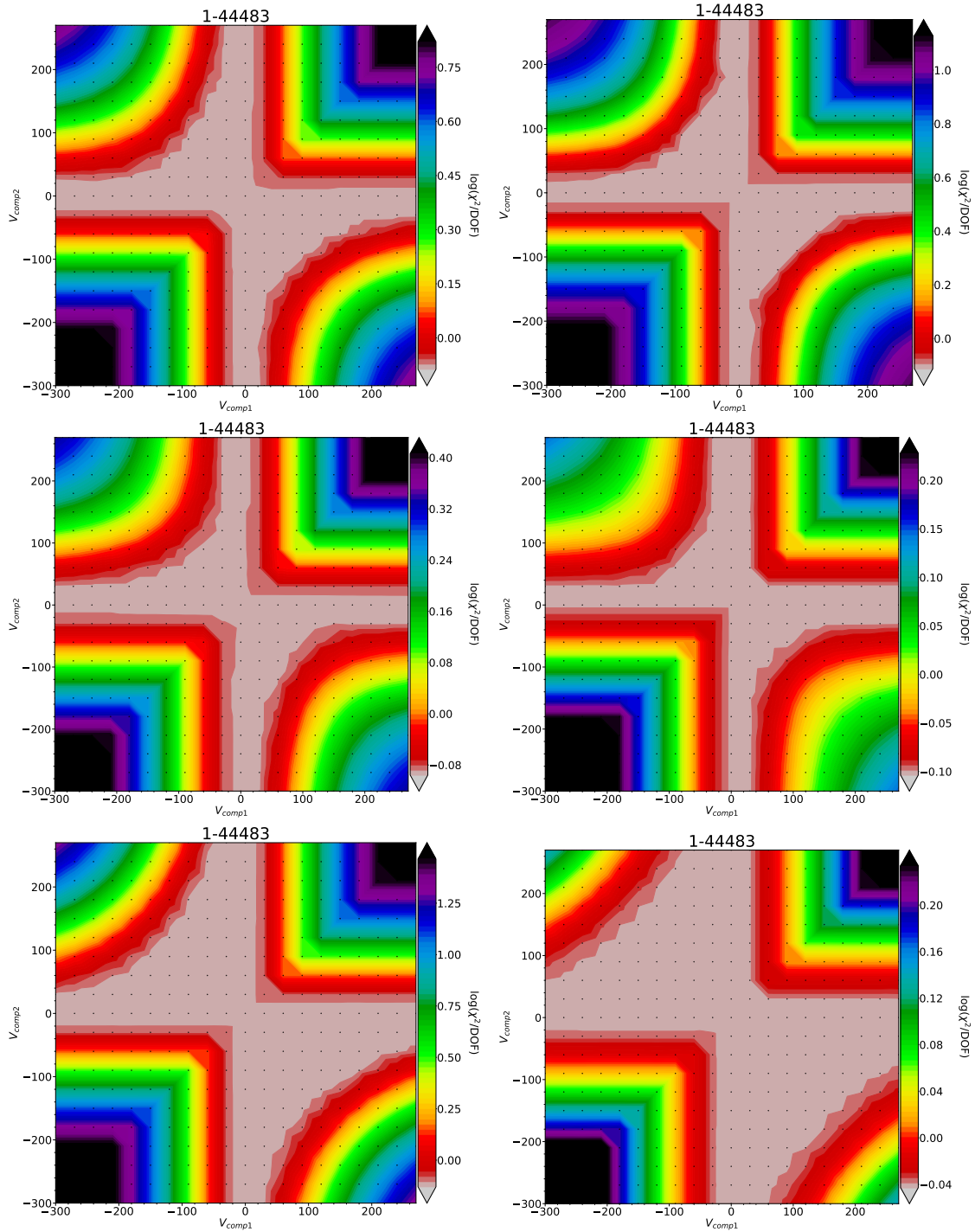


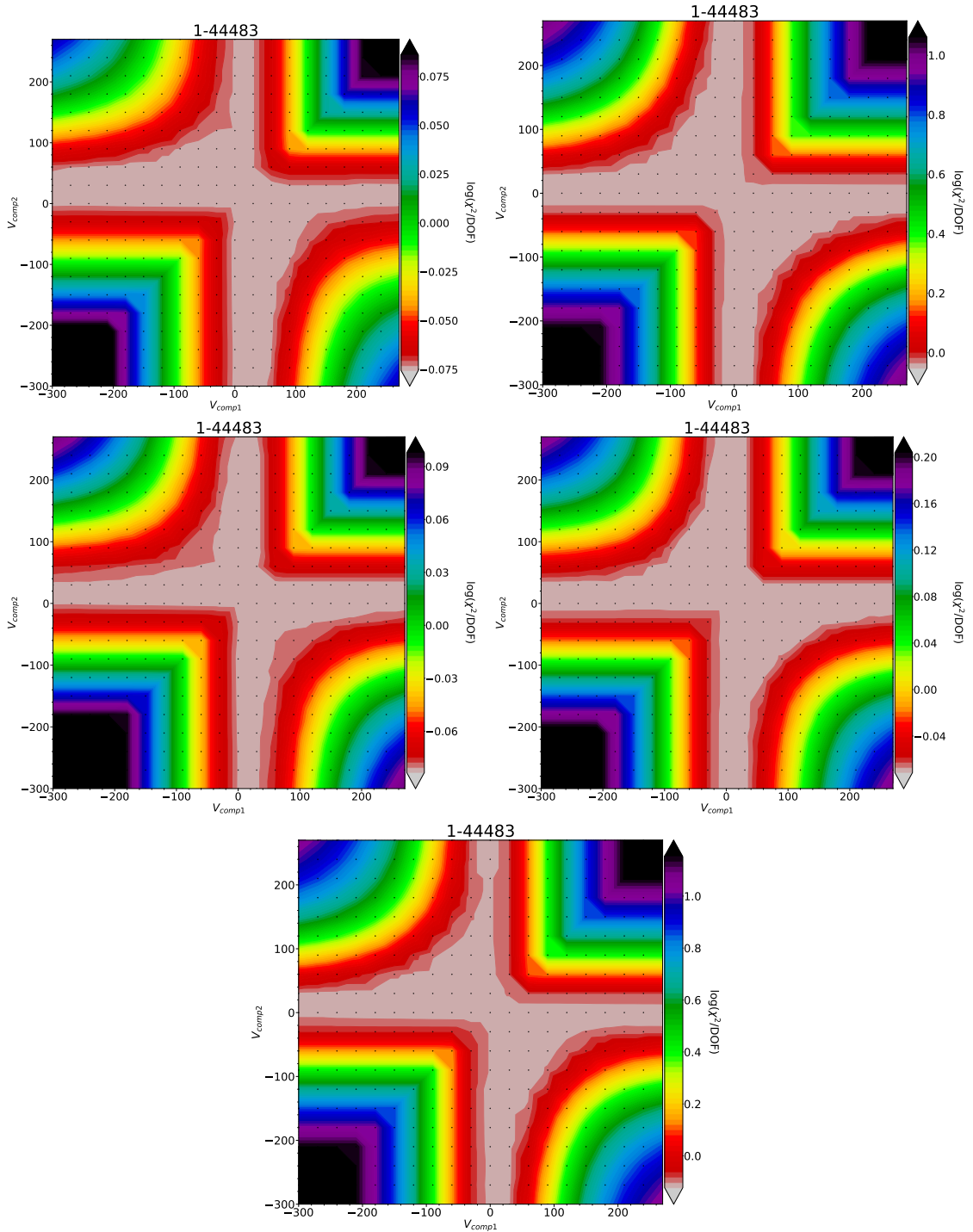










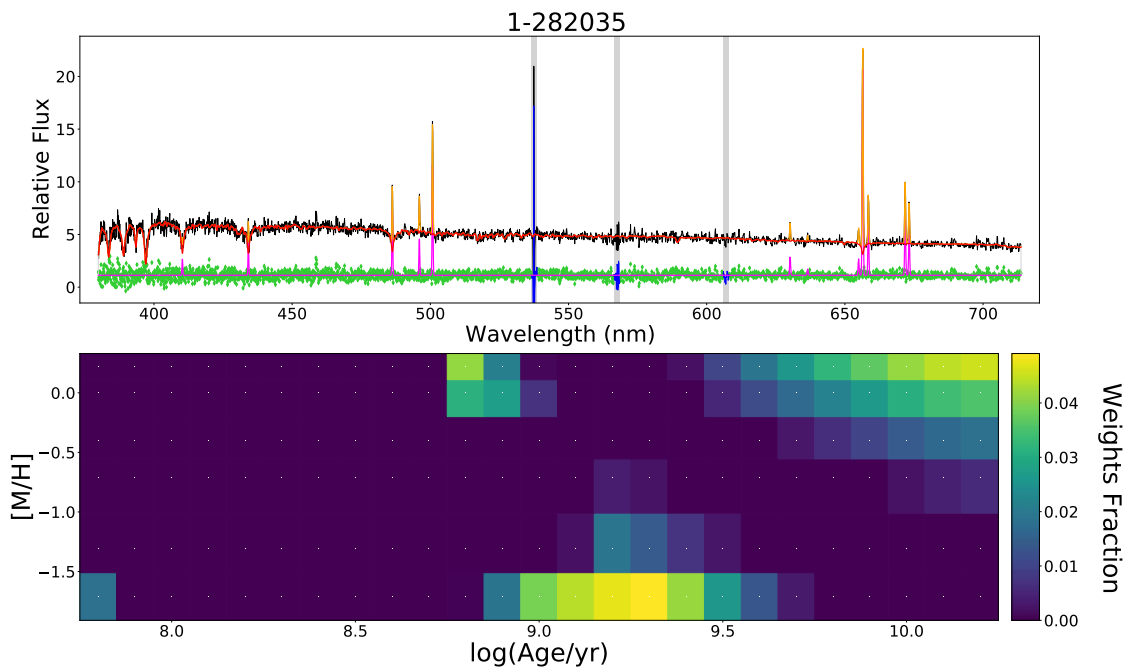
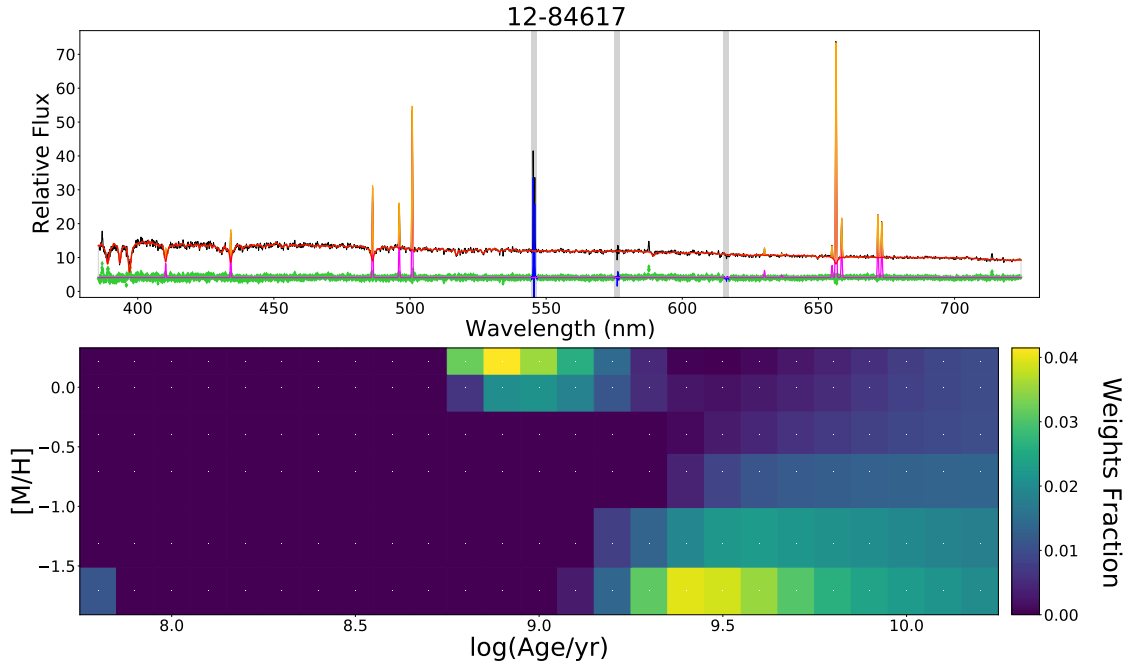


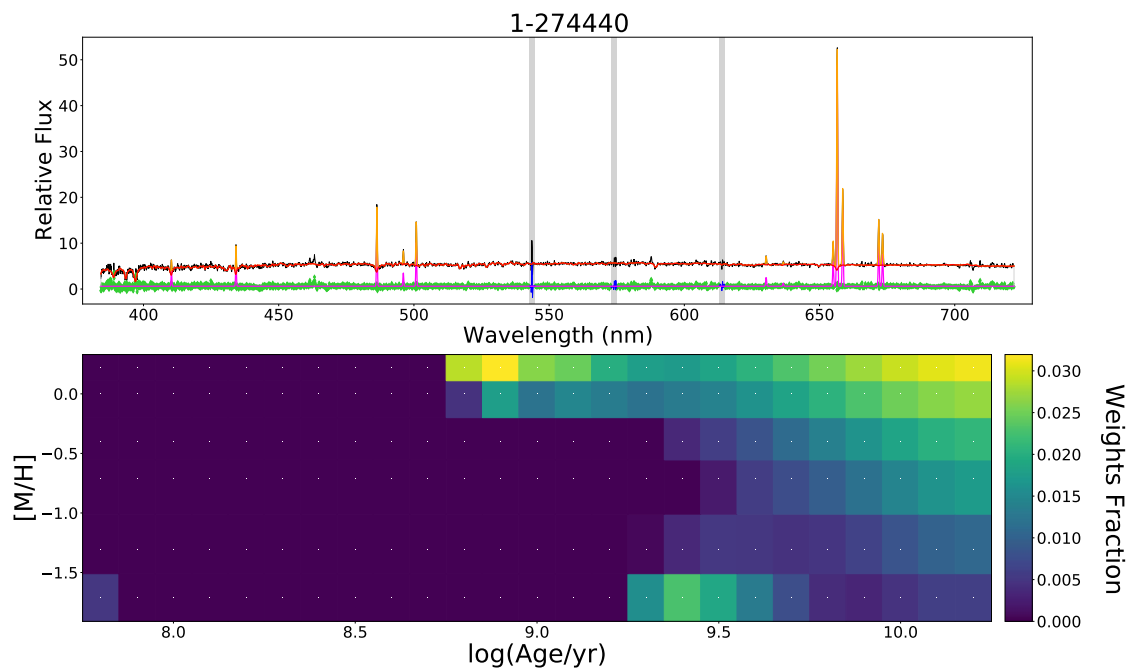
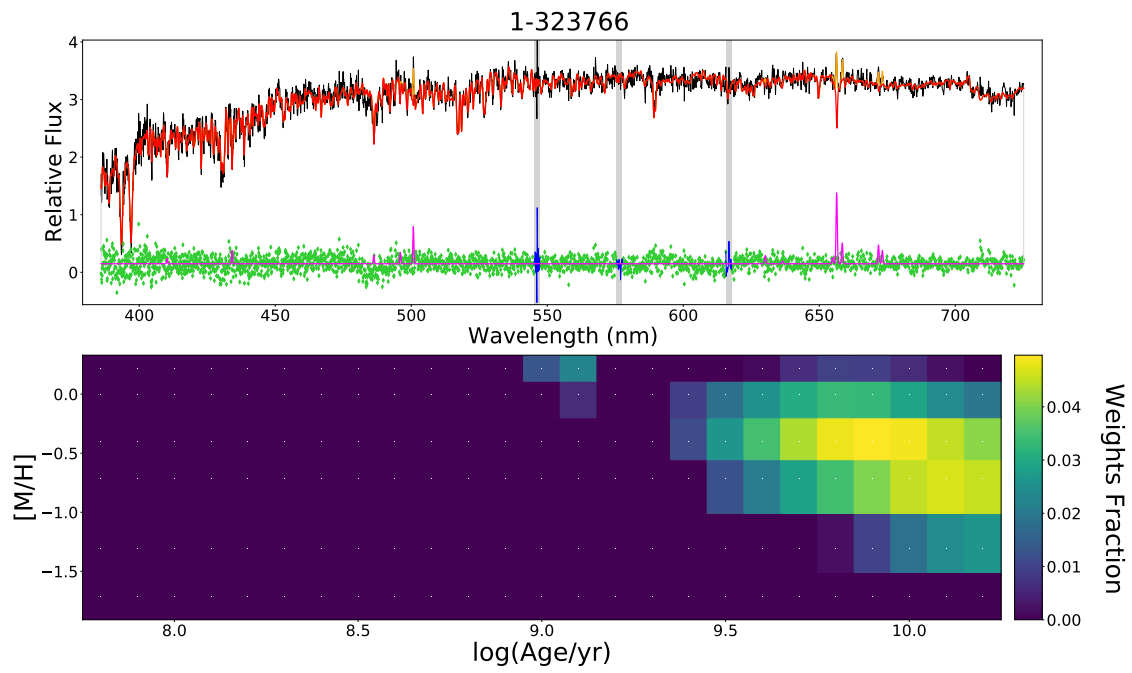
Appendix D

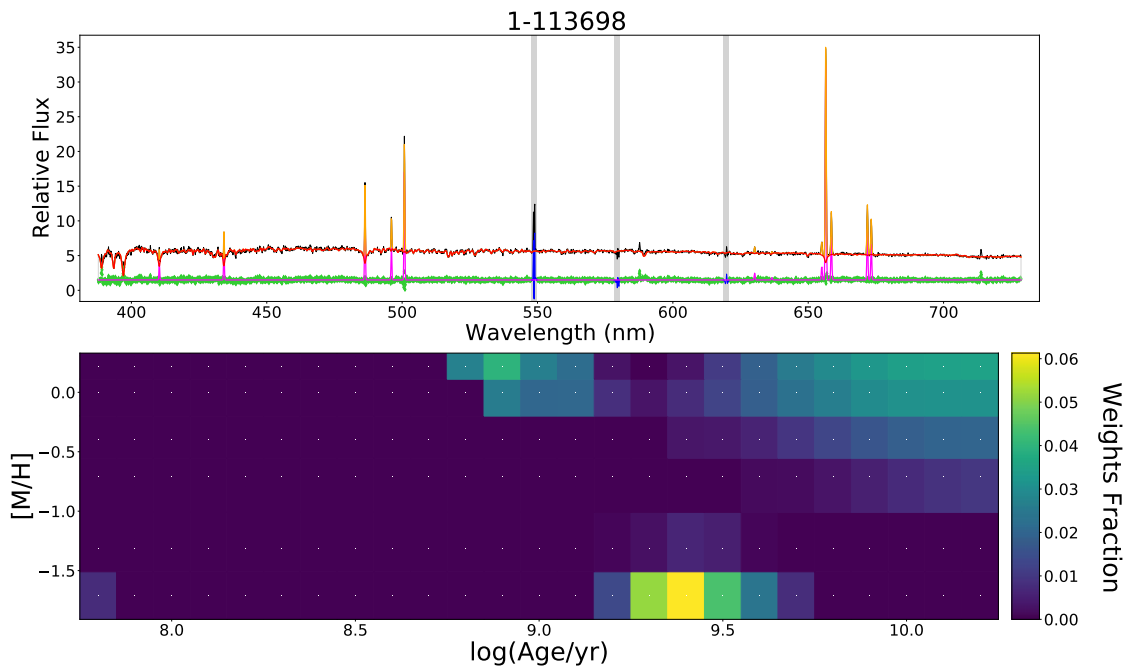
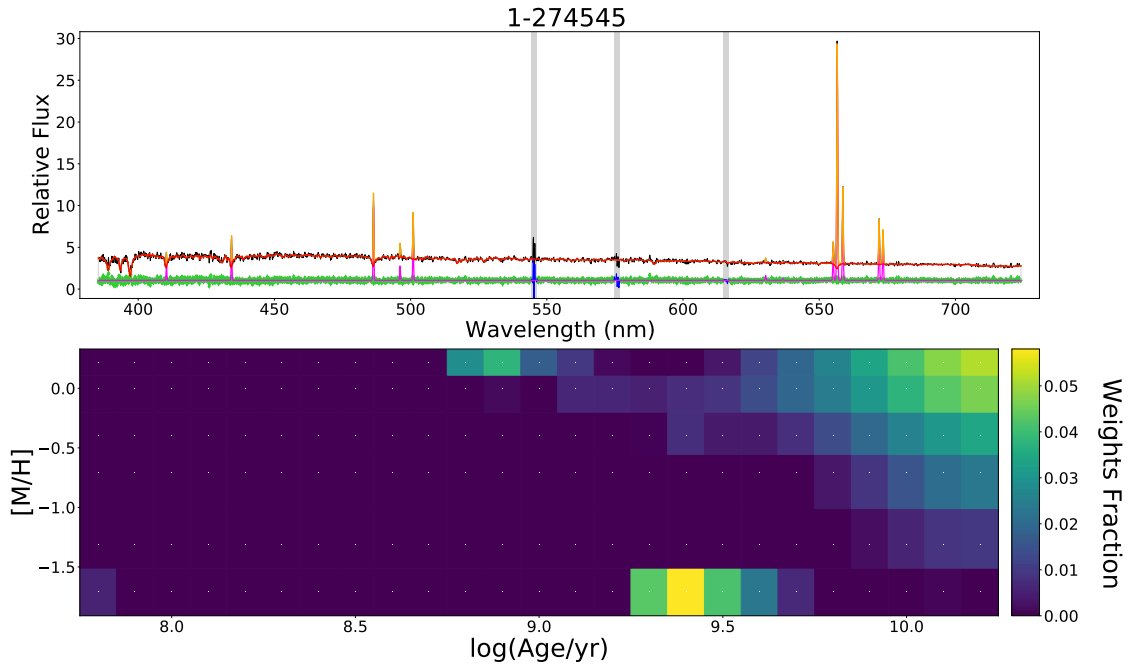
Stellar Population weights maps from regularized fits

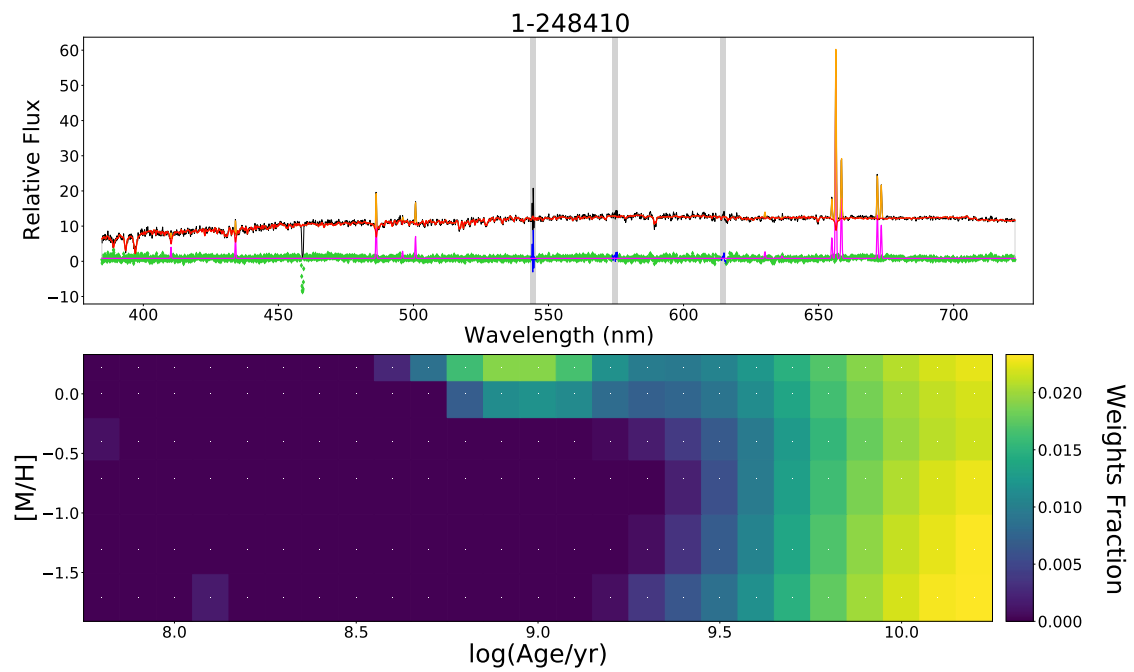
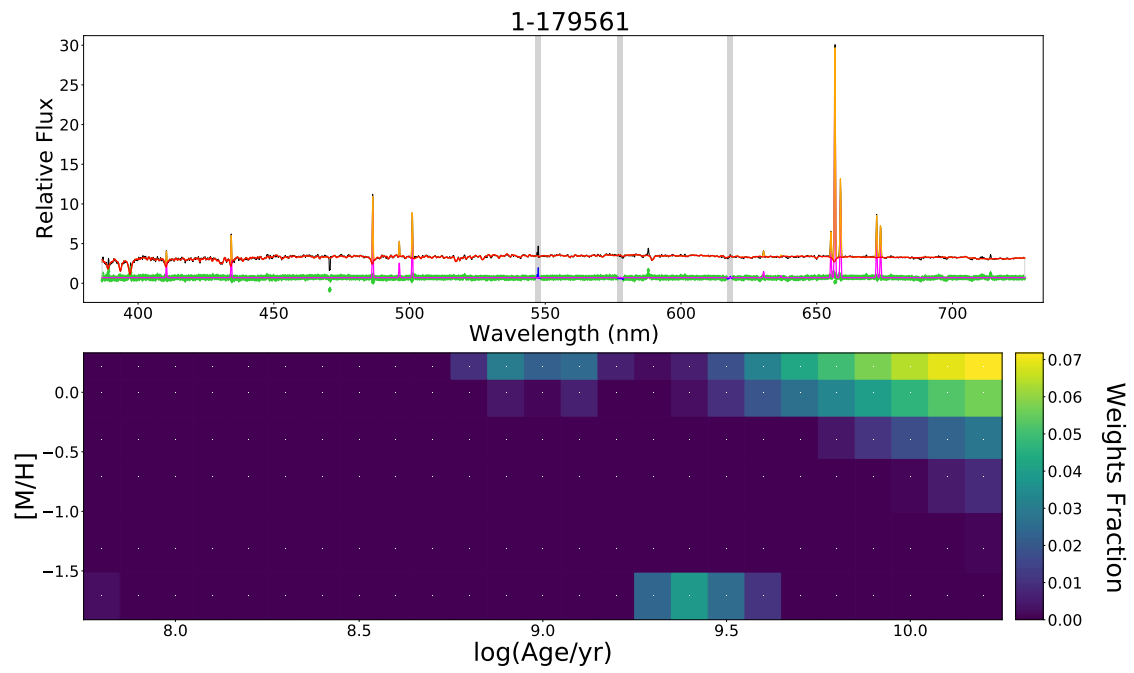
Here we show the weights fraction maps from regularized fits. The fitting procedure is described in section 4.3.1. Maps can show unimodality or multimodality; some maps appear unclear: these are maps where either the fits are not good or the smoothing is too high or the weights distribution is elongated (not a single blob nor two distinct blobs). We extracted maps for ~ 10 -20 bins per galaxy; here we show only one map per galaxy. Together with the weight maps, we plot the corresponding fits. There are twenty-eight galaxies showing unimodality, thirteen galaxies showing multimodality and twelve unclear maps.

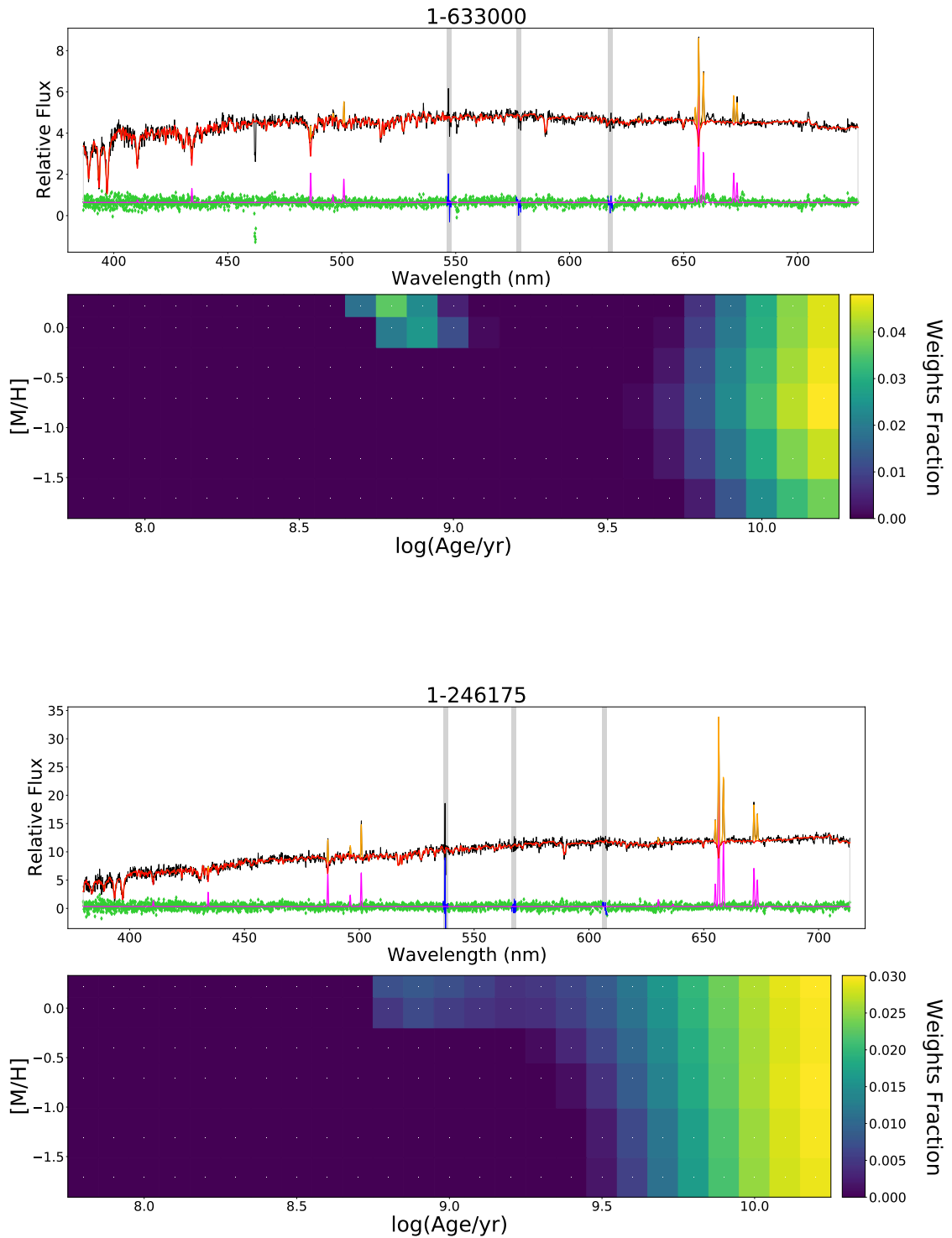
Figure D.1: **Spectrum and weights fraction map of the regularized fit.** *Upper panel:* fitted spectrum of the regularized fit; the black spectrum is the observed spectrum, while the red one is the best-fit spectrum; the green dots are the residuals; the grey columns correspond to the masked spectral regions; the yellow lines correspond the gas emission lines. *Lower panel:* weights fractions relative to the MIUSCAT SSP models used for the fit; each white dot represent age and metallicity of an SSP.

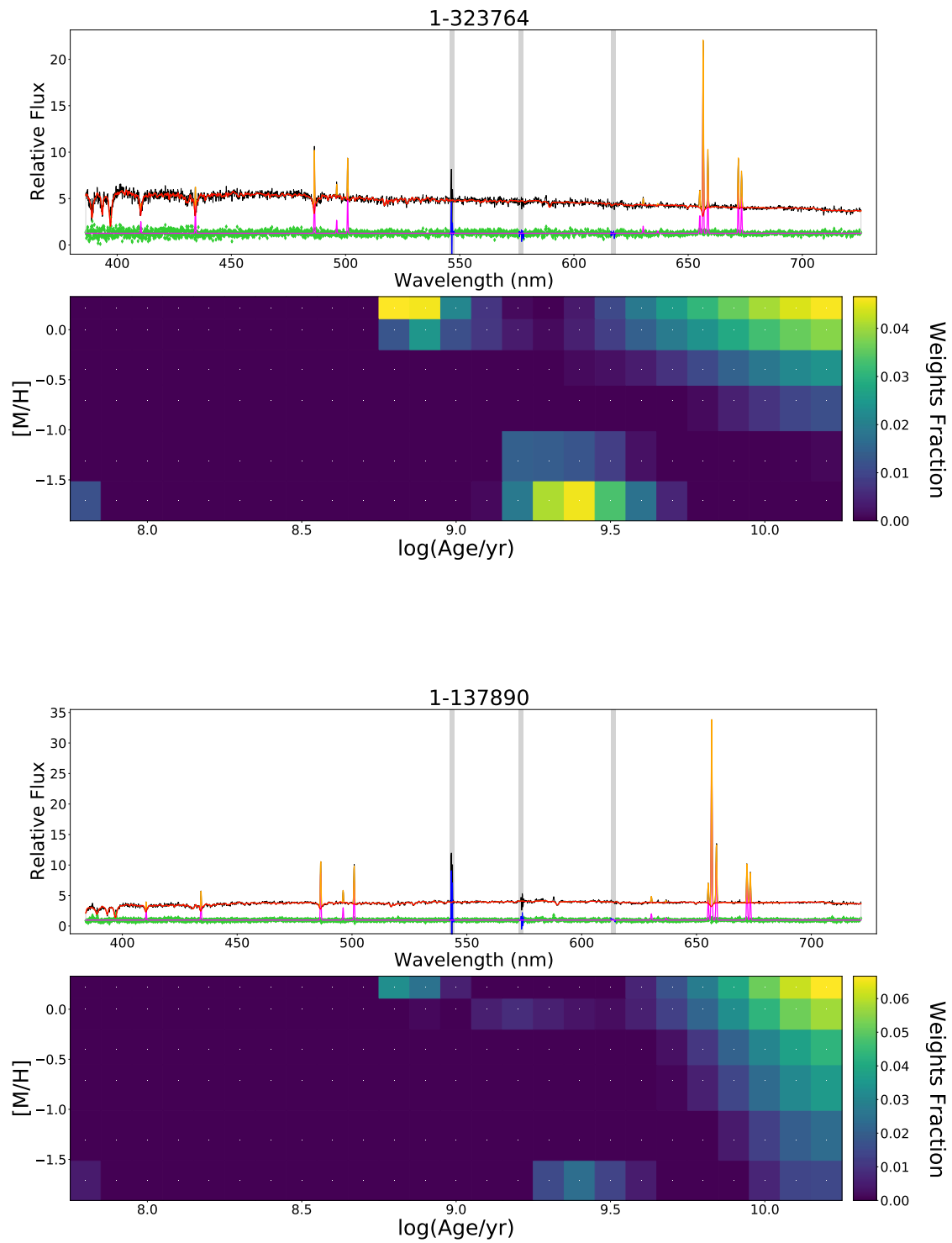


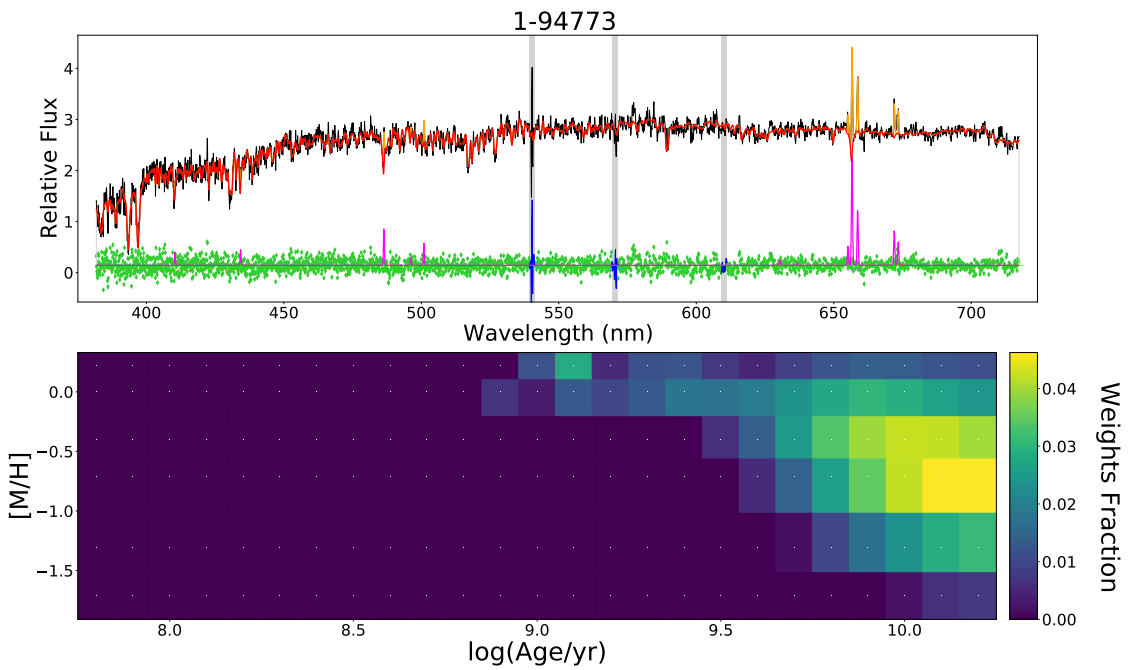
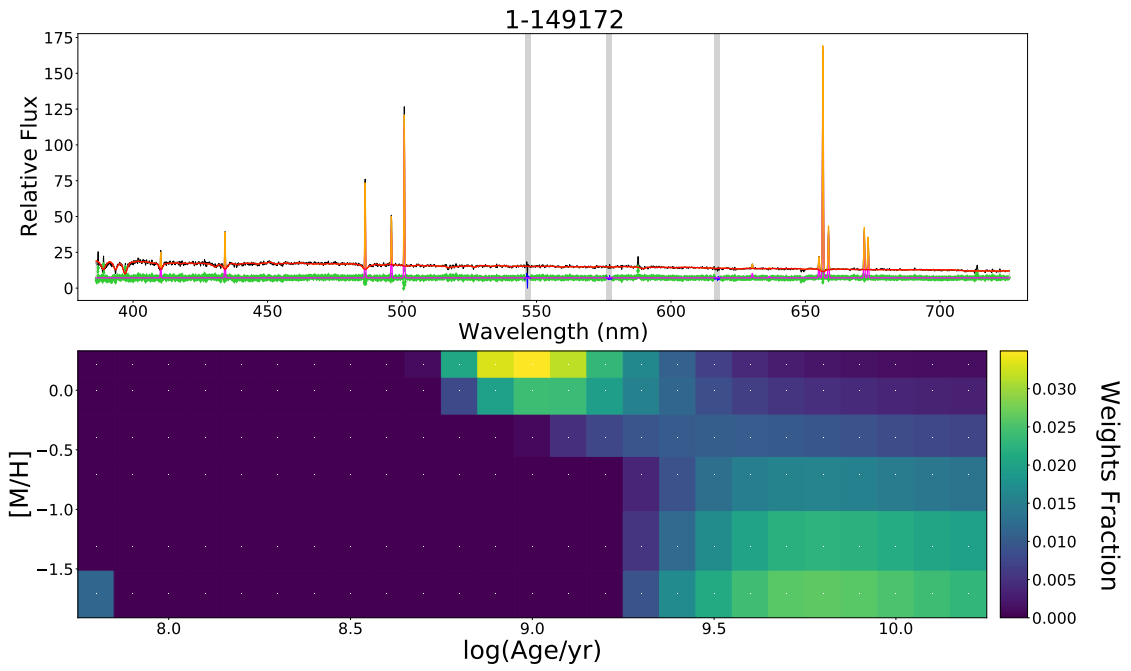


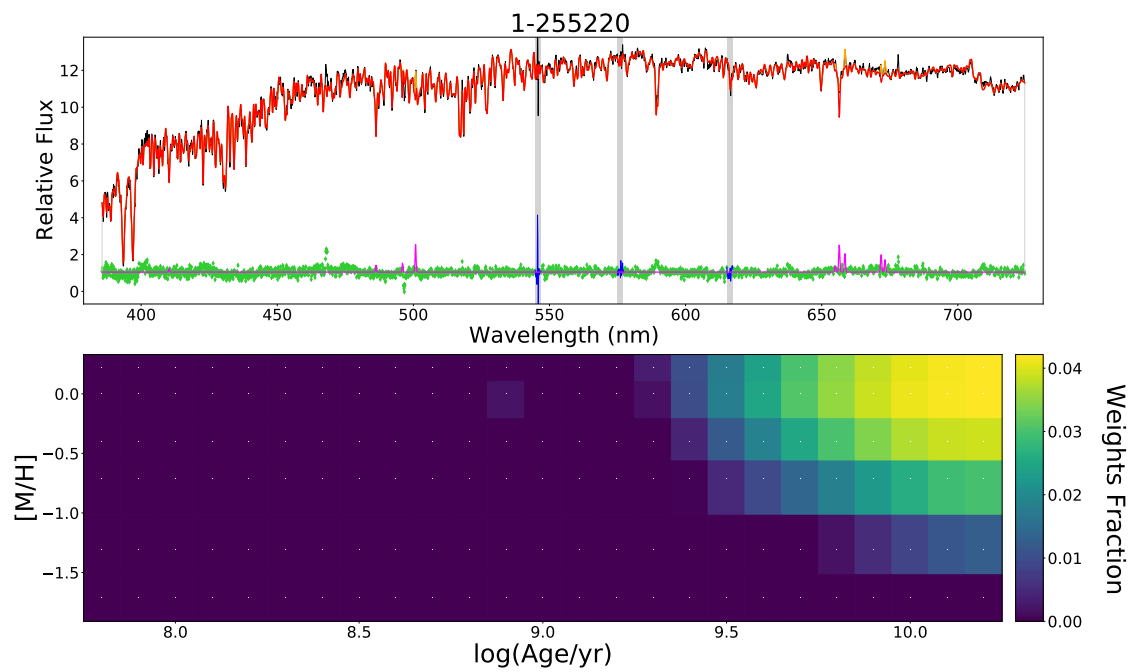
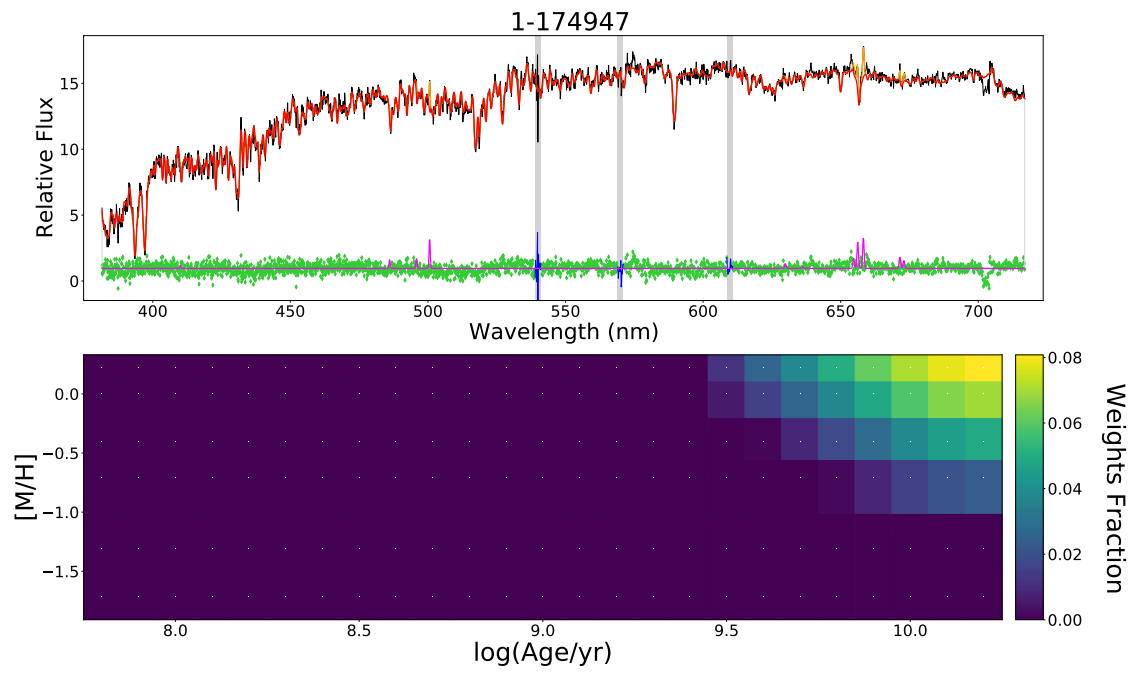


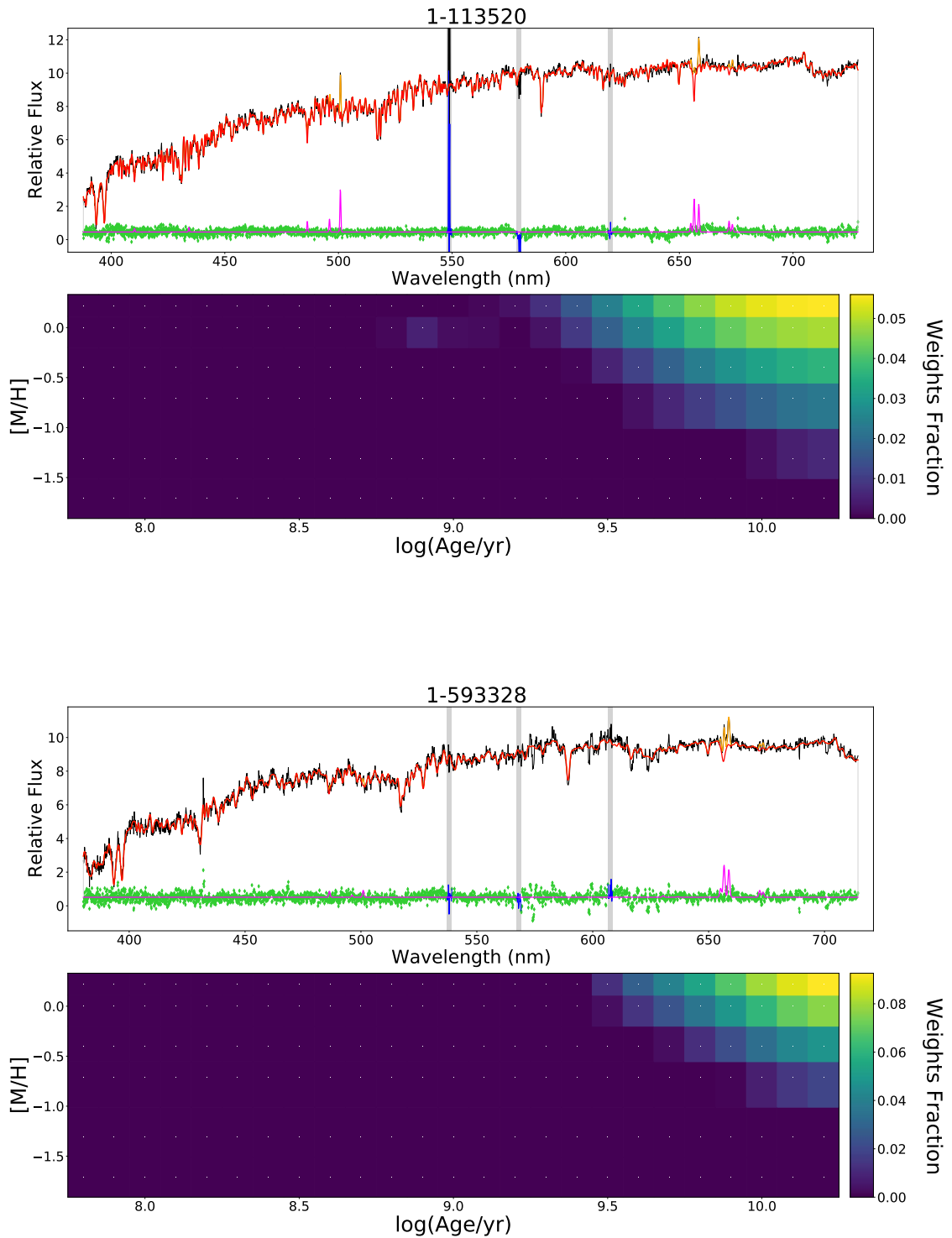


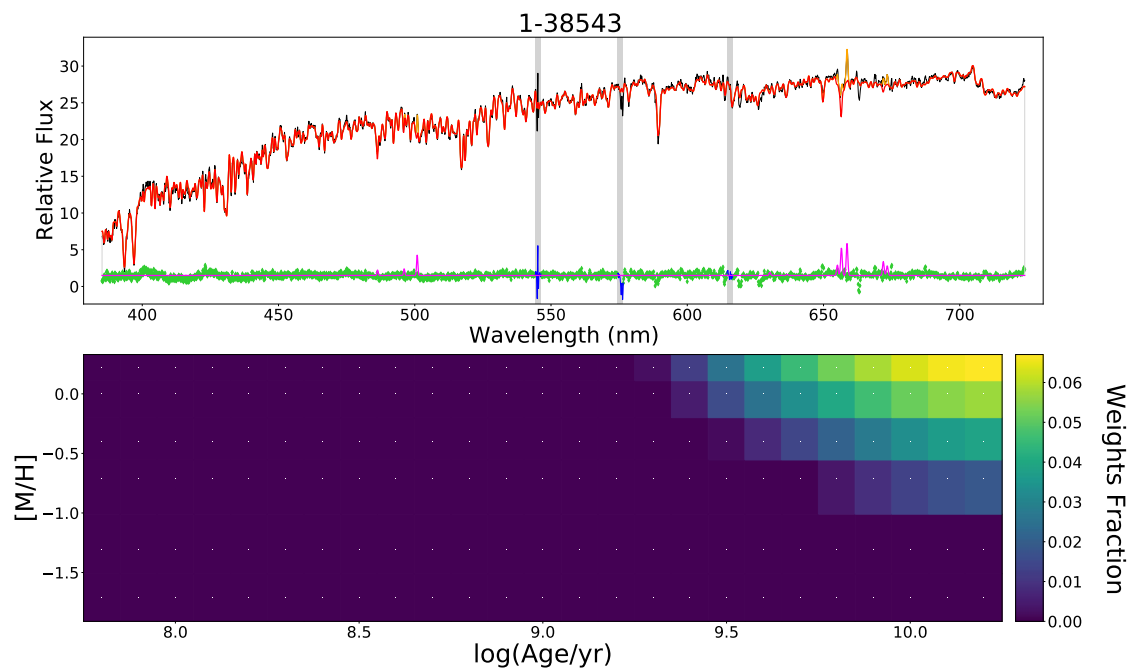
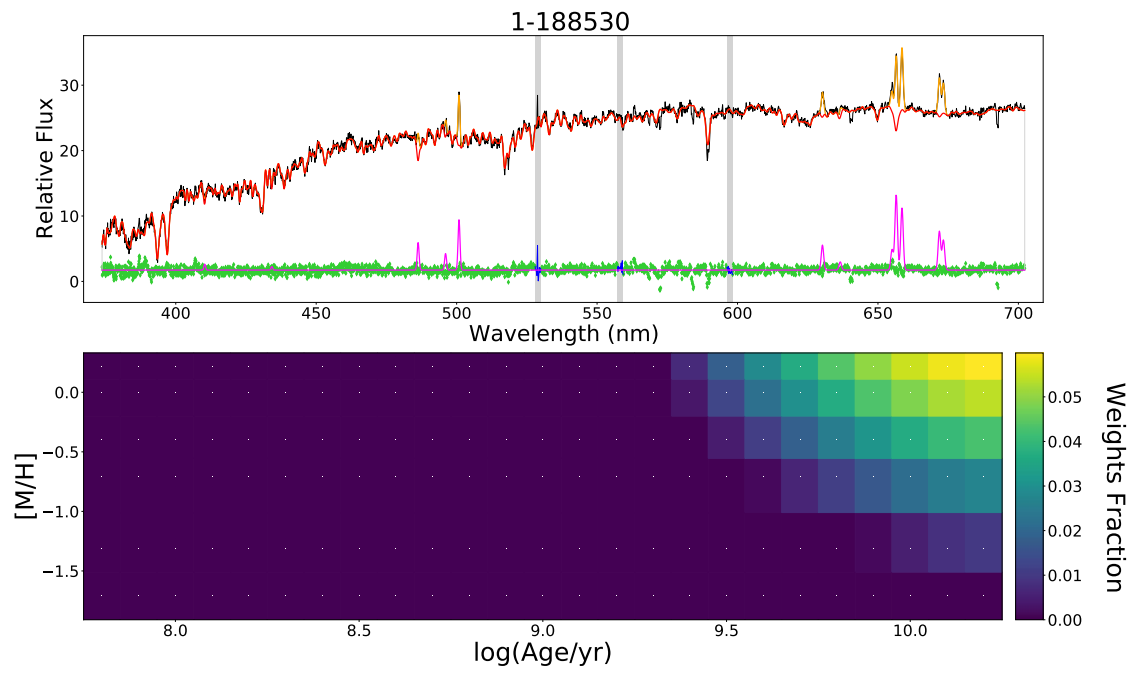


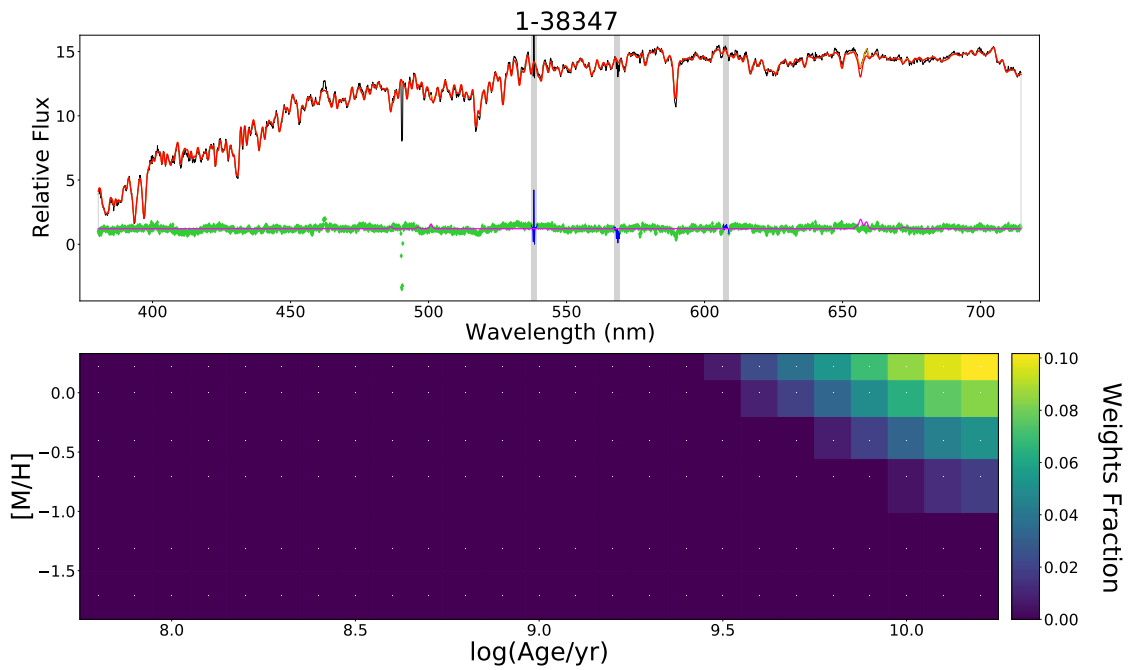
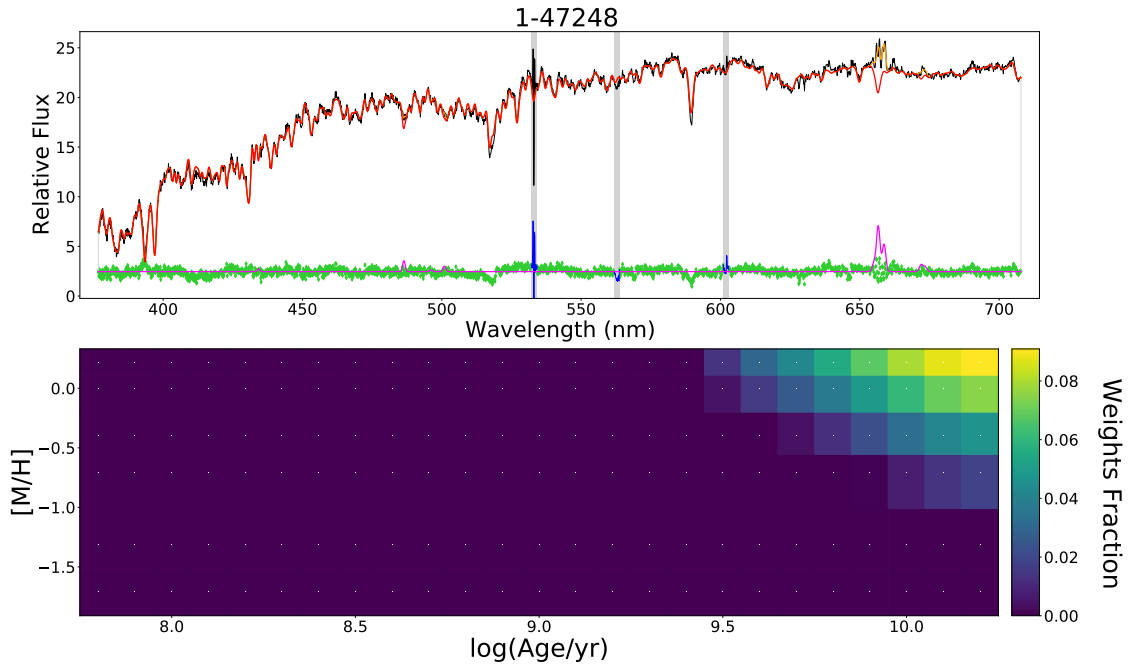


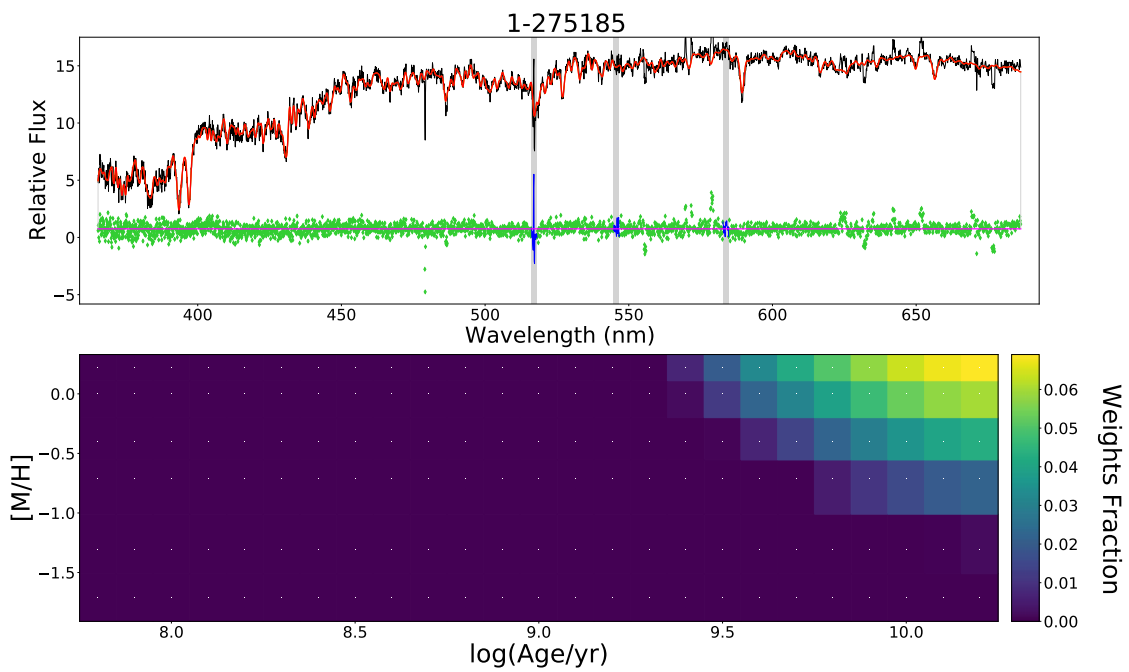
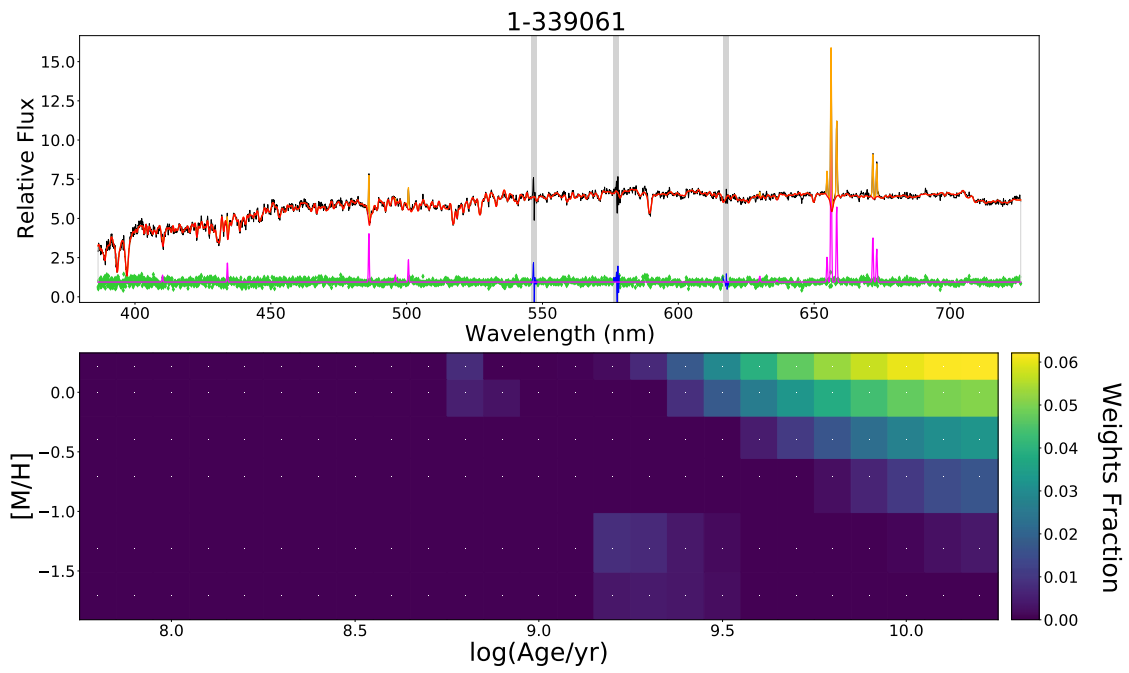


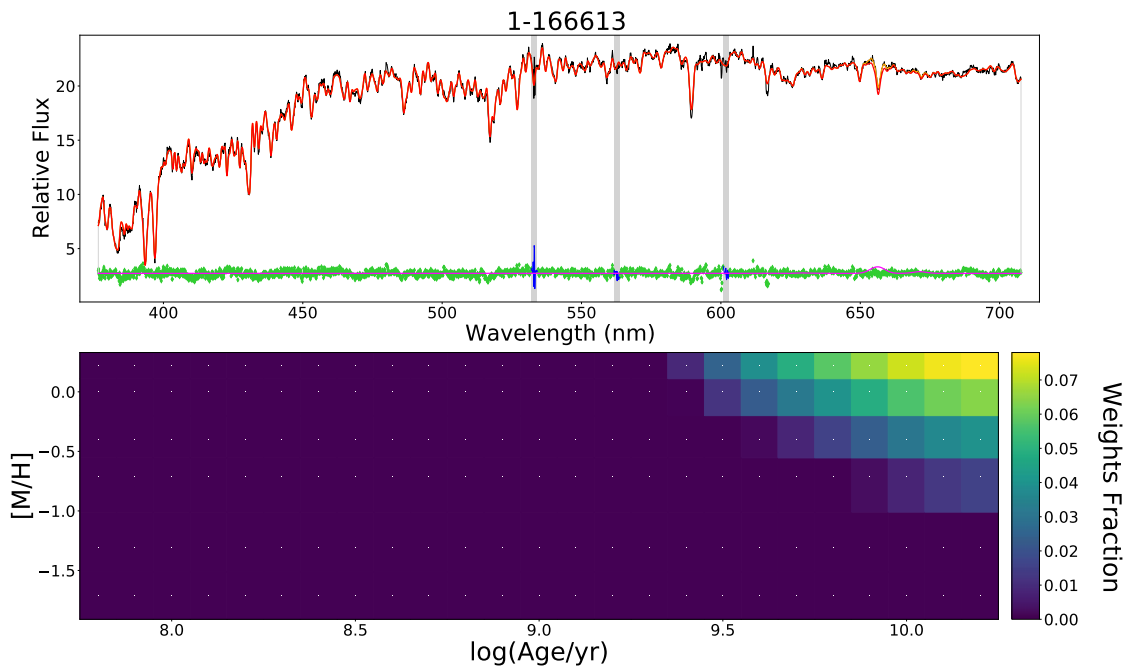
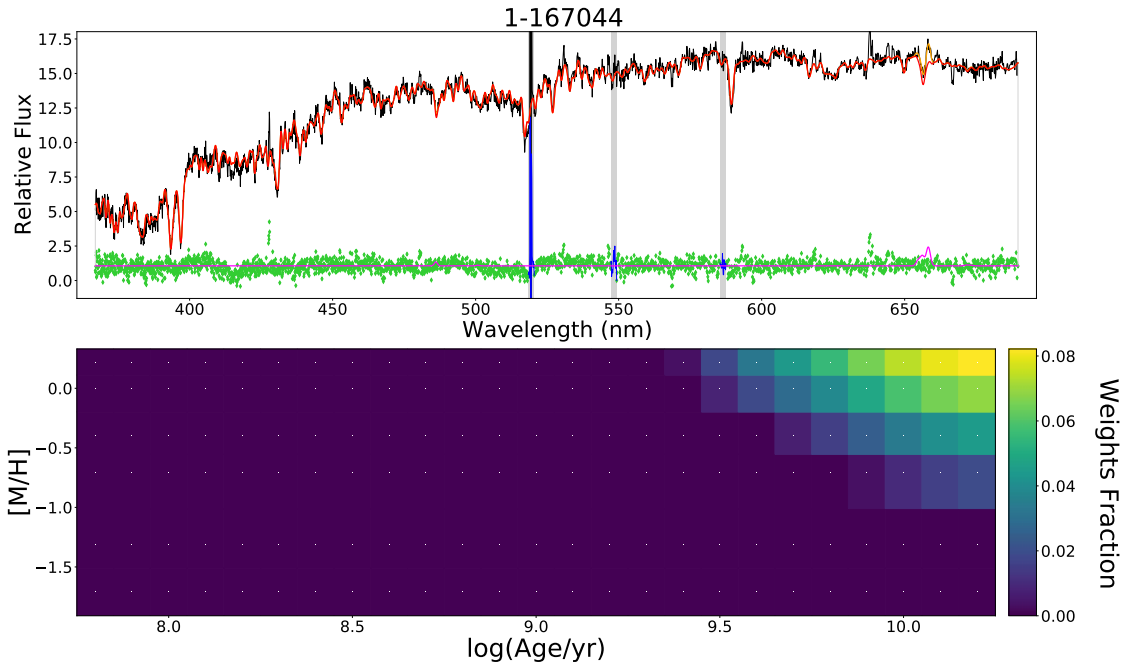


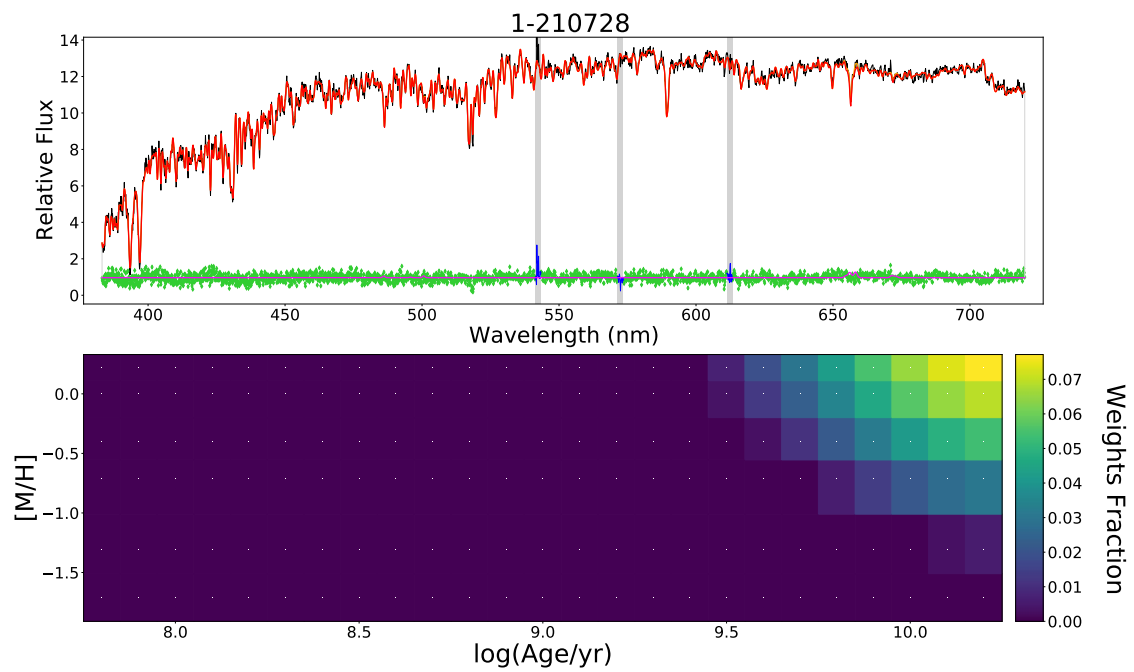
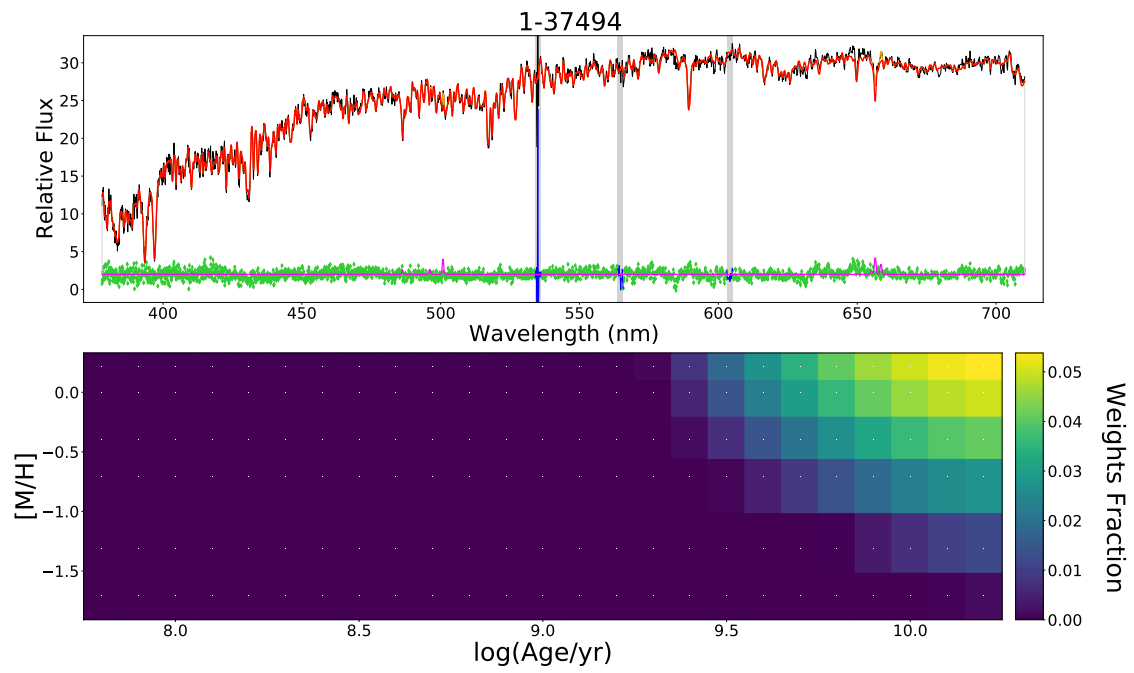


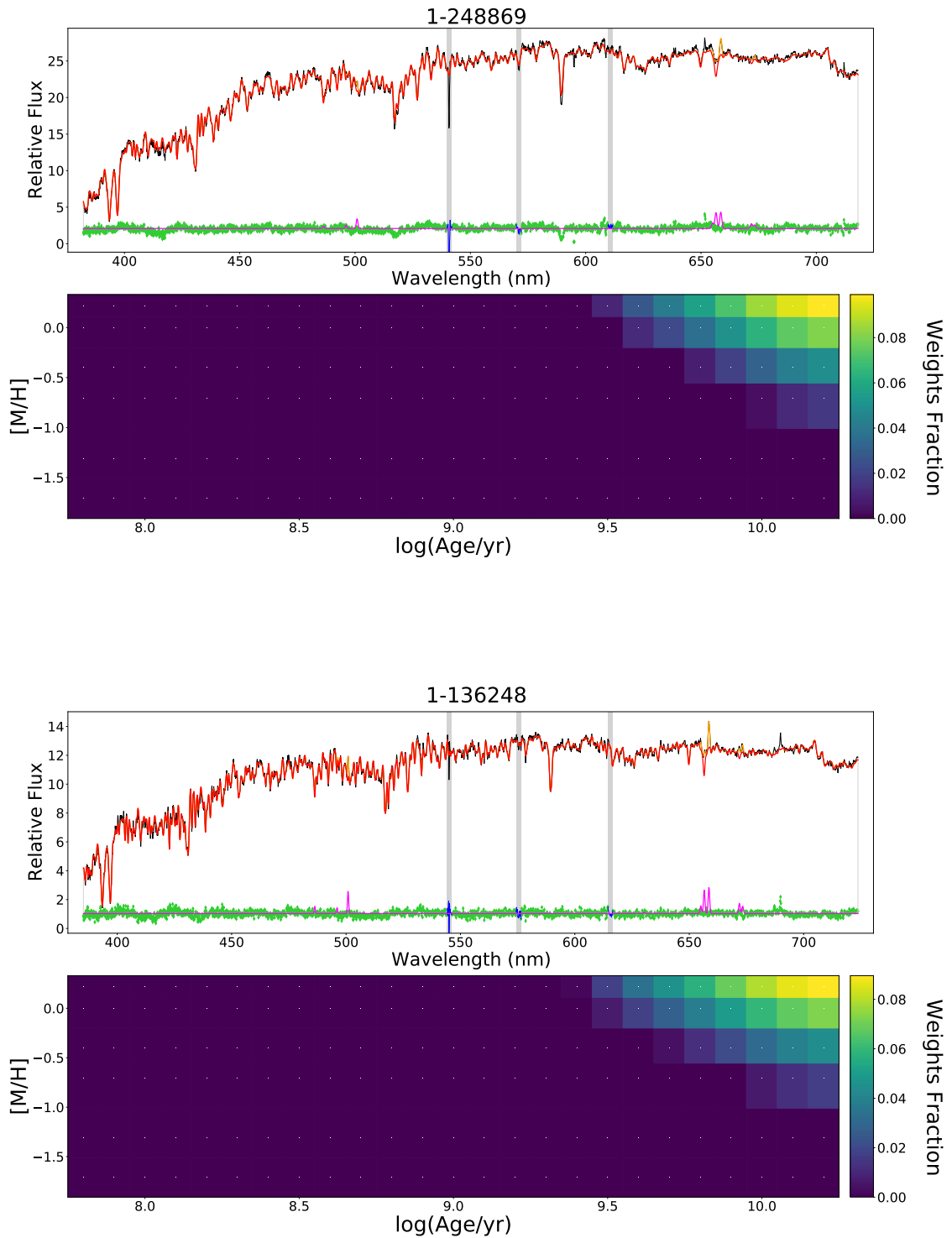


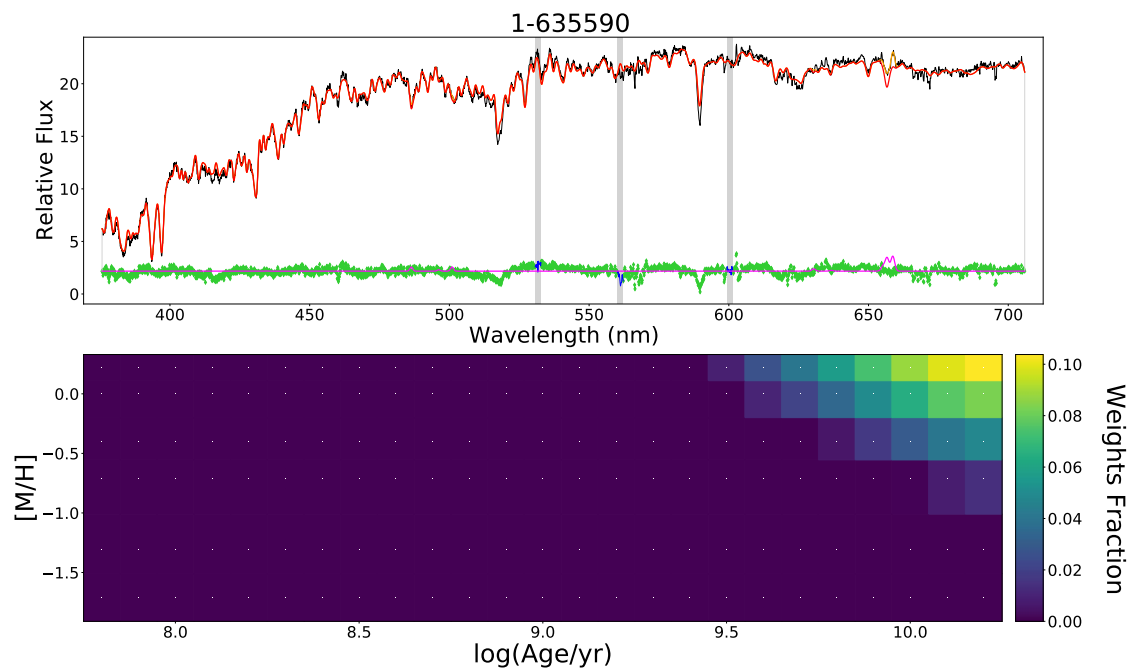
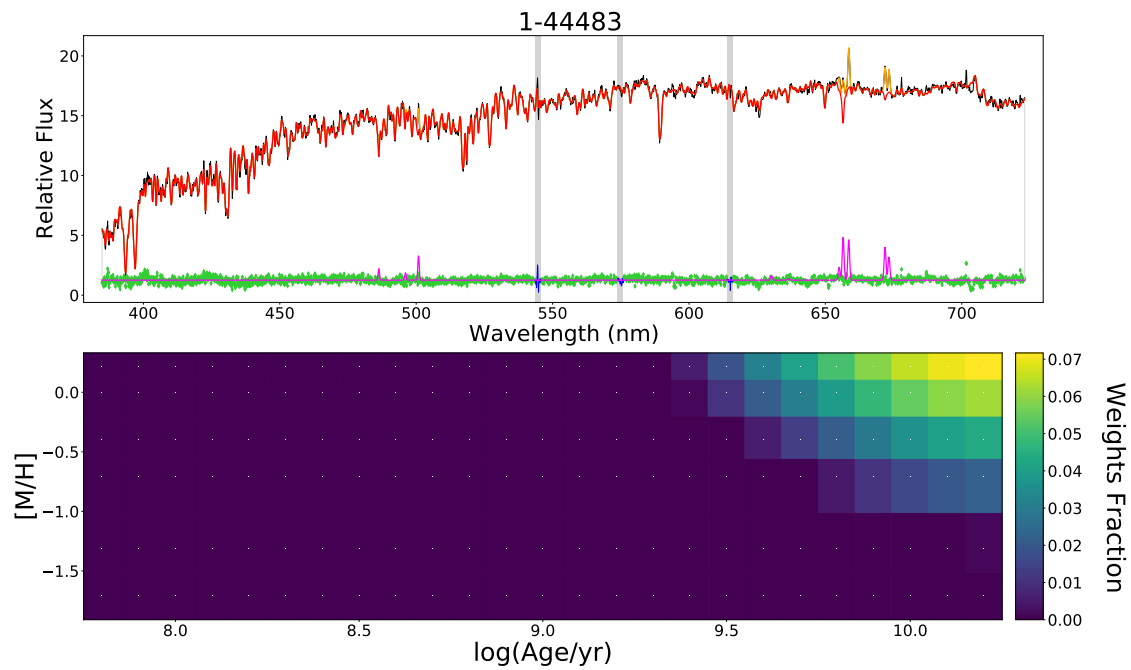


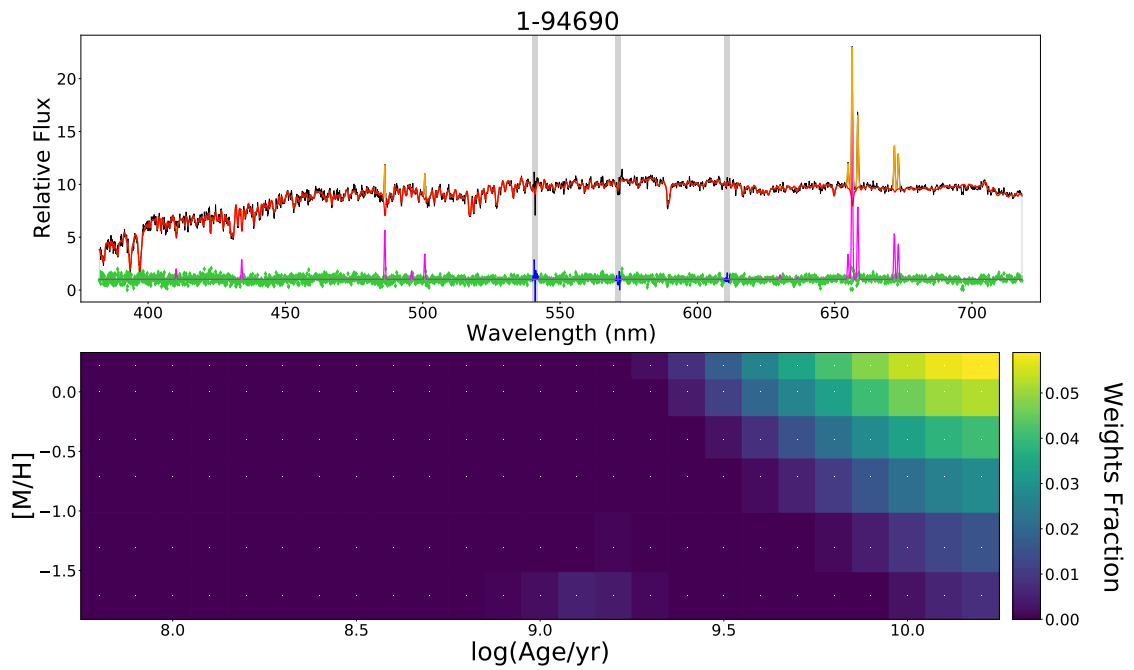
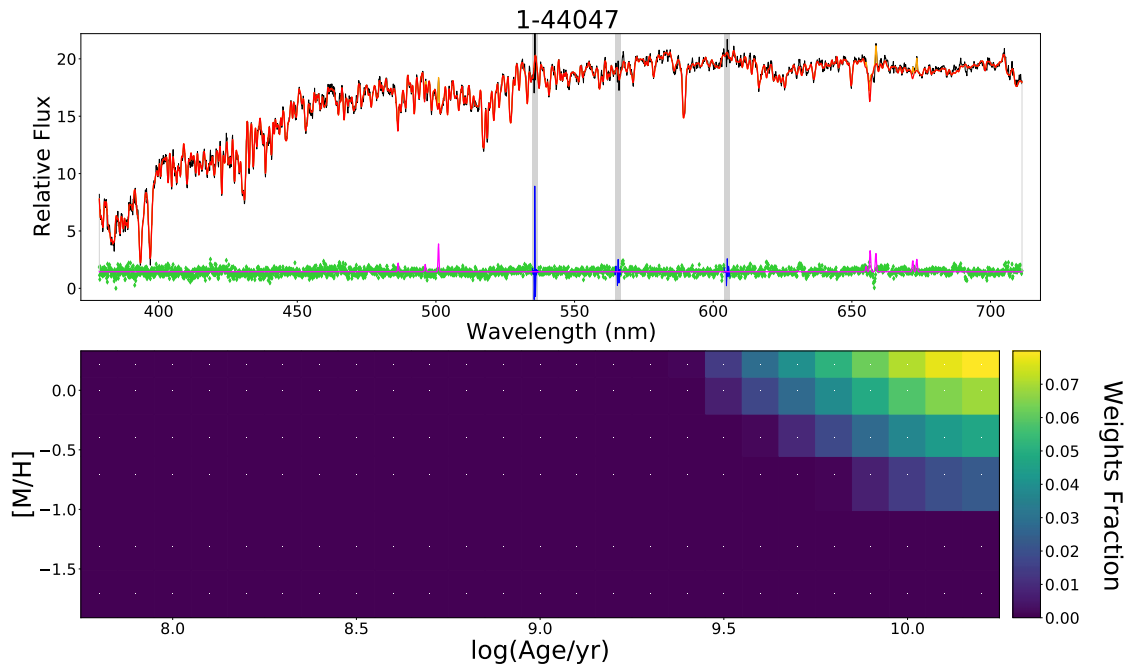


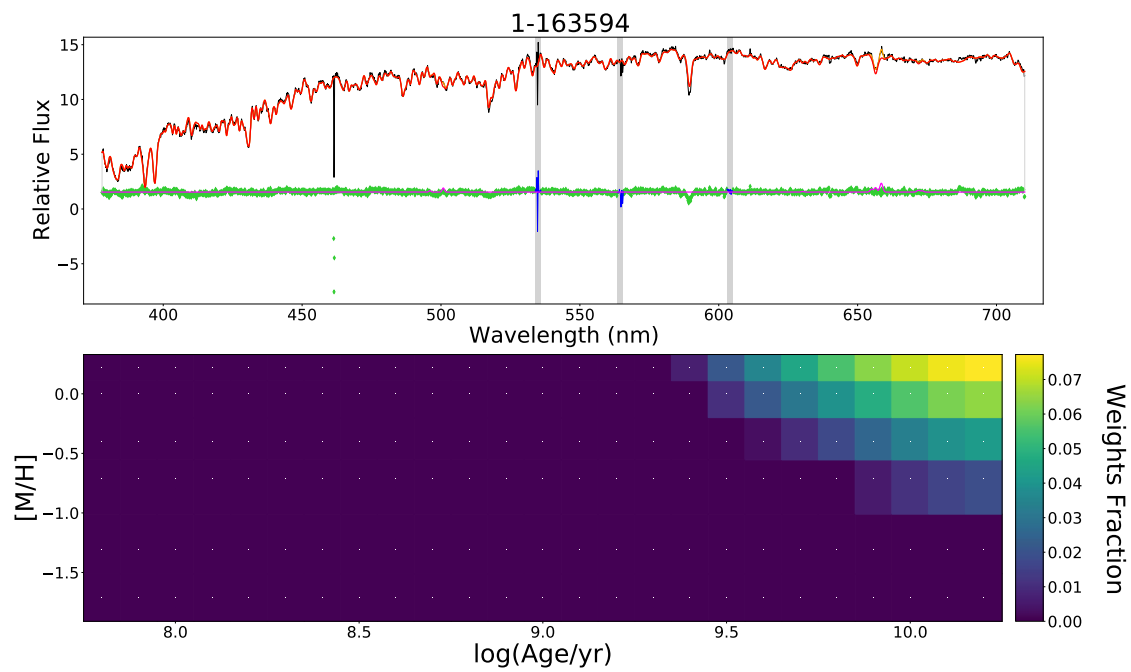
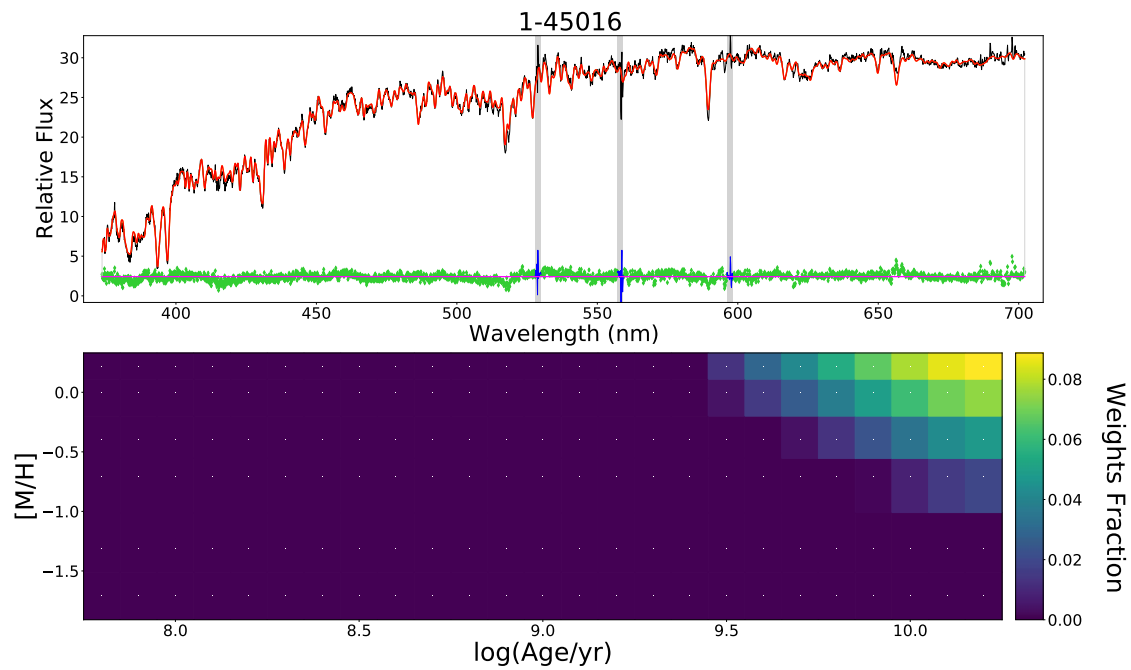


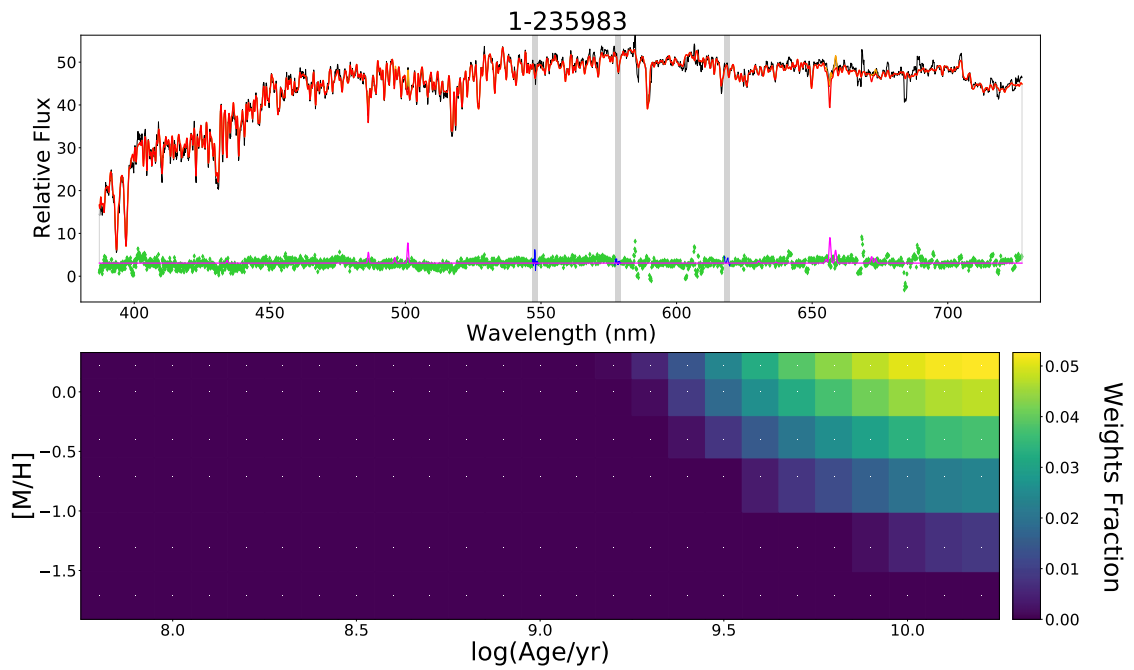
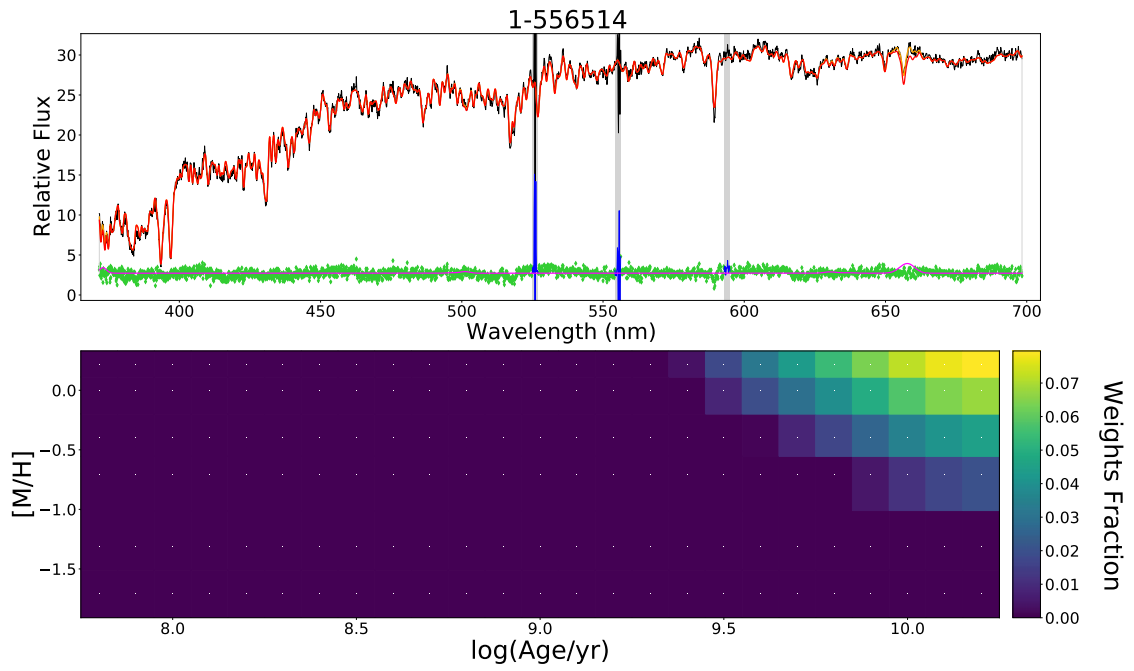


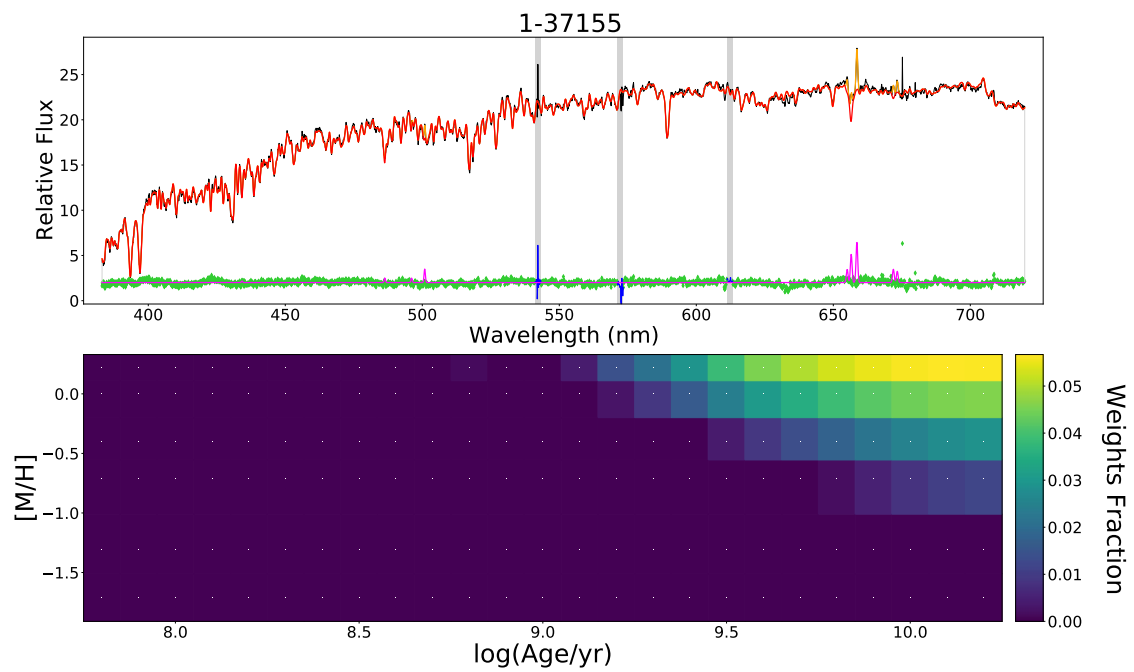
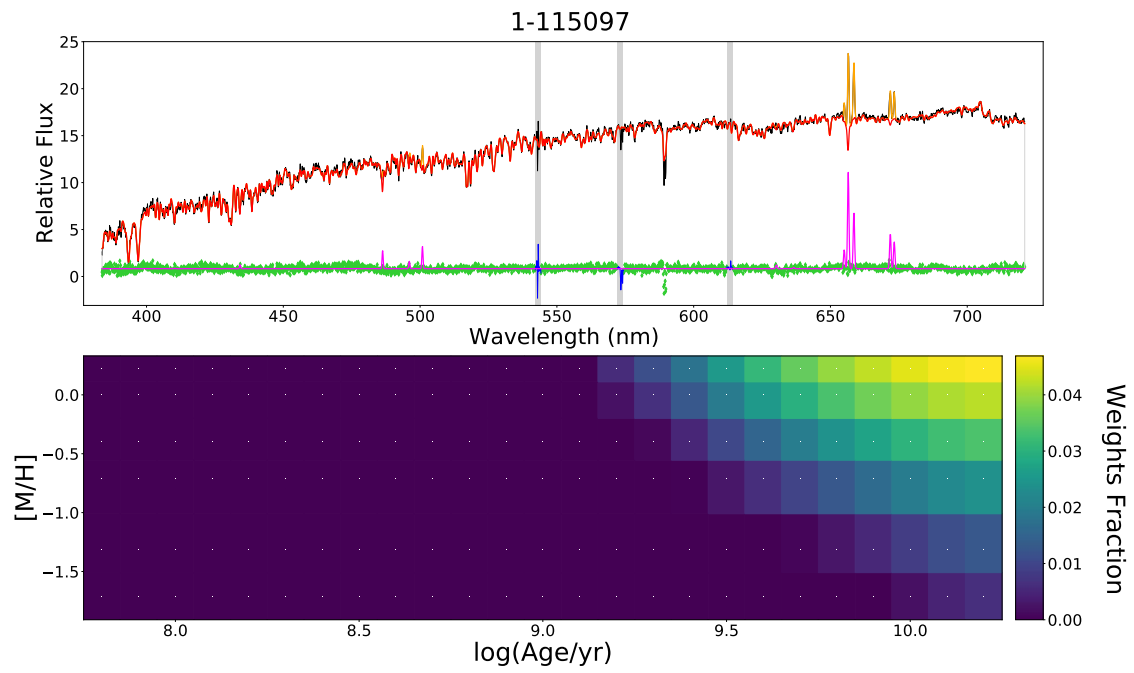


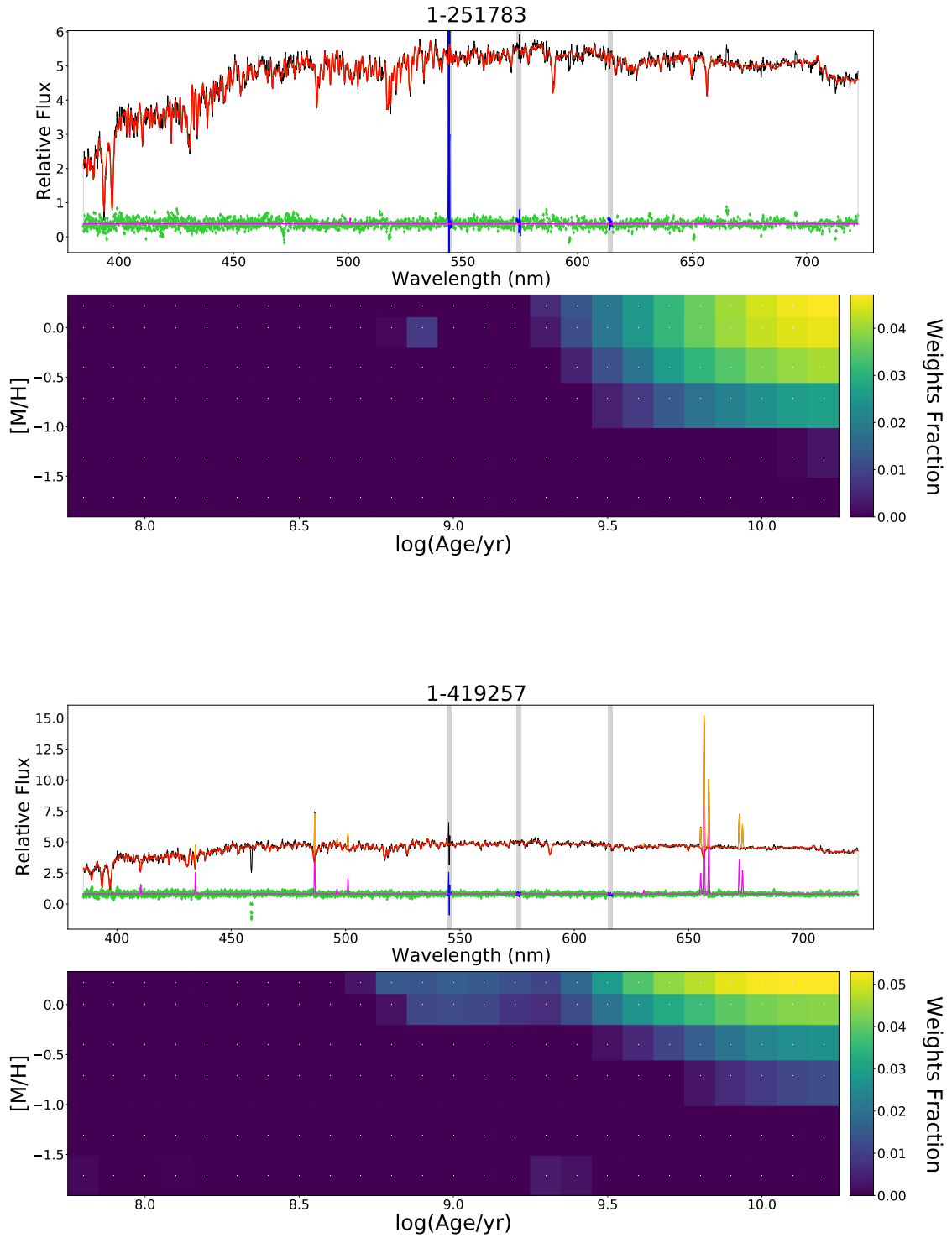


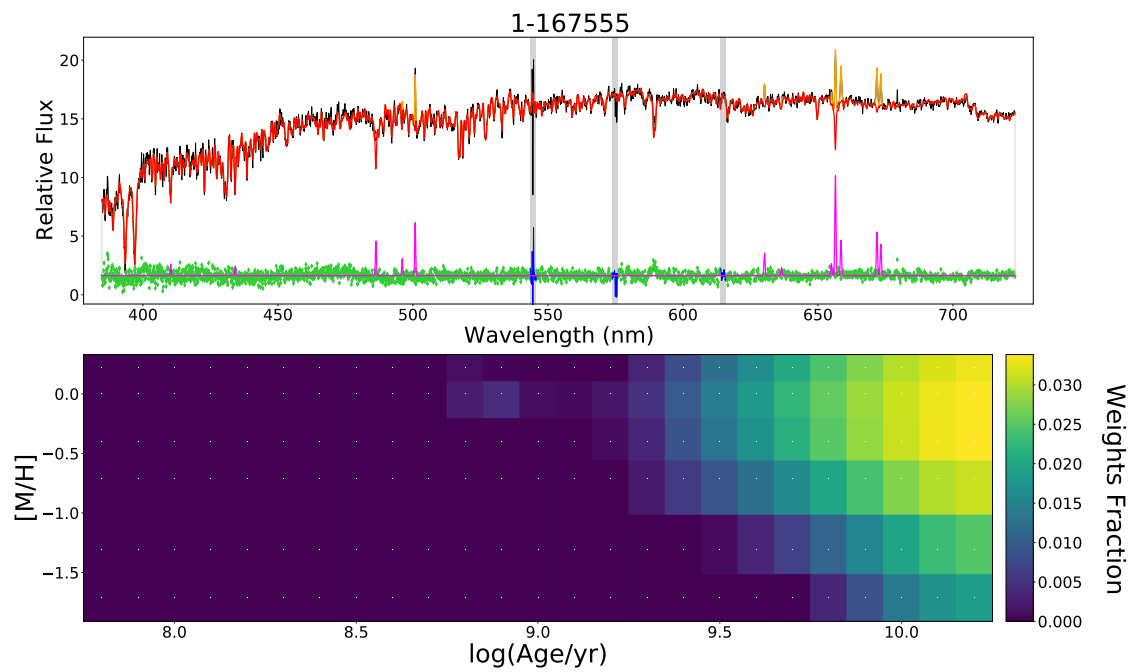
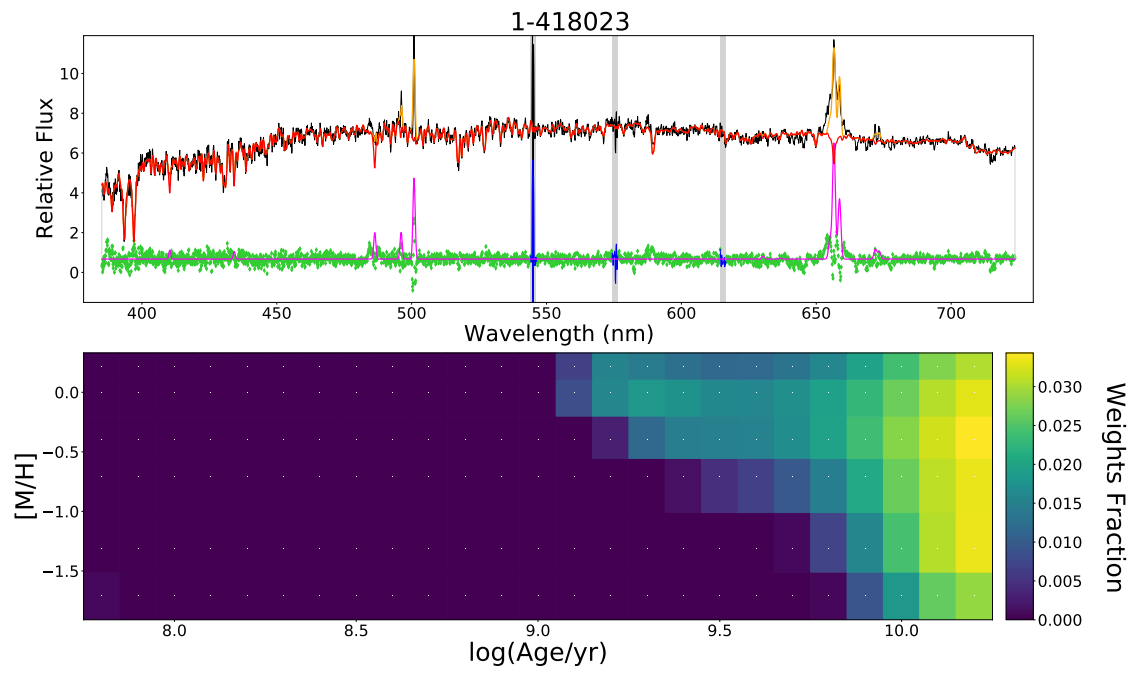


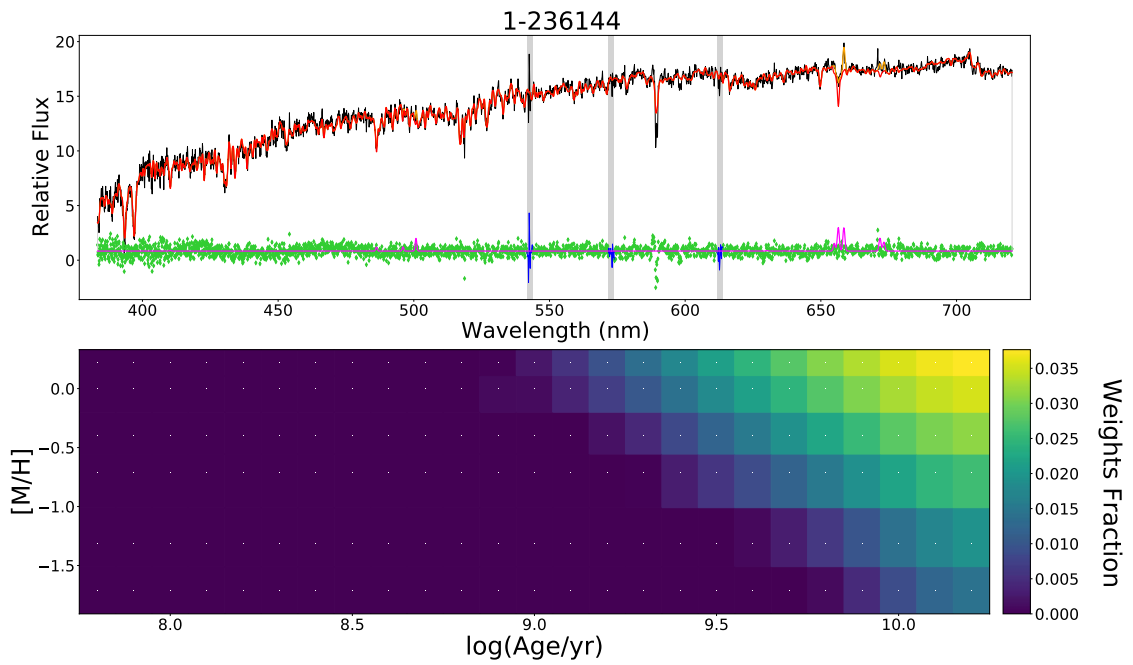
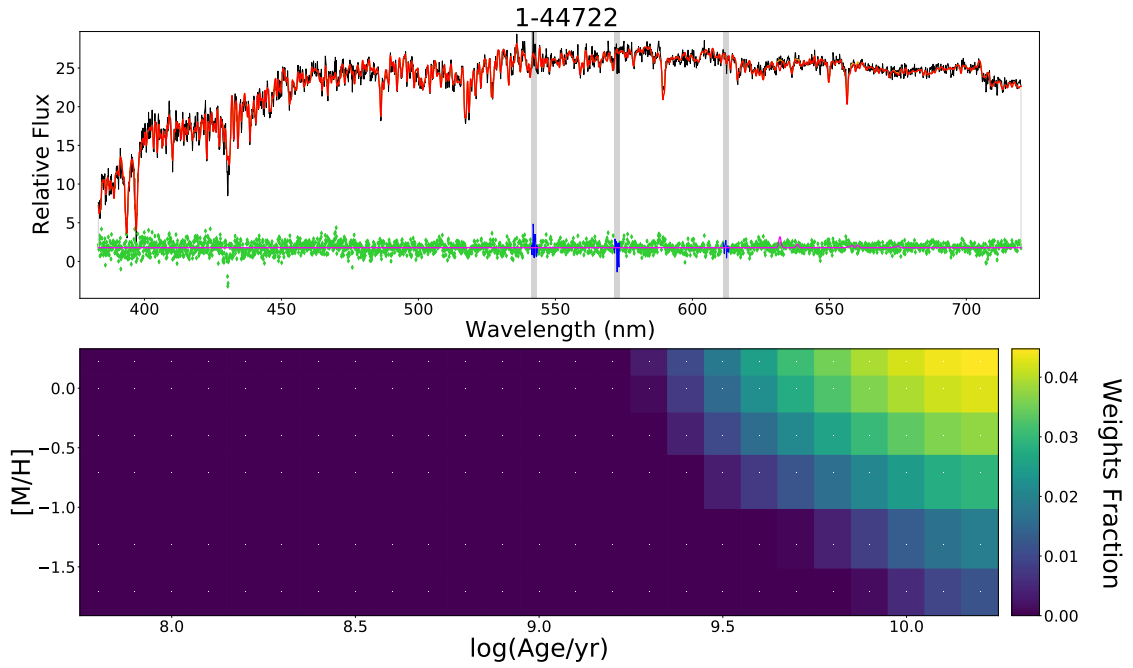


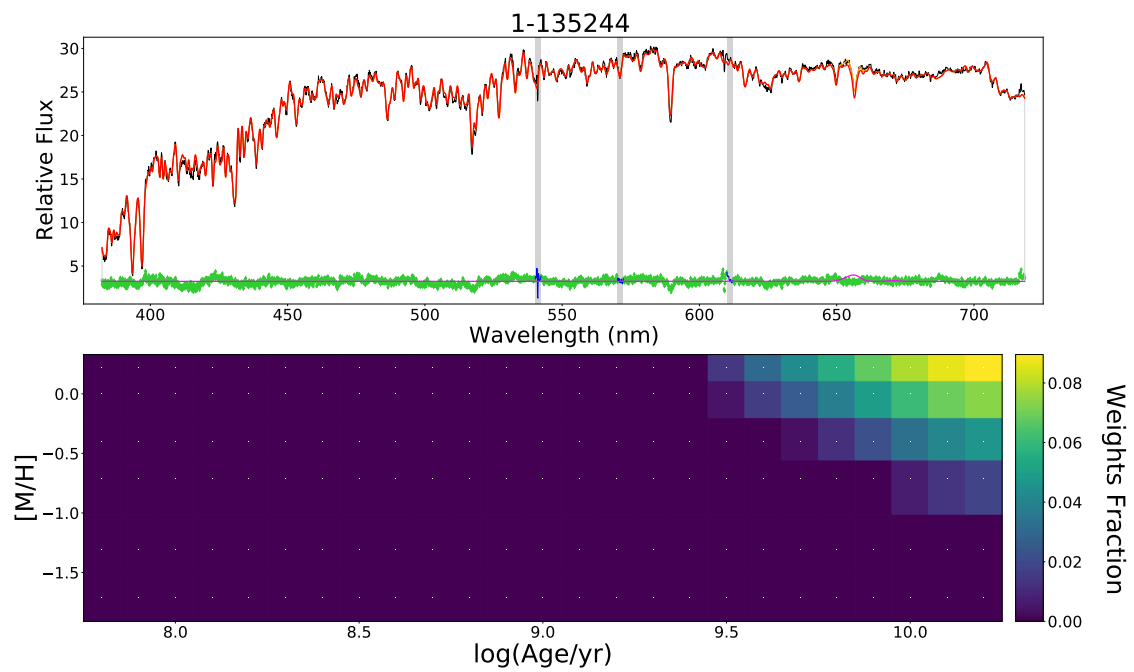
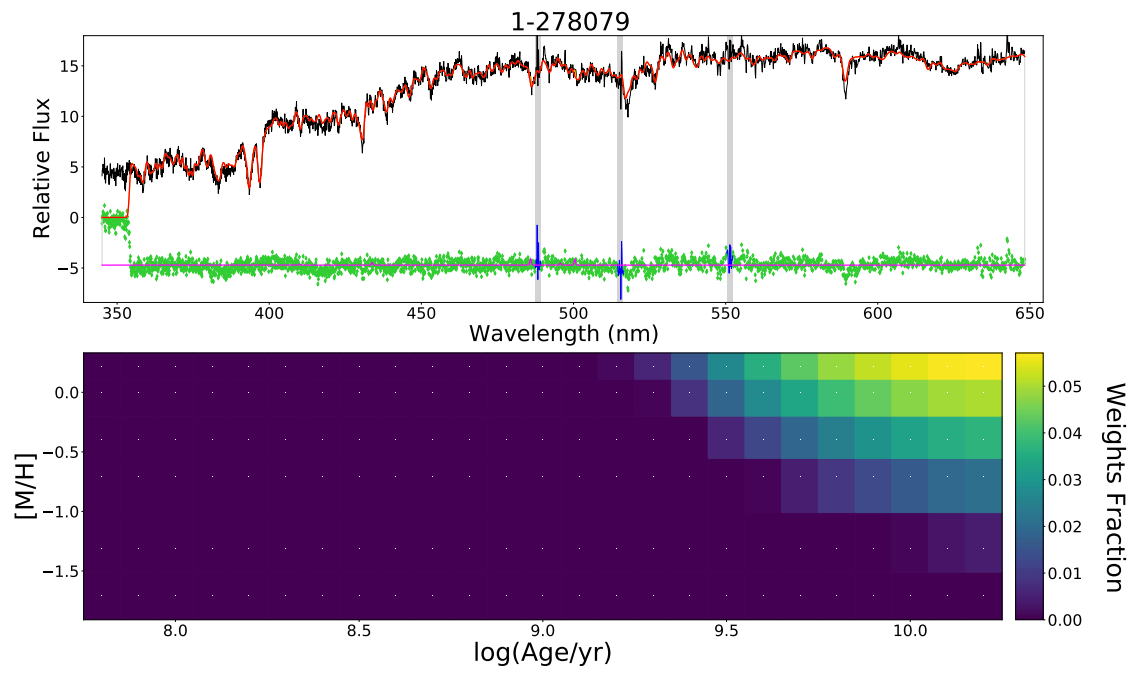


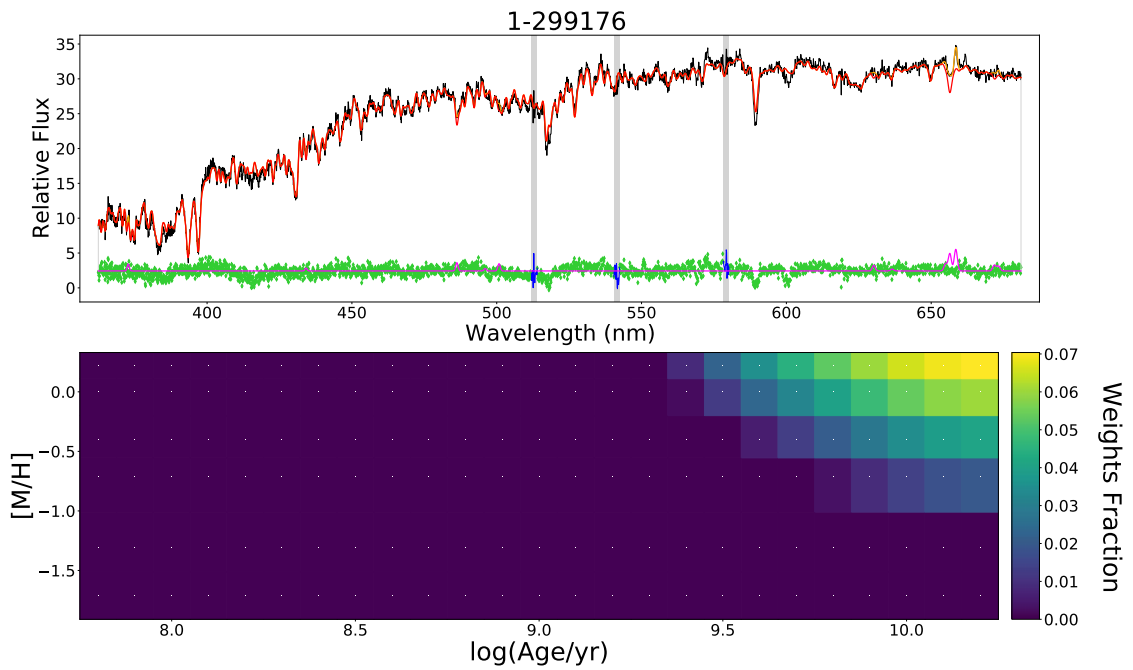
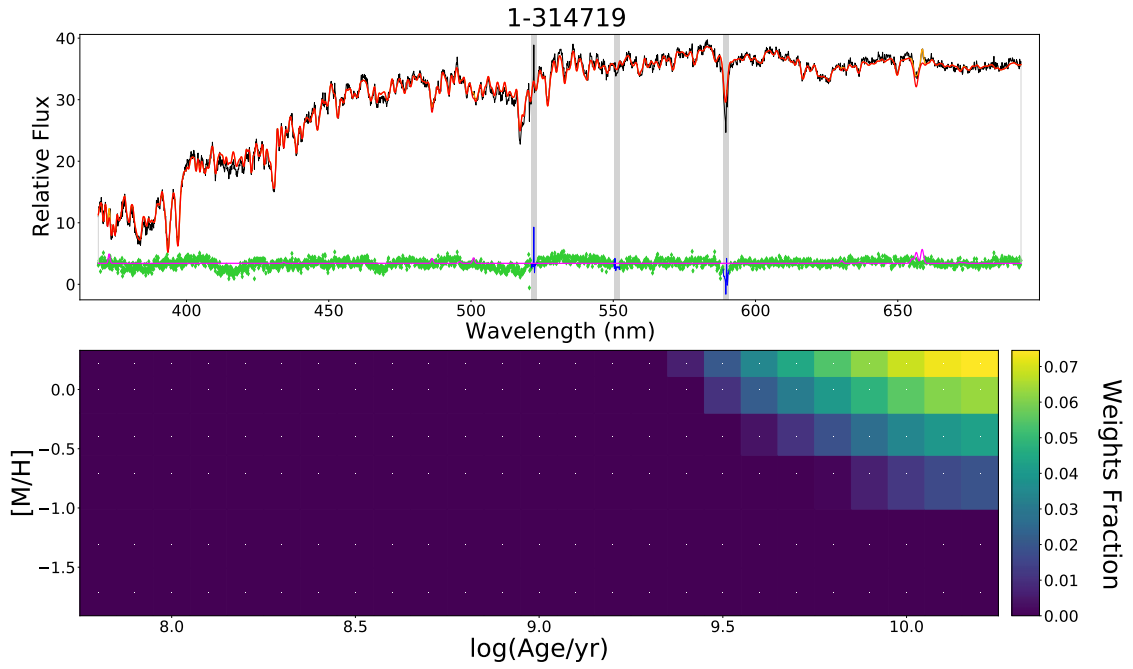


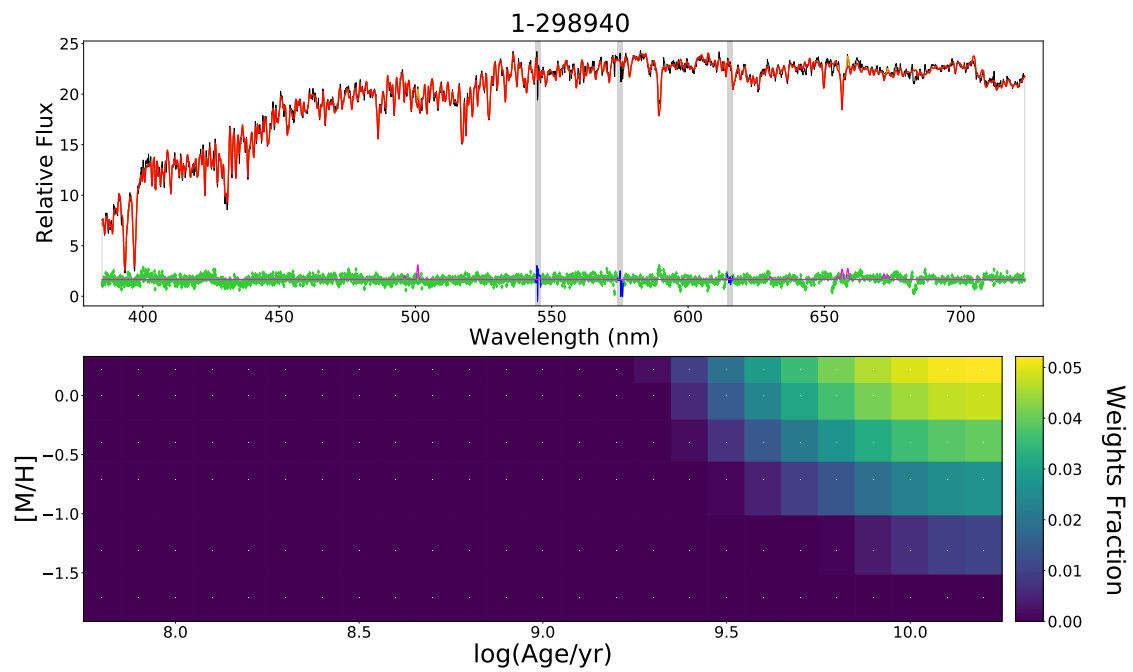
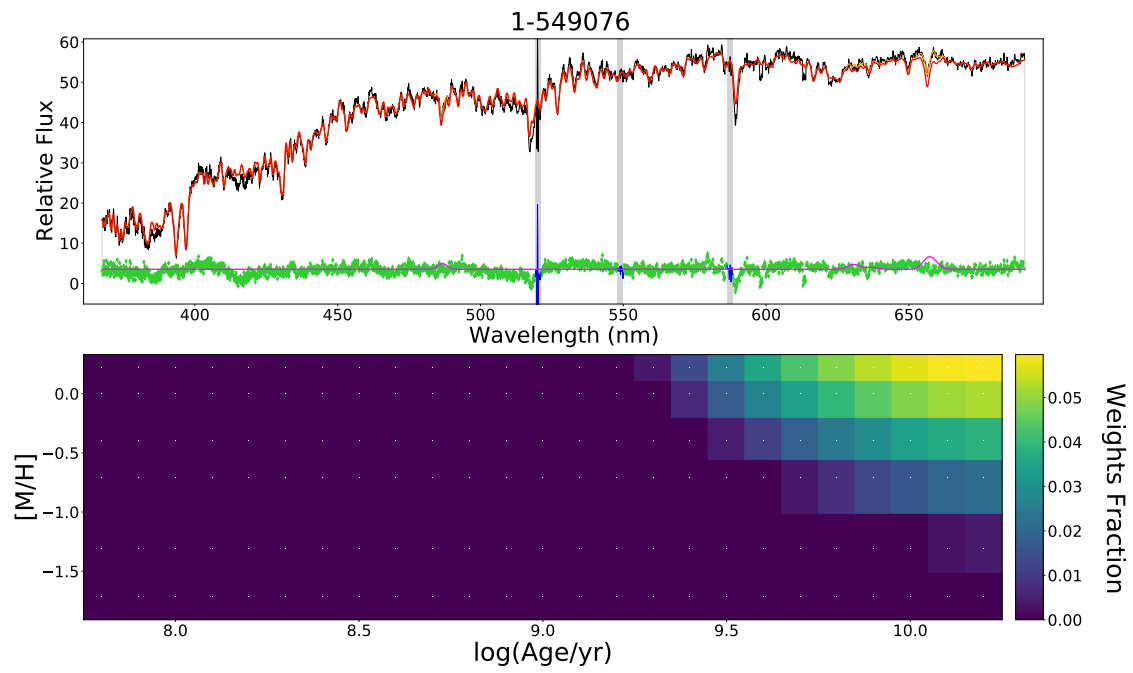


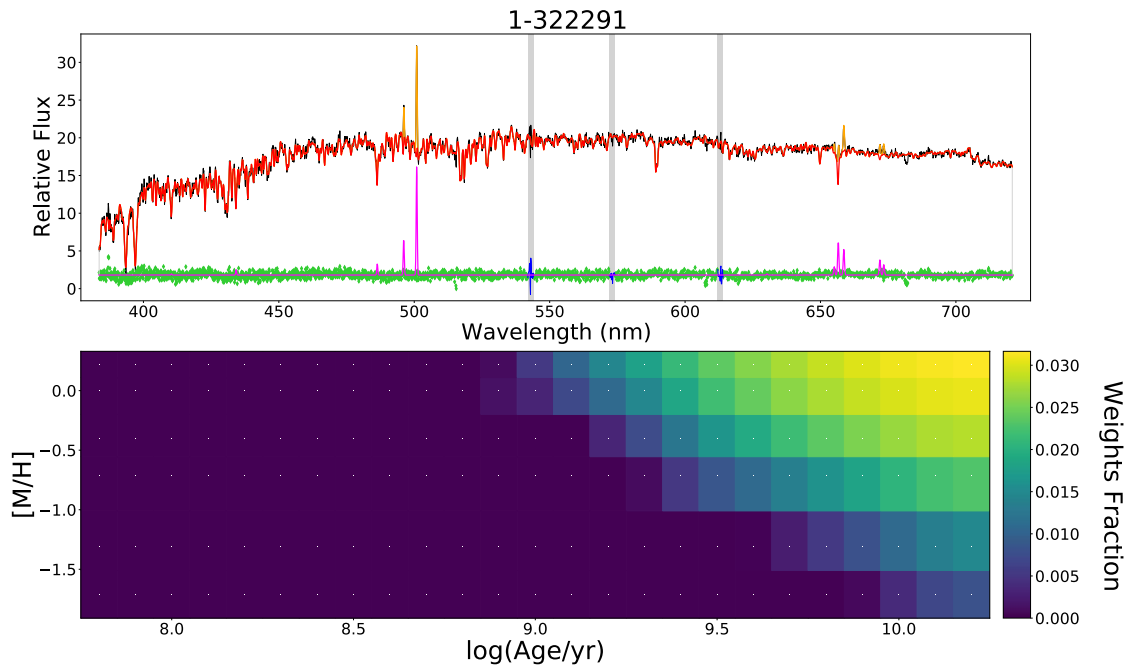












Aknowledgements

I would like to express my sincere gratitude to my supervisor, professor Silvia Pellegrini, for all the support and the encouragement she gave me throughout this thesis project; I learnt a lot under her guidance, and she gave me many causes for reflection for which I am grateful.

I am deeply thankful to my co-supervisor, professor Michele Cappellari, for appreciating my enthusiasm about this project, for his constant guidance and care along these months, and for continuously stimulating and supporting me.

This thesis work would not have been possible without the endless backing of J.S. Bach, P. I. Čajkovskij, S. Rachmaninoff, D. Šostakovič, L. van Beethoven, W. A. Mozart and A. Ďvorák. I would like to express my special thanks to Radiohead for their constant presence and support along these years.

To all my relatives and friends: I hope that my gestures will be more meaningful than few distilled words in a sheet of paper to express my infinite gratitude.

Bibliography

- R. Ahumada, C. A. Prieto, A. Almeida, F. Anders, S. F. Anderson, B. H. Andrews, B. Anguiano, R. Arcodia, and . Eric Armengaud. “The Sixteenth Data Release of the Sloan Digital Sky Surveys: First Release from the APOGEE-2 Southern Survey and Full Release of eBOSS Spectra”. *The Astrophysical Journal*, 249(1), June 2020. ISSN 1545-4282. doi: 10.3847/1538-4365/ab929e. URL <https://doi.org/10.3847/1538-4365/ab929e>.
- D. G. Algorry, J. F. Navarro, M. G. Abadi, L. V. Sales, M. Steinmetz, and F. Piontek. “Counterrotating stars in simulated galaxy discs”. *Monthly Notices of the Royal Astronomical Society*, 437(4):3596–3602, feb 2014. doi: 10.1093/mnras/stt2154.
- J. Binney. “Rotation and anisotropy of galaxies revisited”. *Monthly Notices of the Royal Astronomical Society*, 363(3):937–942, Nov 2005. ISSN 1365-2966. doi: 10.1111/j.1365-2966.2005.09495.x. URL <http://dx.doi.org/10.1111/j.1365-2966.2005.09495.x>.
- J. Binney and S. Tremaine. “*Galactic dynamics*”. Oxford University Press (OUP), 1987. URL <https://ui.adsabs.harvard.edu/abs/1987gady.book.....B>.
- K. Bundy, M. A. Bershady, D. R. Law, R. Yan, N. Drory, N. MacDonald, D. A. Wake, B. Cherinka, J. R. Sánchez-Gallego, A.-M. Weijmans, and et al. “Overview of the SDSS-IV MaNGA survey: Mapping Nearby Galaxies at Apache Point Observatory”. *The Astrophysical Journal*, 798(1):7, Dec 2014. ISSN 1538-4357. doi: 10.1088/0004-637x/798/1/7. URL <http://dx.doi.org/10.1088/0004-637x/798/1/7>.
- M. Bureau and E. Athanassoula. “Bar Diagnostics in Edge-On Spiral Galaxies. III. N-Body Simulations of Disks”. *The Astrophysical Journal*, 626(1):159–173, Jun 2005. ISSN 1538-4357. doi: 10.1086/430056. URL <http://dx.doi.org/10.1086/430056>.
- M. Cappellari. “Measuring the inclination and mass-to-light ratio of axisymmetric galaxies via anisotropic Jeans models of stellar kinematics”. *Monthly Notices of the Royal Astronomical Society*, 390(1):71–86, Oct 2008. ISSN 1365-2966. doi: 10.1111/j.1365-2966.2008.13754.x. URL <http://dx.doi.org/10.1111/j.1365-2966.2008.13754.x>.
- M. Cappellari. “Effect of Environment on Galaxies’ Mass-Size Distribution: Unveiling the Transition from outside-in to inside-out Evolution”. *The Astrophysical Journal Letters*, 778(1):L2, Nov. 2013. doi: 10.1088/2041-8205/778/1/L2.

- M. Cappellari. “Structure and Kinematics of Early-Type Galaxies from Integral Field Spectroscopy”. *Annual Review of Astronomy and Astrophysics*, 54(1):597–665, Sep 2016a. ISSN 1545-4282. doi: 10.1146/annurev-astro-082214-122432. URL <http://dx.doi.org/10.1146/annurev-astro-082214-122432>.
- M. Cappellari. “Improving the full spectrum fitting method: accurate convolution with Gauss–Hermite functions”. *Monthly Notices of the Royal Astronomical Society*, 466(1):798–811, Nov 2016b. ISSN 1365-2966. doi: 10.1093/mnras/stw3020. URL <http://dx.doi.org/10.1093/mnras/stw3020>.
- M. Cappellari and Y. Copin. “Adaptive spatial binning of integral-field spectroscopic data using Voronoi tessellations”. *Monthly Notices of the Royal Astronomical Society*, 342(2):345–354, Jun 2003. ISSN 1365-2966. doi: 10.1046/j.1365-8711.2003.06541.x. URL <http://dx.doi.org/10.1046/j.1365-8711.2003.06541.x>.
- M. Cappellari and E. Emsellem. “Parametric Recovery of Line-of-Sight Velocity Distributions from Absorption-Line Spectra of Galaxies via Penalized Likelihood”. *The Publications of the Astronomical Society of the Pacific*, 116(816):138–147, feb 2004. doi: 10.1086/381875.
- M. Cappellari, E. Emsellem, R. Bacon, M. Bureau, R. L. Davies, P. T. De Zeeuw, J. Falcon-Barroso, D. Krajnovi, H. Kuntschner, R. M. McDermid, and et al. “The SAURON project - X. The orbital anisotropy of elliptical and lenticular galaxies: revisiting the $(V/\sigma, \epsilon)$ diagram with integral-field stellar kinematics”. *Monthly Notices of the Royal Astronomical Society*, 379(2):418–444, Aug 2007. ISSN 1365-2966. doi: 10.1111/j.1365-2966.2007.11963.x. URL <http://dx.doi.org/10.1111/j.1365-2966.2007.11963.x>.
- M. Cappellari, E. Emsellem, D. Krajnović, R. M. McDermid, P. Serra, K. Alatalo, L. Blitz, M. Bois, F. Bournaud, M. Bureau, and et al. “The ATLAS^{3D} project - VII. A new look at the morphology of nearby galaxies: the kinematic morphology-density relation”. *Monthly Notices of the Royal Astronomical Society*, 416(3):1680–1696, Aug 2011. ISSN 0035-8711. doi: 10.1111/j.1365-2966.2011.18600.x. URL <http://dx.doi.org/10.1111/j.1365-2966.2011.18600.x>.
- M. Cappellari, N. Scott, K. Alatalo, L. Blitz, M. Bois, F. Bournaud, M. Bureau, A. F. Crocker, R. L. Davies, T. A. Davis, and et al. “The ATLAS^{3D} project – XV. Benchmark for early-type galaxies scaling relations from 260 dynamical models: mass-to-light ratio, dark matter, Fundamental Plane and Mass Plane”. *Monthly Notices of the Royal Astronomical Society*, 432(3):1709–1741, May 2013. ISSN 0035-8711. doi: 10.1093/mnras/stt562. URL <http://dx.doi.org/10.1093/mnras/stt562>.
- L. Coccato, L. Morelli, E. M. Corsini, L. Buson, A. Pizzella, D. Vergani, and F. Bertola. “Dating the formation of the counter-rotating stellar disc in the spiral galaxy NGC 5719 by disentangling its stellar populations”. *Monthly Notices of the Royal Astronomical Society: Letters*, 412(1):L113–L117, Feb 2011. ISSN 1745-3925. doi:

- 10.1111/j.1745-3933.2011.01016.x. URL <http://dx.doi.org/10.1111/j.1745-3933.2011.01016.x>.
- L. Coccato, L. Morelli, A. Pizzella, E. M. Corsini, L. M. Buson, and E. Dalla Bontà. “Spectroscopic evidence of distinct stellar populations in the counter-rotating stellar disks of NGC 3593 and NGC 4550”. *Astronomy & Astrophysics*, 549:A3, Dec 2012. ISSN 1432-0746. doi: 10.1051/0004-6361/201220460. URL <http://dx.doi.org/10.1051/0004-6361/201220460>.
- L. Coccato, M. Fabricius, L. Morelli, E. M. Corsini, A. Pizzella, P. Erwin, E. Dalla Bontà, R. Saglia, R. Bender, and M. Williams. “Properties and formation mechanism of the stellar counter-rotating components in NGC 4191”. *Astronomy & Astrophysics*, 581:A65, Sep 2015. ISSN 1432-0746. doi: 10.1051/0004-6361/201526560. URL <http://dx.doi.org/10.1051/0004-6361/201526560>.
- E. M. Corsini. “Counter-Rotation in Disk Galaxies”, 2014.
- A. F. Crocker, H. Jeong, S. Komugi, F. Combes, M. Bureau, L. M. Young, and S. Yi. “Molecular gas and star formation in the red-sequence counter-rotating disc galaxy NGC 4550”. *Monthly Notices of the Royal Astronomical Society*, 393(4):1255–1264, Mar 2009. ISSN 1365-2966. doi: 10.1111/j.1365-2966.2008.14295.x. URL <http://dx.doi.org/10.1111/j.1365-2966.2008.14295.x>.
- S. M. Croom, J. S. Lawrence, J. Bland-Hawthorn, J. J. Bryant, L. Fogarty, S. Richards, M. Goodwin, T. Farrell, S. Mizziarski, R. Heald, D. H. Jones, S. Lee, M. Colless, S. Brough, A. M. Hopkins, A. E. Bauer, M. N. Birchall, S. Ellis, A. Horton, S. Leon-Saval, G. Lewis, Á. R. López-Sánchez, S.-S. Min, C. Trinh, and H. Trowland. “The Sydney-AAO Multi-object Integral field spectrograph”. *Monthly Notices of the Royal Astronomical Society*, 421(1):872–893, mar 2012. doi: 10.1111/j.1365-2966.2011.20365.x. URL <https://ui.adsabs.harvard.edu/abs/2012MNRAS.421..872C>.
- N. Drory, N. MacDonald, M. A. Bershad, K. Bundy, J. Gunn, D. R. Law, M. Smith, R. Stoll, C. A. Tremonti, D. A. Wake, and et al. “The MaNGA Integral-Field Unit fiber feed system for the SLOAN 2.5 m telescope”. *The Astronomical Journal*, 149(2):77, Jan 2015. ISSN 1538-3881. doi: 10.1088/0004-6256/149/2/77. URL <http://dx.doi.org/10.1088/0004-6256/149/2/77>.
- E. Emsellem, M. Cappellari, R. F. Peletier, R. M. McDermid, R. Bacon, M. Bureau, Y. Copin, R. L. Davies, D. Krajnović, H. Kuntschner, and et al. “The SAURON project – III. Integral-field absorption-line kinematics of 48 elliptical and lenticular galaxies”. *Monthly Notices of the Royal Astronomical Society*, 352(3):721–743, Aug 2004. ISSN 0035-8711. doi: 10.1111/j.1365-2966.2004.07948.x. URL <http://dx.doi.org/10.1111/j.1365-2966.2004.07948.x>.
- E. Emsellem, M. Cappellari, D. Krajnovi, G. Van De Ven, R. Bacon, M. Bureau, R. L. Davies, P. T. De Zeeuw, J. Falcon-Barroso, H. Kuntschner, and et al. “The SAURON

- project - IX. A kinematic classification for early-type galaxies”. *Monthly Notices of the Royal Astronomical Society*, 379(2):401–417, Aug 2007. ISSN 1365-2966. doi: 10.1111/j.1365-2966.2007.11752.x. URL <http://dx.doi.org/10.1111/j.1365-2966.2007.11752.x>.
- E. Emsellem, M. Cappellari, D. Krajnović, K. Alatalo, L. Blitz, M. Bois, F. Bournaud, M. Bureau, R. L. Davies, T. A. Davis, and et al. “The ATLAS^{3D} project - III. A census of the stellar angular momentum within the effective radius of early-type galaxies: unveiling the distribution of fast and slow rotators”. *Monthly Notices of the Royal Astronomical Society*, 414(2):888–912, May 2011. ISSN 0035-8711. doi: 10.1111/j.1365-2966.2011.18496.x. URL <http://dx.doi.org/10.1111/j.1365-2966.2011.18496.x>.
- N. Evans and J. Collett. “Separatrix Crossing and the Enigma of NGC 4550”. *The Astrophysical Journal Letters*, 420:L67, jan 1994. doi: 10.1086/187164.
- J. Falcón-Barroso, P. Sánchez-Blázquez, A. Vazdekis, E. Ricciardelli, N. Cardiel, A. J. Cenarro, J. Gorgas, and R. F. Peletier. “An updated MILES stellar library and stellar population models”. *Astronomy & Astrophysics*, 532:A95, Jul 2011. ISSN 1432-0746. doi: 10.1051/0004-6361/201116842. URL <http://dx.doi.org/10.1051/0004-6361/201116842>.
- J. Ge, R. Yan, M. Cappellari, S. Mao, H. Li, and Y. Lu. “Recovering stellar population parameters via two full-spectrum fitting algorithms in the absence of model uncertainties”. *Monthly Notices of the Royal Astronomical Society*, 478(2):2633–2649, May 2018. ISSN 1365-2966. doi: 10.1093/mnras/sty1245. URL <http://dx.doi.org/10.1093/mnras/sty1245>.
- L. Girardi, A. Bressan, G. Bertelli, and C. Chiosi. “Evolutionary tracks and isochrones for low- and intermediate-mass stars: From 0.15 to 7 M_{sun} , and from $Z=0.0004$ to 0.03”. *Astronomy & Astrophysics Supplement Series*, 141:371–383, Feb. 2000. doi: 10.1051/aas:2000126.
- M. T. Graham, M. Cappellari, M. A. Bershadsky, and N. Drory. “SDSS-IV MaNGA: New benchmark for the connection between stellar angular momentum and environment: a study of about 900 groups/clusters”, 2019.
- B. Groves, J. Brinchmann, and C. J. Walcher. “The Balmer decrement of Sloan Digital Sky Survey galaxies”. *Monthly Notices of the Royal Astronomical Society*, 419(2): 1402–1412, Nov 2011. ISSN 0035-8711. doi: 10.1111/j.1365-2966.2011.19796.x. URL <http://dx.doi.org/10.1111/j.1365-2966.2011.19796.x>.
- Y. Jin, Y. Chen, Y. Shi, C. A. Tremonti, M. A. Bershadsky, M. Merrifield, E. Emsellem, H. Fu, D. Wake, K. Bundy, and et al. “SDSS-IV MaNGA: properties of galaxies with kinematically decoupled stellar and gaseous components”. *Monthly Notices of the Royal Astronomical Society*, 463(1):913–926, Aug 2016. ISSN 1365-2966. doi: 10.1093/mnras/stw2055. URL <http://dx.doi.org/10.1093/mnras/stw2055>.

- E. J. Johnston, M. R. Merrifield, A. Aragón-Salamanca, and M. Cappellari. “Disentangling the stellar populations in the counter-rotating disc galaxy NGC 4550”. *Monthly Notices of the Royal Astronomical Society*, 428(2):1296–1302, Oct 2012. ISSN 0035-8711. doi: 10.1093/mnras/sts121. URL <http://dx.doi.org/10.1093/mnras/sts121>.
- I. Y. Katkov, O. K. Sil’chenko, and V. L. Afanasiev. “Lenticular galaxy IC 719: current building of the counterrotating large-scale stellar disk”. *The Astrophysical Journal*, 769(2):105, May 2013. ISSN 1538-4357. doi: 10.1088/0004-637x/769/2/105. URL <http://dx.doi.org/10.1088/0004-637X/769/2/105>.
- I. Y. Katkov, O. K. Sil’chenko, I. V. Chilingarian, R. I. Uklein, and O. V. Egorov. “Stellar counter-rotation in lenticular galaxy NGC 448”. *Monthly Notices of the Royal Astronomical Society*, 461(2):2068–2076, sep 2016. doi: 10.1093/mnras/stw1452.
- D. Krajnovic, E. Emsellem, M. Cappellari, K. Alatalo, L. Blitz, M. Bois, F. Bournaud, M. Bureau, R. L. Davies, T. A. Davis, and et al. “The ATLAS^{3D} project - II. Morphologies, kinematic features and alignment between photometric and kinematic axes of early-type galaxies”. *Monthly Notices of the Royal Astronomical Society*, 414(4):2923–2949, Jun 2011. ISSN 0035-8711. doi: 10.1111/j.1365-2966.2011.18560.x. URL <http://dx.doi.org/10.1111/j.1365-2966.2011.18560.x>.
- D. Krajnovic, P. M. Weilbacher, T. Urrutia, E. Emsellem, C. M. Carollo, M. Shirazi, R. Bacon, T. Contini, B. Epinat, S. Kamann, T. Martinsson, and M. Steinmetz. “Unveiling the counter-rotating nature of the kinematically distinct core in NGC5813 with MUSE”, apr 2015.
- D. Krajnović, A. M. Karick, R. L. Davies, T. Naab, M. Sarzi, E. Emsellem, M. Cappellari, P. Serra, P. T. de Zeeuw, N. Scott, and et al. “The ATLAS^{3D} Project – XXIII. Angular momentum and nuclear surface brightness profiles”. *Monthly Notices of the Royal Astronomical Society*, 433(4):2812–2839, Jul 2013. ISSN 0035-8711. doi: 10.1093/mnras/stt905. URL <http://dx.doi.org/10.1093/mnras/stt905>.
- D. R. Law, B. Cherinka, R. Yan, B. H. Andrews, M. A. Bershadsky, D. Bizyaev, G. A. Blanc, M. R. Blanton, A. S. Bolton, J. R. Brownstein, and et al. “The Data Reduction Pipelin for the SDSS-IV MaNGA IFU galaxy survey”. *The Astronomical Journal*, 152(4):83, Sep 2016. ISSN 1538-3881. doi: 10.3847/0004-6256/152/4/83. URL <http://dx.doi.org/10.3847/0004-6256/152/4/83>.
- M. Mitzkus, M. Cappellari, and C. J. Walcher. “Dominant dark matter and a counter-rotating disc: MUSE view of the low-luminosity S0 galaxy NGC 5102”. *Monthly Notices of the Royal Astronomical Society*, 464(4):4789–4806, Oct 2016. ISSN 1365-2966. doi: 10.1093/mnras/stw2677. URL <http://dx.doi.org/10.1093/mnras/stw2677>.
- L. Morelli, A. Pizzella, L. Coccato, E. M. Corsini, E. Dalla Bontà, L. M. Buson, V. D. Ivanov, I. Pagotto, E. Pompei, and M. Rocco. “Kinematic and stellar population properties of the counter-rotating components in the S0 galaxy NGC 1366”. *Astronomy & Astrophysics*, 600:A76, apr 2017. doi: 10.1051/0004-6361/201630046.

- P. Ocvirk, C. Pichon, A. Lançon, and E. Thiébaud. “STECMAP: STEllar Content from high-resolution galactic spectra via Maximum A Posteriori”. *Monthly Notices of the Royal Astronomical Society*, 365(1):46–73, jan 2006. doi: 10.1111/j.1365-2966.2005.09182.x.
- A. Pizzella, L. Morelli, E. M. Corsini, E. Dalla Bontà, L. Coccato, and G. Sanjana. “The difference in age of the two counter-rotating stellar disks of the spiral galaxy NGC 4138”. *Astronomy & Astrophysics*, 570:A79, oct 2014. doi: 10.1051/0004-6361/201424746.
- A. Pizzella, L. Morelli, L. Coccato, E. M. Corsini, E. Dalla Bontà, M. Fabricius, and R. P. Saglia. “Evidence for the formation of the young counter-rotating stellar disk from gas acquired by IC 719”. *Astronomy & Astrophysics*, 616:A22, Aug 2018. ISSN 1432-0746. doi: 10.1051/0004-6361/201731712. URL <http://dx.doi.org/10.1051/0004-6361/201731712>.
- W. Press, S. Teukolsky, W. Vetterling, and B. Flannery. “*Numerical Recipes: The Art of Scientific Computing*”. Cambridge University Press, 3 edition, 2007. ISBN 9780521880688. URL <http://nr.com/>.
- I. Puerari and D. Pfenniger. “Formation Of Massive Counter-Rotating Disks: An Alternative Scenario”. *Astrophysics and Space Science*, 276(2/4):909–914, 2001. ISSN 0004-640X. doi: 10.1023/a:1017581325673. URL <http://dx.doi.org/10.1023/A:1017581325673>.
- H.-W. Rix, M. Franx, D. Fisher, and G. Illingworth. “NGC 4550: A Laboratory for Testing Galaxy Formation”. *The Astrophysical Journal Letters*, 400:L5, nov 1992. doi: 10.1086/186635.
- V. C. Rubin, J. A. Graham, and J. D. P. Kenney. “Cospatial Counterrotating Stellar Disks in the Virgo E7/S0 Galaxy NGC 4550”. *AphJ*, 394:L9, jul 1992. doi: 10.1086/186460.
- P. Sanchez-Blazquez, R. F. Peletier, J. Jimenez-Vicente, N. Cardiel, A. J. Cenarro, J. Falcon-Barroso, J. Gorgas, S. Selam, and A. Vazdekis. “Medium-resolution Isaac Newton Telescope library of empirical spectra”. *Monthly Notices of the Royal Astronomical Society*, 371(2):703–718, Sep 2006. ISSN 1365-2966. doi: 10.1111/j.1365-2966.2006.10699.x. URL <http://dx.doi.org/10.1111/j.1365-2966.2006.10699.x>.
- M. Sarzi, J. Falcón-Barroso, R. L. Davies, R. Bacon, M. Bureau, M. Cappellari, P. T. de Zeeuw, E. Emsellem, K. Fathi, D. Krajnović, H. Kuntschner, R. M. McDermid, and R. F. Peletier. “The SAURON project - V. Integral-field emission-line kinematics of 48 elliptical and lenticular galaxies”. *Monthly Notices of the Royal Astronomical Society*, 366(4):1151–1200, Mar. 2006. doi: 10.1111/j.1365-2966.2005.09839.x.
- S. A. Smee, J. E. Gunn, A. Uomoto, N. Roe, D. Schlegel, C. M. Rockosi, M. A. Carr, F. Leger, K. S. Dawson, M. D. Olmstead, J. Brinkmann, R. Owen, R. H. Barkhouser,

- K. Honscheid, P. Harding, D. Long, R. H. Lupton, C. Loomis, L. Anderson, J. Annis, M. Bernardi, V. Bhardwaj, D. Bizyaev, A. S. Bolton, H. Brewington, J. W. Briggs, S. Burles, J. G. Burns, F. J. Castander, A. Connolly, J. R. A. Davenport, G. Ebelke, H. Epps, P. D. Feldman, S. D. Friedman, J. Frieman, T. Heckman, C. L. Hull, G. R. Knapp, D. M. Lawrence, J. Loveday, E. J. Mannery, E. Malanushenko, V. Malanushenko, A. J. Merrelli, D. Muna, P. R. Newman, R. C. Nichol, D. Oravetz, K. Pan, A. C. Pope, P. G. Ricketts, A. Shelden, D. Sandford, W. Siegmund, A. Simmons, D. S. Smith, S. Snedden, D. P. Schneider, M. SubbaRao, C. Tremonti, P. Wadell, and D. G. York. “The Multi-object, Fiber-fed Spectrographs for the Sloan Digital Sky Survey and the Baryon Oscillation Spectroscopic Survey”. *The Astronomical Journal*, 146(2):32, Aug. 2013. doi: 10.1088/0004-6256/146/2/32.
- M. Tabor, M. Merrifield, A. Aragón-Salamanca, M. Cappellari, S. P. Bamford, and E. Johnston. “Untangling galaxy components: full spectral bulge–disc decomposition”. *Monthly Notices of the Royal Astronomical Society*, 466(2):2024–2033, Dec 2016. ISSN 1365-2966. doi: 10.1093/mnras/stw3183. URL <http://dx.doi.org/10.1093/mnras/stw3183>.
- A. R. Thakar and B. S. Ryden. “Formation of Massive Counterrotating Disks in Spiral Galaxies”. *The Astrophysical Journal*, 461:55, Apr. 1996. doi: 10.1086/177037.
- A. R. Thakar and B. S. Ryden. “Smoothed particle hydrodynamics simulations of counterrotating disk formation in Spiral Galaxies”. *The Astrophysical Journal*, 506(1): 93–115, oct 1998. doi: 10.1086/306223.
- A. R. Thakar, B. S. Ryden, K. P. Jore, and A. H. Broeils. “NGC 4138: a case study in counterrotating disk formation”. *The Astrophysical Journal*, 479(2):702–722, apr 1997. doi: 10.1086/303915.
- R. P. van der Marel and M. Franx. “A New Method for the Identification of Non-Gaussian Line Profiles in Elliptical Galaxies”. *The Astrophysical Journal*, 407:525, apr 1993. doi: 10.1086/172534.
- A. Vazdekis, P. Sánchez-Blázquez, J. Falcón-Barroso, A. J. Cenarro, M. A. Beasley, N. Cardiel, J. Gorgas, and R. F. Peletier. “Evolutionary stellar population synthesis with MILES - I. The base models and a new line index system”. *Monthly Notices of the Royal Astronomical Society*, Mar 2010. ISSN 1365-2966. doi: 10.1111/j.1365-2966.2010.16407.x. URL <http://dx.doi.org/10.1111/j.1365-2966.2010.16407.x>.
- A. Vazdekis, E. Ricciardelli, A. J. Cenarro, J. G. Rivero-González, L. A. Díaz-García, and J. Falcón-Barroso. “MIUSCAT: extended MILES spectral coverage - I. Stellar population synthesis models”. *Monthly Notices of the Royal Astronomical Society*, 424(1):157–171, Jun 2012. ISSN 0035-8711. doi: 10.1111/j.1365-2966.2012.21179.x. URL <http://dx.doi.org/10.1111/j.1365-2966.2012.21179.x>.

- D. Vergani, A. Pizzella, E. M. Corsini, W. van Driel, L. M. Buson, R. J. Dettmar, and F. Bertola. “NGC 5719/13: interacting spirals forming a counter-rotating stellar disc”. *Astronomy & Astrophysics*, 463(3):883–892, mar 2007. doi: 10.1051/0004-6361:20066413.
- B. Wang, M. Cappellari, and Y. Peng. “Physical explanation for the galaxy distribution on the (λ_R, ε) and $(V/\sigma, \varepsilon)$ diagrams or for the limit on orbital anisotropy”. *Monthly Notices of the Royal Astronomical Society: Letters*, 500(1):L27–L31, Jan 2020. ISSN 1745-3933. doi: 10.1093/mnrasl/slaa176. URL <http://dx.doi.org/10.1093/mnrasl/slaa176>.
- K. B. Westfall, M. Cappellari, M. A. Bershad, K. Bundy, F. Belfiore, X. Ji, D. R. Law, A. Schaefer, S. Shetty, C. A. Tremonti, and et al. “The Data Analysis Pipeline for the SDSS-IV MaNGA IFU Galaxy Survey: Overview”. *The Astronomical Journal*, 158(6):231, Nov 2019. ISSN 1538-3881. doi: 10.3847/1538-3881/ab44a2. URL <http://dx.doi.org/10.3847/1538-3881/ab44a2>.